THE EFFECTS OF MULTIPLE LARGE SCALE ASPERITIES ON DEFORMATION AND PERMEABILITY OF A SINGLE FRACTURE

GRAHAM DOUGLAS DILLABOUGH

THE EFFECTS OF MULTIPLE LARGE SCALE ASPERITIES ON DEFORMATION AND PERMEABILITY OF A SINGLE FRACTURE

by

© Graham Douglas Dillabough, B.Sc., P.Geol.

A thesis submitted to the School of Graduate Studies
in partial fulfillment of the Requirements for the degree of
Master of Science

Department of Earth Sciences,
Memorial University of Newfoundland

St. John's, Newfoundland

1996

Abstract

The testing of physical analogues has been shown to be important in the development of theoretical models describing the relationships between fluid flow in fracture systems, and the state of stress and deformation within the host rock of the fracture. The flow and transport characteristics related to fracturing are often enhanced by the effects of the state of stress in the rock walls, which may open up secondary pathways and cause chemical alterations in the wall rocks.

The objective of this study was to describe the influence of two, parallel, large scale fracture roughness asperities on: 1) the fracture stiffness, displacement and hydraulic transmissivity, 2) the local stress field in the adjacent wall rock, 3) the mode and patterns of secondary fracturing, and 4) the effects on host rock permeability all as a function of changes in both normal and shear stress. The overall study approach included a series of experiments on an instrumented high strength concrete model of a fracture plane in a stiff biaxial loading frame, and comparison of the experimental data with numerical model simulations.

The concrete model (200 x 200 x 300 millimetres) was cast with 92 strain gauges mounted on concrete coupons embedded along the centre of the model, and 17 manometer ports intersecting the fracture plane to measure the fluid pressures across the length of the model. The fracture plane was formed by pressing an aluminium plate matching the form of the asperities into the wet concrete. This plate was separated from the wet concrete by a piece of geotextile. When the concrete was set, the second half of the model was cast on the geotextile (which was left in place). This geotextile provided the form of a uniform small scale roughness on the fracture surface after the blocks were separated. Four 6.4 millimetre diameter wells were drilled into the top of the model. These wells were used to estimate the matrix permeability changes of the concrete of the model as it was subjected to changing load conditions.

Results of the study confirmed that the large scale asperities had a significant influence on the local strain field, as seen in the data recovered from the 78 strain gauges that survived the casting and pre-test processes. Three normal and four shear loading cycles showed repeatable internal strain patterns that reflected the effects of the applied boundary conditions.

Fracturing in the model was assumed to be caused by tensile stress concentrations at the base of the asperities, and at the ends of the sample.

Displacement data indicate permanent normal closure of the fracture was greatest for the first normal loading cycle, and decreased over the following two cycles. During the final four cycles, the permanent fracture closure became essentially identical at about 20 per cent of the original closure. This suggests that fracture seating occurred during the first normal loading cycle, which is consistent with other experimental work.

Fracture transmissivity was seen to decrease logarithmically with the cube root of the normal stress applied to the sample, and decreased further as the sample was sheared, causing closure of the aperture at the large scale asperities.

The four wells drilled into the top of the model were pressurised with 345 kPa (50 psi) water, and shut in. The pressure decline of each well was monitored sequentially throughout the shear cycles and these data were used to estimate the relative permeability of the concrete. All four wells showed similar decline curves over the periods that each well was

monitored. There was no indication that the permeability of the concrete was enhanced by the shear stress applied except by the propagation of secondary fracturing through the wells as the concrete failed.

The post-test finite element analysis confirmed the assumption that induced tensile fracturing was the primary mode of failure in this experiment. Under normal load, finite element analysis showed that the large scale asperities caused local changes in the orientation of the stress field. Under combined normal and shear load, there were significant tensile stress concentrations associated with the restraining and releasing bends of the fracture, which provided the focus points for the onset of failure of the blocks.

Acknowledgments

Completion of the research outlined in this thesis and the survival of my return to university after an absence of almost thirteen years has involved the guidance, support, and friendship of numerous individuals and organizations whom I would now like to acknowledge. First of all, I would like to thank my supervisor, Professor John Gale, who took a chance in taking me in as a graduate student on short notice. It was Dr. Gale that provided the initial concept for and directed the research. He provided guidance, feedback and also assisted in the assembly and testing of the physical model, as well as much appreciated financial support. I would like to thank Lisa Pennell and Alison Pye for their assistance in various stages of the laboratory work during this investigation. I would like to thank fellow students Jim Slade, Jason Bourgeois, and Phyllis McCrindle for their able assistance during the marathon testing phase of the project, and their feedback and friendship when I needed it. Steve Butt developed much of the software essential to the testing of this sample, and provided much appreciated input and help at various stages of the project. Austin Bursey and Calvin Ward from the engineering department provided technical advice and the loan of data acquisition and concrete making equipment that was

essential to this project. Irene Meglis read portions of the early drafts of this thesis, and assisted in rewriting an early draft of Chapter 1.

This study was part of an overall research project, headed and directed by Dr. J. E. Gale, examining the impact of fractures on enhanced hydrocarbon recovery from fractured reservoirs and was funded by Supply and Services Canada for the Center for Mineral and Energy Technology, Shell Canada Ltd., Hibernia Management Development Corporation, Fracflow Consultants Inc., Imperial Oil Limited, Tallisman Energy Inc., and PanCanadian Petroleum, with additional funding provided by an NSERC operating grant to Dr. Gale. Thanks are extended to these organizations for funding this research. It should be noted at this point that the copyright on this thesis does not take precedence over the contract report for above noted funding agencies.

Chapters 1, 2 and portions of chapter 3 are based on the manuscript for Dillabough and Gale (1996). I would like to extend my thanks to Dr. Gale for his assistance in preparing those sections and his permission to use them here.

I would like to take this opportunity to thank several individuals that have helped out in ways not directly related to this thesis. Pam Darwin, my former supervisor at Exxon in New Orleans gets a **BIG** thank you for writing all of those university reference letters for me while in the midst of the latter stages of pregnancy, a career change, and moving house to a different city. Also, I cannot forget the contributions of Dale Jones, Allen Berlin, John Hoholick and John Greenhouse for the same bunch of reference letters and help in rewriting my resume. I also would like to thank my many friends at Memorial for being friends and putting up with me. They include Jason Bourgeois and Sandy Archibald, both of whom I shared an office with, Karren Watson, Alan Cull, and Jocelyn Tucker who were more than great students to be a T.A. for, and many others who gave me laughs and good memories. Thank you everyone!

Most importantly, none of this would have been possible without the love, support and tolerance of my family. To my wife Joy, and son Daniel, thank you for your support and love, and I promise I'll make up for all of those lost weekends soon. To all of Joy's family, Dan and Emily (dad and mom), Carol and George, Roy, Perry, Margaret and the kids, and all of the others "out the bay", thanks for making me feel welcome and part of the family. To my

mother Madeline and brother Scott: even though you were far away during these three years at Memorial, your support and love are appreciated.

Finally, much of this work was made possible by the skills, knowledge and mechanical and electrical "horse sense" that I received from my father, over half of my lifetime ago. I wish you were here so that I could say "Thanks Dad".

Table of Contents

List of Figures

List of Tables

List of Symbols and Abbreviations

ASTM	American Society for Testing of Materials
CSFFC	Coupled Stress Fracture Flow Code (Gale 1975)
Gpa	Giga Pascal = 1E9 Newton/metre^2
JRC	Joint Roughness Coefficient
LSR-1	Large Scale Roughness - 1 (Butt, 1994)
LSR-2	Large Scale Roughness - 2 (Dillabough, 1996)
LVDT	Linear Voltage Displacement Transducer
MPa	Mega Pascal = 1E6 Newton/metre^2
N1	Abbreviation for the test cycle Normal 1
N2	Abbreviation for the test cycle Normal 2
N3	Abbreviation for the test cycle Normal 3
PC	Personal Computer, IBM Compatible
PSS	Principal Slip Surface (see Sibson, 1986)
Rosette	Grouping of 3 strain gauges, oriented at 45° to each other.
S1	Abbreviation for the test cycle Shear 1
S2	Abbreviation for the test cycle Shear 2
S3a	Abbreviation for the test cycle Shear 3a
S3b	Abbreviation for the test cycle Shear 3b
W1	Abbreviation for permeability test well 1
W2	Abbreviation for permeability test well 2
W3	Abbreviation for permeability test well 3
W4	Abbreviation for permeability test well 4
σ_{max}	Maximum Principal Stress
σ_{min}	Minimum Principal Stress
σ_{vert}	Stress resolved into vertical direction
σ_{horiz}	Stress resolved into horizontal direction
α	Angle of principal stress from vertical (see CSFFC)

Chapter 1 Introduction

1.1 Statement of Problem

Discontinuities have an important influence on the strength, deformational and flow characteristics of rock systems. Properties of the discontinuities, in the rock mass, include orientation, extent, planarity, roughness, aperture and the strength of wall rock asperities. Roughness, which influences the friction angle, dilatancy and peak shear strength, refers to the local departures from planarity of the discontinuity at both small and large scales, (i.e. short or long lengths of the fracture trace or cross-sectional profile) over which the roughness is measured. The surface friction of smooth rock and mineral surfaces derives from micro-interlocking and adhesion, which may require rock breakage for sliding, as well as "ploughing" of harder minerals into a softer matrix. The friction angle of a rock discontinuity is defined as the critical angle for sliding of one rock block against another as the angle of the discontinuity is increased.

Several authors (Sholtz (1990), Lee et al. (1990)) have shown that the roughness of both fracture and large scale fault planes can be considered to be fractal. As such they are characterised, in a relative sense, by a continuous range of size of roughness features ranging from small scale (microscopic to millimetres) to large scale (centimetres to several tens of metres). While the

relationship between the strength and permeability of small scale roughness can be added by combining the basic surface friction with the local roughness term, the "i" term of Rengers (1970), characterising the contribution of large scale asperities to shear strength and hydraulic properties, has been more problematic. Barton et al (1985) used the Joint Roughness Coefficient (JRC) to include the strength properties of the large scale asperities for regular fracture planes, with trace lengths measuring on the order of metres to tens of metres. The Joint Roughness Coefficient is obtained from physical testing on samples as follows:

$$JRC = \frac{\alpha - \phi_r}{\log(JCS/\sigma'_{no})}, \quad \text{where:}$$

α = tilt angle when sliding occurs;
σ'_{no} = corresponding value of effective normal stress when sliding occurs (weigh upper sample, correct for cosα, measure joint area)
ϕ_r = residual friction angle (friction angle after sliding has commenced)
JCS = joint wall compression strength.

For large scale fault zones, the large scale roughness or asperities, referred to as jogs, are thought to form locking points on fault planes that are in a condition of incipient failure as defined by Scholz (1990) (Figure 1-1). As failure or macroslip approaches, it is assumed that sliding occurs on those parts of the

fault plane that are characterised by small scale roughness. However, at the locking points, the shear displacement or slip is restricted, resulting in zones of stress concentration being created in the rock mass around the jog with corresponding changes in the normal and shear stress acting on the fault/fracture plane.

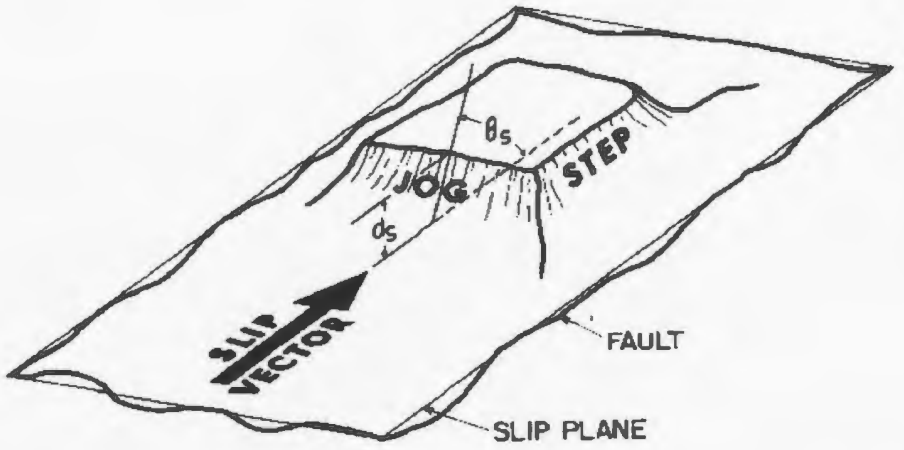

Figure 1-1: Schematic diagram illustrating the definition of jogs and steps. (Scholz, 1990, Fig. 3.28)

Conceptual models for large scale fault jogs presented by both Sibson (1986) and Scholz (1990) suggest the presence of a zone of compressional stress on the restraining bend and tensional stress on the releasing bend of the jog, and thus any slip taking place at the jog would involve volumetric strain. This volumetric strain at the locking point(s) is assumed to take place by the creation

of new fractures in the rock mass and/or by failure along existing fractures in the jog.

It has been seen in field observations that both small and large scale fault/fracture jogs are characterised by a series of "en echelon" tensile or shear fractures, with cross cutting connecting fractures (Gamond, 1987; Sibson, 1986; Segall and Pollard, 1983).

Consistent with the conceptual models discussed above, a map detailing the fracturing associated with the rupture trace of the Borrego Mountain earthquake (Figure 1-2) has been provided by Sibson (1986). It was suggested by Sibson (1986) in this review that the fracturing from this fault movement increased the permeability of the host rock in the vicinity of the fault. However, this paper was mostly conceptual and did not included field measurements to confirm this assumption.

There have been a few indirect field experiments to measure changes in fracture permeability and porosity within and adjacent to fault zones as reviewed by Pratt et al. (1977). However, we are only aware of the direct field measurements by Martin et al. (1990) of both stress concentrations and

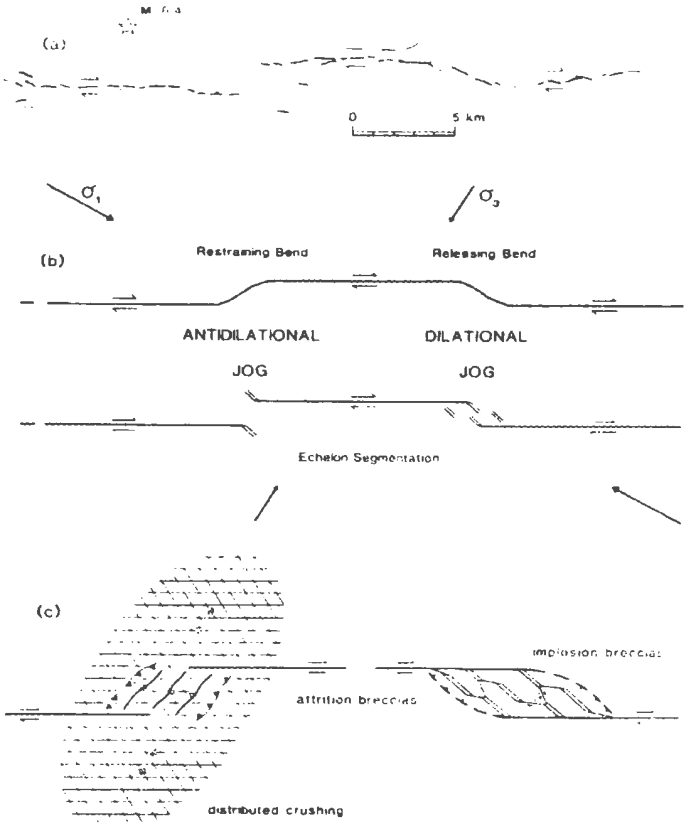

Figure 1-2: Effect of Brittle PSS (Principal Slip Surface) infrastructure on brecciation processes in fault zones: (a) surface-rupture of the 1968 M_L 6.4 Borrego Mountain earthquake (star represents epicentre), showing broad-scale infrastructure; (b) classification of infrastructure into dilational and antidilational jogs with respect to slip sense and far-field principal compressive stresses ($\sigma_1 > \sigma_2 > \sigma_3$); (c) inferred internal structure of strike-slip fault jogs, showing association with different brecciation processes (thrusts represented by sawtooth lines, fold axial traces by thick wavy lines, subsidiary strike-slip faults by cris-cross lines, vertical extension fractures by thin parallel lines, and normal faults by thick dashed lines with tick on downthrown side). (Sibson 1986, Figure 2).

associated changes in fracture permeability at a fault jog. The close association of mineralised zones due to hydrothermal processes with specific

sections of large fault structures have been noted by many workers (Bjorlykke (1993), Kamineni et al. (1993), Morrow and Byerlee (1992) etc.). The hydrothermal alteration of wall rock adjacent to fractures and the presence of infilling vein minerals suggest increased permeability and porosity in these parts of the rock mass along and within the fault zone, relative to other sections along the same fault zone. It is apparent from these observations that a clear understanding of the stress and hydraulic conditions within and adjacent to large scale asperities is critical to understanding the role that the asperities play in fluid movement through fractured and faulted rock masses.

In naturally fractured rock, given that laboratory and field studies have demonstrated that the permeability and porosity of fractures are stress dependent (see Brace (1978) for review), it can be assumed that the stress concentrations created by jogs will have significant impact on the permeability and porosity of the fracture system making up the fault plane as well as in the adjoining rock mass.

The changes in the stress field along the fault trace and within the rock mass will change the normal and shear stress acting on the discrete fracture planes resulting in either closure or opening of the fractures within the zone of stress

concentration, thereby decreasing or increasing the permeability of that zone. In addition, changing stress concentrations can cause the formation of new fractures, which can increase the rock mass fracture permeability through the opening of new interconnections and pathways. Such changes in permeability must be accommodated in engineering and geotechnical applications such as nuclear waste disposal, subsurface contaminant transport, petroleum and minerals exploration and recovery, and dam engineering and construction.

Large scale investigations of fractured rock are complicated by many factors. These factors include limited knowledge of the 3D fracture geometry, and permeability plus unknown flow and stress boundary conditions. Therefore, laboratory testing of physical models, or analogues, under controlled conditions, is an important and convenient process for developing and evaluating theoretical models that describe the relationships between the state of stress and deformation within the host rock and their impact on the fluid flow characteristics of the associated fracture systems.

1.2 Scope and Objectives

Natural fractures and faults rarely contain a single jog or large scale asperity. Therefore, it is important to establish how multiple large scale asperities, or jogs,

affects the changes observed when the fracture plane contain only one large scale asperity (Butt, 1994). It is assumed that when several asperities are in close proximity on the same fracture plane there will be a transfer of shear load between the large scale asperities which cause changing patterns in the matrix/fracture permeability. To investigate the effects of this load transfer on changes in stress, strain, and permeability, both within the fracture plane and the adjacent matrix, a physical model was constructed, containing two large scale asperities. The overall dimensions of the physical model were 200 mm by 200 mm by 300 mm and the two asperities, each 10 mm high, 35 mm wide at the base, 15 mm wide at the top, with a 45 degree slope, crossed the width of the fracture plane perpendicular to the shear direction. The experimental stress, strain and permeability data obtained from a series of tests on this physical model, for a range of normal and shear stress conditions, have been compared to numerical, discrete fracture, coupled stress-flow, simulations of the physical model.

After the testing process, the original and secondary fracture surfaces were observed directly by sectioning and coring of the model. Finite element numerical modelling was done to compare the strain distributions observed during testing with the stress distribution predicted by the Coupled Stress

Fracture Flow Code (Gale 1975). All data were integrated and compared to observations of changes in the flow characteristics of the artificial fracture in the model.

1.3 Previous Work

Most of the initial physical analogue studies (Goodman 1976, 1980) have focused on the effects of the large scale roughness on the stress and deformation along the fracture plane. For example, Fishman (1990), using photoelastic materials, examined the stress distribution and inferred the failure modes in a fabricated 'sawtooth' type joint (Figure 1-3). Fishman's work showed that under shear loading, the compressive stress builds up across the ascending edges of the asperity with the highest concentrations located in the base and tips of the sawtooth asperities. His conclusion, similar to other authors, was that in real joints, "the contact of (joint) walls takes place not on the whole of the surface, but in a limited number of touches, the area of which is often not more than 1 - 5% of the total area of the joint" (Fishman 1990). From this it follows that the prevalent type of failure in a natural joint will be rotation and crushing of the asperities, which will in turn help increase the permeability of the fracture.

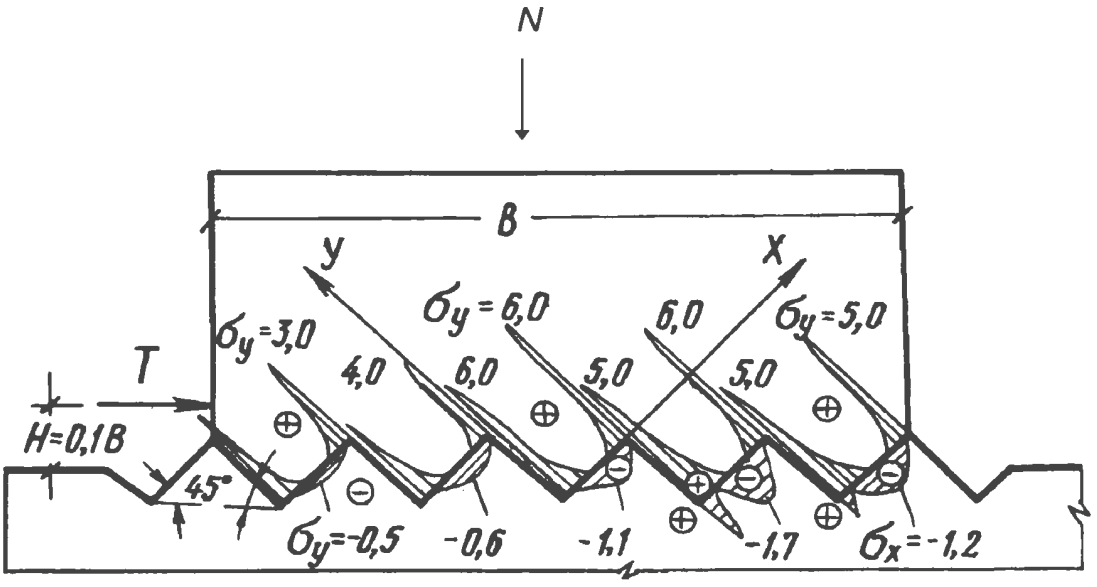

Figure 1-3: Stress Distribution in a "Sawtooth" Joint (Fishman, (1990), Fig. 2)

However, in his experiments the material was not brittle and no measurements of strains or permeability were made.

Hyett and Hudson (1990) cast impressions of natural rough joint surfaces using a photoelastic material, and subjected these reassembled models to various shear and normal loads. Under normal loading, they observed significant stress concentrations at intermittent points of contact between the joint surfaces. With increasing normal load, these concentrations were reduced as the fracture surfaces deformed and the contact area increased. Under shear loading, they observed significant stress concentrations at the restraining bends.

Gamond (1987) shows similar results from observations of small fault zones in the French Alps. He observed evidence of pressure solution along the faces of restraining bends and the precipitation of veins along the dilated releasing bends. Pressure solution is a form of diffusive mass transfer where material in a stressed zone is dissolved by a pore fluid. The dissolved material is subsequently precipitated in a region of available pore space, such as the areas of the releasing bends at other locations along the fault.

Experiments have been conducted by several researchers on rough rock/steel interfaces to examine the failure modes of idealised high angle asperities. Handanyan et al. (1990) sheared triangular, spherical and rectangular models of asperities to failure under non-dilatant conditions. These models were cast using a high strength dental material, which had similar physical properties to a medium strength igneous rock. The authors observed combinations of shear fractures oriented parallel to the mean fracture plane and tensile fractures oriented approximately normal to the loaded bend face. Dilational shear experiments were completed on models constructed of gypsum by Fishman (1990). In these experiments, using the same fracture morphology as in his photoelastic study discussed previously, he observed that the asperities failed by rotation after a tension crack had propagated across the base of the asperity.

He derived equations predicting shear strength and dilatancy as a function of the rock crush strength, applied stresses, and the asperity dimensions. The differences in asperity failure modes between the two Fishman studies appear to be related to dilational constraints, with the rotation failure being easier under dilated conditions. Numerical simulations which predict the development of zones of high shear and tensile microcrack density on both sides of the loaded asperity face have been conducted by Aydan et al (1990) on rock asperities similar to those discussed above.

Jones (1975) conducted studies of fracture permeability in a variety of substances, including natural rock and Portland cement, under various states of normal stress. In relating to the present study, the key conclusion of his work was that the cube root of the permeability contributed by fractures was found to be a linear function of the logarithm of the confining pressure.

As noted earlier, Barton et al. (1985) summarised many years of their work by synthesising a coupled joint behaviour model which simulates stress and size-dependent coupling of normal and shear stress, displacement, closure and dilation, and conductivity. This model uses tilt tests, Schmidt rebound tests, and borehole pumping tests (if available) conducted on jointed core or on exposed

jointed blocks to obtain estimates of the roughness (JRC) and conducting aperture as inputs to their model.

In order to determine the impact of large scale roughness under various stress states on both the distribution of fracture/rock deformation and the corresponding changes in fracture/matrix permeability, a series of laboratory experiments are being undertaken by the Fractured Reservoir Group at Memorial University. In these experiments five samples are being tested: (a) two fabricated fracture surfaces (two physical models), (b) a sandblasted sawcut surface in a limestone block, (c) and two samples of Berea sandstone, one containing an induced fracture surface and a second with a machined fracture surface.

The first physical model, constructed of high strength concrete, was designed to study the effects of a single large scale asperity (jog), on both fracture and rock deformation and the flow properties of the fracture plane. The results of this first experiment have been reported by Butt (1994), and Gale et al. (1994). In this model, strain gauges and manometers were embedded in a similar configuration to that in the present experiment. Butt's work demonstrated that a single large scale fracture roughness does have a significant influence on both

the normal and shear fracture stiffness, on the state of stress in the adjacent wall rock and on the development of secondary fractures. In addition, there was a marked increase in the total volume of fracture porosity in the vicinity of the large scale asperity.

The final three experiments on natural rock samples that are noted above, were done subsequent to this experiment, and therefore are not reported here.

Chapter 2 Design and Experimental Procedures

2.1 Design and Construction of the Physical Model

A physical model has been constructed to investigate in detail the effects of two parallel large scale asperities on the state of deformation and permeability of a single fracture. This model was identical in overall size and general configuration to that of Butt (1994), with the main difference being the presence of two large scale asperities.

The small scale roughness on the fracture surface was created using the impression of a geotextile material in the uncured concrete. This texture was of the form of uniform small asperities, or roughness, averaging 1 mm in height. The shape of the two large scale asperities was superimposed on this small scale roughness. Both of these asperities were 10 mm high, and parallel to each other. They extended across the full width of the model and were oriented perpendicular to the shear direction. These parallel large scale asperities were separated by a distance of 70 mm, equal to seven times their height. The 45 degree ramps of the large scale roughness were designed to increase the tendency for failure to occur at the base of the

asperities, and to minimise the tendency for the fracture to dilate at low normal stresses.

Within the model, 92 strain gauges to measure the matrix deformation of the concrete were mounted on both sides of four 80 mm by 125 mm by 14 mm concrete slabs or coupons (Figure 2-1, 2-2). These coupons, cut from cylinders that were formed using the same mixture used in the construction of this test specimen, were positioned along the centreline of the lengthwise vertical plane (Figure 2-3, Appendix A-3).

Figure 2-3 illustrates the orientation and location of the strain gauges imbedded in this model. Of the gauges, 28 were orientated vertically (perpendicular to fracture plane), 28 were orientated horizontally, and the remainder were in rosette configuration (24 at $\pm$ 45° to the fracture plane, 12 vertical). All gauges and wires were coated with a rubber like waterproof coating to protect them during the casting of the model, and the following testing procedures. In addition to the waterproof coatings, each strain gauge or gauge rosette had a small (10 mm by 15 mm) brass "shim stock" strip epoxied over it to aid in heat dissipation from the gauge during operation. To further aid in internal heat dissipation, small copper cooling

tubes were mounted over both sides of each coupon so that water could be circulated through these tubes to help dissipate the heat generated by the strain gauges.

All of the strain gauges had a gauge length of 240 mils (6.1 mm), except for four of the rosette clusters (5-6-7, 28-29-30, 53-54-55 and 76-77-78), which had a gauge length of 60 mils (1.52 mm). These four rosette clusters are located at the lower centre (L), lower centre (R), upper right and upper left respectively.

After the strain gauge coupons were mounted in the mold, the manometer tubes (17 in total, Figures 2-1, 2-2 and 2-4) and 8 LVDT anchor posts were fixed in place. The lower half of the model form was filled with the cement mixture and internally vibrated to remove air space with a vibrator inserted into the wet concrete. The double large scale roughness feature of the fracture plane was constructed by pressing an aluminium mold of the asperities into the wet concrete (Figure 2-1). This mold was separated from the wet concrete by a geotextile fabric (Miraffi™ 600). After the concrete had hardened in the lower half, the upper half of the model was cast on the geotextile (which had been left in place). As noted previously, the woven texture imprint of the

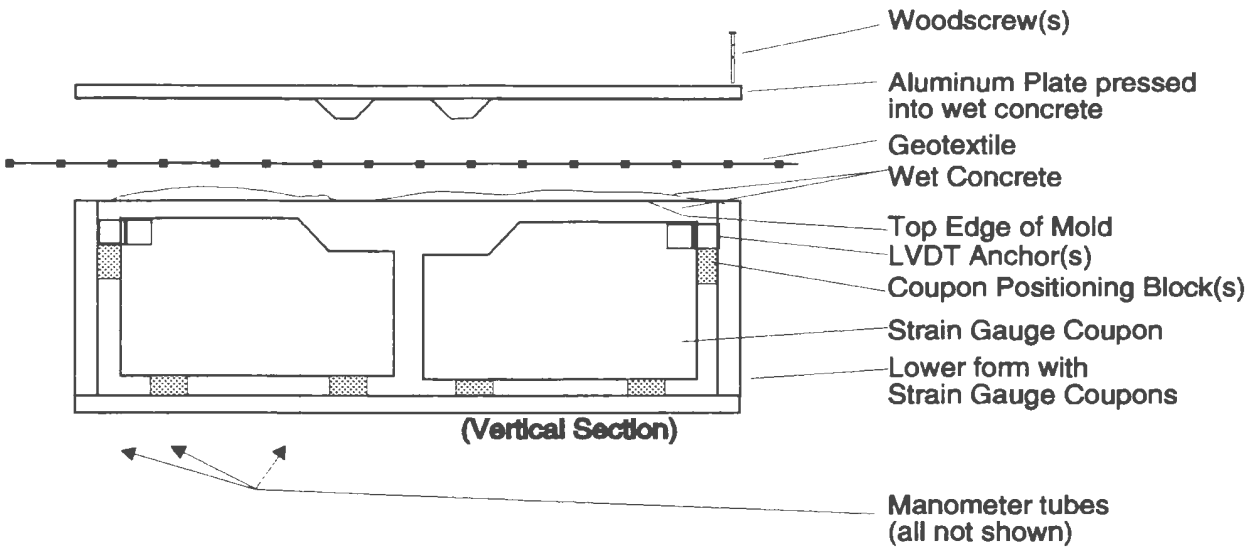

Figure 2-1 Schematic diagram illustrating pouring of lower half of block

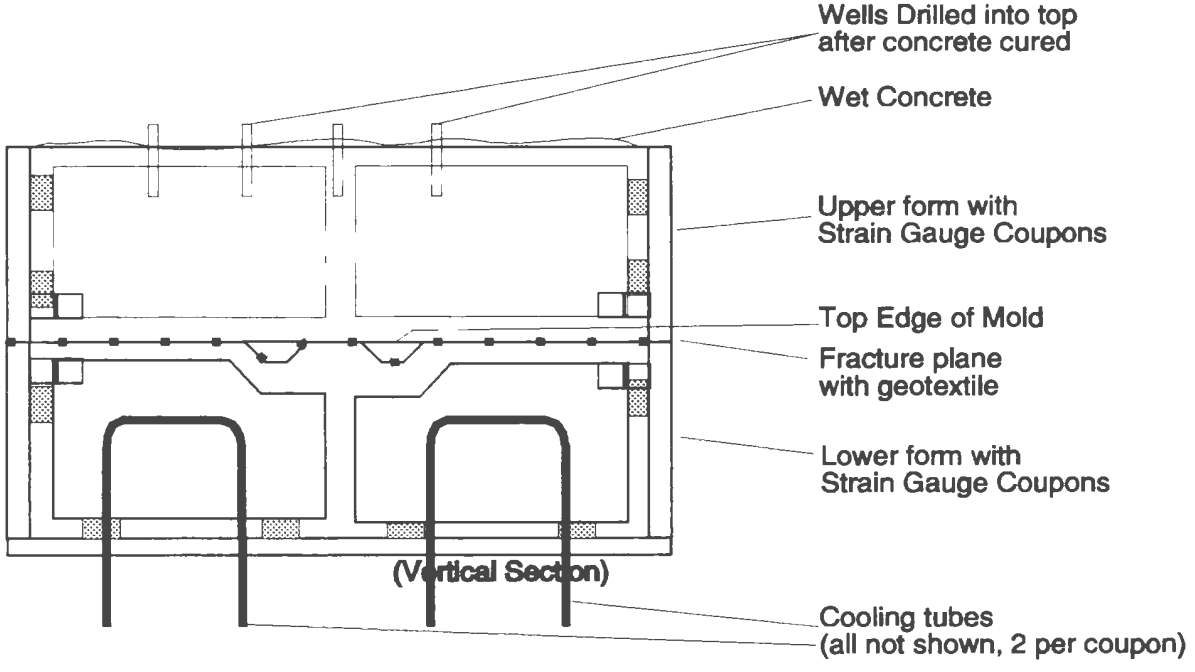

Figure 2-2 Schematic diagram illustrating pouring of upper half of block

geotextile created the uniform small scale roughness on the fracture surface after the blocks were separated.

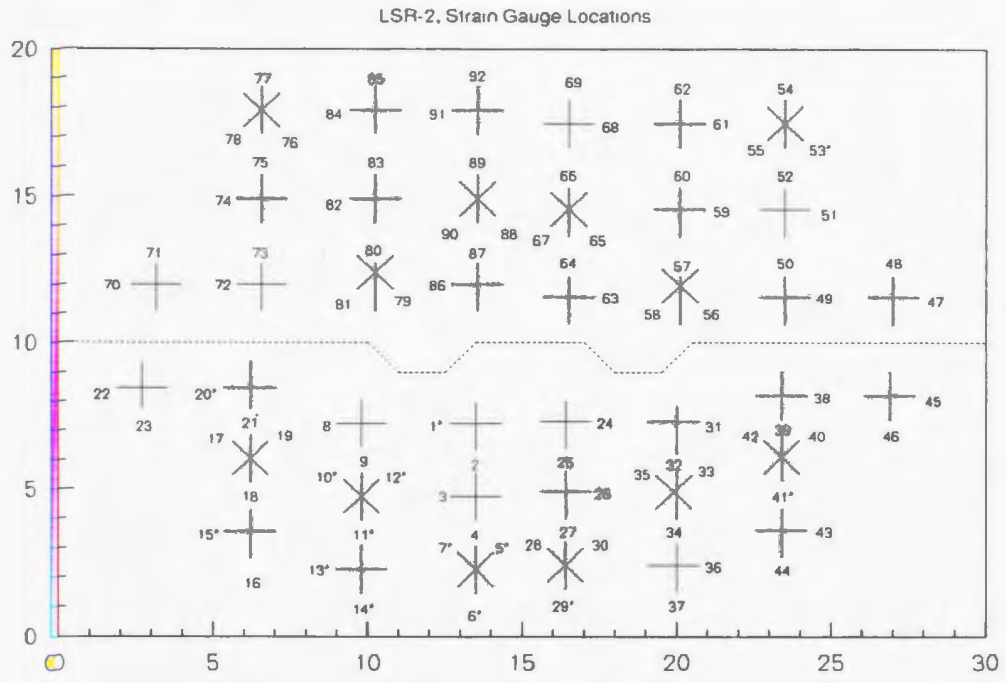

Figure 2-3 Lengthwise vertical section showing the location of the strain gauges in LSR-2. Gauges marked with an asterix failed prior to testing. Scale along both axes is centimetres. The dashed line represents the shape of the artificial fracture plane.

The concrete was allowed to cure in a water bath for 44 days. The wooden forms were then removed, and the model was separated along the fracture plane using steel wedges. The upper and lower halves were carefully reassembled so as not to disturb or contaminate the texture on the fracture

plane, and secured with two stainless steel gear clamps located over the asperities (Figure 2-6a).

Four 65 mm deep, 6.4 mm diameter wells were then drilled on the upper half of the block for matrix permeability experiments (Figures 2-2, and 2-5) into which thin walled brass tubing was epoxied to a depth of 35 mm, leaving 30 mm of open hole.

Finally, the model was cast into the lower half of the steel shear box (Figure 2-6 (a)) using a grouting material made from a mixture of high strength epoxy resin, and a fine to coarse silica sand. After curing for two days, the upper half of the steel sample box was attached to the lower half with machined aluminium plates (to hold sample and shear box in precise alignment), and the assembly was inverted. The upper half was then filled with the same resin mixture, and allowed to cure. After curing, the side plates were removed one at a time, and the edges of the model were cleaned and additional epoxy was added to fill areas that were obscured by the side plates. The plates were replaced, and the model was lifted into the shear frame (Figure 2-6 (b)).

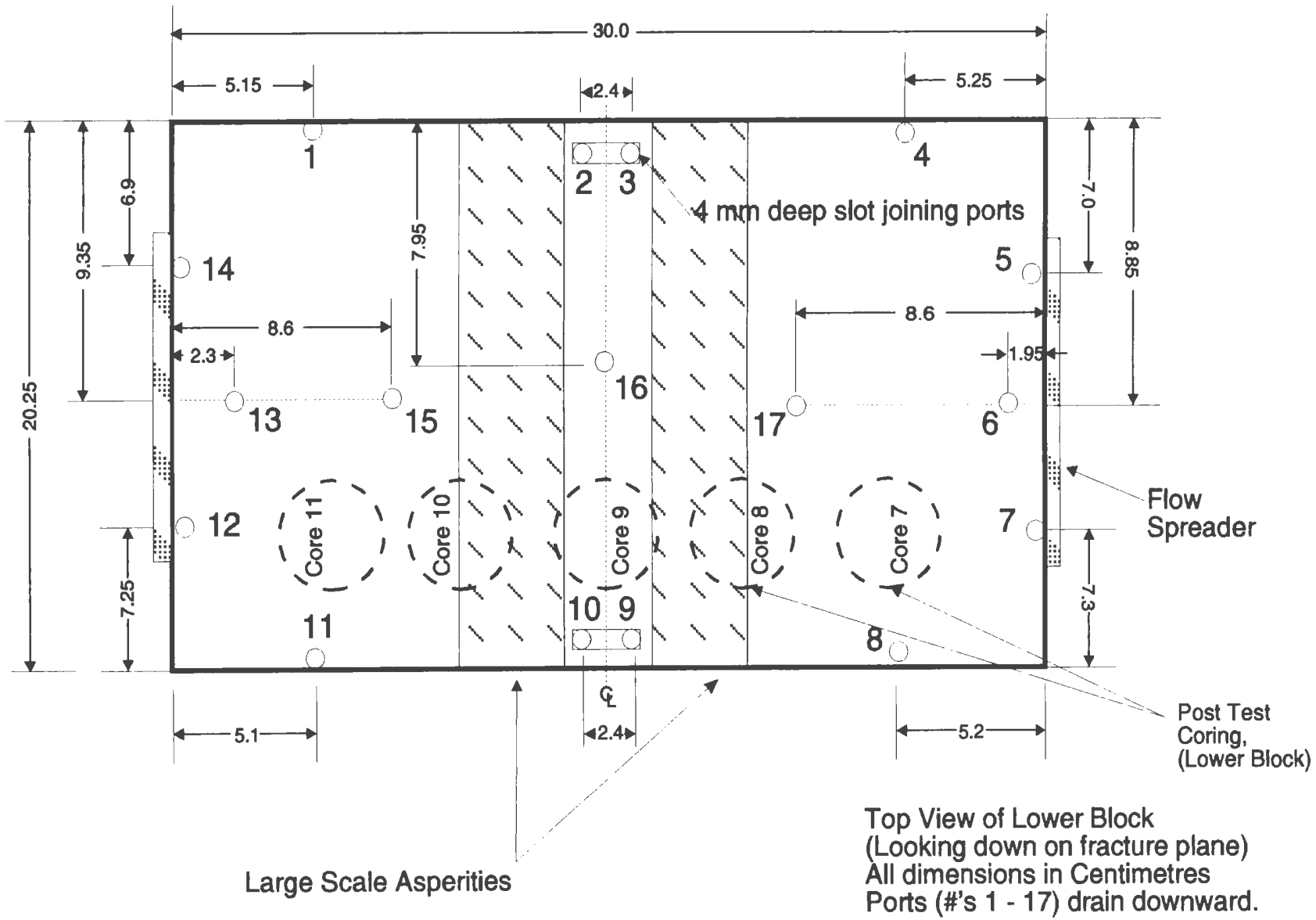

Figure 2-4: LSR-2 Ports Layout (Schematic: Plan view)

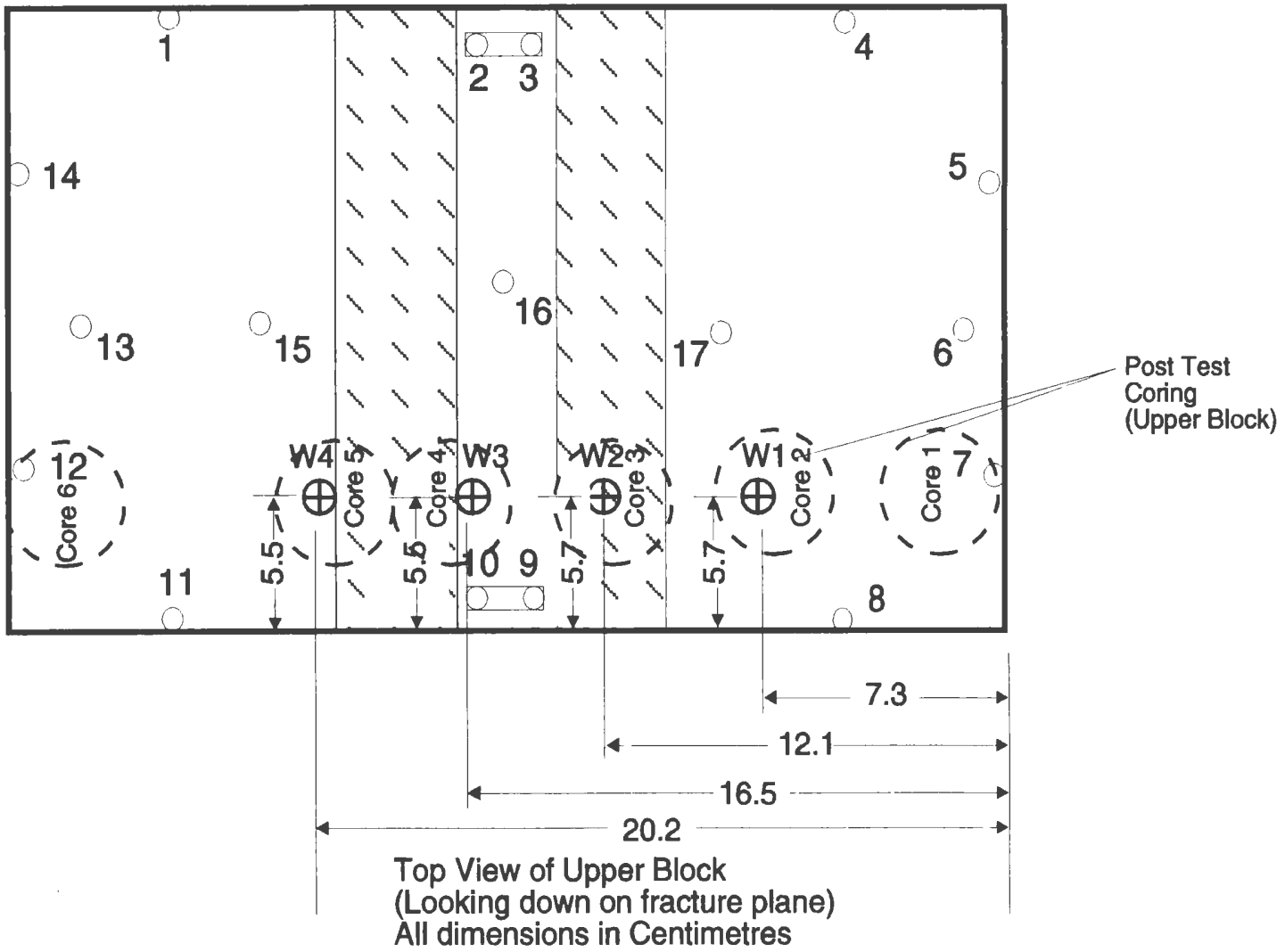

Figure 2-5: LSR-2 Wells Layout (W1 - W4) (Schematic: Plan View)

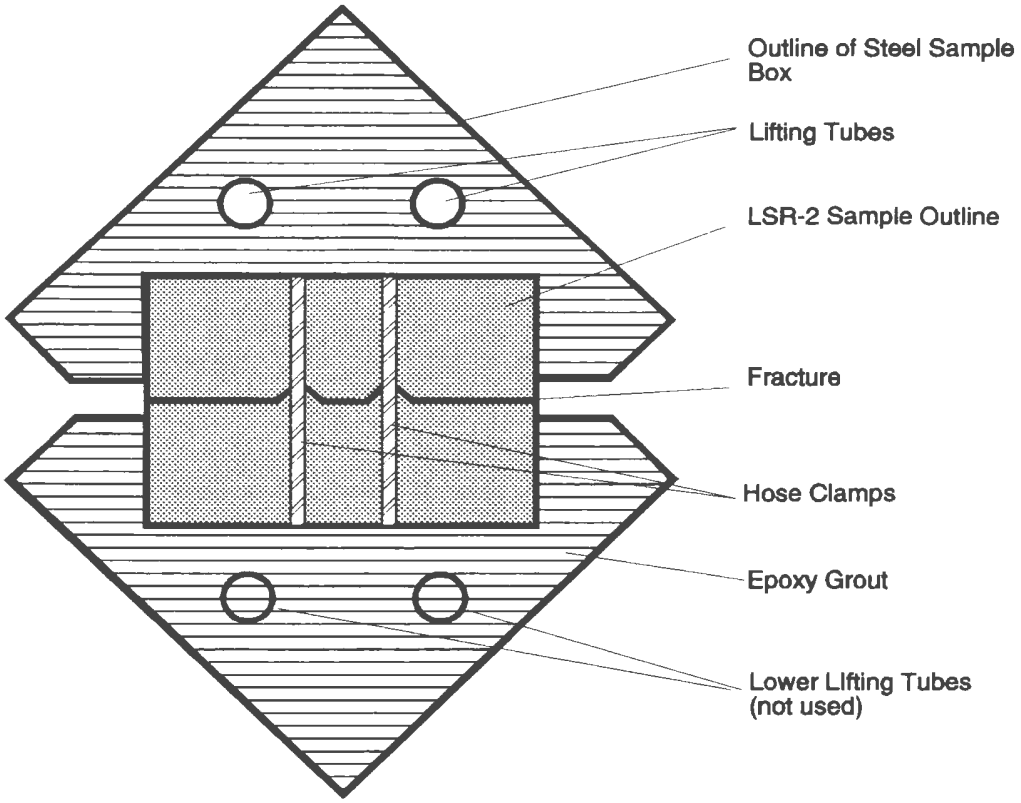

Figure 2-6 (a) Schematic diagram illustrating placement of LSR-2 in steel sample box

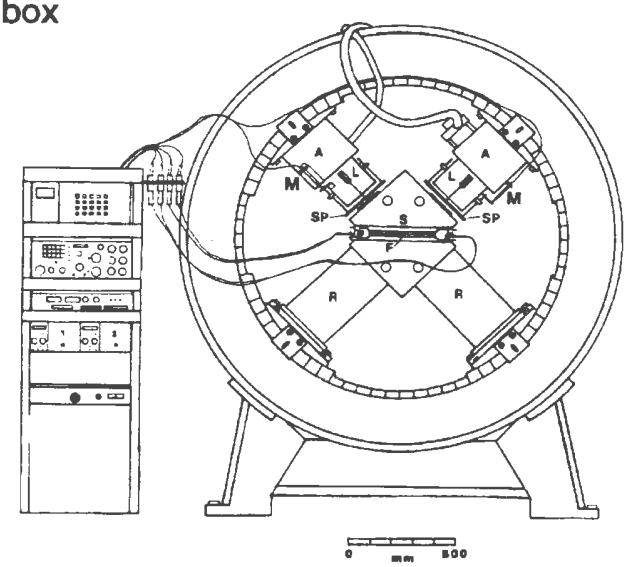

Biaxial shear apparatus: Sample box (S), Fracture plane (F), Actuator (A), Load-cell (L), LVDT (M), Reaction member (R), Swivel pad (SP).

Figure 2-6 (b) Biaxial Shear Apparatus with steel sample box installed. (from Gale, 1990, Figure 2.2)

2.2 Experimental Procedures

Three normal, and four shear loading cycles were conducted (Figure 2-7, Table 2-1) using simultaneous displacement and load control. This was accomplished using an MTS servo controlled hydraulic system interfaced to a PC based control and data acquisition system (Viewdac/Keithley). Loads from the hydraulic actuators were applied to the physical model through hydrodynamic bearings fitted to the sample box (Figure 2-6 (b)). The loads and actuator displacements were measured using a load cell in each actuator assembly, and a LVDT mounted between each actuator piston and its base. The normal and shear displacements at the fracture plane were measured by eight LVDT's and machined steel wedges mounted on the corners of the model, using the anchors previously imbedded in the model. The load cells and actuator mounted LVDT's were scanned five times every second by the control system. These measurements were used in the control loop to generate analogue control signals for the displacement and load control of the biaxial loading frame. The data acquisition and storage loops operated concurrently with the control loop to read and record the strain gauges and thermocouples every 10 minutes. The sample LVDT's were read and recorded every 10 seconds, and the pressure transducers were read every 30 seconds and recorded as needed.

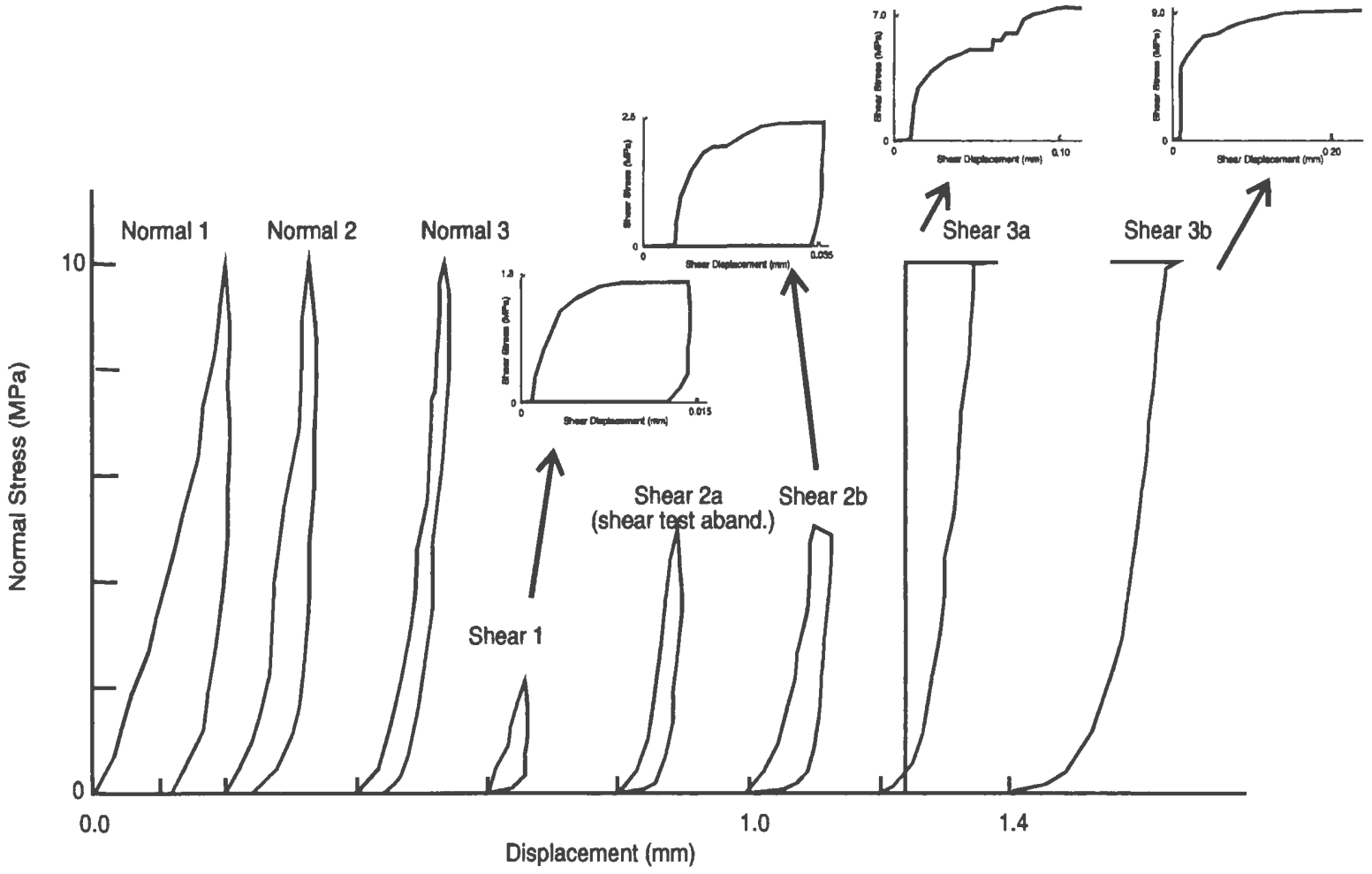

Figure 2-7: Schematic illustrating Normal and Shear Loading Pathways for testing of LSR-2.

Note: Normal Displacement curves have been artificially separated by 0.2 mm along X axis.

Table 2-1: Testing Schedule (see Appendix 2 for details of loading steps)

Test Cycle	Loading Sequence
Normal 1	Normal load only to 10 MPa, then unloading .
Normal 2	Normal load only to 10 MPa, then unloading .
Normal 3	Normal load only to 10 MPa, then unloading .
Shear 1	Normal load to 2 MPa, shear loading to 1 MPa, unload shear, then unload normal.
Shear 2a	Normal load only to 5 MPa, then unloading. Shear portion cancelled due to unstable electrical power caused by inclement weather.
Shear 2b	Normal load to 5 MPa, shear load to 2.5 MPa, unload shear, then unload normal.
Shear 3a	Normal load to 10 MPa, then shear load to 7.58 MPa. A fault in the hydraulic equipment necessitated the removal of the loads by shutting off power to the testing frame.
Shear 3b	Normal load to 10 MPa, then shear load to 9.46 MPa when the model failed. Shear load was reduced to 6.25 MPa for epoxy injection into the fractures.

The exposed edge of the artificial fracture plane was surrounded by a packer and packer retainer constructed from a small bicycle inner tube and a steel channel frame. The retainer was designed as a rigid frame to hold the inflated packer (inner tube) tight against the exposed edges of the fracture, but would still allow for shear movement of the assembly. Under the packer at the ends of the model were flow spreaders, consisting of a section of one half inch OD copper tubing, cut lengthwise, to allow the inlet and outlet water to spread evenly across the ends of the model.

Deionized and partially degassed water was injected continuously into the fracture plane using a second PC controlling a constant displacement pump driven by a linear stepper motor. Water at a constant flow rate of 0.7 cm^3/sec was injected (inflow) by this pump into one end of the model (port 5), and withdrawn from the other end (port 14) in a lengthwise flow configuration (Figure 2-8). Fracture transmissivity was calculated from outflow measurements at selected normal and shear stress levels (Table B2-8). For each stress level, a minimum of three measurements of outflow rate were made. The fluid pressures along the fracture plane were measured at 13 of the manometer ports, at least three times for each flow rate measurement, using 7 pressure transducers that were connected through eight hand operated valves. Each of these valves had 4 ports, two of which were connected to constant head reference tanks for data quality control, and the other two were connected to manometer ports.

The matrix permeability of the concrete was monitored for changes induced by testing by conducting pressure pulse tests (Brace et al., 1968, Forster and Gale, 1980) in the four wells drilled into the top half of the model, every 30 to 45 minutes, throughout the shear test cycles. The wells were

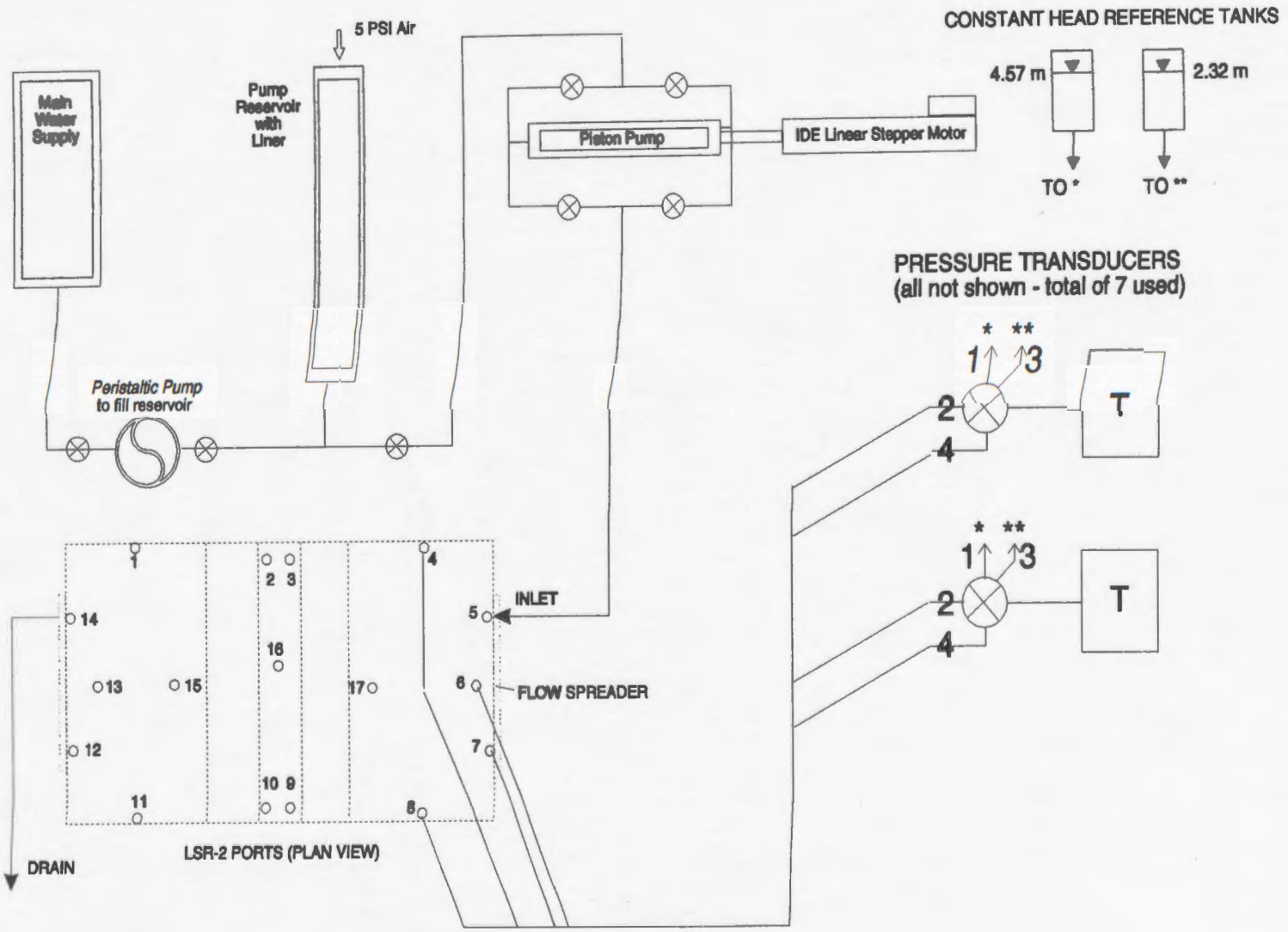

Figure 2-8: Flow Schematic, LSR-2

pressurised with water to 345 kPa (50 psi), and shut in. The decays of these pressure pulses were recorded using a pressure transducer connected to a chart recorder.

To preserve and examine the pore space of the fracture plane and the distribution of the contact points over the fracture surface, the fracture plane was evacuated at the end of the final shear cycle, flushed with alcohol to remove residual water, and injected with a low viscosity coloured epoxy resin. After curing, the machined side plates were replaced on the sample box, and the sample was unloaded and removed from the shear frame. The 45 mm thick slab containing the fracture was then cut from the steel sample box with an industrial concrete diamond saw. This slab was sliced lengthwise into six sections. The resin-filled fracture plane was then photographed using a microscope to produce a final image of the fracture pore space at eighteen times enlargement. In addition, a series of cores were cut from the concrete remaining in the steel sample box to complete a profile of the fracture pattern in the model and to determine the nature of the bonding between the epoxy grout and the top and bottom of the model.

Chapter 3 Experimental Data

3.1 Normal Stress versus Displacements and Strains

The normal stress versus normal fracture displacement (averaged at all four corners of the sample), recorded for each normal loading test cycle, and the normal loading portion of the shear cycles, is illustrated in Figure 3-1. To aid in visualising the data, the starting points of each of the eight curves are artificially displaced by 0.2 millimetres along the X axis to avoid excessive overlapping of the data points. As shown in Figure 3-1, and schematically in Figure 2-7, for the three normal loading cycles, the maximum applied stress was 10 MPa. For the five shear cycles (Shear 1, 2a, 2b, 3a and 3b), the sample was loaded to a normal stress of 2, 5, 5, 10 and 10 MPa, respectively, prior to the shear stress being applied. As was noted in Table 2-1, test Shear 2a had only normal loading to 5 MPa, because the shear portion of the test was cancelled due to inclement weather.

Analysis of the normal displacements for the eight testing cycles showed a strong hysteresis effect between the loading and unloading portions of the tests (Figure 3-1) with permanent closure of the fracture plane being greatest (0.11 mm) for the first loading cycle (Figure 3-2). This permanent normal closure decreased in the second and third test cycles (N2, N3) as the test sample seated itself and stabilised at approximately 0.02 mm for each of

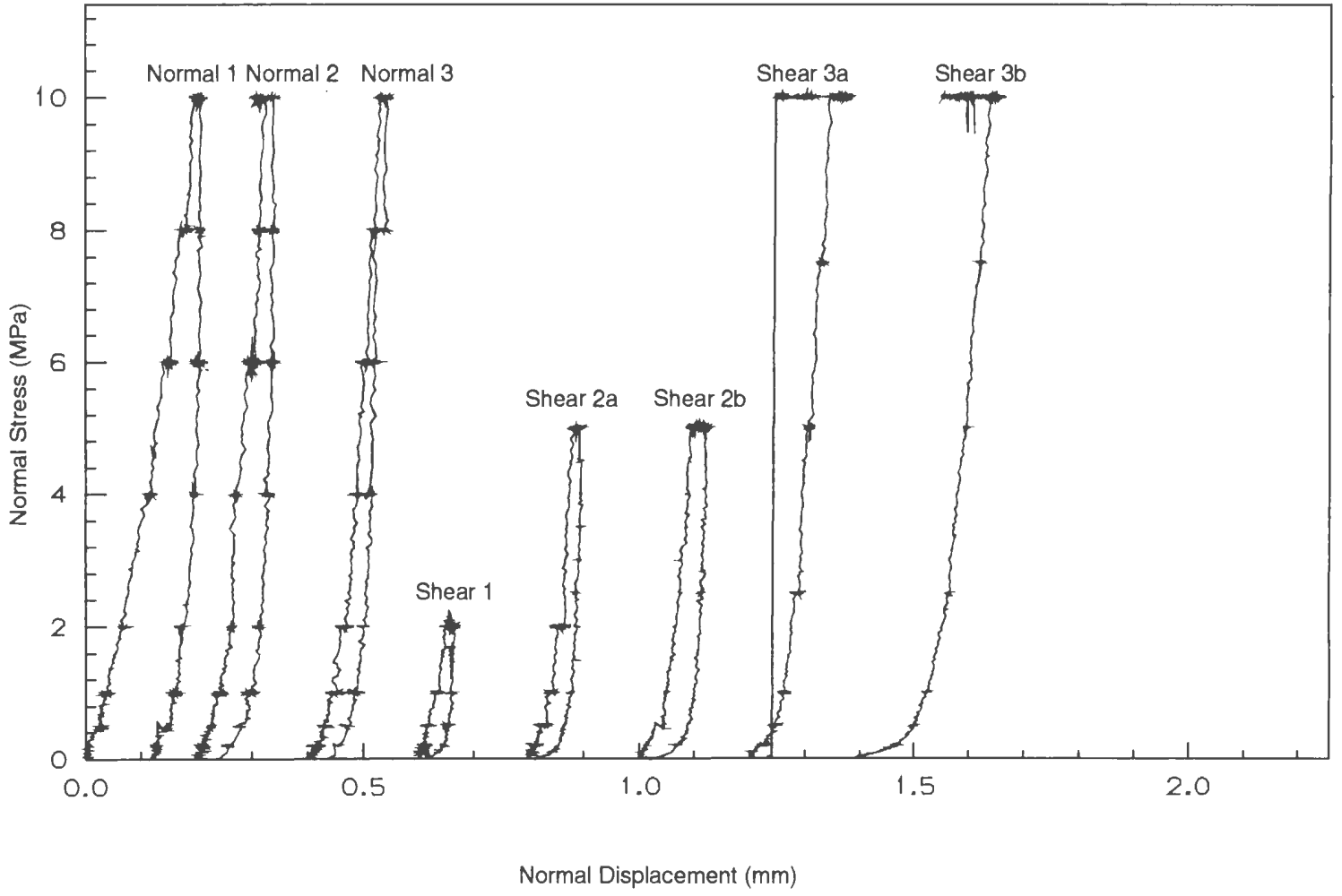

Figure 3-1: LSR-2 Normal Displacements. Note: Curves are artificially separated by 0.2 mm.

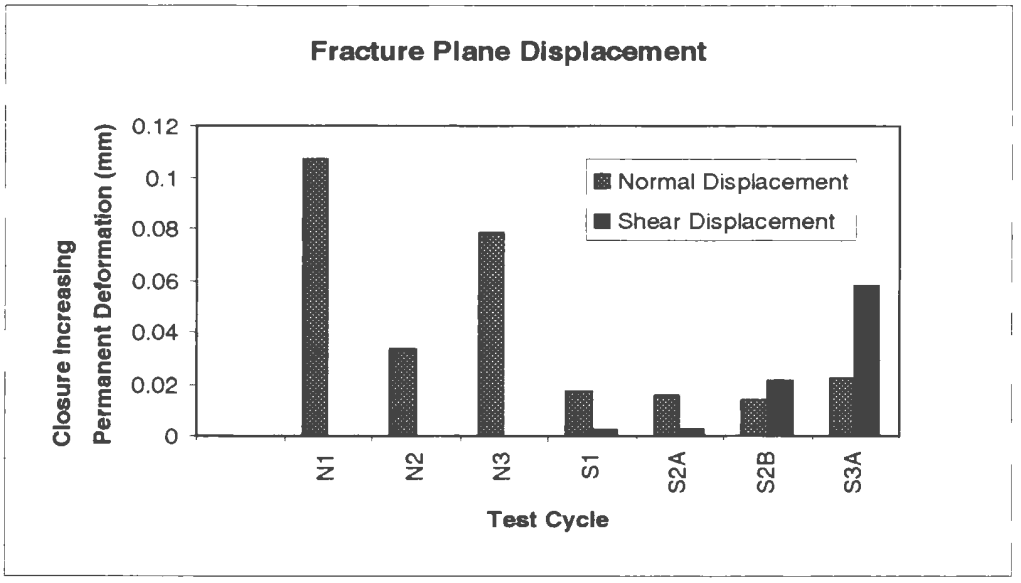

Figure 3-2: Effect of loading on permanent fracture closure at end of each test cycle.

the shear cycles. The large closure seen for cycle N3 was likely due to the model being disturbed slightly by the packer pressure around the edge of the model at the end of the second normal cycle. These observations indicate that the artificial fracture plane seated during the first normal loading cycle and exhibited progressively higher stiffness in the following cycles. In all cases, the hysteresis effect gives an apparent lower fracture stiffness for the loading portion of the tests than the unloading due to the permanent deformation taking place. This is consistent with data from other experimental work (Raven and Gale 1985, Butt, 1994, Gale et al. 1994). This stiffness effect must be accounted for when doing the numerical

simulations and is discussed further in Chapter 4. It should also be noted in this discussion, that the total permanent closure of the fracture is the sum of the individual normal fracture closures seen in the seven test cycles illustrated in Figure 3-2. No normal closure was determined for cycle 3B, due to the fractures intersecting the LVDT anchors. These fractures invalidated much of the displacement data for that cycle.

The internal strains recorded during the three normal loading cycles show a similar pattern throughout the three test cycles. This is illustrated in Figures 3-3 (a-j), which show the strains changing with the changing loads that were recorded during the loading portion of normal cycle 2 which was considered to be a typical cycle. The strain distribution recorded for all three of the normal cycles at peak load (10 MPa) is illustrated in Figures 3-4a to 3-4c, (Strain at Peak Load, Normal Cycles 1, 2, and 3).

Relatively uniform, mostly compressional strains at low average normal stress levels (Figure 3-3 (a) and 3-3 (b)) are seen in a typical normal loading cycle. As the average normal stress level is increased to peak, however, the strains continue to change, breaking into compressional zones at the ends of each block, with extensional zones developing in the centres

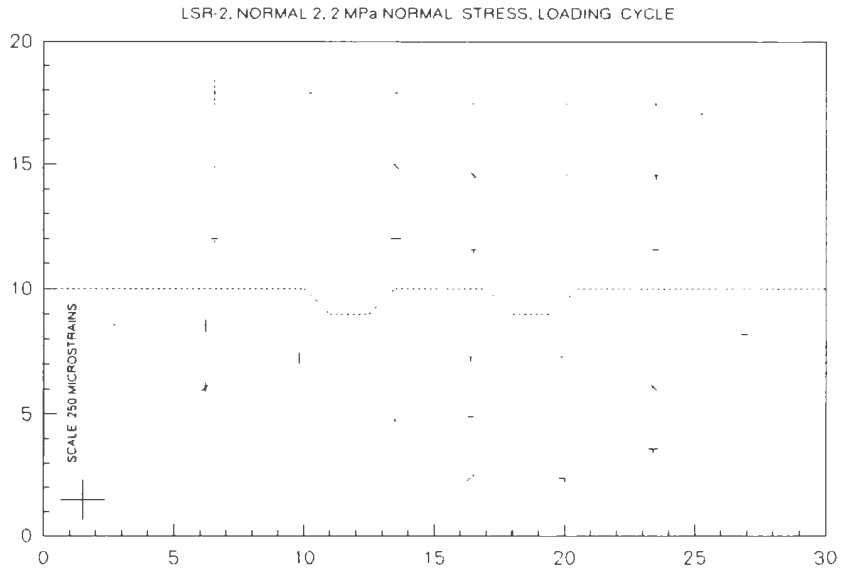

Figure 3-3 (a): Strain Distribution, Normal Cycle 2, at 2 MPa Normal, Loading Cycle (0 MPa Shear). Numbers along axes are scale in centimetres, dashed vectors represent tensile microstrains, solid represent compressional microstrains. (See Figure 2-3 for strain gauge locations)

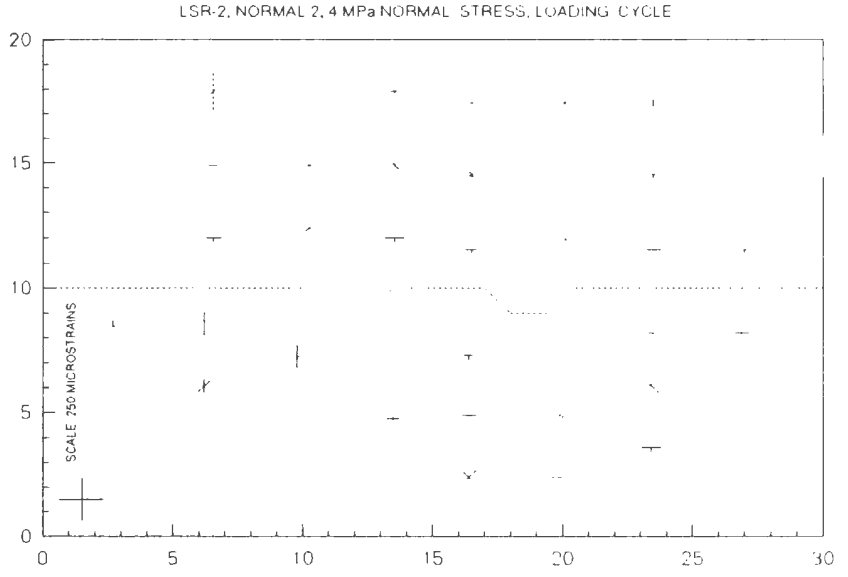

Figure 3-3 (b): Strain Distribution, Normal Cycle 2, at 4 MPa Normal, Loading Cycle (0 MPa Shear). (See Figure 2-3 for strain gauge locations)

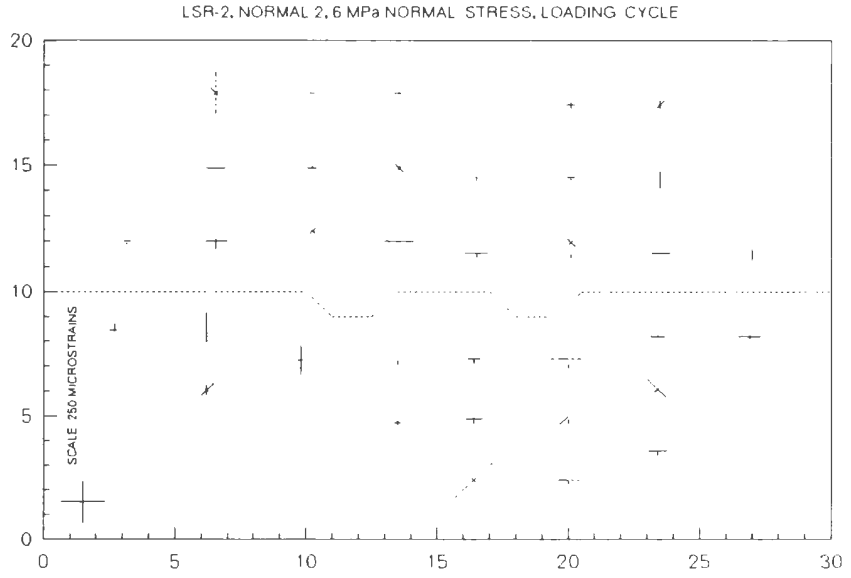

Figure 3-3 (c): Strain Distribution, Normal Cycle 2, at 6 MPa Normal, Loading Cycle (0 MPa Shear). (See Figure 2-3 for strain gauge locations)

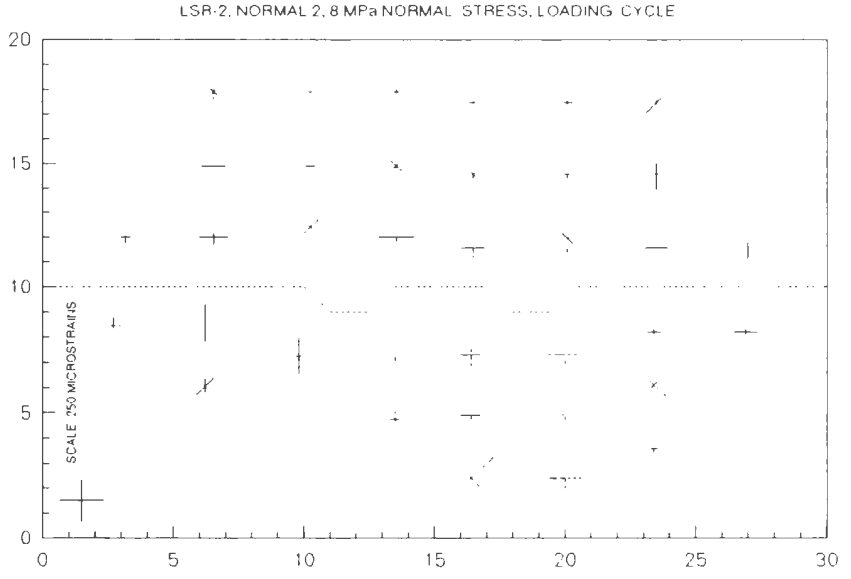

Figure 3-3 (d): Strain Distribution, Normal Cycle 2, at 8 MPa Normal, Loading Cycle (0 MPa Shear). (See Figure 2-3 for strain gauge locations)

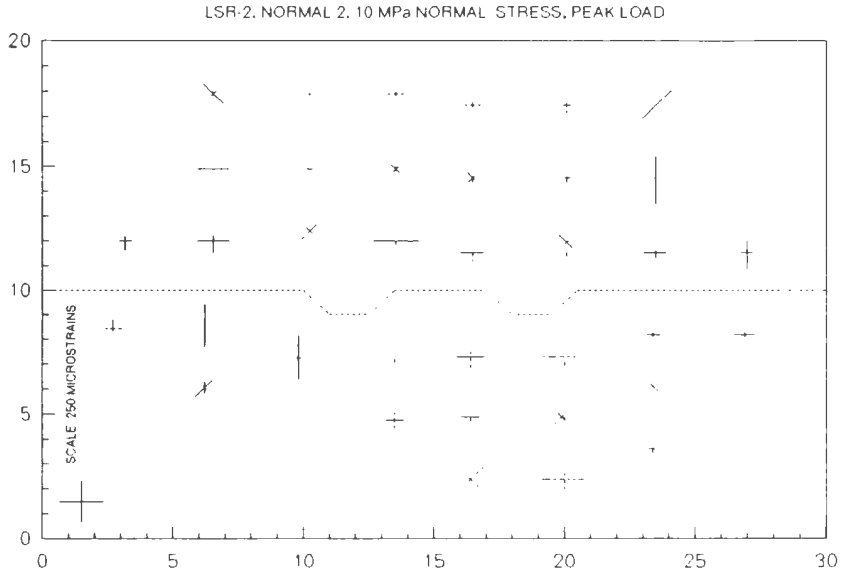

Figure 3-3 (e): Strain Distribution, Normal Cycle 2, at 10 MPa Normal, Loading Cycle (0 MPa Shear). (See Figure 2-3 for strain gauge locations)

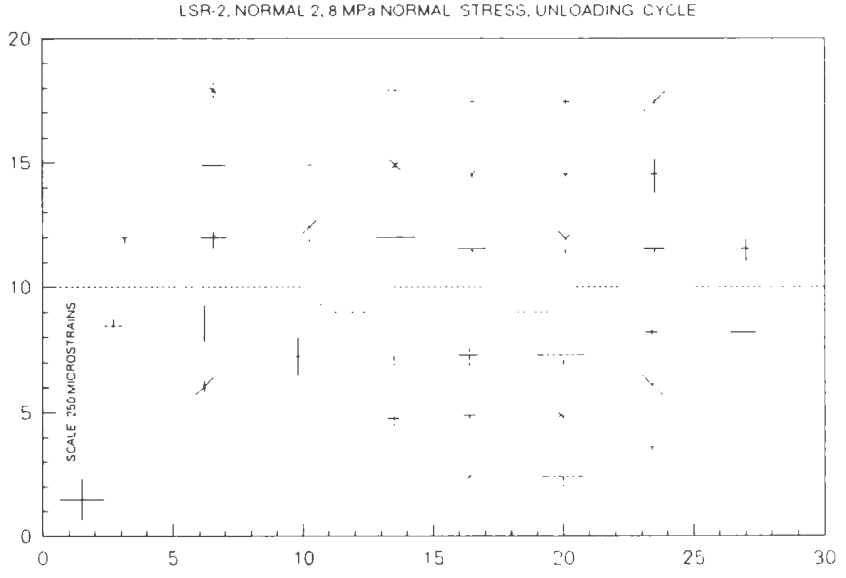

Figure 3-3 (f): Strain Distribution, Normal Cycle 2, at 8 MPa Normal, Unloading Cycle (0 MPa Shear). (See Figure 2-3 for strain gauge locations)

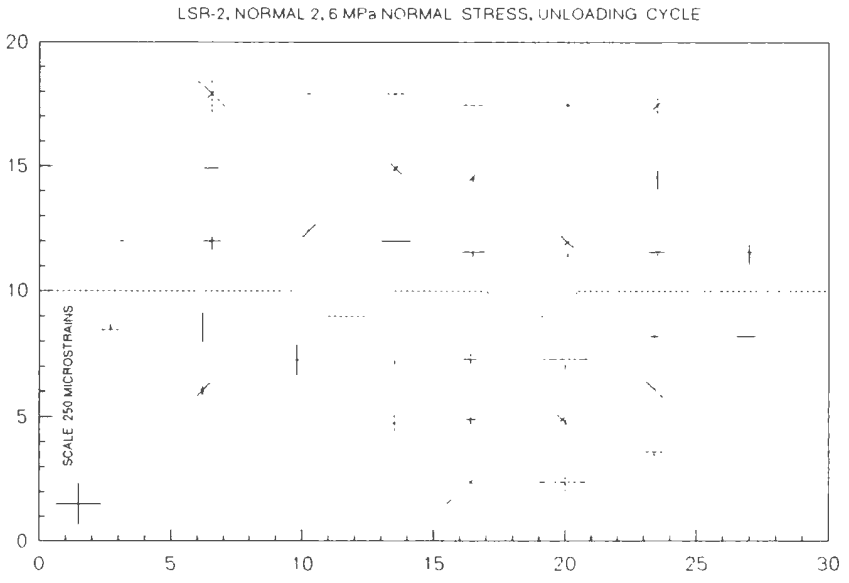

Figure 3-3 (g): Strain Distribution, Normal Cycle 2, at 6 MPa Normal, Unloading Cycle (0 MPa Shear). (See Figure 2-3 for strain gauge locations)

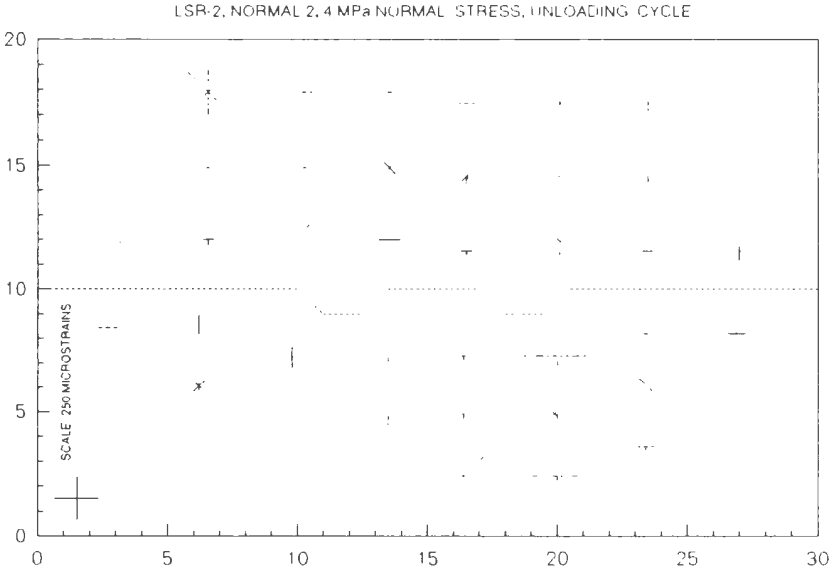

Figure 3-3 (h): Strain Distribution, Normal Cycle 2, at 4 MPa Normal, Unloading Cycle (0 MPa Shear). (See Figure 2-3 for strain gauge locations)

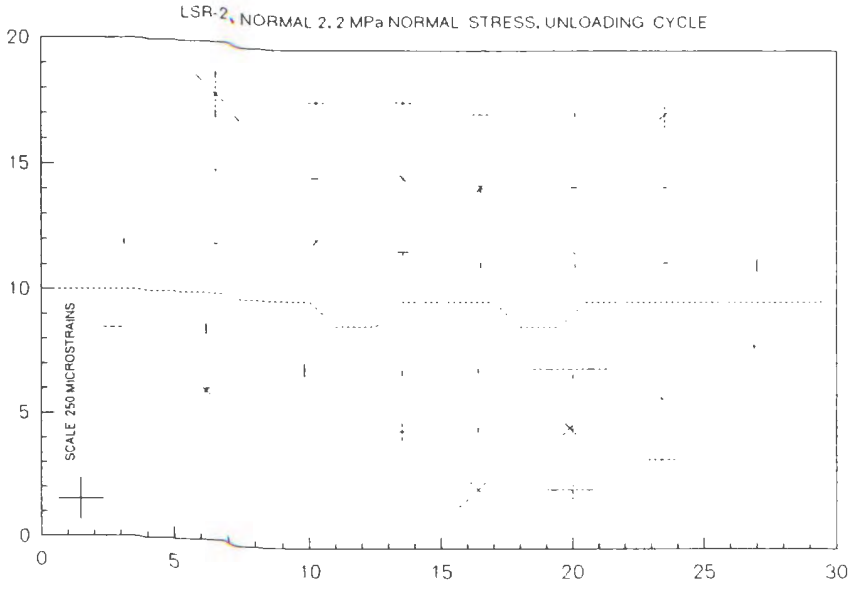

Figure 3-3 (i): Strain Distribution, Normal Cycle 2, at 2 MPa Normal, Unloading Cycle (0 MPa Shear). (See Figure 2-3 for strain gauge locations)

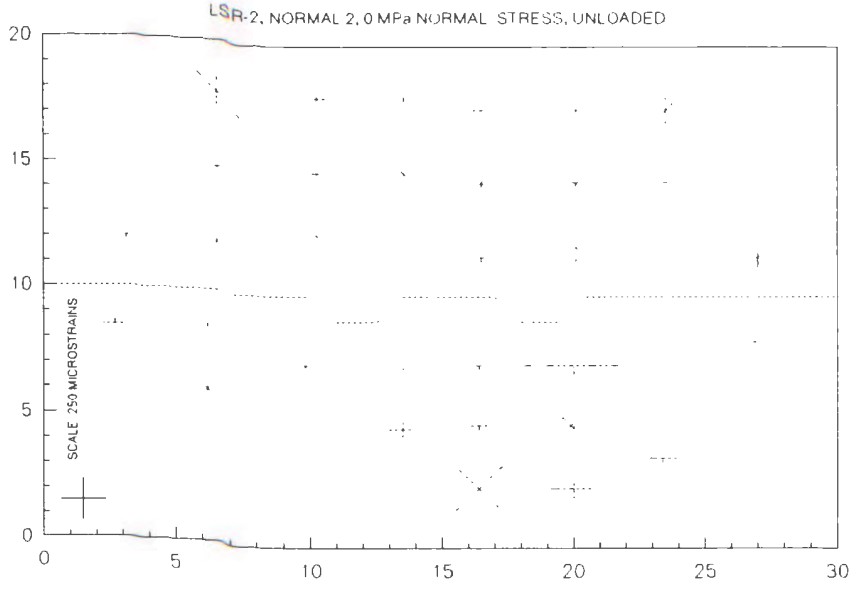

Figure 3-3 (j): Strain Distribution, Normal Cycle 2, at 0 MPa Normal, Unloaded. (See Figure 2-3 for strain gauge locations)

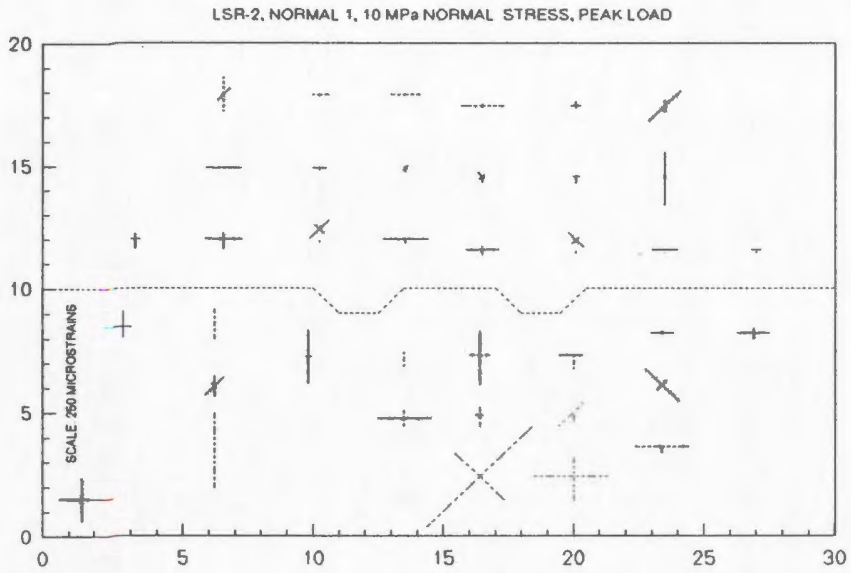

Figure 3-4 (a): Strain Distribution at Peak Load (10 MPa), Normal Cycle 1. Numbers along axes are scale in centimetres, dashed vectors represent tensile microstrains, solid represent compressional microstrains. (See Figure 2-3 for strain gauge locations)

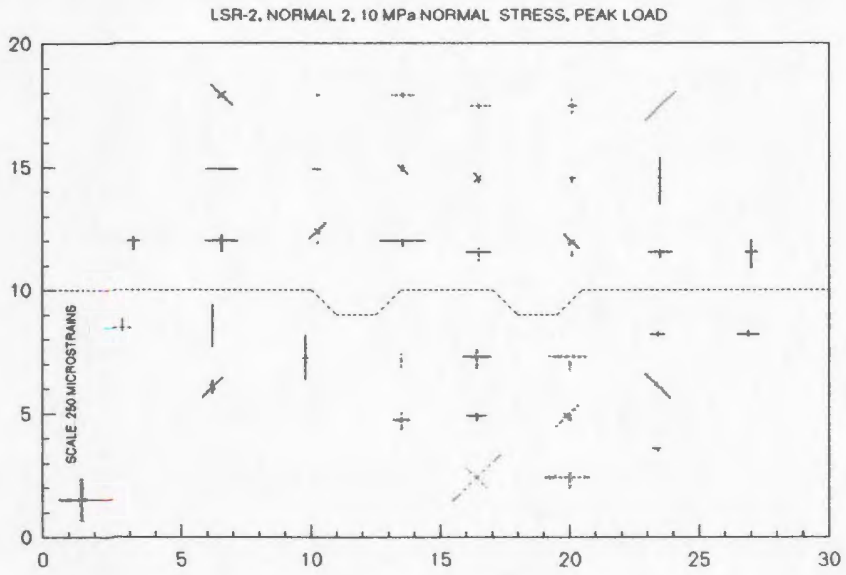

Figure 3-4 (b): Strain Distribution at Peak Load (10 MPa), Normal Cycle 2. (See Figure 2-3 for strain gauge locations)

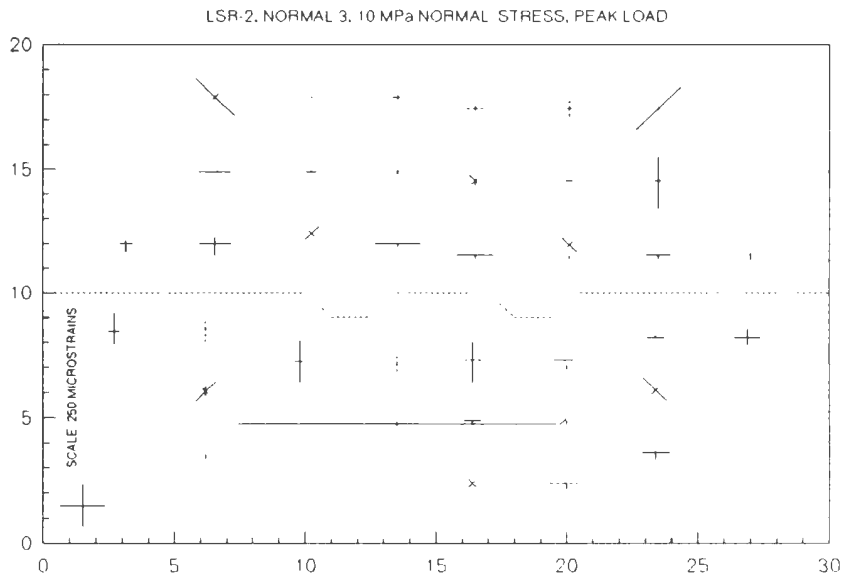

Figure 3-4 (c): Strain Distribution at Peak Load (10 MPa), Normal Cycle 3. (See Figure 2-3 for strain gauge locations)

(Figures 3-3(c), 3-3(d), 3-3 (e), Figures 3-4 (a), 3-4 (b), 3-4 (c)). The extensional zones, in roughly the centre of the upper and lower blocks, suggest bridging or pivoting on the large scale asperities causing rotation about the centre and closing of the fracture plane at the ends, and/or incomplete grouting or poor bonding of the grout above and below the centre of the sample.

Post-test coring of the concrete and grout within the steel sample box confirmed that the above noted extensional strains were produced at least in part by incomplete grouting above and below the centre of the sample. It

can be seen in Figure 3-4 (a, b, and c), that development of these zones appear to decrease as the sample was repeatedly loaded. The rosette clusters closest to the corners of the block, 17-18-19, 40-41-42, 53-54-55, and 76-77-78 (see Figure 2-3) show greater strains in the line of action of the loading actuators, suggesting that transfer of the load from the actuator through the hydrodynamic bearing to the sample box produces a zone of stress concentration, which is reflected in the strain measurements. This suggests the principal stress directions undergo some degree of rotation within this part of the sample/shear box system.

It can be seen that at rosette clusters 56-57-58 and 79-80-81 located directly above the fracture plane, the principal stress directions rotate by as much as 90 degrees due to the influence of the extensional zone above the two large scale asperities, possibly caused by the incomplete epoxy grouting, and/or the large scale asperities themselves. In the immediate vicinity of the top side of the fracture plane, the horizontal strain components appear larger than the vertical, except at the ends, where the vertical components are slightly larger. This effect is likely due to edge effects produced by the exposed nature of the perimeter of the sample adjacent to the fracture plane. The distribution appears to be reversed in the lower block, where the pattern

of the measured strains close to the fracture plane are reversed relative to those above the fracture plane. The presence of residual strains at the ends of all of the loading cycles (as seen in Figure 3-3 (j)) suggest that the sample underwent plastic deformation. These primarily extensional residual strains were referenced to zero strain at the beginning of each subsequent loading cycle.

3.2 Shear Stress versus Displacements and Strains

Figure 3-5 shows the shear stress versus average shear fracture displacement recorded for each shear portion of the three shear test cycles, averaged at all four corners of the sample. To avoid excessive overlapping of the data points, the starting points of each of the four curves have been displaced along the X axis by 0.1 millimetres. During shear cycle 3a, one of the servo valves malfunctioned, requiring that the test be terminated and the sample was unloaded abruptly by shutting down the servo controlled actuators, producing the straight line shown in Figures 3-1 and 3-5. The curve for Shear 3b reflects a temporary malfunction of the servo valve on the loading frame at approximately 7.5 MPa shear stress. The sample appeared to have completely failed by 9.25 MPa, as seen by the horizontal line in the displacement curve. The shear stress was increased to 9.5 MPa and the

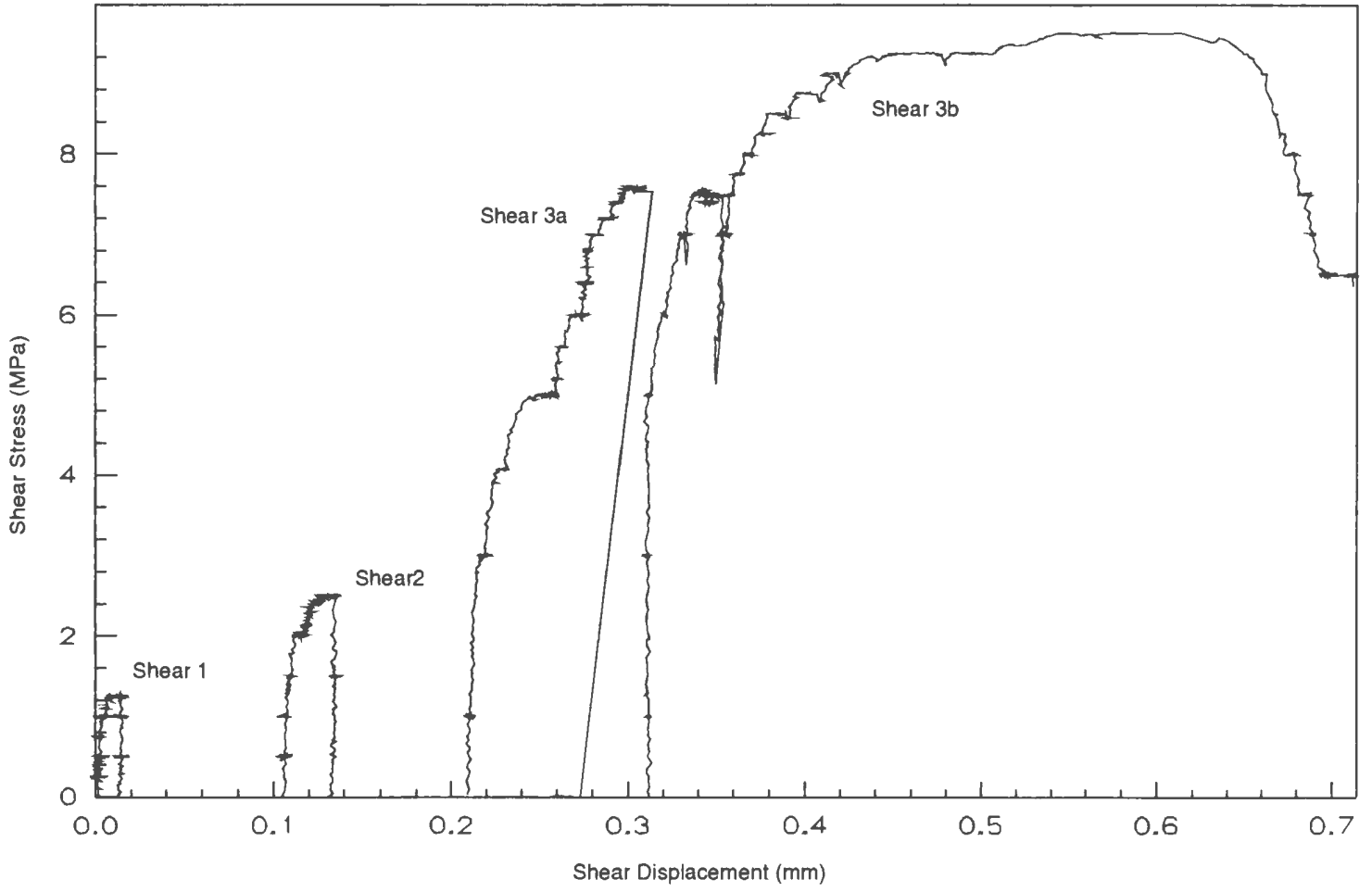

Figure 3-5: LSR-2 Shear Displacements. Note: Curves are artificially separated by 0.1 mm.

shear movement continued (Note that the sample was being loaded under displacement control). In order to stop the shear displacement, the shear stress was reduced to 6.4 MPa. The normal and shear loads were maintained, and epoxy was injected into the fracture plane to preserve the form of the fracture surface for the measured load and displacement conditions.

Figure 3-6 (a to d) illustrates the patterns of normal and shear fracture displacements that are produced by the applied normal and shear stresses. The plots for shear 1 and 2 both show no fracture dilation (normal opening during shear displacement) with the application of 1.25 and 2.5 MPa shear stress, respectively. In both of these cases, all shear displacement recorded by the LVDT's took place after the peak normal stress of 2.0 and 5.0 MPa, respectively, was reached. The shear displacement returned almost completely to its original unloaded displacement only after complete unloading of the test specimen. Shear 3a showed a slight increase in closure at 5.5 MPa, then sudden dilation (0.8 mm) of the fracture plane at about 5.7 MPa for a total of 0.13 mm. During shear 3b, there appears to be a steady dilation totalling 0.1 mm, starting at 3.5 MPa shear stress, until failure at 9.46 MPa shear stress. The graph of shear 3b suggests further

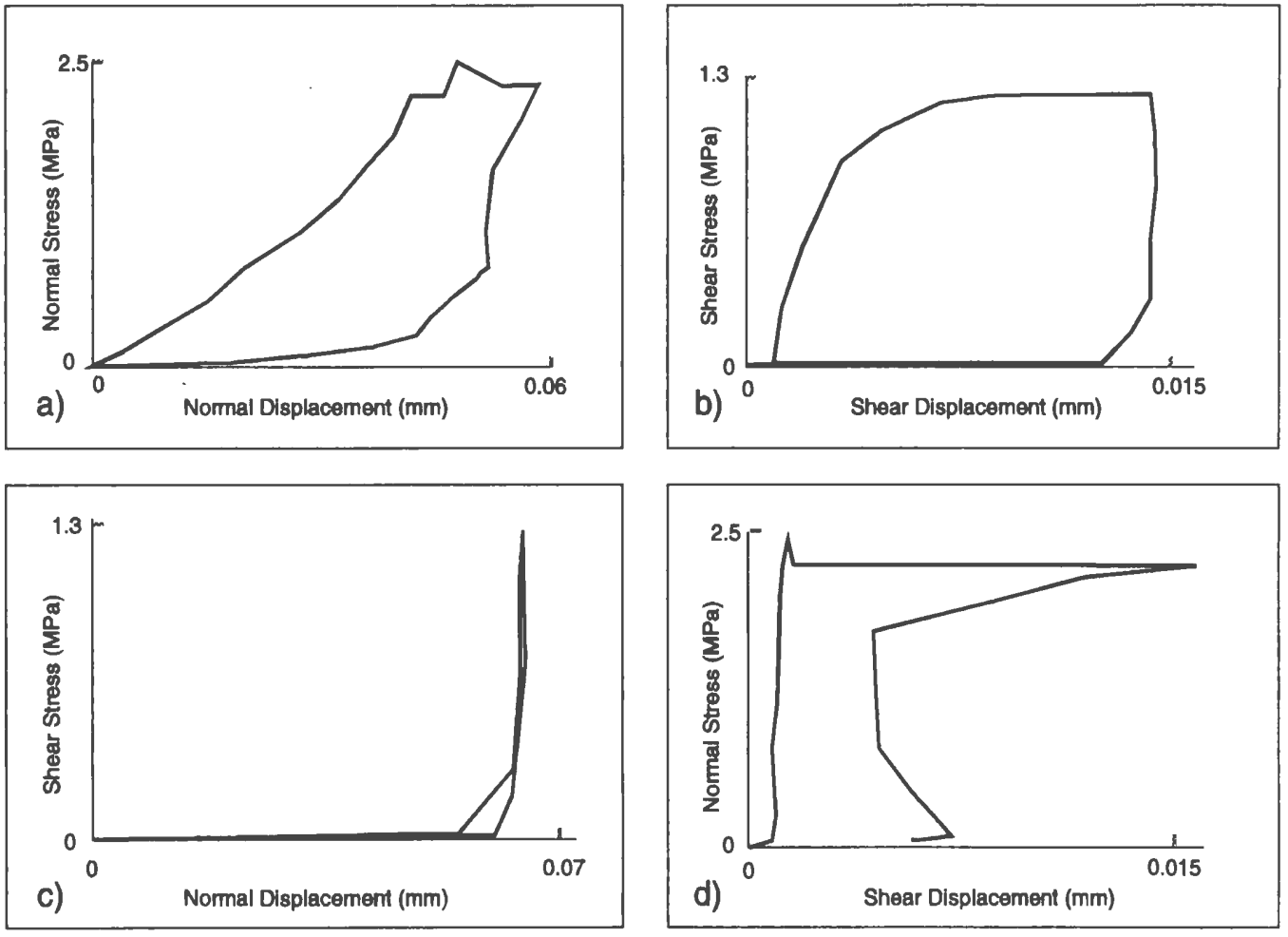

Figure 3-6 (a): Shear 1, Displacement versus Stress.
a) Normal Displacement versus Normal Stress, b) Shear Displacement versus Shear Stress,
c) Normal Displacement versus Shear Stress and d) Shear Displacement versus Normal Stress.

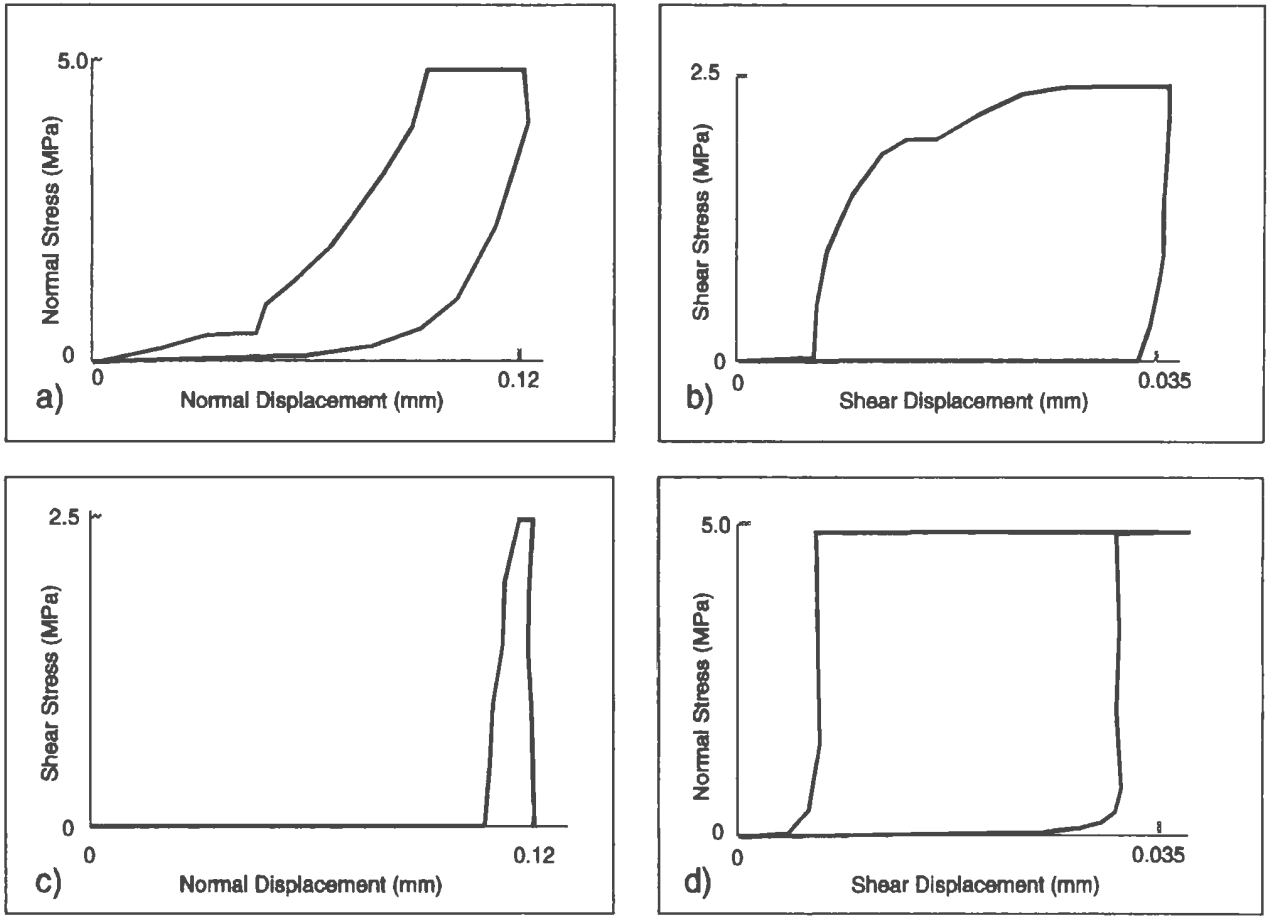

Figure 3-6 (b): Shear 2, Displacement versus Stress.
a) Normal Displacement versus Normal Stress, b) Shear Displacement versus Shear Stress,
c) Normal Displacement versus Shear Stress and d) Shear Displacement versus Normal Stress.

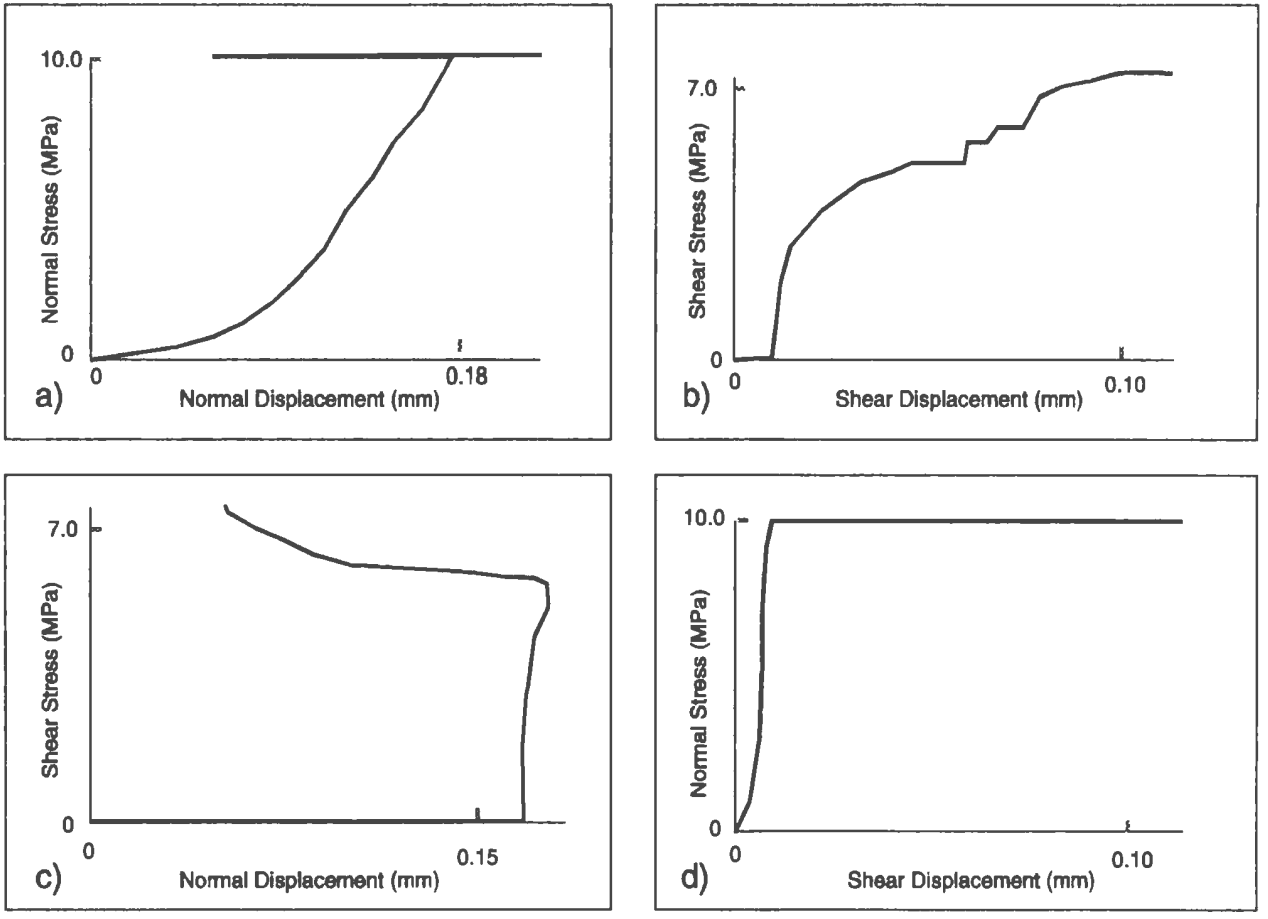

Figure 3-6 (c): Shear 3a, Displacement versus Stress.
a) Normal Displacement versus Normal Stress, b) Shear Displacement versus Shear Stress,
c) Normal Displacement versus Shear Stress and d) Shear Displacement versus Normal Stress.

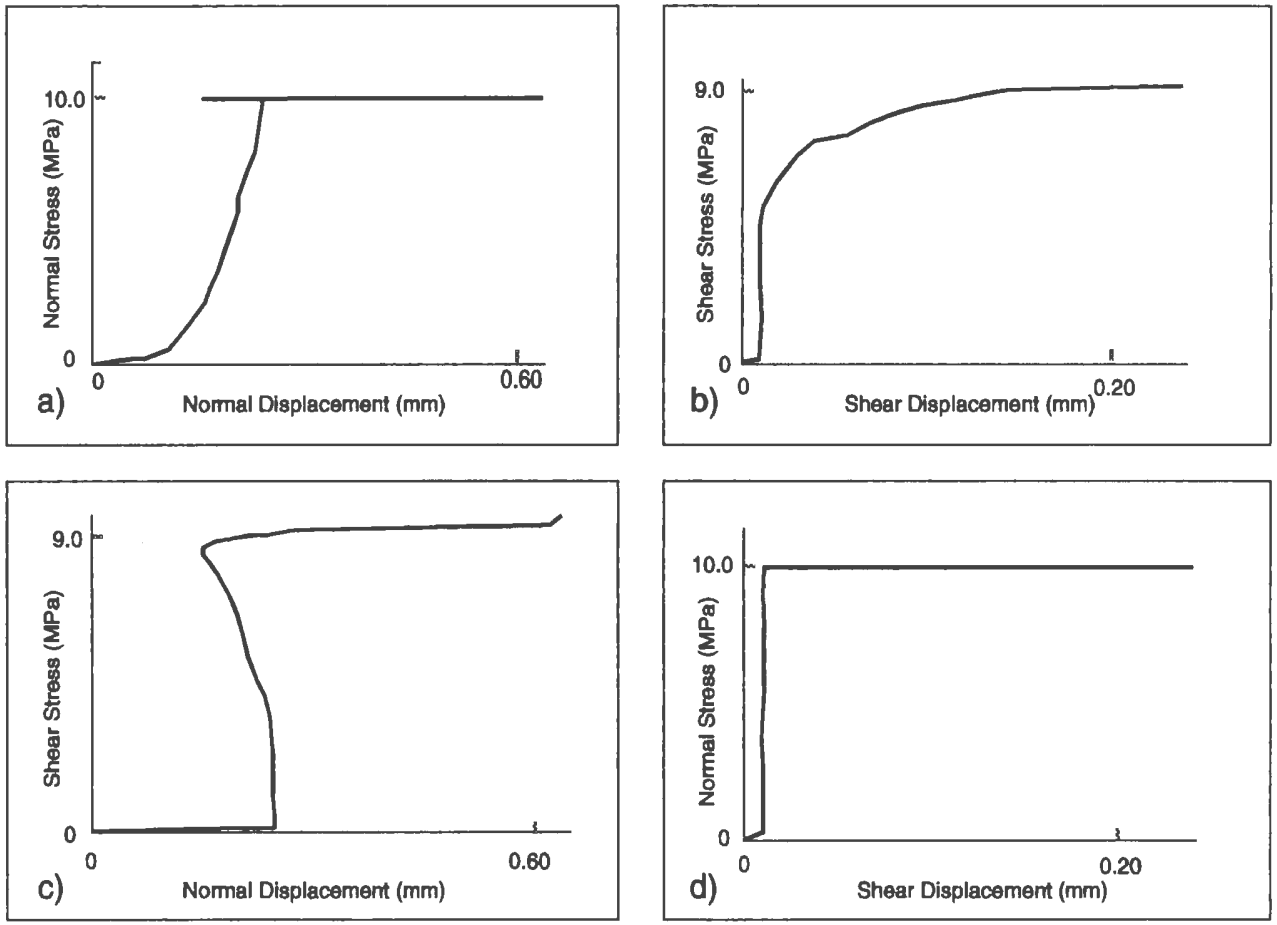

Figure 3-6 (d): Shear 3b, Displacement versus Stress.
a) Normal Displacement versus Normal Stress, b) Shear Displacement versus Shear Stress,
c) Normal Displacement versus Shear Stress and d) Shear Displacement versus Normal Stress.

closure at failure which is due to the failure of the block and the corresponding uncontrolled movements of the LVDT's.

Figures 3-7 (a to d) (Strain Distribution at Peak Load) represent the strain distribution seen in LSR-2 during the shear loading cycles at the peak shear stress for each cycle. During the application of shear stress in each shear cycle, strain gauges 55 and 78 (see Figure 2-3) show the stress concentration effects produced by the actuators in the upper right of the sample.

Unfortunately, two of the three corresponding rosettes in the lower left quadrant (5-6-7, 10-11-12) had failed prior to testing, so the corresponding compressional strain field is not obvious in this area. It is significant to note, however, that it is only during shear cycle 3b (Figure 3-7(d)), that rosette 17-19 reflects the effects of the applied load. This is likely due to the effects of permanent deformation of the model at the end of shear cycle 3a, (Figure 3-7(c)). This caused the stresses to be transferred from the upper block to the lower block by the left asperity in cycle 3b, rather than the right asperity, which appeared to be the case in shear cycles 1 to 3a. The transfer of stresses by the right asperity during S1, S2 and S3a would place the area of

high compressional strains in the lower left quadrant of the model in the area with no functional strain rosettes. By cycle 3b, the model had deformed sufficiently that the left asperity was transferring the load, and this is reflected in rosette 17-19.

Corresponding to the zone of compressional strains acting diagonally across the model from the lower left to upper right, there are zones in the upper left and lower right showing large extensional strains (Figure 3-7 (c,d)).

Post test observation suggests that the displacement profile for cycle 3b may not be completely due to shear movement on the fracture plane (Figure 3-5). The sample fractured at the base of the left large scale asperity, and at the ends (Figure 3-8, 3-9). At least some of these fractures extended through the concrete to the epoxy grouting holding the model in the steel sample box causing the grouting to became partially detached from both the model and the steel. Much of the apparent fracture displacement seen for cycle 3b (Figure 3-5) can be attributed to the fracturing of the ends of the sample, to which the displacement LVDT's were attached.

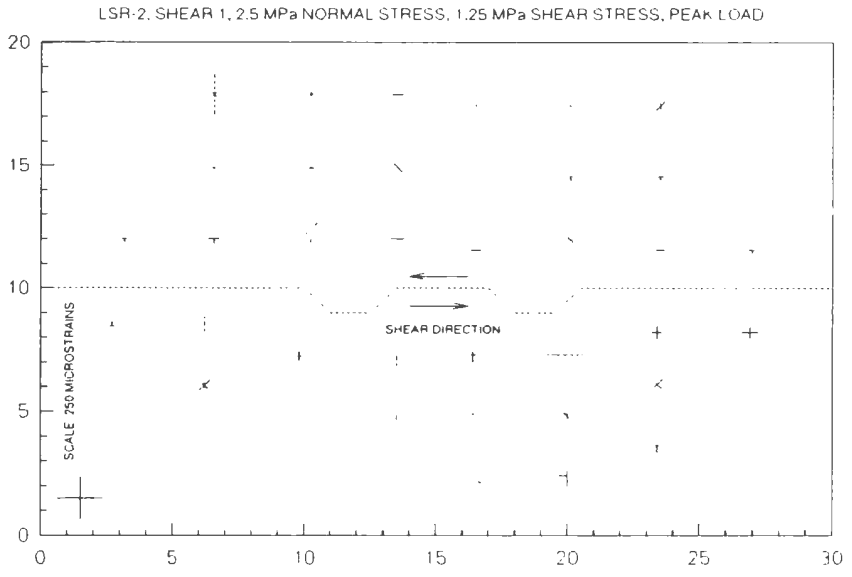

Figure 3-7 (a): Strain Distribution at Peak Load (2.0 MPa Normal, 1.25 MPa Shear), Shear Cycle 1. Numbers along axes are scale in centimetres, dashed vectors represent extensional microstrains, solid represent compressional microstrains. (See Figure 2-3 for strain gauge locations)

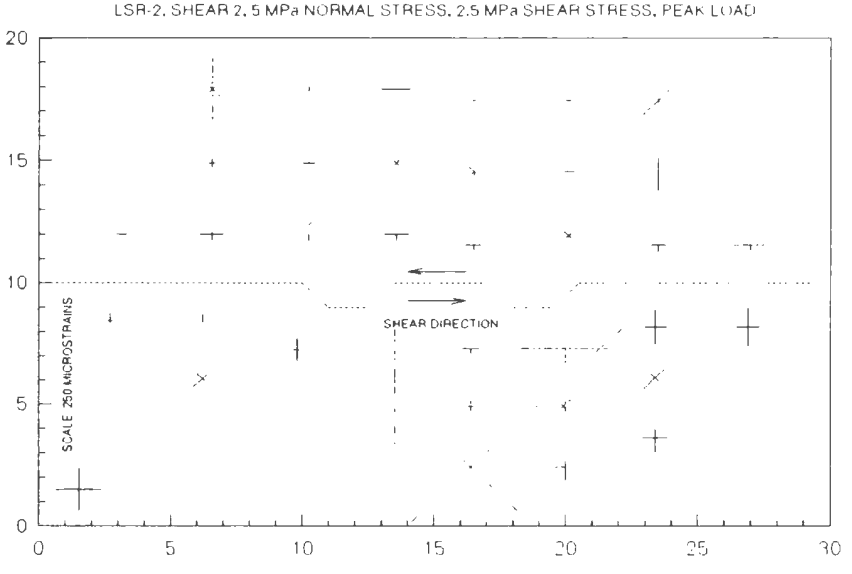

Figure 3-7 (b): Strain Distribution at Peak Load (5.0 MPa Normal, 2.5 MPa Shear), Shear Cycle 2. (See Figure 2-3 for strain gauge locations)

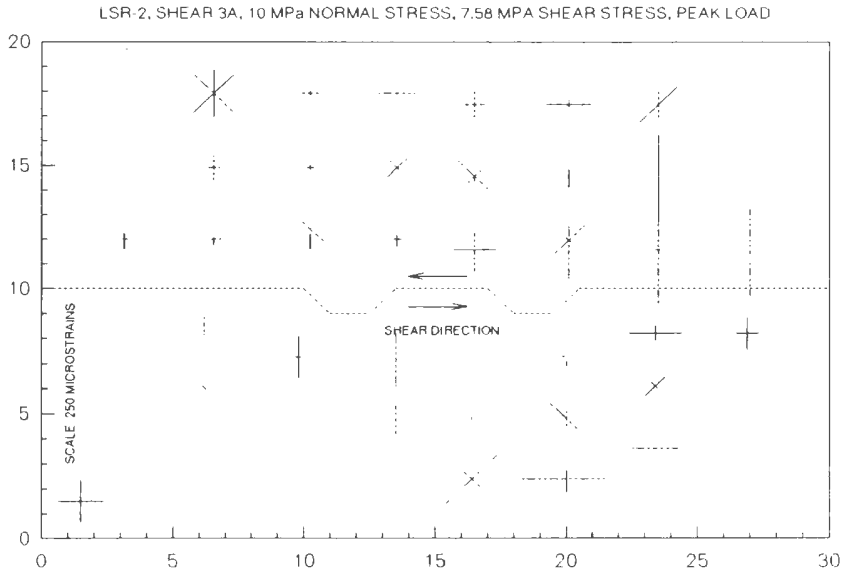

Figure 3-7 (c): Strain Distribution at Peak Load (10.0 MPa Normal, 7.58 MPa Shear), Shear Cycle 3a. (See Figure 2-3 for strain gauge locations)

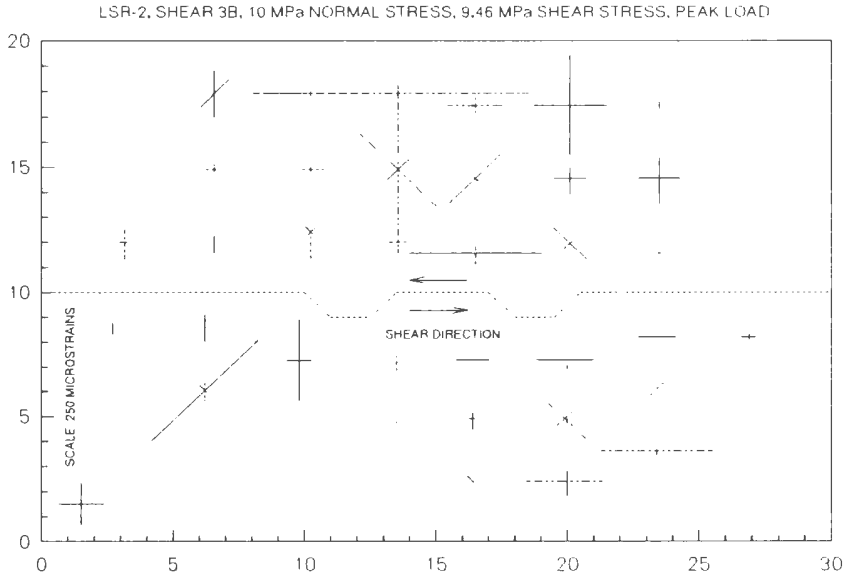

Figure 3-7 (d): Strain Distribution at Peak Load (10.0 MPa Normal, 9.46 MPa Shear), Shear Cycle 3b. (See Figure 2-3 for strain gauge locations)

3.3 Geometry and Timing of Induced Fractures

To preserve both the artificial and induced fractures, the model was evacuated, flushed with alcohol, and injected with coloured epoxy at the end of the final shear cycle. The centre section was then sliced out of the steel sample boxes with a diamond saw. It was cut lengthwise into 6 slices, giving 5 profiles showing the form of the fractures and fracture porosity near the artificial fracture plane (Figure 3-8). A series of cores were cut out of the remaining concrete in the sample boxes to complete a profile of the fractures in the model (Figures 3-9, 2-4, and 2-5). Once the cores were removed, it was seen that the epoxy-concrete grouting under both the top and bottom blocks was very porous, and was not even in contact with the concrete over much of the surfaces. This condition was suspected from the strain data.

During shear cycle 3a, somewhere between 1 and 5 MPa shear stress (as determined from the index times on the well data), the model started separating from the grout in the upper box. This was seen in the failure of test well W1 imbedded in the concrete in the top of the model (Figures 2-2, 2-5 and 3-9). The exact time of failure is impossible to determine, since only one well at a time was being monitored. The four wells were being

pressurised and monitored sequentially for 30 minutes each, giving an unmonitored window of 1.5 hours where the failure occured. On removal of the core containing this well, it was seen that the brass tube that was the casing for this well was sheared off outside of the concrete, and no fractures intersected the open portion of the well bore. By the end of shear cycle 3a, the model had begun to leak water from the extensional fractures on both ends of the profile illustrated in Figure 3-9. These fractures were probably induced by the centre of the model being pushed up into the cavity above and below the model caused by the incomplete grouting, and the ends being held in place by the better quality grouting around the edges. During shear cycle 3b, an extensional fracture extending upwards from the base of the left asperity started opening (Figure 3-9). This was seen in the test failure of wells W2 and W3, and confirmed by visual observation of the fracture in the cores. This fracture eventually extended to the top of well 4, which had failed after wells 2 and 3, and before the end of the test.

The lower half of LSR-2 showed several small internal fractures of limited length which were difficult to trace, in addition to the major ones at the ends of the profiles.

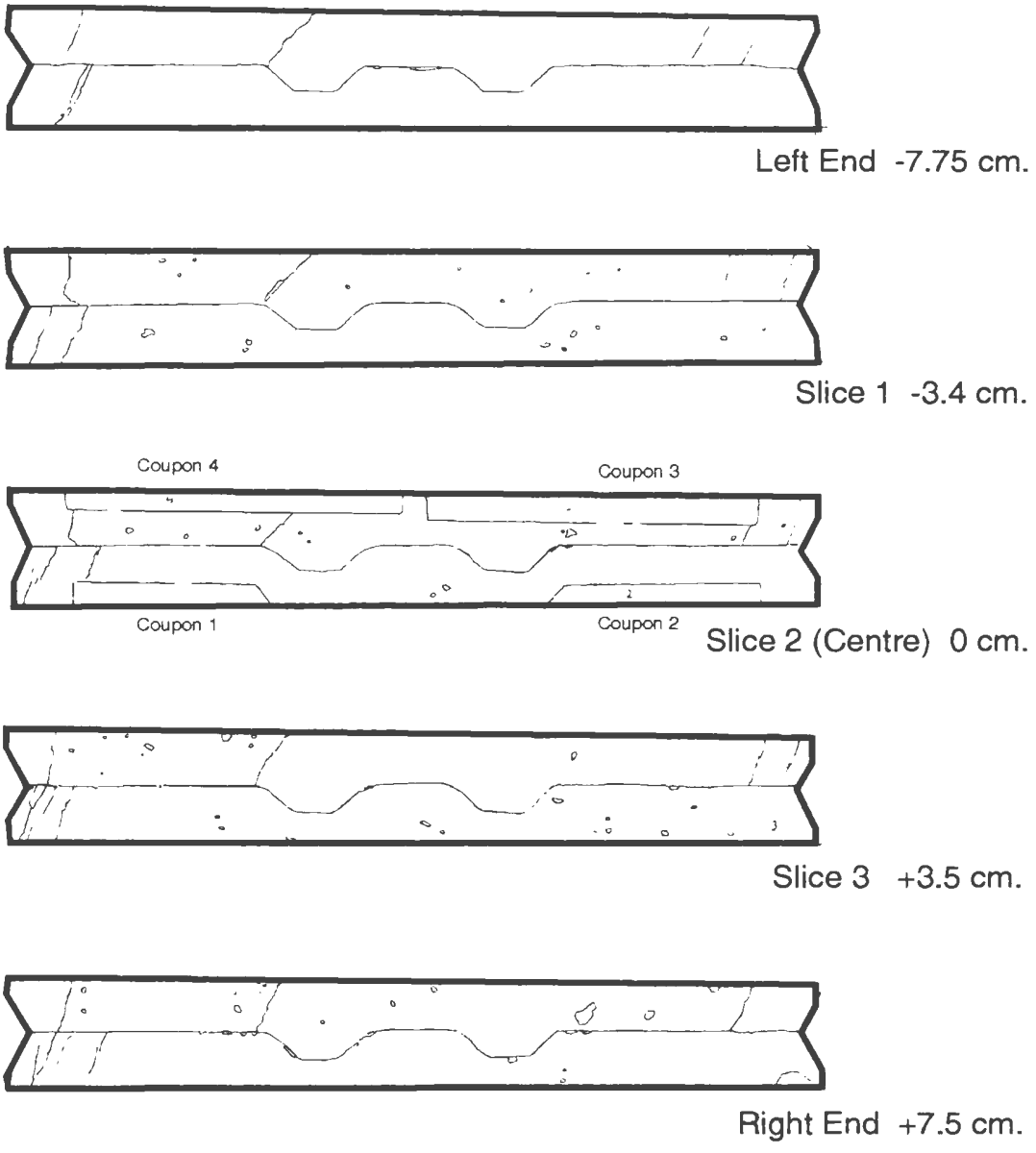

Figure 3-8: Profiles of post test fracture patterns from centre section of LSR-2

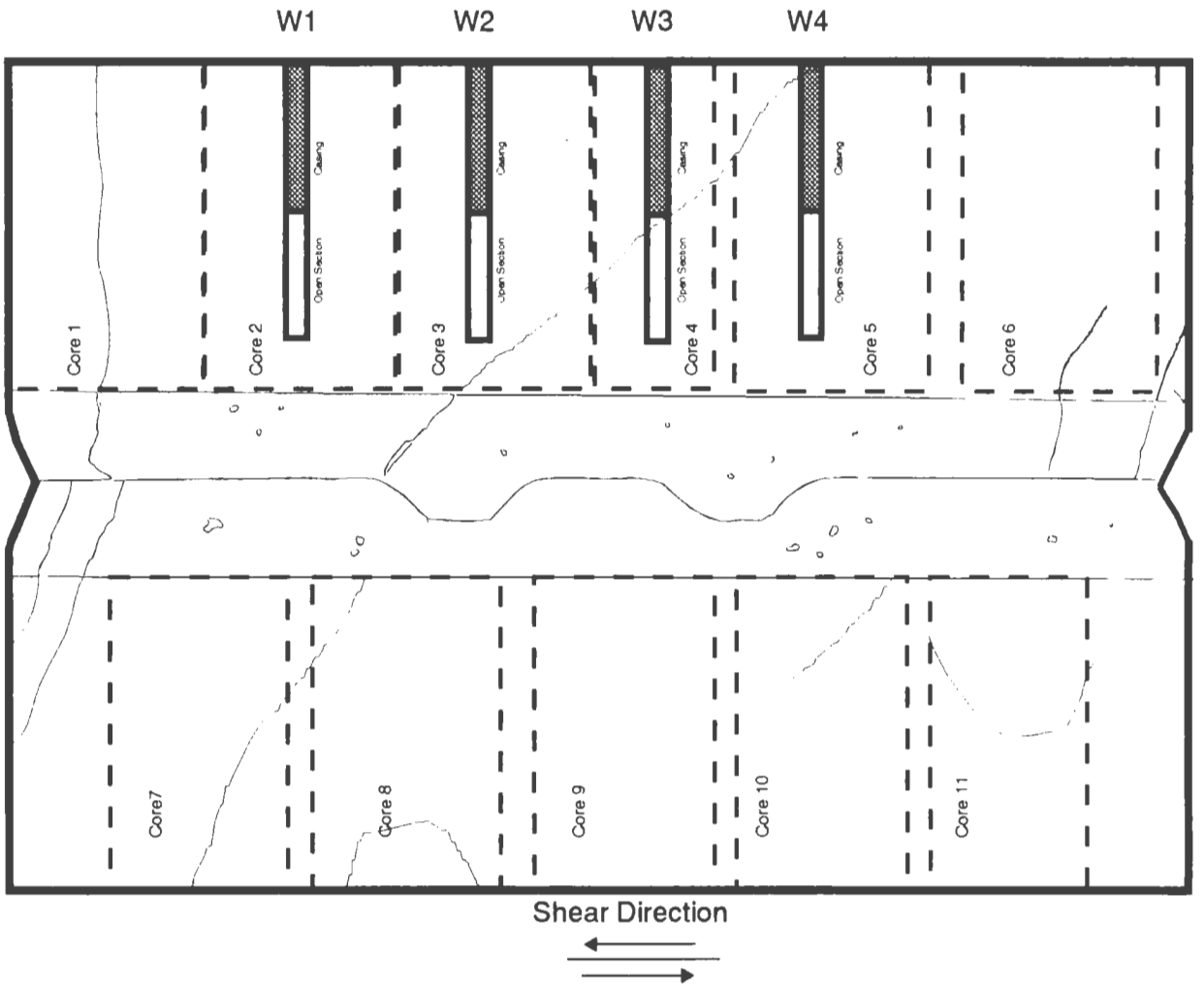

Figure 3-9: Reconstruction of fracture patterns taken along the profile of slice 1, and incorporating cores taken from the portion of the model remaining in the steel sample box.

3.4 Flow Data

Flow data recorded during this experiment were used to calculate the fracture transmissivity as 1) a function of normal and shear stress, and 2) as a function of time, to see the effects on the permeability and deformation of the artificial fracture plane.

Fracture transmissivity was calculated (Gale, personal communication, 1995; Raven and Gale, 1985) by substituting Darcy's law

$$Q = K*\frac{dh}{dl}*A = K*\frac{dh}{dl}*(b*w)$$

in the transmissivity equation

$$T = K*b$$

to give the form

$$T = \frac{Q}{\frac{dh}{dl}*w}$$

where: b= aperture
T = transmissivity (L^2/t),
Q = flow rate (L^3/t),
K = hydraulic conductivity (L/t),
$\frac{dh}{dl}$ = hydraulic gradient,
and w = width of the sample.

This form of the equation is independent of the aperture term "b". The transmissivity was calculated and plotted throughout the testing. Once the values appeared to stabilise, the test was allowed to proceed to the next step.

The following figures (3-10 (a-f)) clearly show the effects of increasing stress on the transmissivity of the fracture plane. Shear cycle 3b is not included, as the model had begun to fracture by this stage of the testing process, giving many uncontrollable leaks which invalidated the flow measurements. In Figures 3-10 (d, e and f), the shear portion of the loading cycle has been "combined" with the normal load and plotted incrementally from the end of the normal loading cycle, by adding the shear stress value to the normal stress value. This was done as a plotting "trick" to to help visualise the incremental change in fracture transmissivity as the sample is sheared. All test cycles show a decrease in the fracture transmissivity with increasing

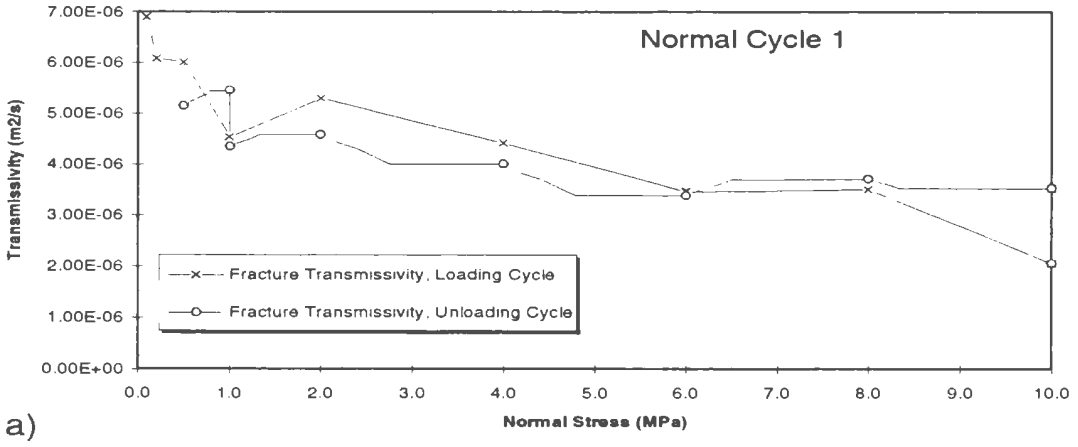

a)

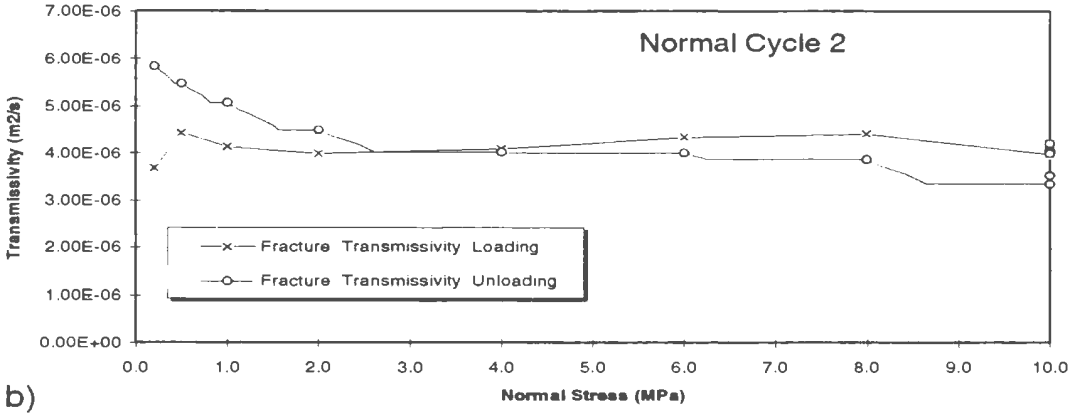

b)

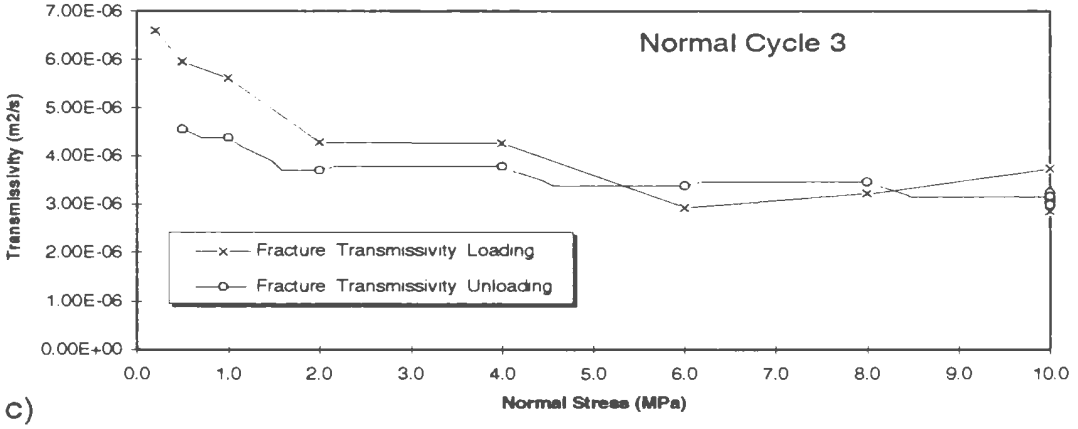

c)

Figure 3-10 (a to c): Fracture transmissivity versus applied normal stress for normal cycles 1, 2, and 3.

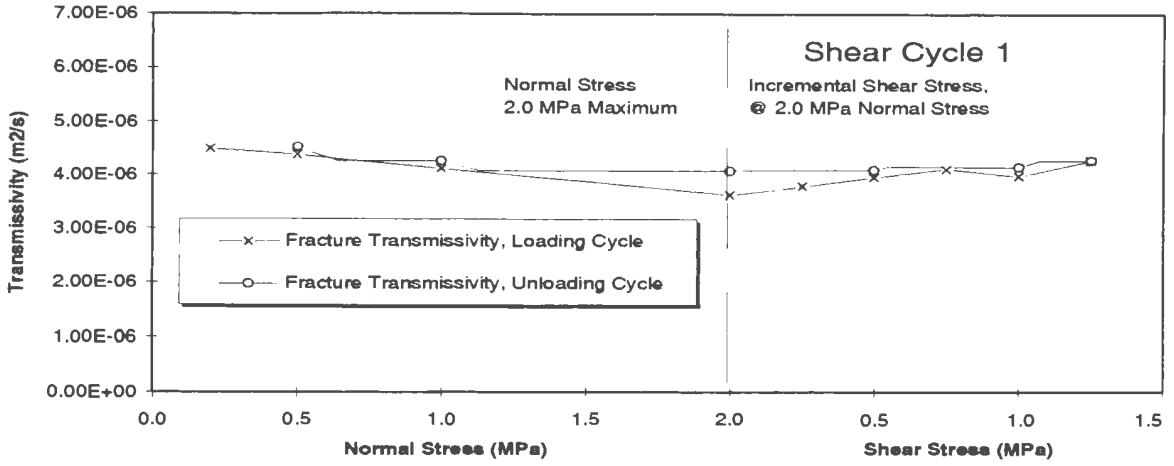

d)

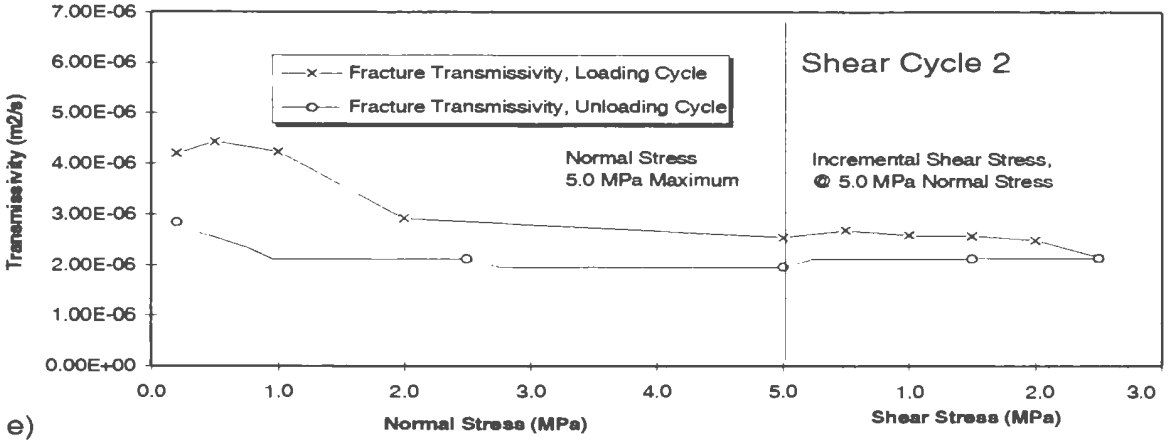

e)

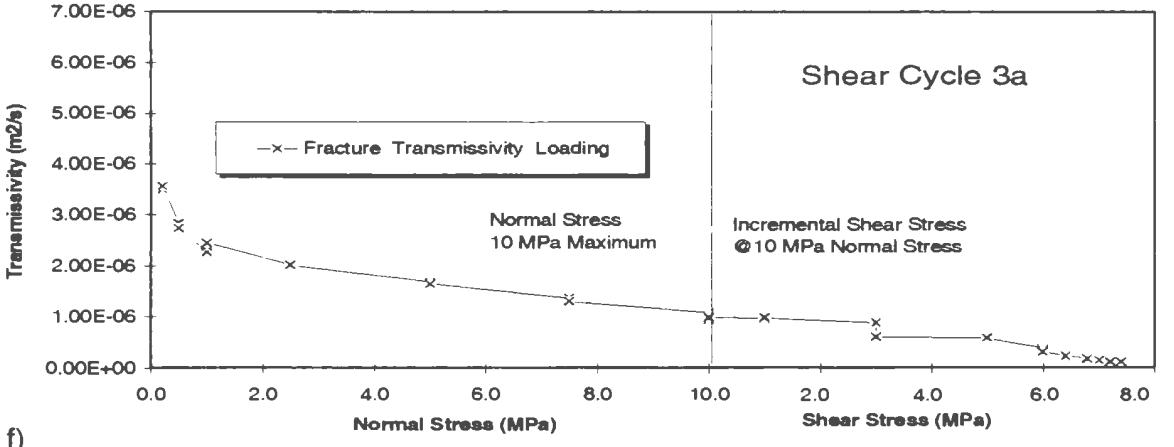

f)

Figure 3-10 (d to f): Fracture transmissivity versus applied combined normal and shear stress for shear cycles 1, 2, and 3a.

normal load. This reduction in transmissivity is at least partially recovered as the sample was unloaded, mirroring the fracture closure hysteresis seen in Figure 3-1.

Figures 3-11 (a and b) show the detail of flow data for shear cycle 3a. Figure 3-11 (a) shows the drop in transmissivity with time at each loading step as the fracture deforms and the transmissivity stabilises at its new value. Figure 3-11(b), seen previously as Figure 3-10(f), illustrates the overall relationship of transmissivity in relation to the applied stress, suggesting a logarithmic relationship of some sort between the transmissivity and the normal stress applied. This figure also illustrates the effect of the further closing of the aperture at the large scale asperities, as the sample is sheared. To further illustrate this apparent logarithmic relationship between stress and the transmissivity, the log of the fracture transmissivity was plotted against the cube root of the applied stress (Figure 3-12), as suggested by the work of Jones (1975). As was done above on the linear plots of stress and transmissivity, the shear stress was combined with the normal stress, to cause a continuation of the plot after the end of the normal stress data to show the effect as the sample is sheared

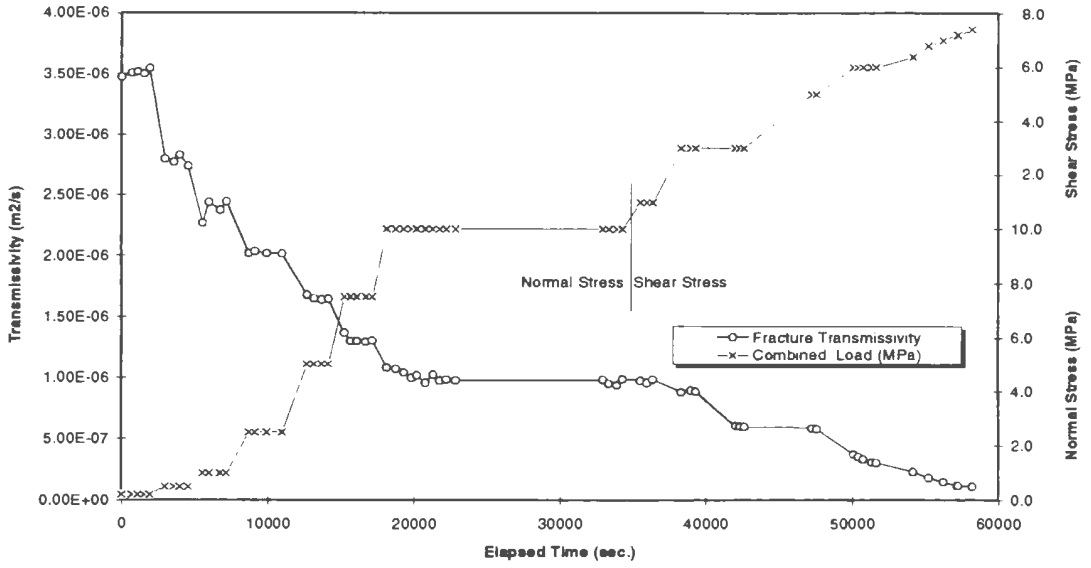

Figure 3-11 (a): Fracture Transmissivity as a function of time for shear cycle 3a. Note the changes in transmissivity at each loading step.

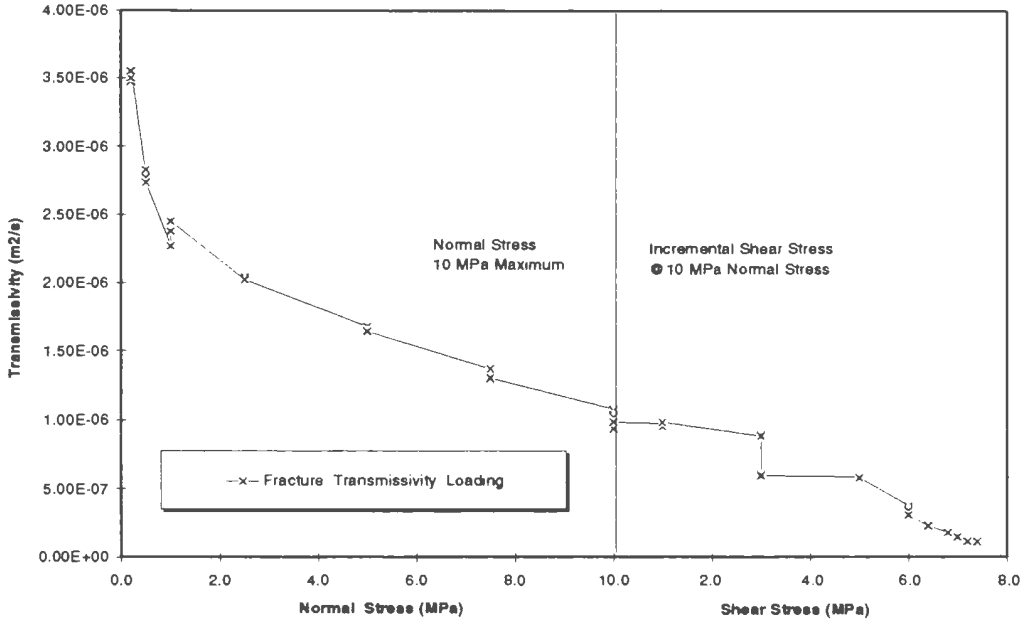

Figure 3-11 (b): Fracture transmissivity as a function of stress applied for shear cycle 3a. Note the apparent logarithmic decrease in transmissivity with stress applied.

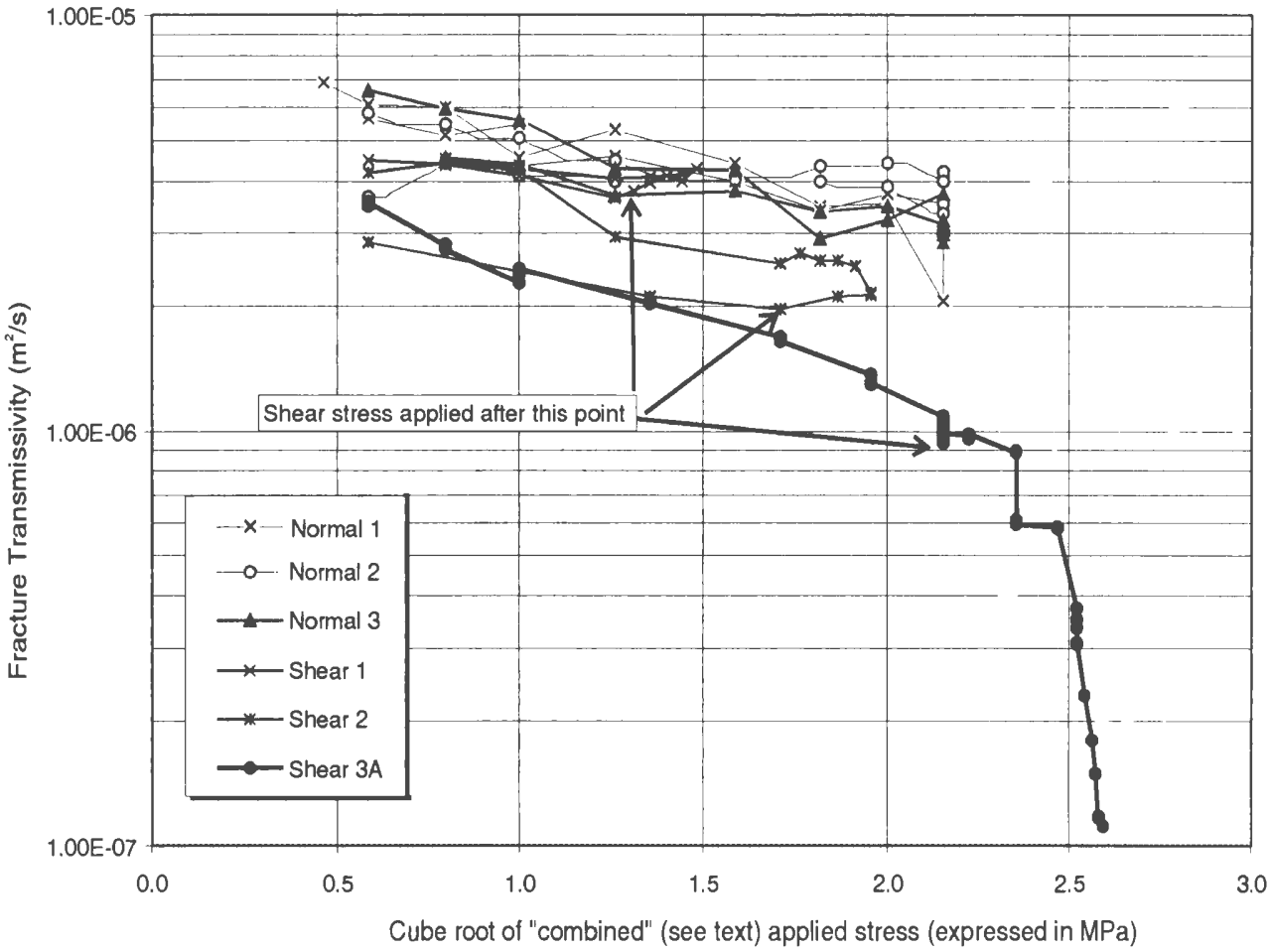

Figure 3-12: Plot of the log of the fracture transmissivity versus the cube root of the applied stress

(i.e. all data points to the right of 1.26, 1.71 and 2.15 for shear cycles 1, 2, and 3a, respectively, are shear stress transmissivity measurements taken at 2.0, 5.0, and 10.0 MPa applied normal stress). For the normal portion of the loading cycles, and over the range of stresses used, a linear relationship is seen in Figure 3-12. For the shear portions of the cycles, a slight increase in transmissivity (indicating dilation of the fracture) can be seen in Figures 3-10 (d, e) and 3-12 for shear cycles 1 and 2, and a significant reduction of transmissivity, indicating closure, at the large scale asperities for shear cycle 3a (Figures 3-10 (f), 3-11(b), 3-12).

The fracture transmissivity was calculated using the data from shear cycle 3a by examining the gradients between the manometers along a lengthwise cross section of the test specimen to compare with the modelled fracture closures discussed in Chapter 4. These are shown in Figures 3-13 (a and b). The data points are plotted at the midpoints between adjacent pairs of manometers along the lengthwise cross section, showing the transmissivity at both the inlet and outlet ends, and across each of the large scale asperities (Figure 2-8). Figure 3-13 (a) suggests an uneven fracture closure caused either by bridging at the asperity closest to the outlet, or rotation of

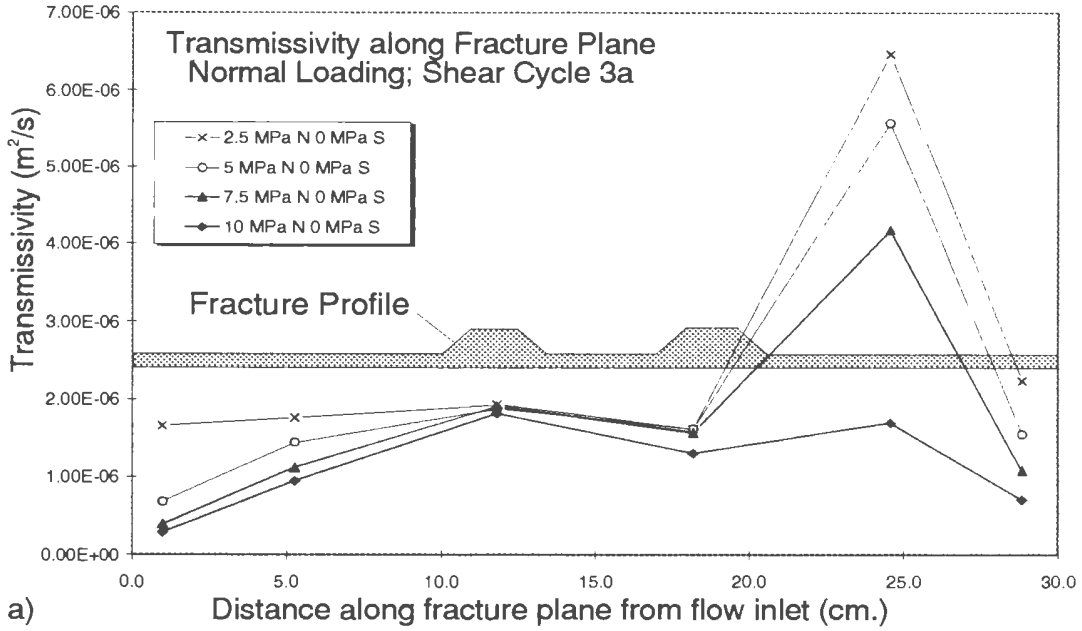

a)

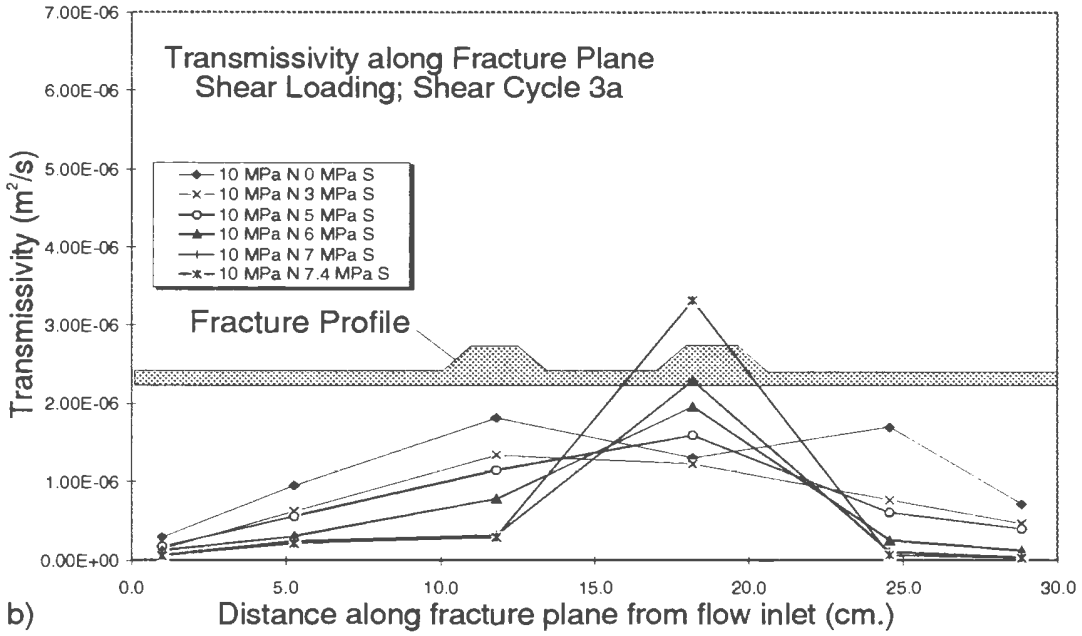

b)

Figure 3-13: Profile of Fracture Transmissivity along Fracture Plane measured from flow inlet. Note: data points plotted at midpoint between manometer ports along lengthwise centre

the sample box in the test apparatus, at low normal stress levels. As the normal stress is increased to 10 MPa, this variation is reduced significantly as the fracture deforms, leaving a relatively uniform fracture transmissivity (or closure) across the sample, with slightly more closure at the unsupported ends of the test specimen. As the model is sheared, the fracture transmissivity is further decreased along the model, except at the asperity closest to the outlet (Figure 2-8), which shows a significant increase, suggesting dilation at that asperity.

Chapter 4 - Comparison of Experimental Results with Numerical Model Simulation

After the testing process was completed, finite element numerical modelling was used to compare the actual strain distribution observed with the stress distribution predicted by the Coupled Stress Fracture Flow Code (CSFFC) (Gale, 1975). Modelling was completed over a range of normal and shear fracture stresses, incorporating friction angles and material properties determined from standard tables and previous experimental work.

4.1 Numerical Model: CSFFC (Coupled Stress Fracture Flow Code)

The method used in this study employs a fluid flow and plane strain finite element program described by Gale (1975), and adapted to run under SUN FORTRAN by Butt (1994). Numerical solutions are provided by an iterative process with convergence to user specified tolerances. Initial stress conditions, or non linear material loading behaviour can be included in the model in the form of easily varied input material and loading parameters and as residual stress components in the input file. This enables material properties used in the numerical simulation to conform to experimentally determined values throughout the loading path.

4.1.1 Mesh

The finite element mesh (FEM) used in this study was modified from the work of Butt (1994), by repositioning the nodal co-ordinates to give two asperities matching the form of LSR-2. The dimensions and geometry were based on a vertical cross section through the biaxial shear frame sample box, sample and fractured plane as shown in Figure 4-1 (a and b). A plane strain formulation was considered suitable for this configuration, as most of the concrete model is constrained from deforming out of the plane of the model by the steel sample box. The model was rotated 45 degrees from its physical testing configuration to simplify the application of the boundary forces, which were applied along the X and Y axes of Figure 4-1 (b). Roller boundary constraints were applied where the lower half of the sample box was restrained by the reaction members in the biaxial frame, and the loads applied to the nodes indicated in the upper half (Figure 4-1 (a)).

4.1.2 Physical Properties

Two intact concrete cylinders, and five epoxy concrete cylinders of the materials used in the assembling of this model were tested using the appropriate ASTM (D2938-86, D3148-86, D4543-85) standards and procedures. The results of these tests enabled the determination of the

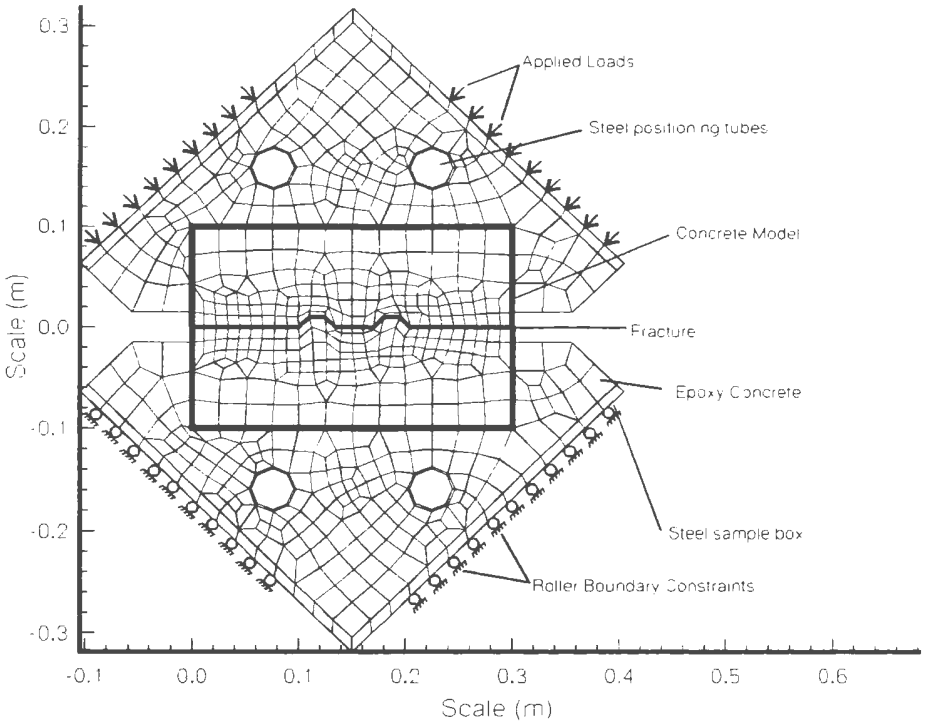

Figure 4-1(a): Finite Element mesh for LSR-2

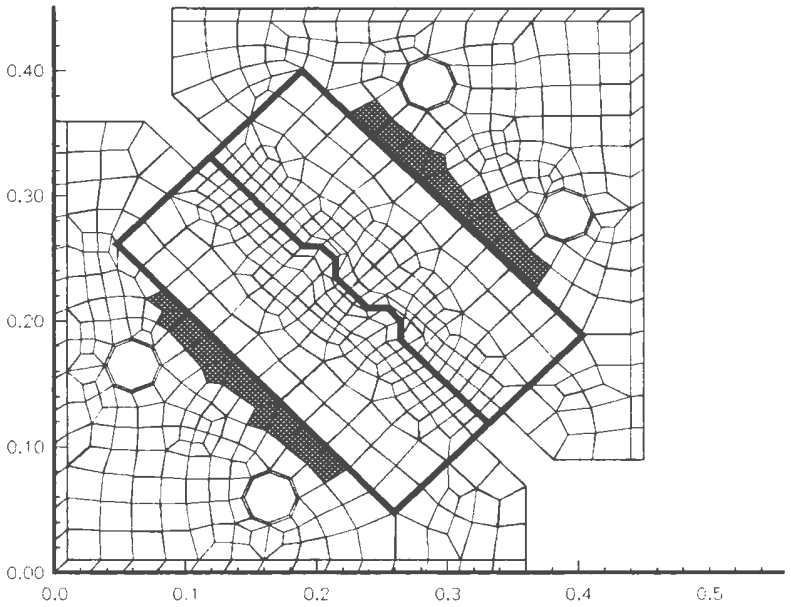

Figure 4-1(b): Finite Element mesh for LSR-2, as oriented for numerical modeling.
Note: Shaded area represents modified epoxy characteristics (see text).

elastic constants of the intact concrete and epoxy grout over and above the range of applied loads available from the biaxial loading apparatus. The full results of these independent tests are detailed in Appendix A4 and A5. The values used for the numerical model have been extracted from these data, averaged and presented in Tables 4-1 and 4-2.

Table 4-1 Material Properties - Steel and Epoxy Concrete

	Young's Modulus (Pa)	Poisson's Ratio
Steel*	200.E9	0.250
Epoxy Concrete**	13.E9	0.260
Modified Epoxy Concrete***	1.3E9	0.450

* Value for steel estimated from standard tables (Beer and Johnson, 1981).
**Value for epoxy concrete estimated from average of five small diameter cores.
***See text, section 4-2, Fig. 4-1b

Table 4-2 Material Properties - High Strength Concrete

@ Stress (MPa)	Young's Modulus (Pa)	Poisson's Ratio
0.5	22.50 E9	.295
1.0	24.15 E9	.285
2.0	26.20 E9	.255
5.0	29.80 E9	.240
8.0	31.20 E9	.230
10.0	31.90 E9	.230

Fracture stiffness (Table 4-3) was determined for the purposes of the modelling from normal cycle 2 for the normal stiffness, and from shear cycle 3a for the shear stiffness. The finite element code required the estimation of the stiffness by the secant method, rather than the tangent method.

Table 4-3 Fracture Stiffness

Normal Loading Steps			Shear Loading Steps			
Normal Stress (MPa)	Shear Stress (MPa)	Normal Stiffness (GPa/m)	Normal Stress (MPa)	Shear Stress (MPa)	Shear Stiffness (GPa/m)	Friction Angle (deg.)
0.5	0.0	20.0	10.0	0.0	3550	22
1.0	0.0	23.3	10.0	1.0	3550	22
2.0	0.0	31.3	10.0	3.0	3550	22
5.0	0.0	60.2	10.0	5.0	9081	67
8.0	0.0	70.2	10.0	6.0	674.6	67
10.0	0.0	82.6	10.0	7.0	348.6	67
8.0	0.0	57.6	10.0	8.0	141.5	67
5.0	0.0	38.2	10.0	9.0	84.8	67
2.0	0.0	17.5	10.0	10.0	84.8	67
1.0	0.0	10.4				
0.5	0.0	6.33				

4.2 Comparison of Numerical Model Simulation and Normal Loading Experiments

The output from the finite element code CSFFC (Coupled Stress Fracture Flow Code) gives the two principal stresses at the centre of each cell (σ_{max}

and σ_{min}), and the angle α to σ_{max} (Figure 4-2). Plotting the magnitude and direction of the principal stresses is the ideal method of presentation of the state of internal stress of the model in that it enables one to easily see magnitude and direction of the stresses and the rotation of the stress field as the stress field changes. Since most of the strain gauges are in either a horizontal or vertical orientation, the stress field must be transformed using the Mohr's circle equations to resolve the principal stresses into directions perpendicular and parallel to the fracture plane for ease of comparison with the test data. This was accomplished by calculating both a horizontal (parallel to fracture plane) and vertical (perpendicular to fracture plane) component of σ using:

$$\sigma = \frac{\sigma\max + \sigma\min}{2} + \frac{\sigma\max - \sigma\min}{2}\cos\alpha ,$$

where α is calculated for the horizontal σ as $\alpha_h = 2^*(\alpha\text{-}45^\circ)$, and $\alpha_v = 2^*(\alpha + 45^\circ)$ for the vertical σ. This is illustrated in Figure 4-2.

The material properties were modified in selected cells of the finite element mesh to compensate for the poor bonding characteristics of the epoxy grouting above and below the model. These cells are highlighted in Figure

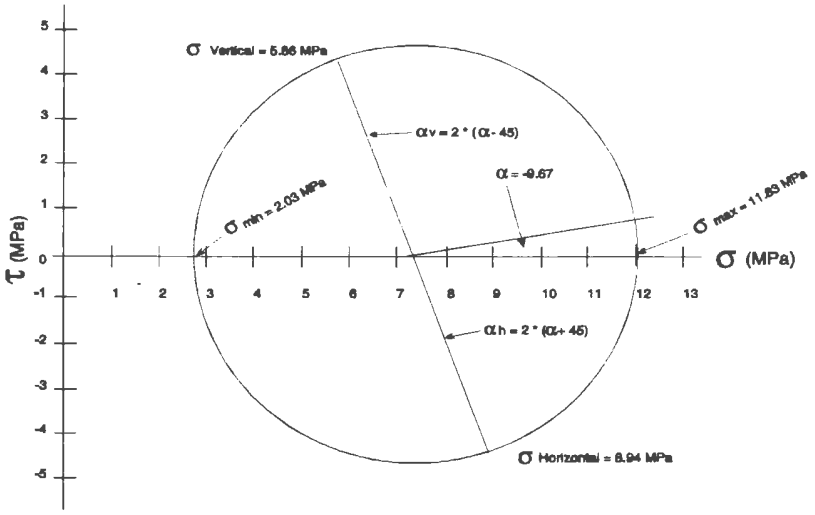

Figure 4-2: Mohr's Circle illustrating a) position of σ_{max}, σ_{min}, and α in relation to σ and τ, and b) 45° rotation of principal stresses to local co-ordinates for LSR-2 because of tilted FEM mesh (Figure 4-1). Data from element 666, lower right corner.

4-1(b), and the parameters are included in Table 4-1. The effect of these gaps is seen to be very dramatic in the simulations. When the epoxy grout bond is good above and below the model, the horizontal and vertical stress distribution across the top and bottom is uniform (Figure 4-3 (a)). When the bond is poor, using the modified epoxy characteristics (Table 4-1), the vertical component is reduced to near zero near the centre (Figure 4-3 (b)). This stress reduction corresponds to the zone of extensional and lower compressional strains seen in the same areas of LSR-2, as discussed in Chapter 3. It is interesting to note that the effect of the incomplete epoxy bonding on the strain field appears larger in the physical experiment than in

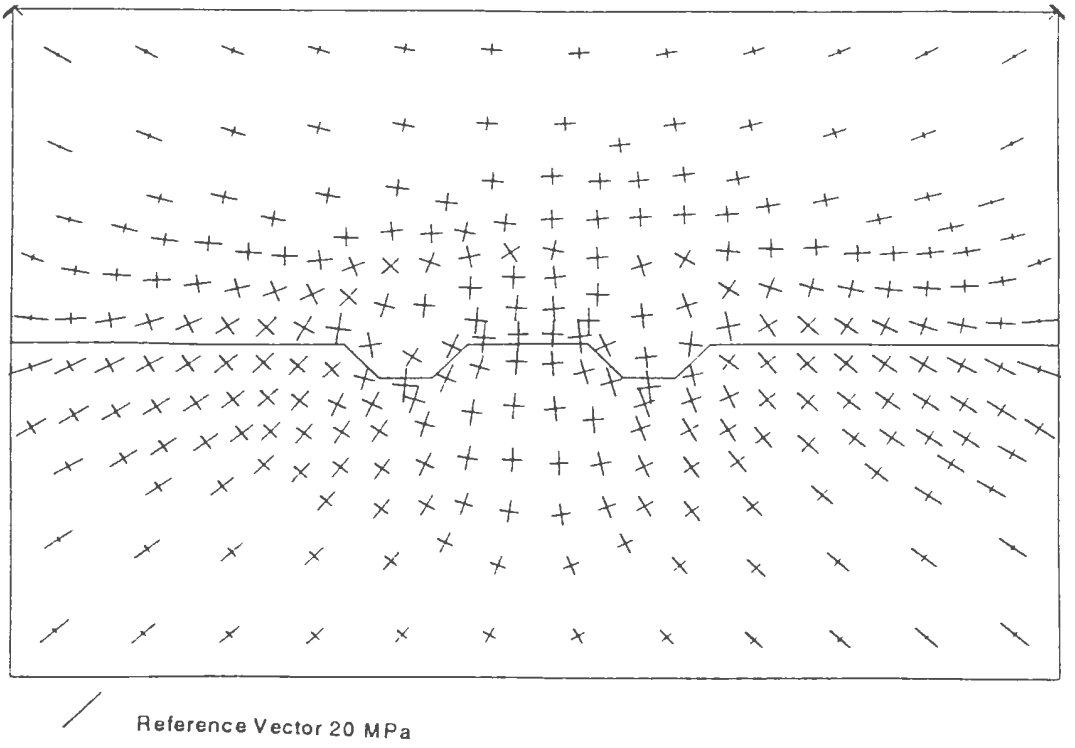

Figure 4-3 (a): Comparison of FEM Results - Principle stress vectors for complete epoxy bonding case at 10 MPa. normal stress (see Table 4-1).

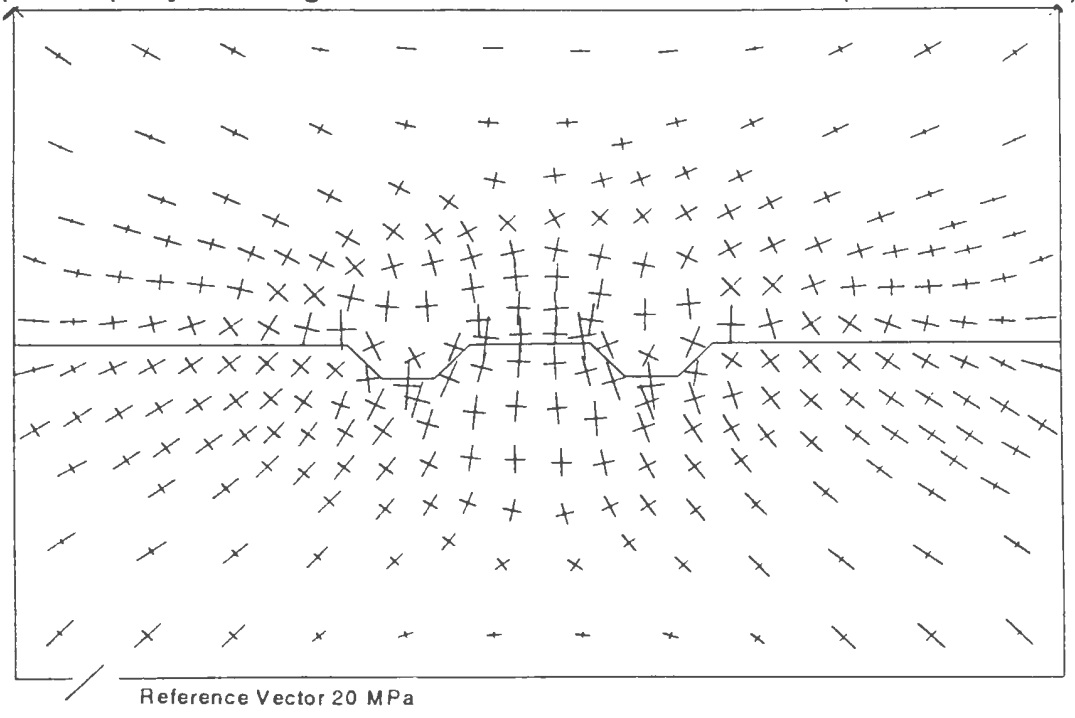

Figure 4-3 (b): Comparison of FEM Results - Principal stress vectors for incomplete epoxy bonding case at 10 MPa. normal stress (see Table 4-1).

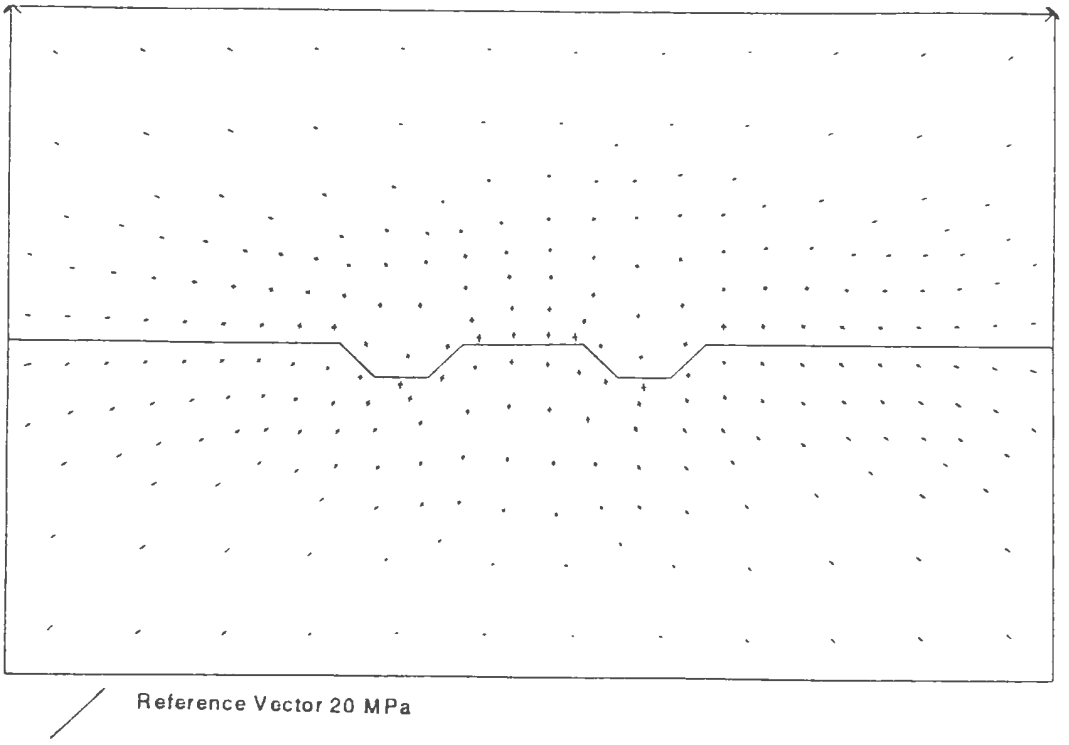

Figure 4-4 (a) (i) FEM Results - Normal Loading Cycle at 2 MPa (loading), principal stress vectors.

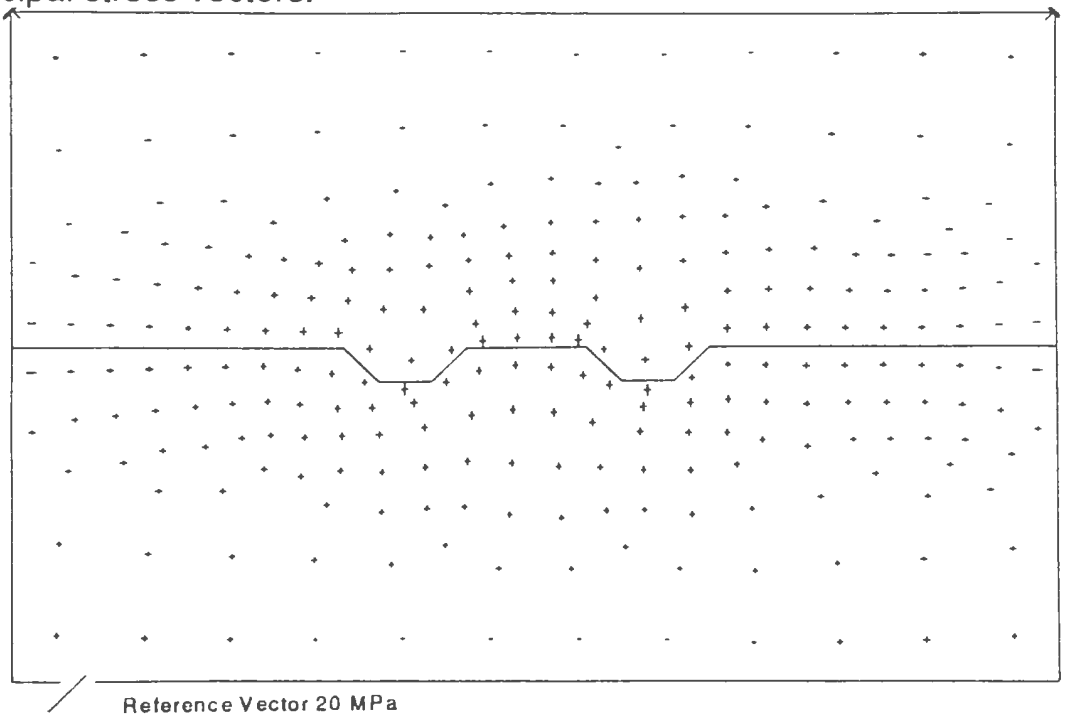

Figure 4-4 (a) (ii) FEM Results - Normal Loading Cycle at 2 MPa (loading), stress vectors resolved into vertical and horizontal components.

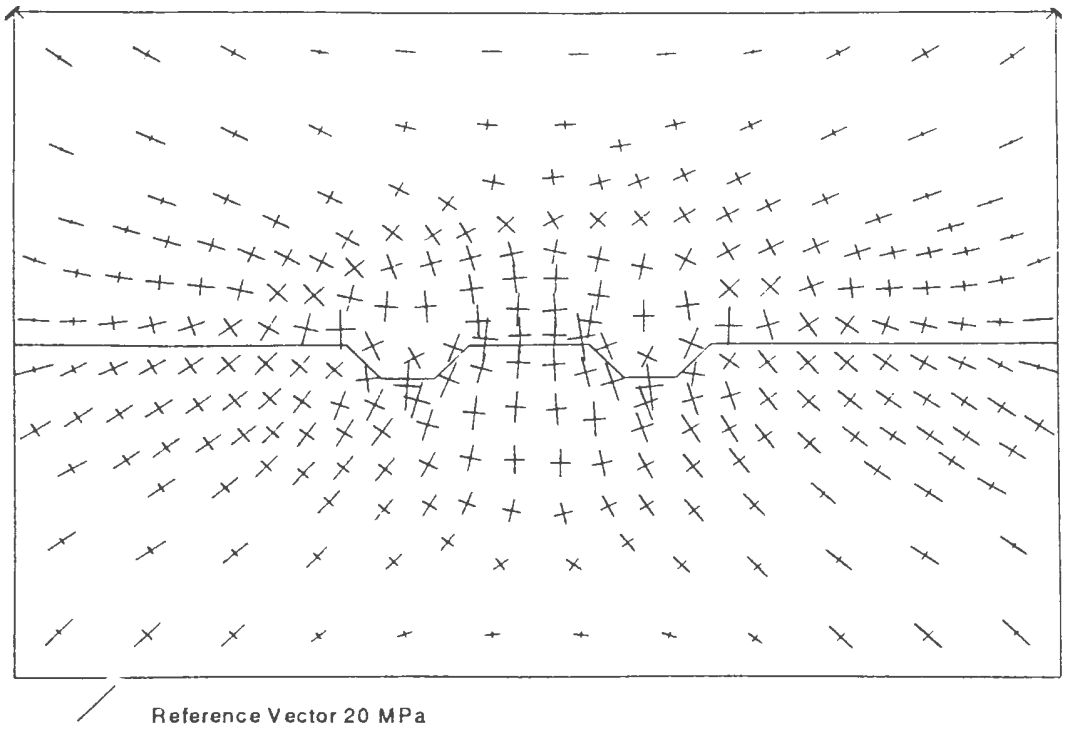

Figure 4-4 (b) (i) FEM Results - Normal Loading Cycle at 10 MPa (loading), principal stress vectors.

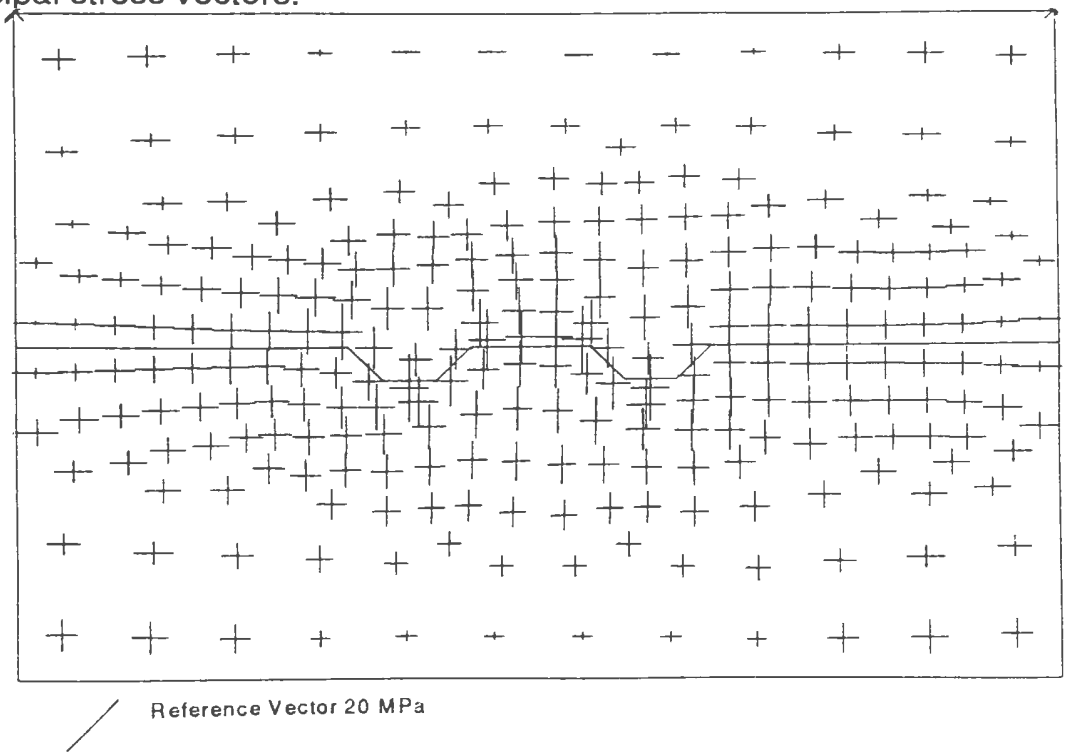

Figure 4-4 (b) (ii) FEM Results - Normal Loading Cycle at 10 MPa (loading), stress vectors resolved into vertical and horizontal components.

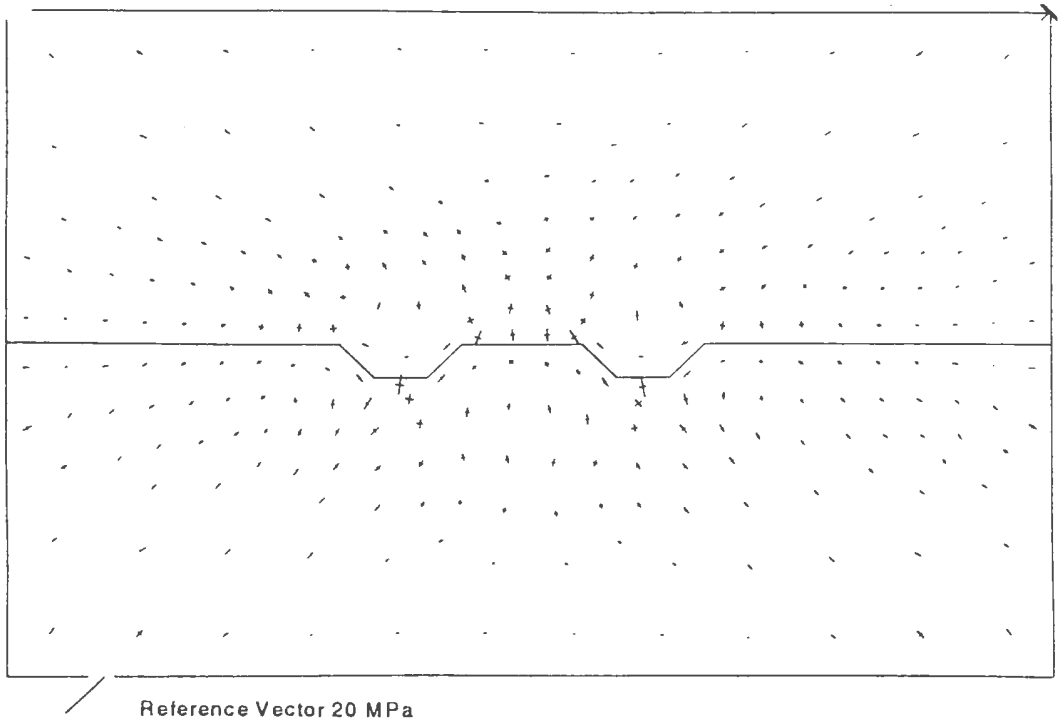

Figure 4-4 (c) (i) FEM Results - Normal Loading Cycle at 2 MPa (unloading), principal stress vectors.

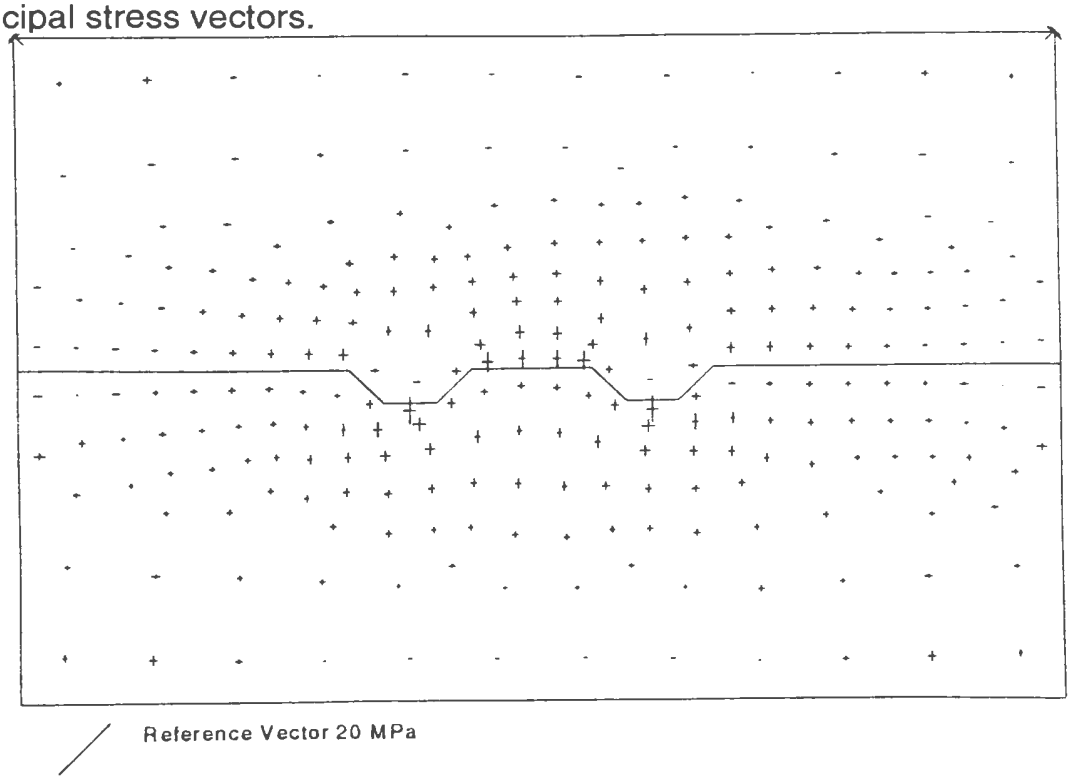

Figure 4-4 (c) (ii) FEM Results - Normal Loading Cycle at 2 MPa (unloading), stress vectors resolved into vertical and horizontal components.

the numerical modelling. This effect has also been noted by Handanyan et al (1990) in their discussion of the role of tension in failure of jointed rock. They noted that "the finite element tensile stresses were lower than the measured surface stresses, but exceeded the tensile strength of the material". This is likely due to differences in the compressive and tensile Young's Modulus and Poisson's Ratio values for the concrete as only the compressive values were used in the modelling that relates to this discussion.

Figure 4-4 (a to c) illustrates the internal stress distribution within LSR-2, through a typical normal loading cycle at average normal stresses of 2 (loading), 10 (peak), and 2 (unloading) MPa. Each stress level in the loading cycle is presented as a plot of principal stress directions and magnitudes (i), and as the same data resolved into their vertical and horizontal components (ii). It is seen in this set of plots that there is a significant increase in the vertical and horizontal stress components in the vicinity of the asperities (Figure 4-4 (c) (i, ii)) to approximately 20 MPa vertical and 15 MPa horizontal, with an average normal stress applied to the model of 10 MPa. There is an increase in the horizontal component of the stresses at the ends of the fracture. This is a local effect caused by the

edges of the concrete being exposed in the vicinity of the fracture to allow for the placement of the packer and flow spreaders. The asperities are noted to cause rotation of the stress field in their immediate vicinity, with the principal stress direction σ_{max} generally parallel with the 45 degree sides of the asperities. During unloading, the stress distribution around the asperities show an increase in both the vertical and horizontal (or σ_{max} and σ_{min}) components above the asperities, and a corresponding decrease below. This is due to a "binding" of the bumps, in the matching sockets.

Figure 4-5 shows the fracture stresses and displacements across a lengthwise profile of the fracture plane of the model. Three stress levels are illustrated, 2 MPa during the loading cycle, 10 MPa at peak load, and 2 MPa during the unloading cycle. The stress and displacement normal to the fracture appears to drop over the 45 degree sloping faces of the asperities. In fact, these lower values reflect the effect of the 45 degree angle, and the stresses and displacements at these points are close to the values at the adjacent fracture elements. The closure profile shows larger closures at the ends of the fracture, reinforcing the supposition of pivoting action on the asperities suggested by the strain and stress data from the physical and numerical modelling. As the model is unloaded (Figure 4-5 (c)), it is seen

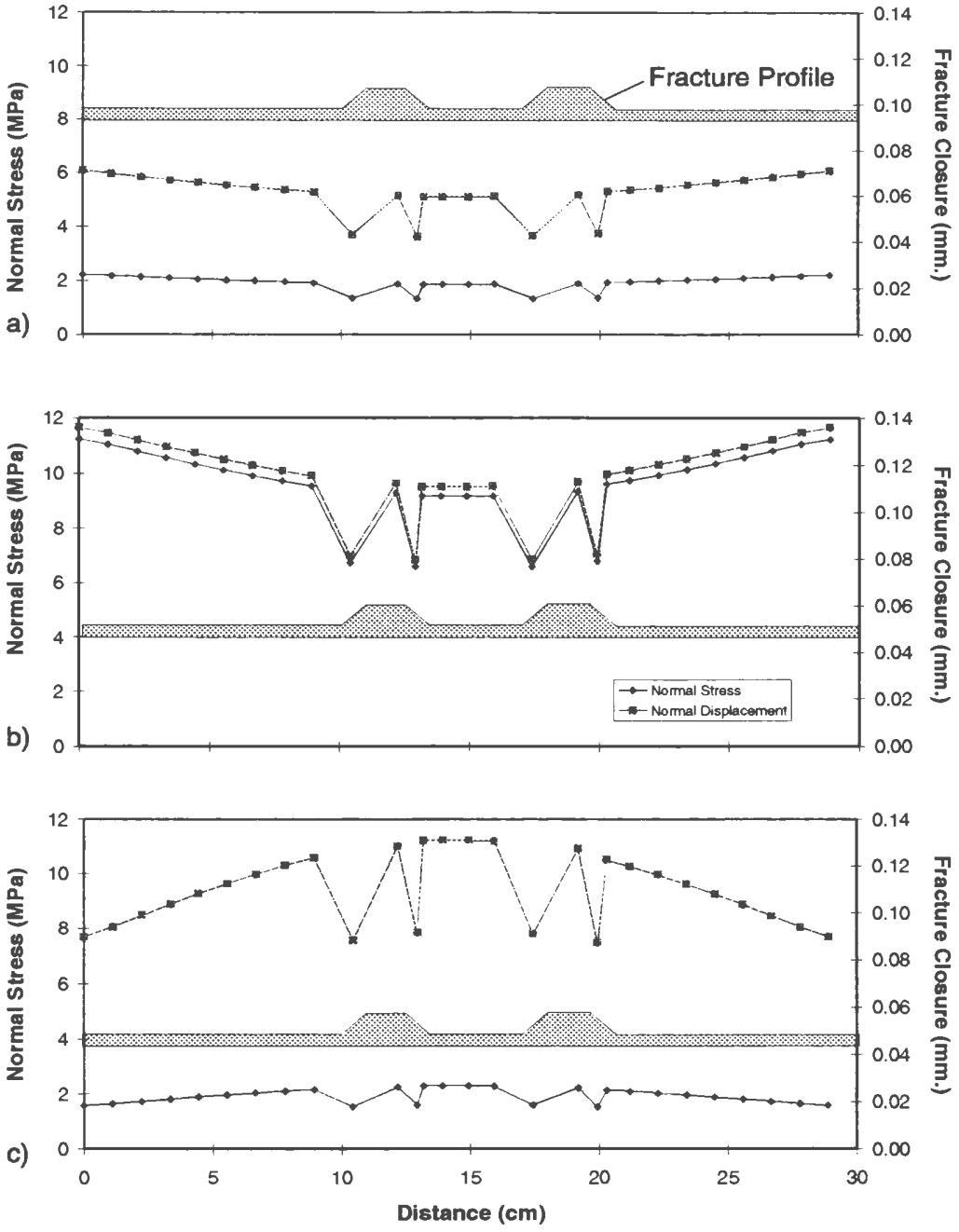

Figure 4-5: Normal Fracture Stress and Displacement Profiles across LSR-2. Note: Fracture closure increases in upward direction. a) at 2 MPa Loading, b) at 10 MPa Peak, c) at 2 MPa Unloading

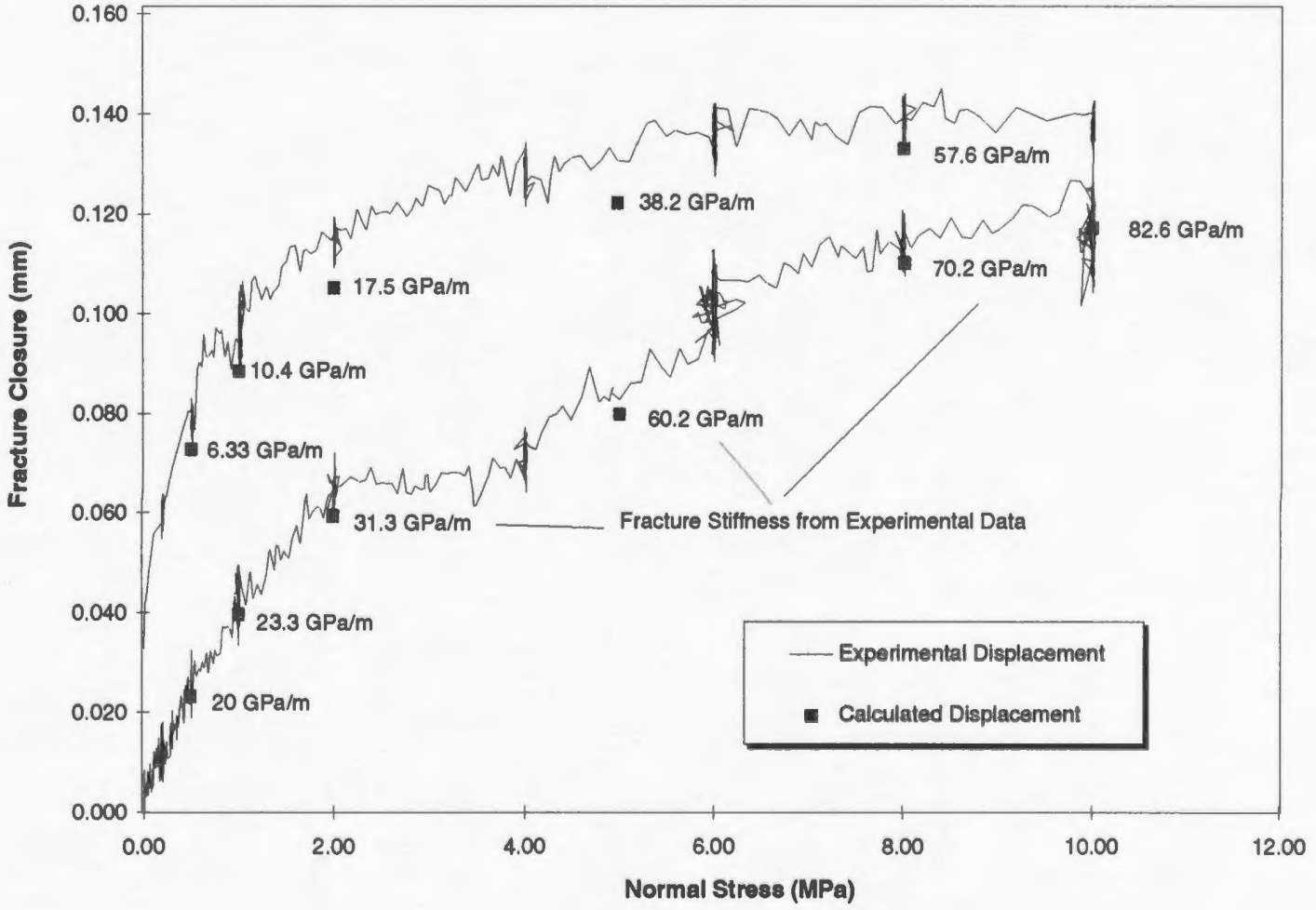

Figure 4-6: Actual and Numerical Displacements (Normal Run 2).

that the closure at the asperities in the centre of the model is permanent, suggesting that the previously noted "binding" is taking place, and the ends of the fracture open to values close to the aperture during the corresponding portion of the loading cycle.

The average normal displacements calculated from the finite element model are in close agreement with the actual displacements measured during the testing of LSR-2 (Figure 4-6). These values are calculated as an average of all of the element displacements along the length of the fracture plane, and appear slightly low since they reflect the "lower" values at the angled portion of the asperities.

4.3 Comparison of Numerical Model Simulation and Shear Loading Experiments

Stress distribution within LSR-2 during shear modelling is illustrated in Figures 4-7 and 4-8. Figure 4-7 shows the principal stress distribution at shear stresses of 3, 6, and 9 MPa, while maintaining a normal stress of 10 MPa. Figure 4-8 illustrates the stresses resolved into directions perpendicular and parallel to the average fracture plane, for comparison to the strain gauge data. Figure 4-4 b (i and ii) represent the start of this shear

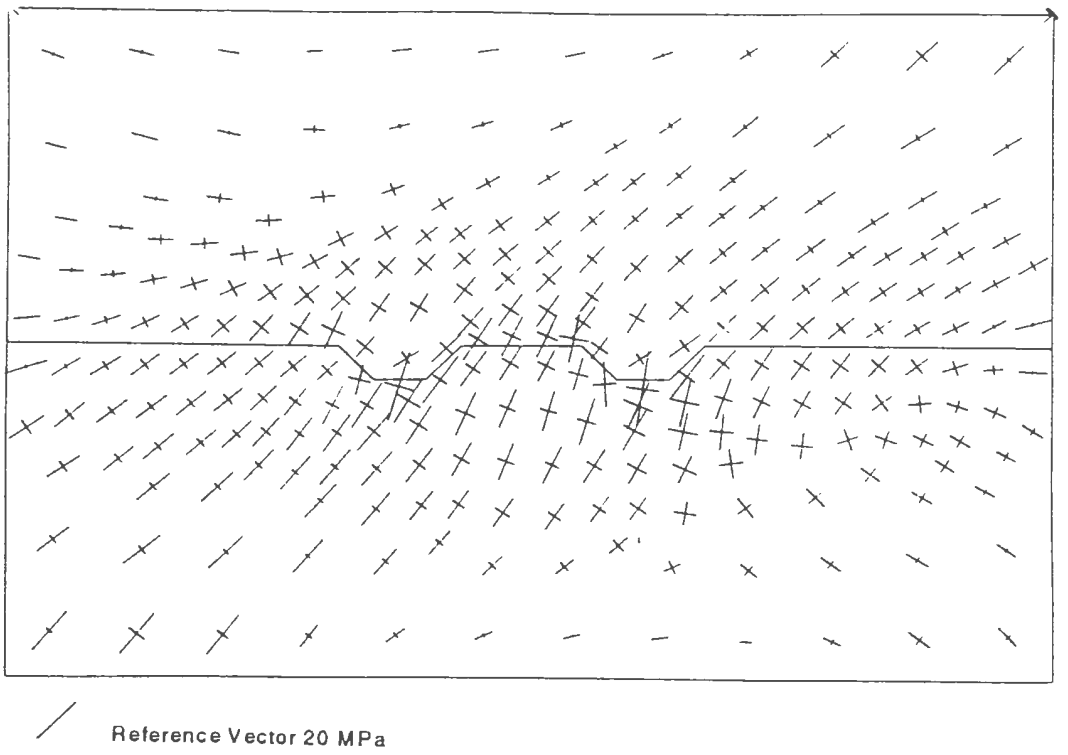

Figure 4-7 (a) (i): FEM Results - Shear Loading Cycle at 3 MPa (loading), principal stress vectors, compressive component.

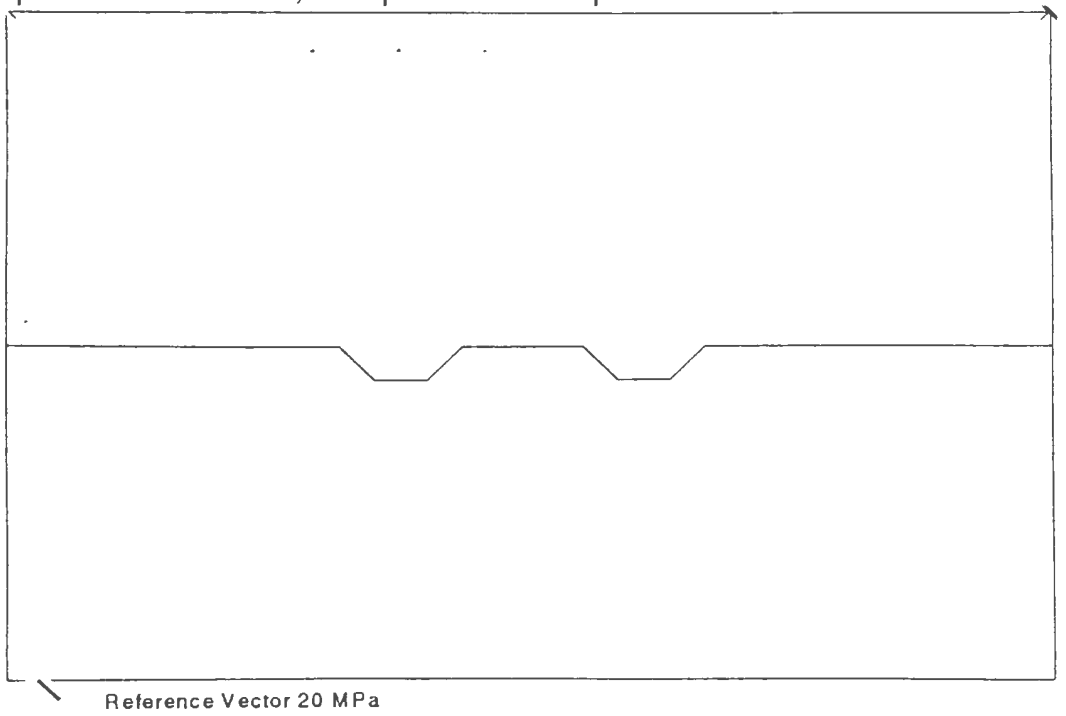

Figure 4-7 (a)(ii): FEM Results - Shear Loading Cycle at 3 MPa (loading), principal stress vectors, tensile component.

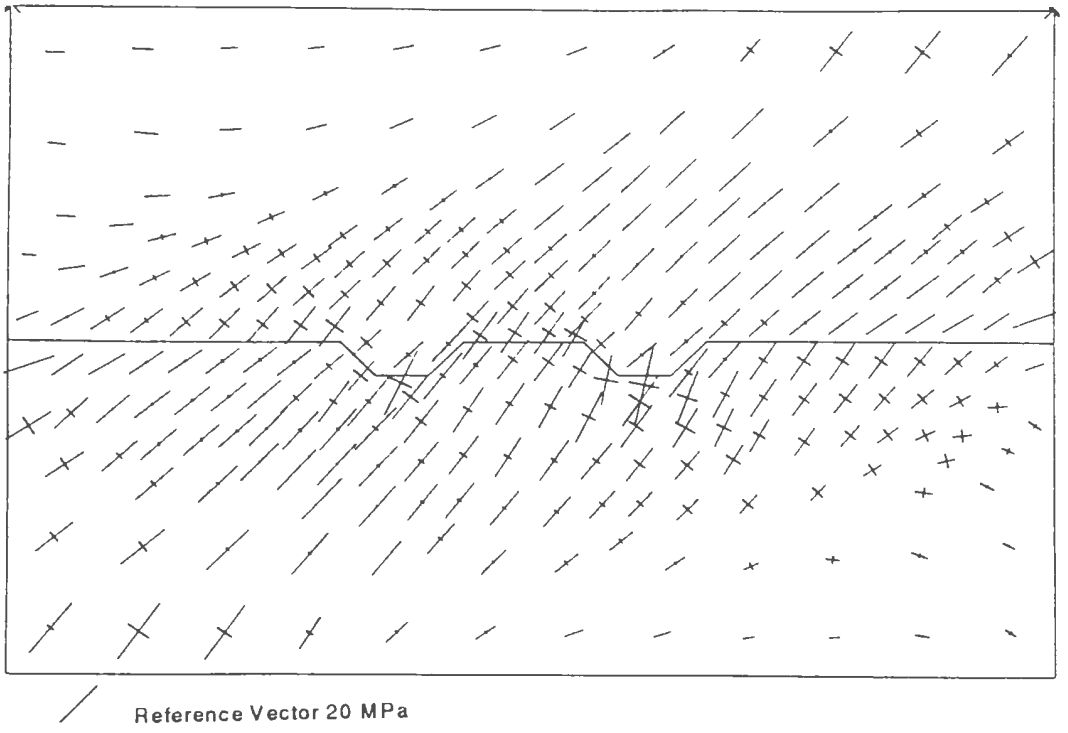

Figure 4-7 (b)(i): FEM Results - Shear Loading Cycle at 6 MPa (loading), principal stress vectors, compressive component.

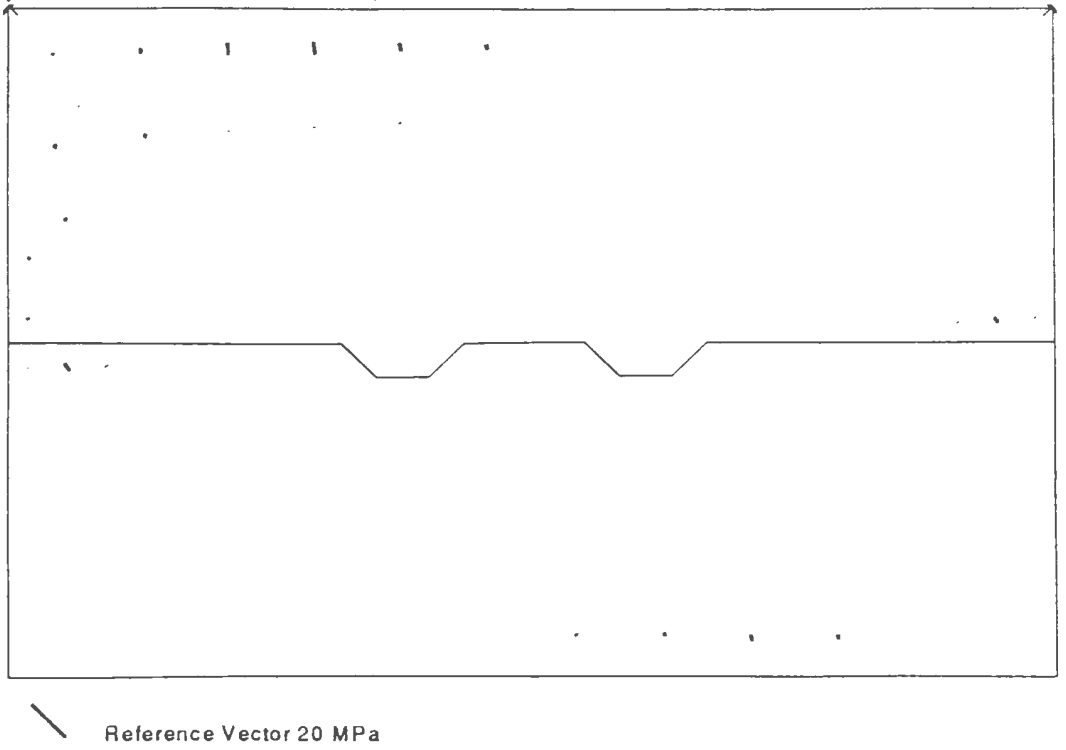

Figure 4-7 (b)(ii): FEM Results - Shear Loading Cycle at 6 MPa (loading), principal stress vectors, tensile component.

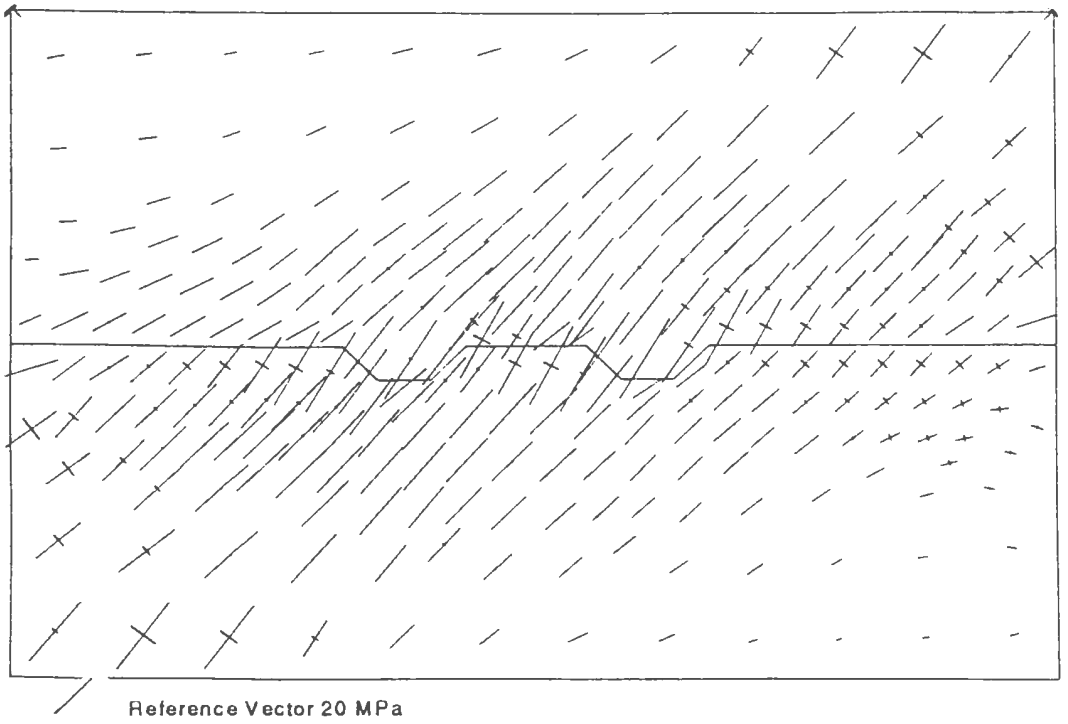

Figure 4-7 (c)(i): FEM Results - Shear Loading Cycle at 9 MPa (loading), principal stress vectors, compressive component.

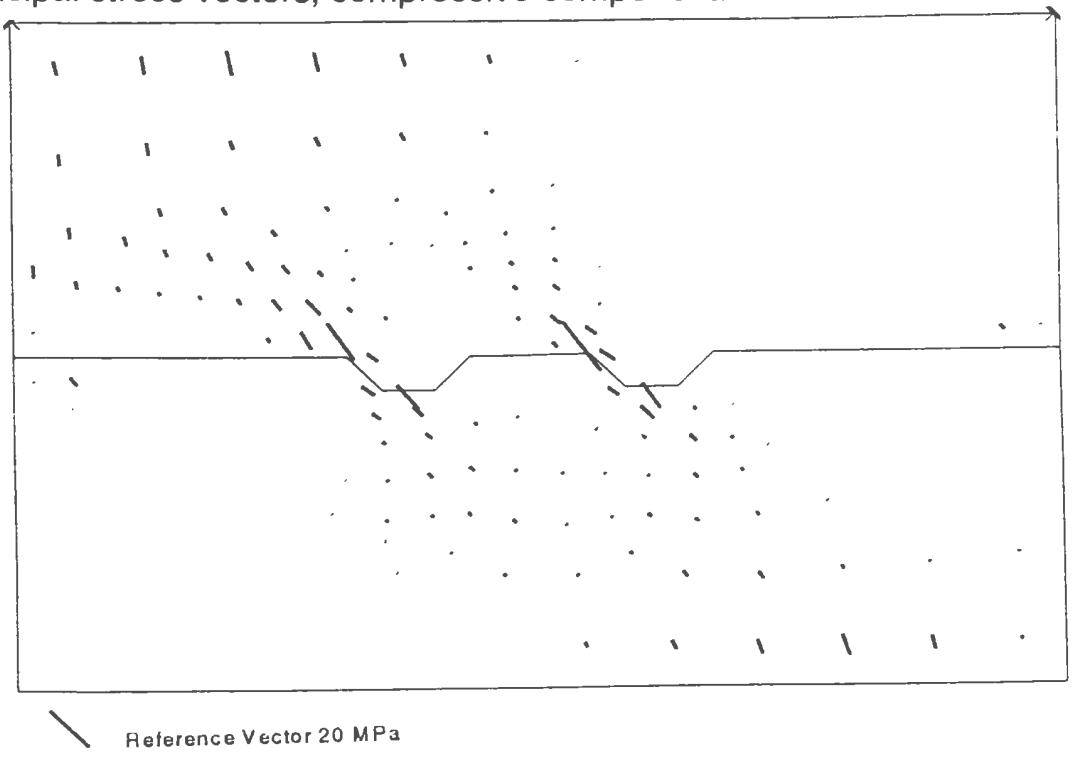

Figure 4-7 (c)(ii): FEM Results - Shear Loading Cycle at 9 MPa (loading), principal stress vectors, tensile component.

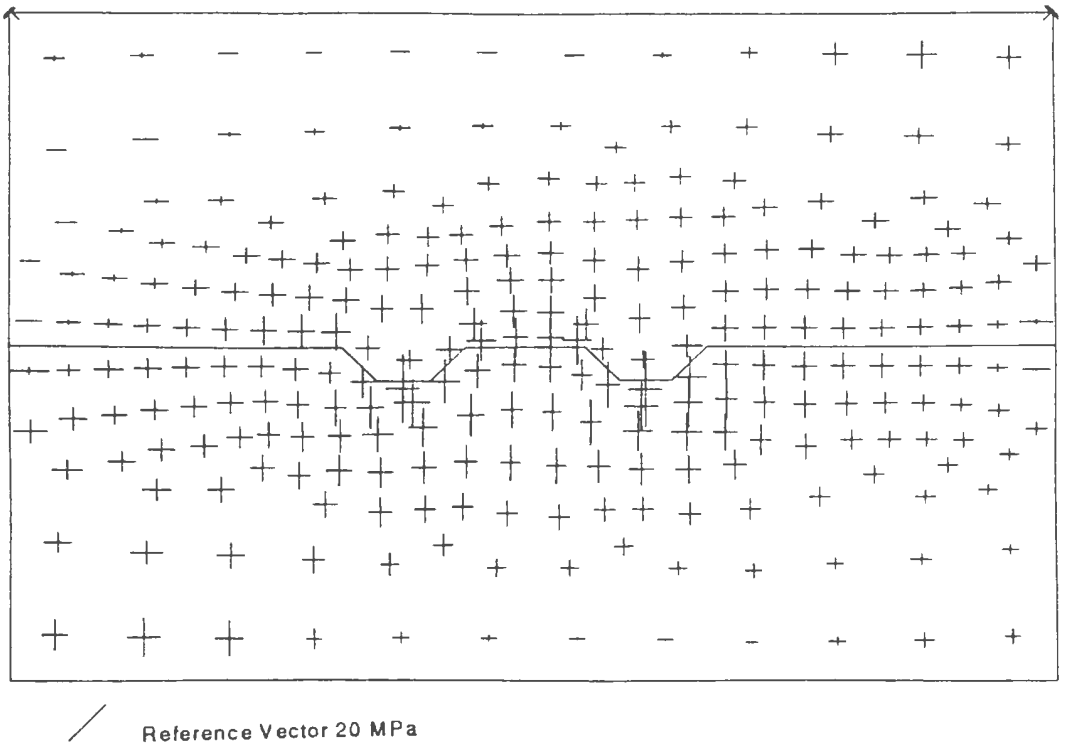

Figure 4-8 (a)(i): FEM Results - Shear Loading Cycle at 3 MPa (loading), resolved stress vectors, compressive component.

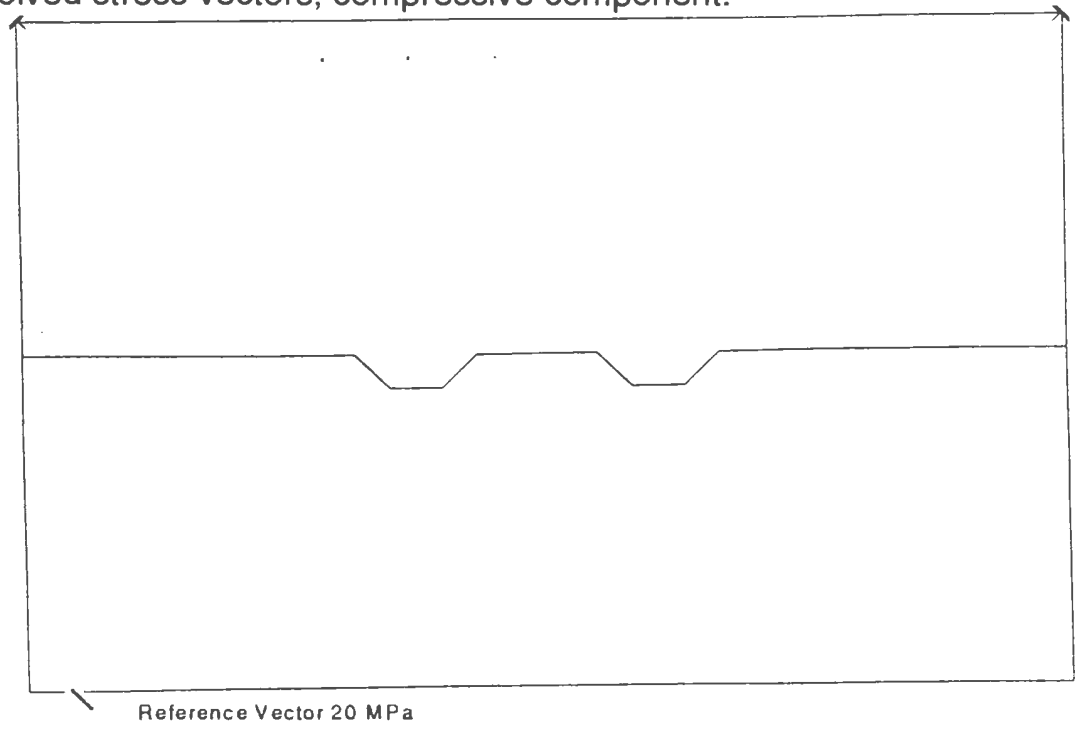

Figure 4-8 (a)(ii): FEM Results - Shear Loading Cycle at 3 MPa (loading), resolved stress vectors, tensile component.

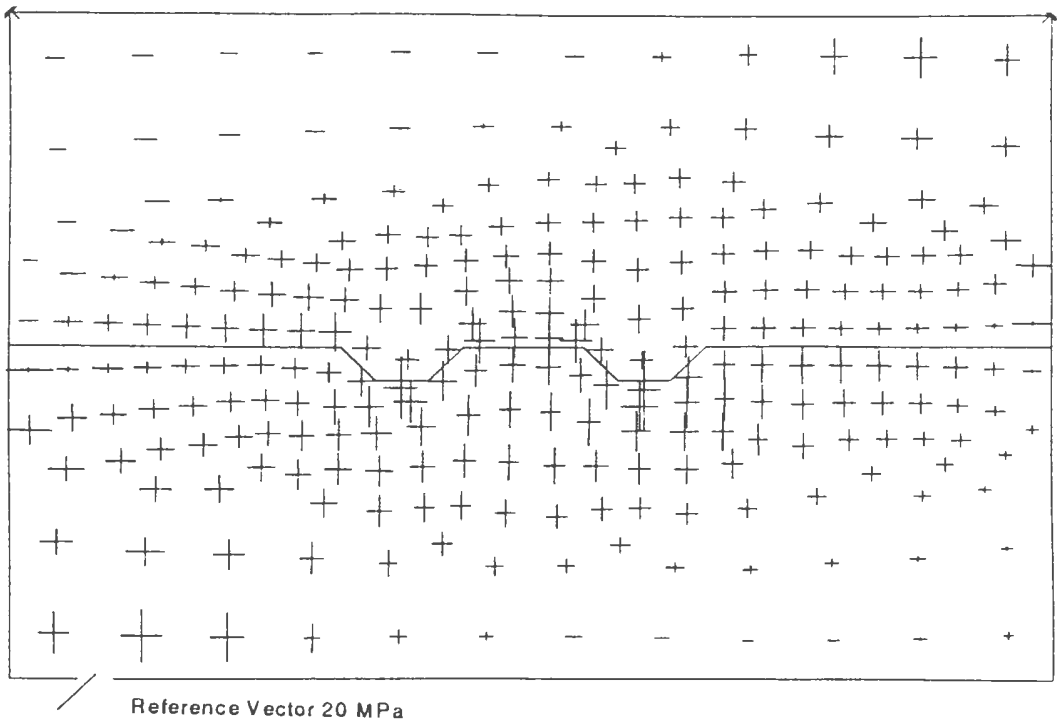

Figure 4-8 (b)(i): FEM Results - Shear Loading Cycle at 6 MPa (loading), resolved stress vectors, compressive component.

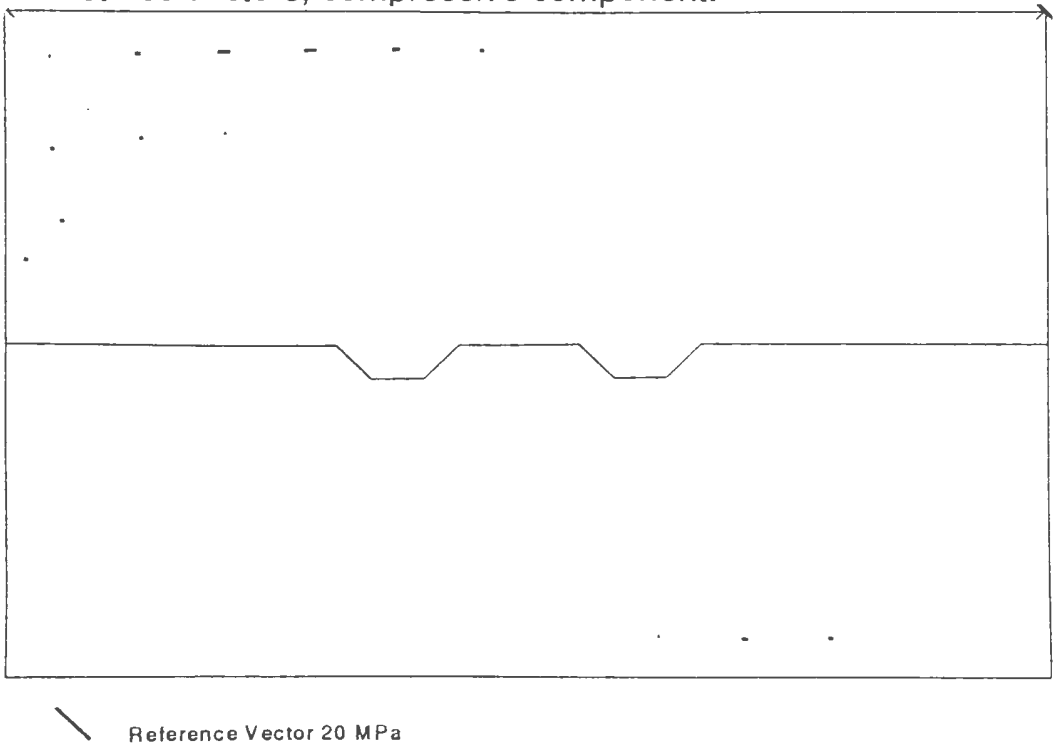

Figure 4-8 (b)(ii): FEM Results - Shear Loading Cycle at 6 MPa (loading), resolved stress vectors, tensile component.

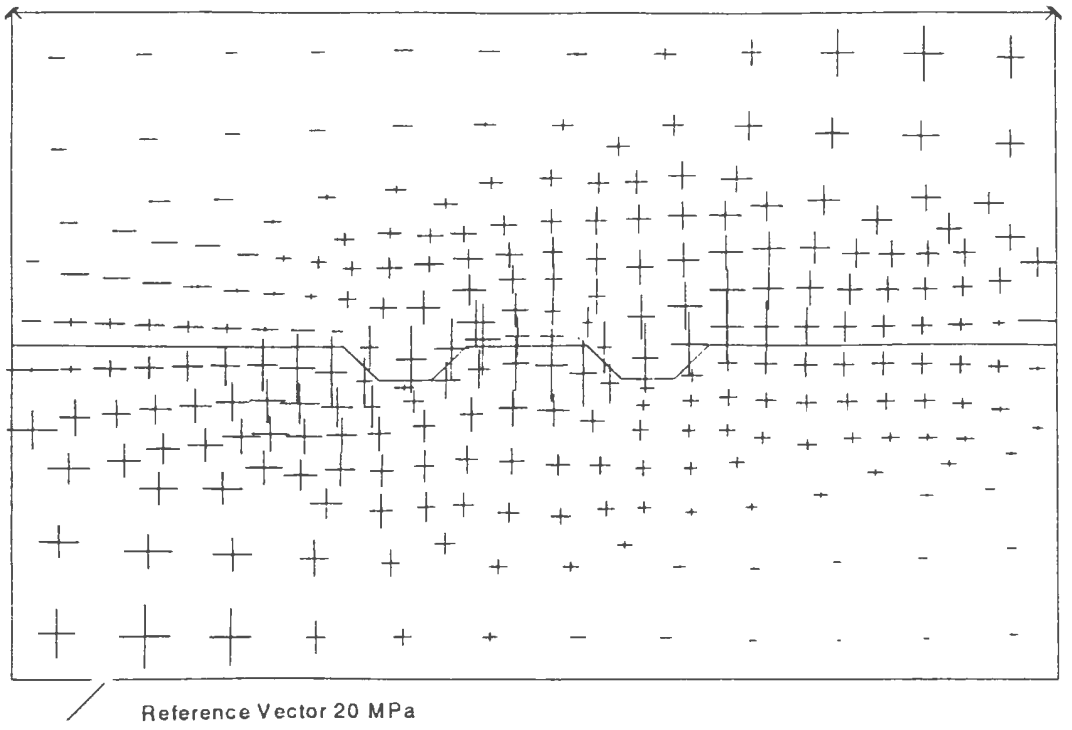

Figure 4-8 (c)(i): FEM Results - Shear Loading Cycle at 9 MPa (loading), resolved stress vectors, compressive component.

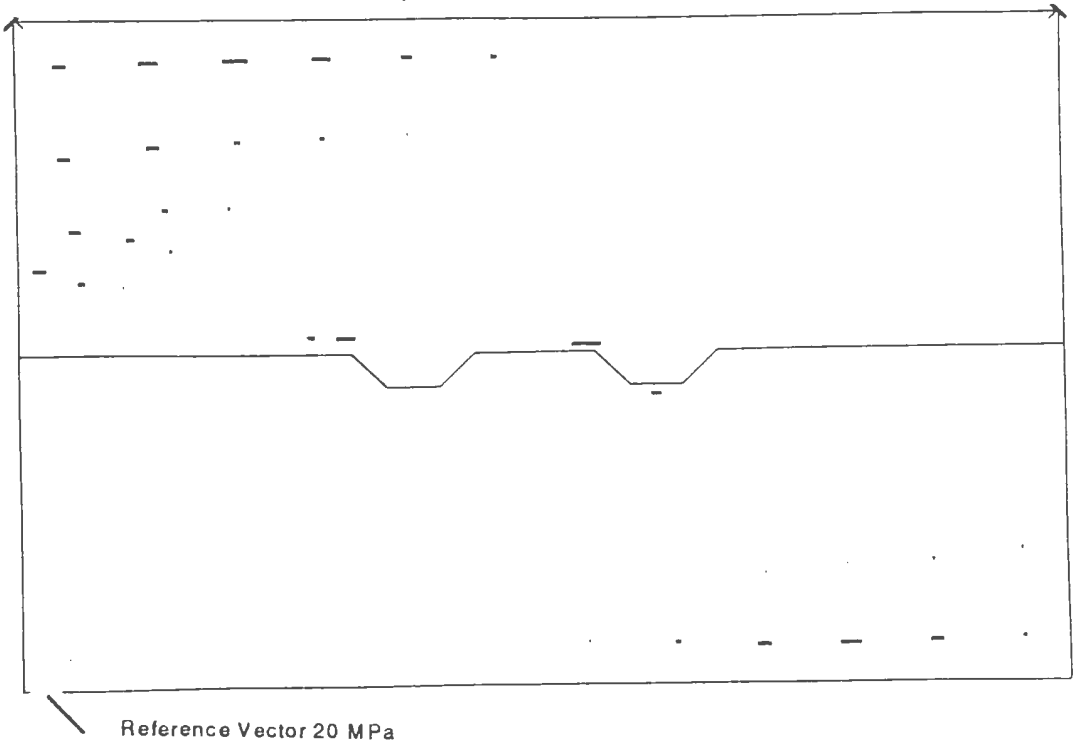

Figure 4-8 (c)(ii): FEM Results - Shear Loading Cycle at 9 MPa (loading), resolved stress vectors, tensile component.

cycle, at 0 MPa shear stress. Both 4-7 and 4-8 are presented as separate plots of compressive and tensile stresses for clarity.

As the shear load increases, it can be seen in Figures 4-7 and 4-8 that there is a corresponding increase in $\sigma_{max.}$ and σ_{min} (or $\sigma_{vert.}$ and $\sigma_{horiz.}$) on the loaded corners, and the compressive stress field lines itself up diagonally across the model, from upper right to lower left. There are no signs of tensile stresses appearing until the shear stress reaches 3 MPa, and these do not become significantly large until approximately 7 MPa. Between 7 and 8 MPa, a significant tensile stress field has developed in the upper left half of the block, with the peak tensile stress focused at the base of both asperities. The tensile stress at these points is at least 10 MPa, at 8 MPa average shear stress and increases to approximately 20 MPa at 9 MPa shear (Figure 4-7c). The compressional stresses locally reach values of 40 MPa in the immediate vicinity of the asperities at an applied shear stress of 9 MPa .

It was noted previously that the shear stiffness parameters used in modelling were determined from the displacement data for run shear 3a. Several modelling runs were completed, in which the friction angle of the fracture was varied from 22 to 67 degrees, bracketing the actual test friction angle of

27 degrees, as determined from the displacement data. The calculated displacements are plotted against the actual displacements on Figure 4-9. It is evident from these data that more displacement was expected than was actually measured. The best fit to the experimental data was seen to be when the friction angle started out low at 22 degrees (0, 1, 3 MPa shear) , and increased to 67 degrees (22 degree friction angle, plus 45 degree asperity angle) after the fracture had slipped and closed up the gap in the fracture at the asperity (5 MPa and above) as shown schematically in Figure 4-10. This slip and aperture closure essentially locks the fracture portion of the model into a solid block. Since the friction angle for the fracture plane was determined to be 27 degrees from the displacement data, this displacement profile is not unexpected since the physical model had reached the friction angle of 27 degrees twice previously to shear 3a, and had more than likely slipped and was in fact locked.

The normal and shear stresses and displacements along the fracture plane are shown in Figures 4-11 and 4-12. Figure 4-11 shows the effects of fracture shear stresses of 3, 6, and 9 MPa on the normal components of fracture stress and displacement. The plots show closure and increasing normal stress on the leading side of the large scale asperities (left side), as

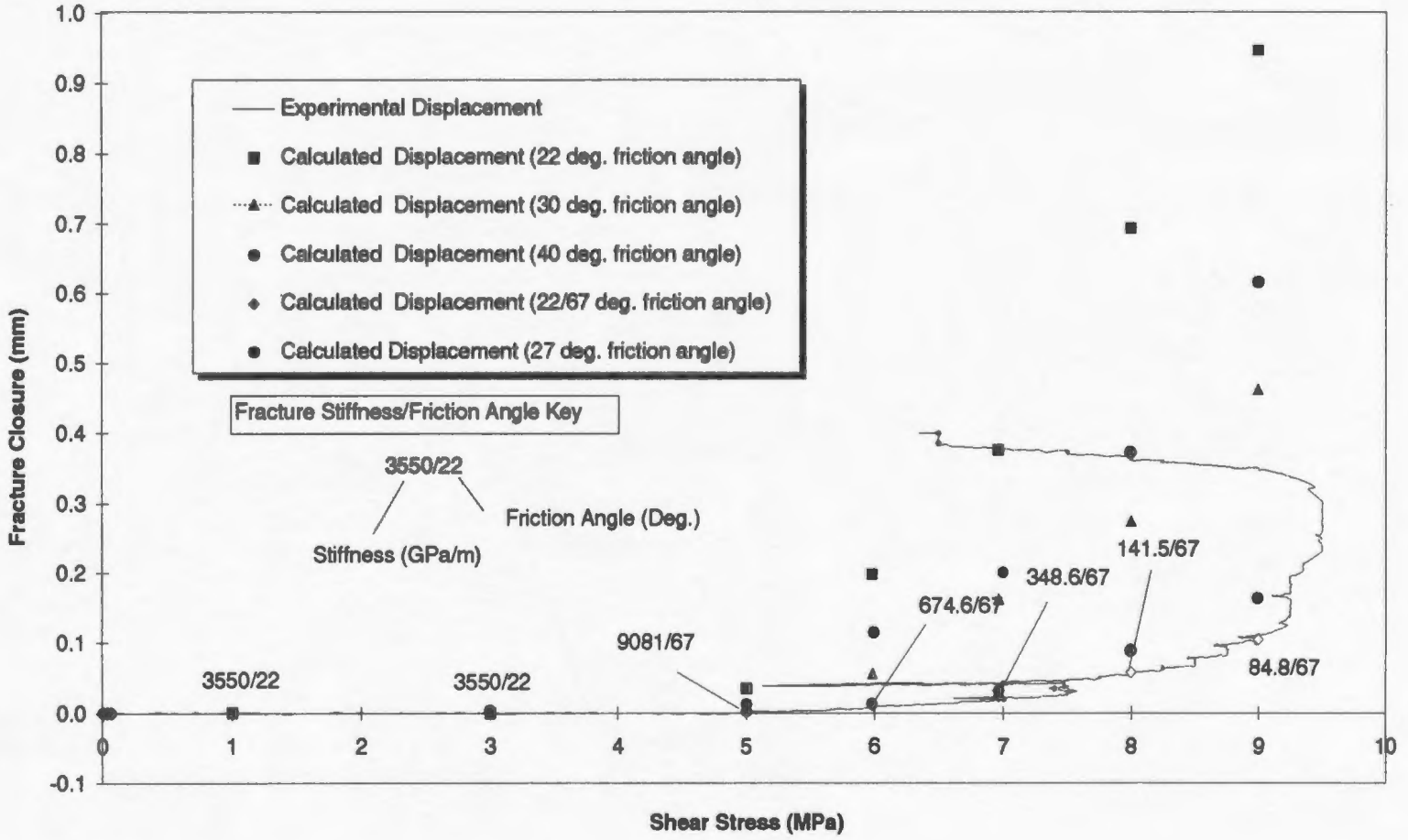

Figure 4-9: Actual and Numerical Displacements (Shear Run 3b).

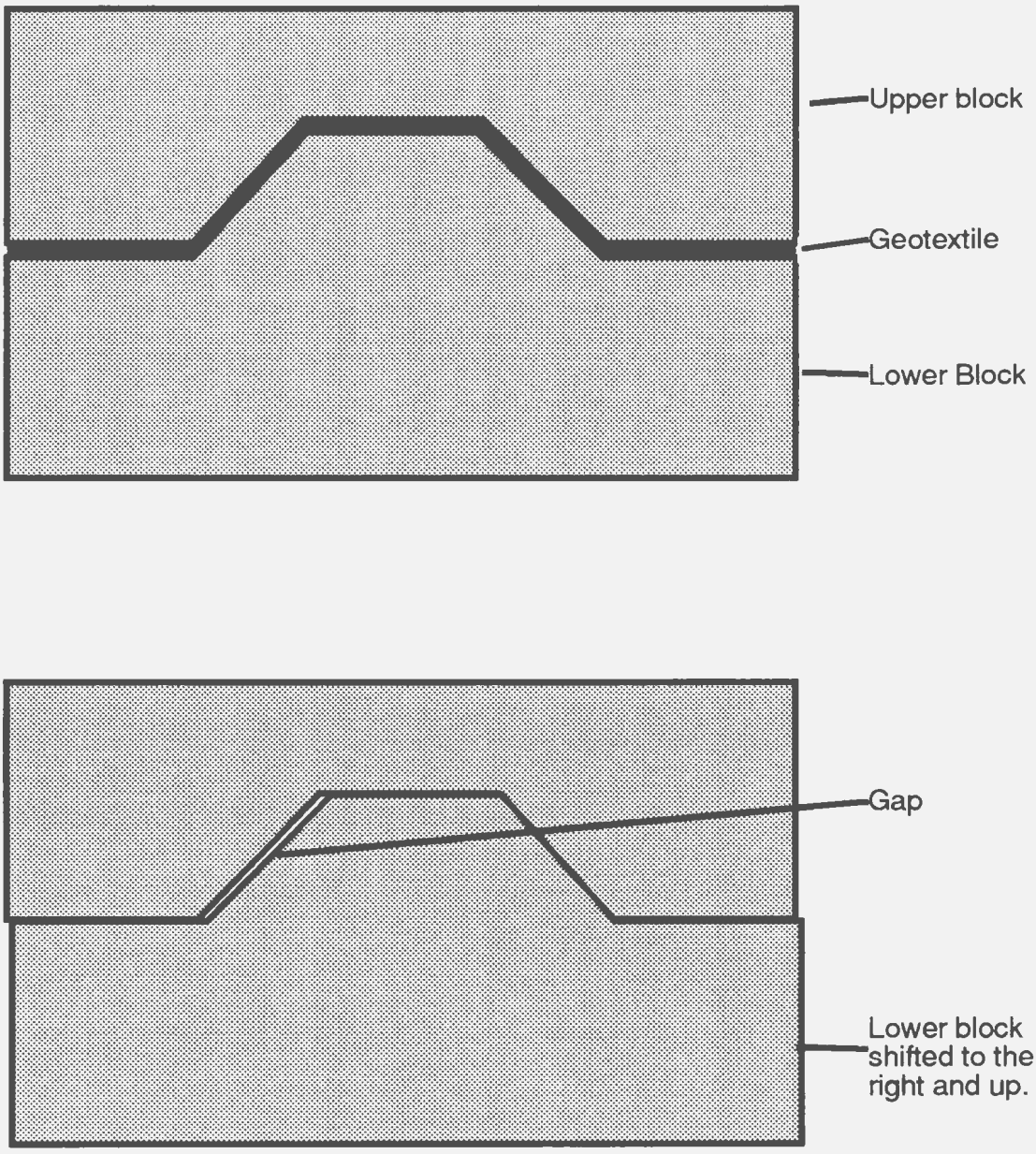

Figure 4-10: Schematic representation of a single asperity illustrating the resulting gap after the geotextile is removed.

the shear stress increases. The right side of the asperities shows unloading and dilation.

The shear components at 3, 6, and 9 MPa show fracture shear stress decreasing in Figures 4-12 (a) and (b). In these two plots, the shear stress down the right side of the asperities is caused by the vertical component of the applied normal stress. This exceeds the upward component of the shear stress acting in the opposite direction, resulting in a net decrease in shear stress. In Figure 4-12(c), the shear stress component exceeds the normal (downward) stress component on the left side of the asperities, causing the fracture shear stresses to increase to approximately 23 MPa. The displacement profile at 3 MPa shear (Figure 4-12 (a)) is virtually identical to the displacement profile of 0 MPa applied shear stress. At 6 MPa shear, which is a load step just above the friction angle of the fracture plane (Figure 4-12(b)), the shear displacement profile shows a uniform displacement of approximately 0.13 mm along the fracture plane. At 9 MPa shear, the profile shows significant displacement (closure) of approximately 0.66 mm on the right hand side of both asperities, and dilation on the left side of the asperities.

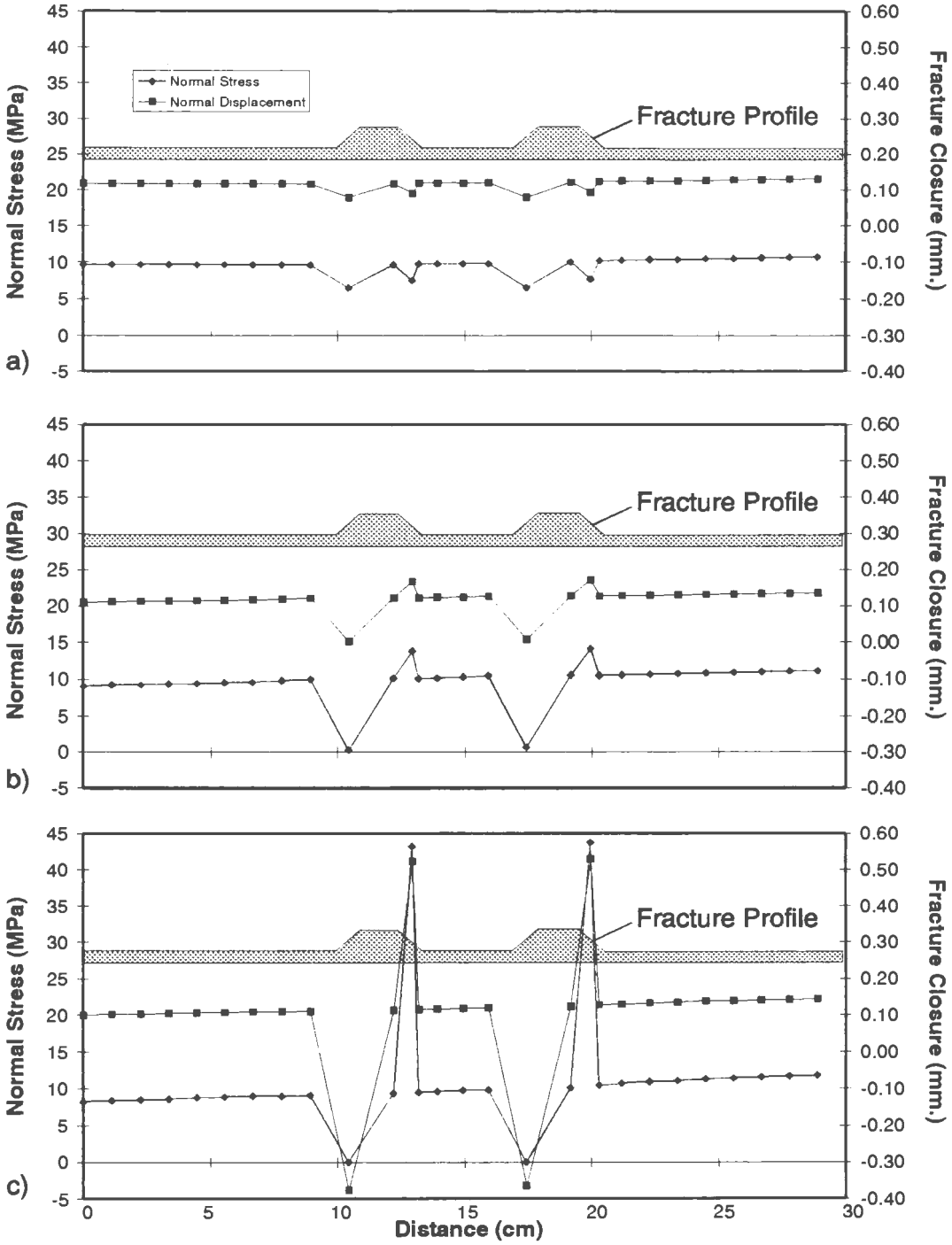

Figure 4-11: Normal Fracture Stress and Displacement Profiles across LSR-2. Note: Fracture closure increases in upward direction.
a) at 3 MPa Shear, b) at 6 MPa Shear, c) at 9 MPa Shear, All at 10 MPa Normal Stress

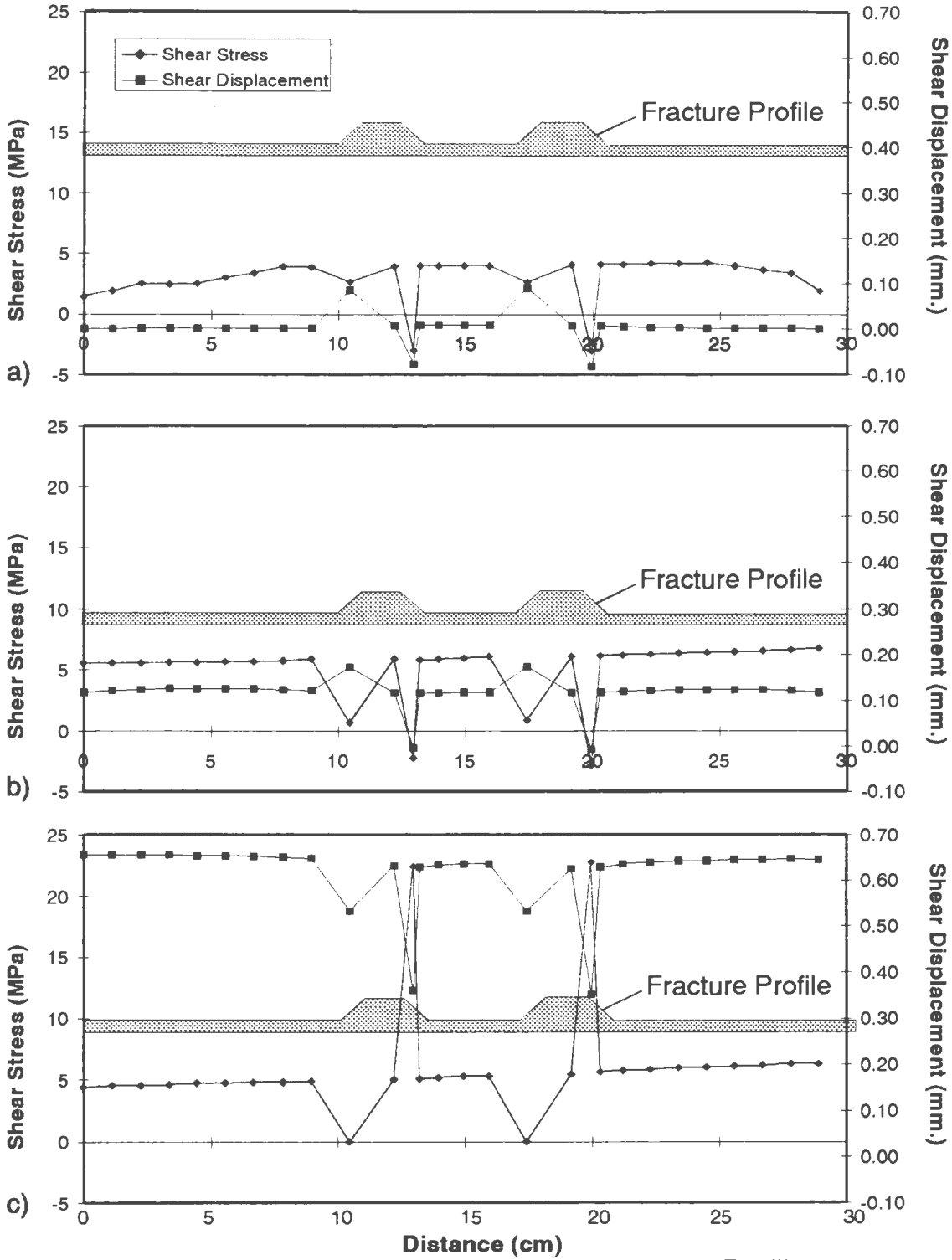

Figure 4-12: Shear Fracture Stress and Displacement Profiles across LSR-2. Note: Fracture closure increases in upward direction. a) at 3 MPa Shear, b) at 6 MPa Shear, c) at 9 MPa Shear All at 10 MPa Normal Stress

The uniaxial compressive strength of the concrete used as a modelling material is approximately 57 MPa (Appendix A5) based on unconfined uniaxial compressive testing. Since the concrete was confined by the steel sample box and epoxy grout, its compressive strength is likely higher. The tensile strength of the concrete mixture used is estimated to be approximately 5 to 10 percent of its uniaxial compressive strength (Butt, 1994 quoting CPCA handbook, 1991). Thus, the tensile strength of the concrete used in the model would be in the range of 3 to 6 MPa. Therefore the most likely failure mode will be from the tensile stresses which locally exceed 3 to 6 MPa , since it is unlikely the local compressive stress concentrations would be high enough to cause failure of the sample. Examination of the post test fracturing patterns (Figure 3-12) in reference to these modelled tensile zones supports the premise that the failure was caused by tensile stress.

Chapter 5 Discussion, Conclusions and Recommendations

5.1 Discussion

5.1.1 Normal Loading Cycles

Strain records for the physical model clearly show the extensional zones created by the incomplete epoxy grout in both halves of the block. The presence of these extensional zones is supported by, but not matched by, the numerical modelling. In the numerical modelling, these zones are seen as zones of decreased vertical stress, extending across the middle third of the top and bottom of the two halves, to a depth of approximately 3 to 4 centimetres. In the physical model, this same zone is much more extensive, reaching 6 to 7 centimetres into the model, with components of vertical and horizontal extension. The incomplete epoxy grouting over portions of the top and bottom of the model was determined to be the major cause for these zones of extension, but was likely enhanced by more bridging on the large scale asperities than was accounted for in the modelling. As well, the physical parameters used for the numerical modelling (Young's Modulus, Poisson's ratio) were determined from tests done on 2 unconfined cylinders, which may not fully represent the internal triaxial conditions of the sample tested.

The rotation of the stress field seen in the numerical model was seen in the rosette data in the physical model. However, more rosettes should have been placed closer to the large scale asperities to see the effect of the asperities on the strain field. Rosette clusters 56-57-58 and 79-80-81, located just above both large scale asperities (Figure 2-3), hint at possible rotation caused by the asperities. However, the positions of these two rosette clusters are far enough back from the fracture plane (2.5 cm) that they may not be seeing any of these local effects. In the numerical simulation, the equivalent positions to these rosettes show the principal stress directions pointing toward the middle of the block. In the physical model, the strain field appears to have been rotated by 90 degrees. The corresponding vertical gauges show almost no vertical component at these locations, whereas the simulation shows a significant vertical component when the strains are resolved into that direction. It can be concluded that these strain gauges are probably seeing more of the overall stress field in the block, reflecting significant influence of the extensional zone discussed above, than the local effects of the large scale asperities. As well, the numerical modelling was two dimensional only, and the physical model is likely seeing out of plane effects.

The rosette clusters located closer to the corners of the model (17-18-19, 40-41-42, 53-54-55 and 76-77-78) (Figure 2-3) clearly show the effects of the applied stress field in the physical model as the model is loaded normally. The relative magnitudes of the minimum and maximum strains correspond well to the relative magnitudes of σ_{max} and σ_{min} from the numerical simulations. Using an approximate conversion of 40 microstrains per MPa of applied stress (calculated using an average Young's Modulus of 25 GPa/m (see Table 4-2)), a measured strain value of 244 microstrains at strain gauge 55 (normal cycle 2, 10 MPa normal stress) would represent , for example, 6.1 MPa. The numerically determined stress in the same location would be approximately 10 to 12 MPa, using the material parameters of Tables 4-1 and 4-2. If the conversion factor used by Butt (1994) was used (20 microstrains/MPa, based on a Young's Modulus of 50 GPa/m), then the relationship would appear to be closer (12.2 MPa). It can be seen from this example the sensitivity of the simulations to the physical parameters input into the simulation. As noted above, the Young's Modulus for the simulations was determined from two unconfined test cylinders, which may not accurately represent all of the physical characteristics of the test block. Thus, this could account for the discrepancy between the data and the predictions.

The physical model generally showed a higher horizontal than vertical component to the strain field in the vicinity of the fracture plane. The cause of this is unknown, but it is suspected that it may be due to a combination of uneven loading from the incomplete epoxy grout, and the unconfined perimeter in the vicinity of the fracture plane. The numerical displacements were similar to the measured displacements of the physical model. This was expected since the numerical simulations were run using fracture stiffness values from the physical data.

There was no allowance in the numerical model for the plastic deformation that was seen in the physical model. All residual strains were zeroed out at the beginning of the following cycle so the resultant cumulative strain level in the model is unknown. The presence of significant extensional strains during both loading and unloading portions of the test cycles suggest the possibility of some tensile fracturing during the normal loading cycles. However, as will be discussed, it is most likely that the resulting fracture patterns resulted from the shear testing.

5.1.2 Shear Loading Cycles

Both the numerical modelling and shear testing of the physical model showed a corresponding increase in the internal stress and strain field from the loaded corners within the outlines of LSR-2, and an increase in the tensile and extensional fields in the unloaded corners. The numerical modelling suggest the development of a tensile strain field starting at about 3 MPa, which reached significantly high values at approximately 7 MPa shear stress. These stress levels suggest zones for tensile failure at the base of the large scale asperities, and vertically along the ends of the model, both of which were seen in the physical model. The physical model appeared to have larger zones of tensile strains caused by the incomplete epoxy grout. These larger zones would enhance the likelihood of tensile failure.

The numerical simulations suggest maximum compressive stress values of approximately 40 MPa at the top of the asperities when the numerical model was set for both 10 MPa normal and shear stress combined. Since the concrete of the model could be considered to be confined, and 10 MPa shear was not reached, it is doubtful that this 40 MPa stress level could cause compressional failure. Post test examination of the blocks showed

some localised crushing of aggregate grains on and near the fracture plane, but no indication of compressional failure.

It is probably significant to note here that there appeared to be a significant failure at the end of the shear 3a cycle. It was during this cycle that a sticking servo valve on the shear frame apparatus caused loss of control of the equipment. Control was re-attained by shutting off the hydraulic power supply while the model was loaded at 10 MPa normal and 7.58 MPa shear stress, resulting in a near instantaneous return to unloaded conditions. It was seen in the data from the following cycle (shear 3B), that the strain field had changed significantly within the model. It was only in this final cycle (shear 3B) that the rosette cluster 17 and 19 (Figure 2-3), located below and to the left of the left asperity, detected any significant deformation in the concrete. This suggests the applied stress was now being observed in that area of the model for the first time.

5.1.3 Well and Flow Data

The well data provided a convenient means of monitoring for the presence of cracks in the concrete of the model. Actual permeabilities of the concrete could be estimated (Brace et al., 1968, Forster and Gale, 1980) by using the

injection well decline curves. However, due to the very low permeability of the concrete used in the model, it was unknown whether the pressure decline data measured were due to bleed-off into the concrete, leakage from the connections between the well and the pressure transducer, or the compliance (yielding, stretch) of the plastic tubing that made up the connections. The data were used, therefore, as an indicator whether the concrete was "tight", or fractured. When each well failed, the change was dramatic, enabling the time of failure to be pinpointed if the well was being monitored at that time.

Flow data along the artificial fracture plane showed systematic fracture closure and decrease in fracture transmissivity with normal stress. The transmissivity was further decreased as the sample was sheared, closing the aperture at the asperities even further. Figures 3-11 and 3-12 show the apparent logarithmic relationship between the cube root of the average normal stress and fracture transmissivity that has been noted by Jones (1975), Gale et al. (1990) and others. This above noted relationship does not appear to hold up when a shear component is added. Gale et al. (1990) noted that the effect of shear on transmissivity was small for small displacements of the fracture plane. He pointed out that with larger

displacements one would expect to see a greater change in transmissivity. This pattern was seen in the data from the current tests. The fracture transmissivity decreased from 1E-6 m^2/s at the end of the normal loading cycle, to approximately 0.2E-6 m^2/s at 7.58 MPa shear. Figure 3-13 (b) clearly shows an increase in fracture transmissivity due to shear stress at the downstream large scale asperity (for shear cycle 3a), whereas the numerical simulations suggest dilation at both. Visual inspection after shear cycle 3b shows that both large scale asperities were dilated on their downstream sides. From this, it can be concluded that the upstream asperity was bearing all of the load for shear cycle 3a, and was responsible for most of the decrease in the overall fracture transmissivity. The numerical simulations, however, start with a uniform aperture across the length of the test model. As a result, the load appears to be carried by both large scale asperities throughout the simulation resulting in the closure and dilation profiles seen in Figures 4-11 and 4-12.

It is significant to note that when the specimen began to fail, it opened up many new pathways for the fluids to travel through, which effectively increased the fracture zone transmissivity.

5.2 Conclusions

The results of this study confirmed that large scale asperities have significant influence on the local strain field, as seen in the data recovered from the 78 strain gauges that survived the casting and pre-test processes. Three normal and four shear loading cycles showed repeatable internal strain patterns that reflected the effects of the applied boundary conditions.

Displacement data indicate that permanent closure was greatest for the first normal loading cycle, and decreased over the following two cycles. During the final four shear loading cycles, the permanent fracture closure became essentially identical at about 20 per cent of the original closure. This suggests that the fracture seating occurred during the first normal loading cycle, which is consistent with other experimental work.

It was concluded from both the finite element and the physical model analysis that induced tensile fracturing was the primary mode of failure in this experiment. The observed fracture patterns coincided nicely with the patterns of tensile stresses predicted by the finite element analysis. Under normal load the finite element analysis showed that the large scale asperities caused local changes in the orientation of the stress field. This effect was

not completely obvious in the model tested because of the masking effect of the incomplete epoxy grout, and the lack of strain gauges immediately adjacent to the artificial fracture plane. Under shear load there were significant tensile stress concentrations associated with the restraining and releasing bends of the fracture which provided the focus points for the onset of failure of the blocks.

The fracture transmissivity was seen to decrease logarithmically with the cube root of the normal stress applied to the sample, and decreased further as the sample was sheared, and the aperture at the asperities closed. There was no obvious relationship between applied stress and transmissivity for this further noted decrease. All fracturing induced in the model through testing enhanced the fracture porosity characteristics of the artificial fracture plane. This was very obvious during the latter stages of testing shear cycles 3A and 3B when the secondary fractures caused many problems through leaks and new pathways in the fracture and well permeability measurements. The resin injection at the completion of testing confirmed this by preserving the fracture porosity decrease on the restraining bends and the corresponding increase on the releasing bends.

There was no indication that the permeability of the concrete was enhanced by the shear stress applied except by the propagation of secondary fracturing through the test wells as the concrete failed.

From a large scale perspective, the enhancement of fracture porosity by stress can cause or enhance the accumulation and transport of fluids. This is significant in both long term (geological) and short term time frames. Enhanced fracture porosity controls mineralization processes, entrapment and transport of petroleum and other fluids in the long term. Such fracturing can also influence mechanical characteristics and production rates of producing wells. In the short term, enhanced fracture porosity has significant engineering ramifications in the prevention and control of excavation and tunnelling problems .

5.3 Recommendations

5.3.1 Future Research

Future research in this area can examine numerous related topics, some of which are planned and already undertaken as part of the ongoing research program in fractured rock at Memorial University. These could include the use of natural rock materials for the physical modelling (work in progress),

including both flat surfaces and artificial large scale asperities, a "no bump" case in concrete (now completed), investigations of the stress and strain variations in the out of plane dimension, and investigations of the matrix permeability changes in the vicinity of the fracture plane. As well, from the data set acquired from this experiment, future work could examine in greater detail the nature of the fracture transmissivity (such as the cross flow data), or the microscopic aperture variations seen in the resin preserved fracture.

If possible, the numerical modelling code could be modified to accomodate additional types of deformation, such as plastic strain, brittle fracturing and out of plane deformation. If some way can be determined to measure the uniformity of fracture mating prior to testing, these data could be incorporated into the simulations to better predict the transfer of stress between large scale asperities.

5.3.2 Recommendations for Changes in Testing Procedures

The following list has several recommendations for changes (some of which have been implemented) for the testing and analysis procedures that have come from the completion of this project that may help prevent future technical problems. They are listed mainly to provide a record for future

workers and don't necessarily provide any scientific insight into this project. They are listed in no particular order.

- The gauges that failed prior to the testing were for the most part in one quadrant of the model. If their location relative to the shearing direction had been known, the model would have been sheared in the opposite direction to see the full extent of the compressive strain field.

- More rosettes should be used to see the changes in the internal stress field. As well, strain gauges should have been placed closer to the large scale asperities.

- Better bonding is required between the epoxy grout and the model. A less viscous mixture would have ensured a better bond under and over the centre of the block.

- The model could have had more test wells imbedded in it. If more wells are used, they could be hooked up in parallel so they could all be monitored simultaneously, and as they failed, eliminated from the testing. This would give a better picture of the growth and timing of fractures as

the model failed. As well, the tubing used for the well casings should be as continuous as possible to the outside of the model to eliminate the tubing material compliance considerations, and the leakage from multiple connections. Perhaps the use of gas (i.e. Nitrogen) instead of water as the injection fluid would give better indication of the permeability of very tight materials, such as the concrete used in this test. Care would be needed if using a technique such as this as the escape of gas through an induced fracture into the fracture plane could disturb the flow characteristics of the fracture plane. As well, the implications of using a gas injected into a water saturated matrix for permeability measurements would have to be considered.

- A better means of sealing the fracture plane is required. The packer arrangement worked well until the model started breaking up, and then it was found to be almost impossible to make the seal effective. A good seal around the fracture is also crucial to obtain a good resin injection of the model.

- The strain gauge equipment worked well, but would have worked better if heavier gauge wiring had been used on all of the strain gauges. As well,

the heat drift problem required corrections to be made to the data. The best way of taking strain readings for gauges mounted such as these would be to instantaneously turn on the power to each gauge, take the reading, and then turn it off.

- The constant displacement piston pump used for the flow tests caused a pressure surge whenever the pump changed direction. A constant head tank connected to the output of the pump would act as a buffer during pump turn around.

- A great deal of time was lost at the beginning of each test cycle waiting for the air in the fracture plane to be removed by the water. Continuous flooding of the fracture plane by water flowing at low rates during periods of non-testing was determined to eliminate much of this problem.

References

ASTM D2938 - 86 Standard Test Method for Unconfined Compressive Strength of Intact Rock Core Specimens, American Society for Testing and Materials, Philadelphia, PA., 1986

ASTM D3148 - 86, Standard Test Method for Elastic Moduli of Intact Rock Core Specimens in Uniaxial Compression., American Society for Testing and Materials, Philadelphia, PA., 1986

ASTM 4543-85, Standard Practice for Preparing Rock Core Specimens and Determining Dimensional and Shape Tolerances, American Society for Testing and Materials, Philadelphia, PA., 1985

Aydan, O., Ebisu, S., Komura, S., and Watanabe A., (1990), Studies on interfaces and discontinuities and an incremental elasto-plastic constitutive law in: Rock Joints, ISRM Symposium, Barton and Stephansson (eds), Balkema, Norway, pp 595-602.

Barton, N., Bandis, S., and Bakhtar, K., (1985), Strength, Deformation and Conductivity Coupling of Rock Joints, Int.J. Rock Mech. Min. Sci. and Geomech. Abstr. Vol. 22, No. 3, pp. 121-140.

Bjorlykke, K., (1993), Fluid-Flow in Sedimentary Basins, Sedimentary Geology, Jul. 93, v.86, pp. 137-158.

Brace, W. F., Walsh, J. B., and Frangos, W. T., (1968), Permeability of Granite under High Pressure, Journal of Geophysical Research, Vol 73, No. 6., pp. 2225-2236.

Brace, W. F., (1978), A Note on Permeability Changes in Geologic Material Due to Stress, Pure and Applied Geophysics, Vol. 116, pp. 627-633.

Butt, S. D., (1994), A physical and numerical model study of the state of stress and deformation associated with large scale fracture roughness, MSc thesis, Memorial University of Newfoundland, St. John's, Newfoundland.

Dillabough, G. D., and Gale, J. E. (1996), The Effects of Multiple Large Scale Asperities on Deformation and Permeabiliyt of a Single Fracture, (in preparation)

Fishman, Y. A. (1990), Failure mechanism and shear strength of joint wall asperities in: Rock Joints, ISRM Symposium, Barton and Stephansson (eds), Balkema, Norway, pp. 627 - 631.

Forster, C. B., and Gale, J. E. (1980), A Laboratory Assessment of the use of Borehole Pressure Transients to Measure the Permeability of Fractured Rock Masses, Technical Information Report No. 28, Swedish Nuclear Fuel Supply Co., Stockholm, Sweden.

Gale, J. E. (1975), A numerical, field and laboratory study of flow in rocks with deformable fractures, PhD dissertation, University of California, Berkeley.

Gale, J. E, MacLeod, R. and LeMessurier, P., (1990) Site Characterization and Validation - Measurement of Flowrate, Solute Velocities and Aperture Variation in Natural Fractures as a Function of Normal and Shear Stress, Stage 3, Technical Report, Swedish Nuclear Fuel and Waste Management Co., Stockholm, Sweden.

Gale, J. E., Slade, J., Lemessurier, P., and Dillabough, G., 1994, Large Scale Physical Model Studies of Single and Two Phase Flow in Discrete Fractures with Variable Surface Roughness, 1994 AGU Fall Meeting.

Gamond, J. F. (1987) Bridge structures as sense of displacement criteria in brittle fault zones, Journal of Structural Geology, Vol. 9, No. 5/6, pp 609-620.

Goodman, R. E. (1976), Methods of Geological Engineering in Discontinuous Rocks, West Publishing Company, Boston, USA.

Goodman, R. E. (1980), Introduction to Rock Mechanics, John Wiley & Sons, New York, USA.

Handanyan, J. M., Danek, E. R., D'Andrea, R. A., and Sage, J. D. (1990), The role of tension in failure of jointed rock, in: Rock Joints, ISRM Symposium, Barton and Stephansson (eds), Balkema, Norway.

Hyett, A. J. and Hudson, J. A. (1990), A photoelastic investigation of the stress state close to rock joints, Rock Joints, ISRM Symposium, Barton and Stephansson (eds), Balkema, Norway.

Jones, F. O., (1975), A Laboratory Study of the Effects of Confining Pressure on Fracture Flow and Storage Capacity in Carbonate Rocks, Journal of Petroleum Technology, January 1975, pp. 21 - 27

Kamineni, D. C., Kerrich, R., and Brown, A., (1993), Effects of differential reactivity of minerals on the development of brittle to semibrittle structures in granitic-rocks - Textural and oxygen isotope evidence, Chemical Geology, Mar. 15, 1993, v.105, pp. 215-232.

Lee, Y.-H., Carr, J. R., Barr, D. J., and Haas, C. J., (1990), The Fractal Dimension as a Measure of the Roughness of Rock Discontinuity Profiles, Int. J. Rock Mech. Min. Sci. & Geomech. Abstr. Vol. 27, pp 453-464.

Martin, C.D., Davison, C.C., and Kozak, E.T., (1990), Characterizing Normal Stiffness and Hydraulic Conductivity of a Major Shear Zone in Granite, Proceedings of the International Symposium on Rock Joints, Norway, June 4-6.

Morrow, C. A., and Byerlee, J. D., (1992), Permeability of core samples from Cajon Pass scientific drill hole - Results from 2100 to 3500-M depth, Journal of Geophysical Research - Solid Earth Apr. 10, 1992, v.97, pp. 5145 - 5151.

Pratt, H. R., Swolfs, H. S., Brace, W. F., Black, A. D., and Handin, J. W., (1977), Elastic and Transport Properties of an In Situ Jointed Granite, Int. J. Rock Mech. Min. Sci. & Geomech. Abstr. Vol. 14, pp. 35-45.

Raven, K. G., and Gale, J. E., (1985), Water Flow in a Natural Rock Fracture as a Function of Stress and Sample Size, Int. J. Rock Mech. Min. Sci. & Geomech. Abstr. Vol. 22, pp. 251-261.

Rengers, N., (1970), The influence of surface roughness on the friction properties of rock planes, Proc. 2nd Cong. ISRM, Belgrade, V1, paper 1-31.

Scholz, C. H., (1990) The mechanics of earthquakes and faulting, Cambridge University Press, Cambridge.

Sibson, R. H., (1986), Brecciation Processes in Fault Zones: Inferences from Earthquake Rupturing, Pure and Applied Geophysics, Vol. 124, Nos. 1/2, pp. 159-175.

Segall, P., and Pollard, D. D., (1983), Nucleation and Growth of Strike Slip Faults in Granite, Journal of Geophysical Research, Vol. 88, No. B1, pp. 555-568.

Appendix A- Details of Model Construction

A1- Fine Aggregate Concrete Mix

Table A-1 Fine Aggregate Concrete Mix

	1/2 Test Block (300x200x100 mm)	
Cement	3.34 kg	0.0011 m^3
Silica Fume	0.29 kg	0.0001 m^3
Coarse Aggregate (#2)	7.25 kg	0.0027 m^3
Fine Aggregate (#00)	3.63 kg	0.0014 m^3
Water	1.60 L	0.0016 m^3
Daracem 100	33.36 ml	0.00003 m^3
Total Mass/Volume	16.13 kg	0.0069 m^3

All dry components are pre-weighed and placed in mixing bowl. The bowl is mounted on mixer assembly, using the paddle mixer rather than the "dough hook". Combine the water and Daracem 100. Start the mixer, and add all but 10 percent of the water mixture to the dry mix. Mix thoroughly, adding the last 10 percent of the water slowly, so that the mix does not become too runny. A proper mix will look slightly dry, but will liquefy readily when the internal vibrator is inserted into the bowl. After mixing, the concrete is placed in the forms, and thoroughly vibrated with the internal vibrator.

A2- Epoxy Resin Potting Mixture (per half box)

Table A-2 Epoxy Resin Potting Mixture

Aggregate	2 - 4.67 mm	7.7 kg.
Silica Sand	#2	13.23 kg
Epoxy (Ciba Geigy)		3-4 cans resin + hardener

Wash and thoroughly dry the aggregate and sand. Mix aggregate and sand together. Mix epoxy resin and aggregate mixture, stirring thoroughly. A good mix will require slightly more than 3 cans of resin/hardener mix for maximum strength. Pack aggregate into sample box to minimise porosity in the final mixture. Extra epoxy mixture is poured over the exposed top surfaces as a seal and to improve bonding of potting compound to the model and box.

A3- Strain Gauge and Coupon Coordinates

Note: Refer to Figure 2-3 for rosette orientations.

Block Co-ordinates

X	Y
0	0
30	0
30	20
0	20
0	0

Fracture Co-ordinates

X	Y
0	10
10	10
11	9
12.5	9
13.5	10
17	10
18	9
19.5	9
20.5	10
30	10

*** Denotes Failed Gauge Prior to Testing**

Strain Gauge Co-ordinates

Gauge #	X	Y	Type
1*	13.5	7.25	H
2	13.5	7.15	V
3	13.5	4.75	H
4	13.5	4.75	V
5*	13.5	2.25	R
6	13.5	2.25	R
7*	13.5	2.25	R
8	9.8	7.25	H
9	9.8	7.25	V
10*	9.8	4.75	R
11*	9.8	4.75	R
12*	9.8	4.75	R
13*	9.8	2.25	H
14*	9.8	2.25	V
15*	6.2	8.45	H
16	6.2	8.55	V
17	6.2	6.05	R
18	6.2	6.05	R
19	6.2	6.05	R
20*	6.2	3.55	H
21	6.2	3.45	V
22	2.7	8.45	H
23	2.7	8.55	V
24	16.4	7.3	H
25	16.4	7.2	V
26	16.4	4.9	H

Strain Gauge Co-ordinates (cont.)

Gauge #	X	Y	Type
27	16.4	4.8	V
28	16.4	2.4	R
29*	16.4	2.4	R
30	16.4	2.4	R
31	19.9	7.3	H
32	20	7	V
33	19.9	4.9	R
34	20	4.8	R
35	19.9	4.9	R
36	19.9	2.4	H
37	20	2.3	V
38	23.4	8.2	H
39	23.4	3.5	V
40	23.4	6.1	R
41*	23.4	6.1	R
42	23.4	6.1	R
43	23.4	3.6	H
44	23.4	8.2	V
45	26.9	8.2	H
46	26.9	8.2	V
47	27	11.55	H
48	27	11.45	V
49	23.5	11.55	H
50	23.5	11.45	V
51	23.5	14.55	H
52	23.5	14.45	V

A3- Strain Gauge and Coupon Coordinates (cont.)

Strain Gauge Co-ordinates (cont.)

Gauge #	X	Y	Type
53*	23.5	17.45	R
54	23.5	17.45	R
55	23.5	17.45	R
56	20.1	11.95	R
57	20.1	11.45	R
58	20.1	11.95	R
59	20.1	14.55	H
60	20.1	14.45	V
61	20.1	17.45	H
62	20.1	17.45	V
63	16.5	11.55	H
64	16.5	11.45	V
65	16.5	14.55	R
66	16.5	14.45	R
67	16.5	14.55	R
68	16.5	17.45	H
69	16.5	17.45	V
70	3.15	12	H
71	3.15	11.9	V
72	6.55	12	H

Strain Gauge Co-ordinates (cont.)

Gauge #	X	Y	Type
73	6.55	11.9	V
74	6.55	14.9	H
75	6.55	14.9	V
76	6.55	17.9	R
77	6.55	17.9	R
78	6.55	17.9	R
79	10.25	12.4	R
80	10.25	11.9	R
81	10.25	12.4	R
82	10.25	14.9	H
83	10.25	14.9	V
84	10.25	17.9	H
85	10.25	17.9	V
86	13.55	12	H
87	13.55	11.9	V
88	13.55	14.9	R
89	13.55	14.9	R
90	13.55	14.9	R
91	13.55	17.9	H
92	13.55	17.9	V

A4- Summary of Mechanical Characteristics of Epoxy Aggregate

Five test cylinders of the epoxy aggregate used in potting LSR-2 into the sample testing box were prepared and tested to ASTM standards D 2938-86, D3148-86 and D 4543-85. Following is a summary of the mechanical characteristics determined.

Table A4 Summary of Mechanical Characteristics of Epoxy Concrete

Test Core	Maximum Unconfined Compressive Strength 'C' (MPa)	Young's Modulus (@50% C) (Pa)	Poissons Ratio (@50% C)	Description
A	29.6083	-1.40E+10	0.24	High Porosity (30%)
B	37.8162	-1.24E+10	0.23	High Porosity (30%)
C	24.6842	-1.24E+10	0.25	High Porosity (30%)
D	37.0939	-1.30E+10	0.23	High Porosity (30%)
E	52.3454	-1.30E+10	0.33	Low Porosity (10%)
Average	36.3096	-1.30E+10	0.26	

The test cylinders failed in the zones of highest porosity as a bulging in the aggregate.

A5- Summary of Mechanical Characteristics of Concrete

Two test cylinders of the concrete mixture used in the construction of LSR-2 were prepared and tested to ASTM standards D 2938-86, D3148-86 and D4543-85. Following is a summary of the mechanical characteristics determined.

Table A5 Summary of Mechanical Characteristics of Concrete

Test Core	Maximum Unconfined Compressive Strength 'C' (MPa)	Young's Modulus (@50% C) (Pa)	Poissons Ratio (@50% C)	Description
H	50.9	-2.80E+10	0.22	6 inch cylinder cast during construction of large scale physical model, bottom block, not vibrated.
I	63.4	-3.28E+10	0.28	6 inch cylinder cast during construction of large scale physical model, top block, not vibrated
Average	57.2	-3.04E+10	0.25	

The test cylinders exhibited conical/splitting failure.

Appendix B1: Tabulated Strain Gauge Data

Tables B1-1 through B1-7 provide the strain gauge data used to produce the strain plots presented in Chapter 3. One table is given for each loading cycle.

Only the gauges that survived the initial testing of the block are listed. If the values for any given strain gauge are listed as 0.0 microstrains, that gauge has failed, and the erroneous reading replaced with 0.0 for plotting purposes. All residual strains have been eliminated at the start of each loading cycle.

Table B1-1: Strain Data, Normal Cycle 1

Strain Gauge	2 MPa (UP)	4 MPa (UP)	6 MPa (UP)	8MPa (UP)	10 MPa (Peak)
2	-7.8	31.8	70.7	83.1	98.6
3	-48.0	-123.1	-181.4	-245.1	-300.7
4	53.2	72.4	109.6	117.7	135.9
8	15.5	32.1	42.7	41.9	35.6
9	-69.0	-145.2	-212.9	-266.4	-317.7
16	46.8	101.5	144.4	162.7	191.2
17	18.1	19.2	23.8	38.1	58.1
18	-17.6	-51.1	-72.7	-92.6	-116.3
19	-40.8	-81.7	-112.2	-142.2	-140.5
21	-0.3	132.4	417.1	456.2	481.3
22	-19.8	-45.3	-65.3	-82.8	-97.9
23	-27.5	-59.0	-88.8	-124.0	-149.0
24	43.7	76.9	98.5	107.4	116.3
25	-71.8	-148.3	-214.0	-263.7	-311.1
26	-42.7	-98.3	-125.5	-139.6	-41.3
27	17.9	31.1	79.2	98.3	122.3
28	29.3	505.6	813.7	859.7	907.5
30	-60.1	179.9	401.7	414.5	428.0
31	3.8	-50.8	-77.9	-101.8	-129.8
32	24.3	46.8	70.7	83.0	87.8
33	15.4	39.6	75.8	125.1	209.5
34	31.8	43.4	57.2	54.2	47.1
35	-17.5	-48.5	-67.0	-68.6	2.8
36	-12.9	88.8	245.2	336.8	456.4
37	14.0	-3.2	-17.1	-14.4	280.9
38	-42.1	-66.8	-84.7	-111.4	-123.9
39	-51.1	-61.3	-47.1	-53.5	-46.8
40	-45.8	-61.9	-64.7	-75.6	-69.6
42	-75.1	-148.3	-198.3	-239.9	-263.6
43	-77.9	-122.5	-166.5	-161.1	323.5
44	-9.6	11.1	13.4	-14.5	-24.3
45	-75.9	-120.7	-120.1	-166.8	-171.1
46	-40.7	-51.8	-50.8	-62.5	-67.0
47	24.4	17.8	-11.0	-36.1	-58.0
48	35.3	10.2	5.2	-10.0	-5.6
49	-33.4	-78.7	-115.4	-137.6	-146.8
50	13.7	7.0	15.1	1.8	-5.6
51	40.4	-4.3	11.5	-27.8	4.3
52	-4.6	-34.2	-75.6	-143.3	-316.5

Table B1-1: Strain Data, Normal Cycle 1

Strain Gauge	2 MPa (UP)	4 MPa (UP)	6 MPa (UP)	8MPa (UP)	10 MPa (Peak)
54	-36.2	-69.3	-91.2	-107.4	-71.6
55	-30.8	-50.6	-39.7	-180.7	-249.2
56	16.0	-16.9	-40.0	-81.3	-116.5
57	10.1	13.9	25.2	19.1	20.9
58	-17.2	-45.4	-46.3	-67.8	-55.9
59	7.7	-19.6	-25.5	-64.3	-44.9
60	-12.5	-20.5	-24.4	-42.5	-48.3
61	8.2	-7.1	-32.6	-78.7	-54.9
62	7.7	7.6	23.2	26.6	46.0
63	-30.3	-76.8	-109.1	-170.7	-183.4
64	25.7	34.9	67.9	58.8	74.9
65	3.8	-2.1	34.2	5.9	75.6
66	6.3	13.2	31.2	27.7	42.7
67	-31.3	-39.8	-26.7	-53.0	-43.3
68	8.4	11.9	15.6	110.7	260.6
69	13.9	15.4	14.0	11.9	26.6
70	-12.5	-25.5	-28.3	-45.8	-47.8
71	-27.3	-50.8	-53.2	-82.4	-81.6
72	-38.3	-98.1	-148.3	-193.0	-206.2
73	-15.9	-59.2	-60.3	-92.7	-103.1
74	-25.0	-74.8	-117.9	-163.8	-195.5
75	5.7	-5.8	-5.6	-8.1	4.3
76	-46.9	-77.2	-103.5	-130.3	-23.7
77	11.6	26.0	64.7	132.6	220.4
78	-7.8	-12.4	-30.7	-1.8	-99.6
79	-5.5	-29.6	-44.8	-57.2	-65.8
80	-3.1	-9.7	-4.5	-8.0	-12.4
81	-33.5	-76.4	-107.5	-133.2	-144.5
82	-14.0	-47.6	-65.2	-86.5	-70.2
83	12.9	16.2	30.2	25.1	19.9
84	11.5	13.8	35.1	6.7	100.6
85	19.5	5.7	-3.1	-19.0	-10.6
86	-40.5	-106.0	-160.0	-207.6	-253.8
87	3.8	5.4	27.5	21.5	30.7
88	0.8	-11.4	-21.2	-24.7	-25.0
89	15.5	23.2	42.1	39.8	46.5
90	0.1	-15.4	-26.4	-40.5	-45.2
91	3.9	13.3	33.8	114.3	176.9
92	2.3	-6.1	-12.7	-10.8	2.5

Table B1-1: Strain D

Strain Gauge	8 MPa (DN)	6 MPa (DN)	4 MPa (DN)	2 MPa (DN)
2	93.5	88.1	73.9	62.0
3	-252.4	-204.0	-148.1	-85.9
4	147.3	143.5	157.7	147.8
8	42.7	39.3	40.4	33.4
9	-277.6	-239.0	-185.8	-131.8
16	235.0	253.4	278.0	271.2
17	76.1	65.4	70.4	73.0
18	-90.4	-72.4	-51.8	-28.0
19	-101.0	-72.1	-42.1	-2.4
21	532.9	551.7	565.2	562.8
22	-74.1	-54.9	-32.7	-13.7
23	-99.0	-55.3	-15.2	28.4
24	112.6	105.0	97.4	95.9
25	-269.8	-225.4	-179.3	-109.2
26	102.4	130.6	163.8	196.3
27	135.6	134.5	134.3	126.9
28	955.8	976.8	989.5	951.5
30	448.3	452.5	435.9	440.1
31	-88.5	-47.8	4.8	28.4
32	90.5	85.5	84.4	72.2
33	251.0	239.9	229.9	208.2
34	39.1	31.2	42.2	27.8
35	57.4	66.7	93.4	92.4
36	513.0	524.6	534.8	519.7
37	353.6	365.7	371.3	361.9
38	-104.7	-77.0	-63.3	-27.4
39	-47.2	-34.9	-48.2	-31.8
40	-67.9	-51.9	-60.1	-41.5
42	-229.9	-194.0	-162.5	-125.0
43	495.4	540.2	558.2	582.7
44	-55.1	-68.3	-81.2	-94.6
45	-168.8	-124.6	-137.0	-78.2
46	-39.6	-9.8	3.4	21.4
47	-52.5	-31.7	-14.2	-12.8
48	49.3	97.2	137.9	159.6
49	-119.4	-88.8	-58.9	-24.9
50	4.8	28.3	37.8	45.2
51	-26.5	45.5	33.4	74.4
52	-297.7	-230.4	-240.7	-249.6

Table B1-1: Strain D

Strain Gauge	8 MPa (DN)	6 MPa (DN)	4 MPa (DN)	2 MPa (DN)
54	-8.7	28.9	55.8	79.2
55	-221.0	-109.4	-95.0	-69.3
56	-116.4	-81.2	-66.1	-42.7
57	22.6	29.2	25.0	21.3
58	-51.4	-20.5	-22.5	-3.2
59	-29.8	24.4	26.2	52.1
60	-38.0	-21.2	-17.3	-14.7
61	-38.6	-13.1	-10.4	3.4
62	33.3	32.9	16.5	10.6
63	-148.3	-92.6	-79.3	-35.7
64	64.1	77.5	58.5	53.8
65	74.6	119.3	88.6	97.3
66	38.5	44.1	29.0	21.8
67	-19.5	8.4	-6.7	-3.6
68	296.1	323.6	330.2	345.1
69	14.0	11.4	4.4	3.1
70	-13.2	16.7	33.4	44.5
71	-32.8	14.9	29.3	48.3
72	-157.8	-113.5	-72.2	-27.7
73	-83.6	-39.0	-32.9	-6.4
74	-145.4	-83.2	-39.9	7.5
75	9.1	15.3	15.7	16.1
76	197.0	243.0	266.5	284.3
77	269.7	317.1	312.9	311.8
78	-47.0	-3.2	-16.9	-17.5
79	-42.6	-21.0	-3.3	11.1
80	-14.4	-7.7	-13.3	-11.1
81	-123.3	-102.0	-77.4	-45.2
82	-42.2	-10.7	10.1	40.6
83	21.9	33.0	23.2	22.6
84	156.1	207.7	241.4	266.1
85	-19.0	2.3	-19.4	1.0
86	-210.8	-159.7	-116.5	-66.6
87	22.2	38.5	8.9	17.0
88	-15.7	-6.9	2.5	12.7
89	42.0	45.7	31.3	32.7
90	-31.0	-21.6	-10.6	-1.0
91	235.0	277.6	294.6	300.8
92	-6.0	-6.0	-20.6	-17.0

Table B1-2: Strain Data, Normal Cycle 2

Strain Gauge	2 MPa (UP)	4 MPa (UP)	6 MPa (UP)	8MPa (UP)	10 MPa (Peak)
2	-6.3	16.9	51.6	76.4	93.4
3	-16.2	-72.8	-38.7	-56.8	-99.7
4	24.1	31.1	78.0	95.8	122.2
8	10.4	18.5	37.2	36.9	36.2
9	-75.0	-135.0	-173.6	-218.7	-259.2
16	-74.0	-137.9	-174.2	-217.5	-255.6
17	14.9	13.4	30.2	32.9	51.7
18	-60.6	-84.2	-69.7	-84.6	-82.3
19	-51.9	-88.3	-108.3	-136.7	-162.4
21	0.0	0.0	0.0	0.0	0.0
22	6.4	30.4	69.0	80.3	100.0
23	-17.1	-39.9	-49.2	-65.5	-72.4
24	-22.3	-56.9	-81.9	-117.5	-153.4
25	34.9	51.8	86.4	98.9	116.4
26	-43.3	-84.8	-97.7	-115.2	-106.8
27	1.6	9.0	36.4	47.1	65.7
28	-53.5	111.0	305.5	371.7	426.0
30	12.0	85.1	157.6	166.3	183.5
31	-24.9	3.3	176.9	188.7	225.3
32	6.4	18.0	47.6	59.1	70.7
33	9.7	24.2	92.3	133.3	191.3
34	8.8	16.6	47.8	56.6	57.9
35	-13.8	-23.1	7.2	15.5	56.0
36	40.1	91.8	185.3	216.6	268.7
37	-28.6	-0.9	69.0	98.2	135.7
38	-13.6	-38.4	-78.2	-85.4	-74.8
39	-27.2	-29.5	-36.3	-35.7	-24.2
40	-20.5	-30.2	-44.3	-40.8	-14.6
42	-85.1	-129.9	-158.3	-183.3	-197.7
43	-65.3	-115.0	-103.0	-54.2	68.0
44	-5.1	3.6	18.7	31.7	36.9
45	-52.1	-87.0	-124.5	-136.9	-117.6
46	-1.9	-14.2	-27.7	-42.0	-35.4
47	32.2	29.3	14.0	11.0	-72.1
48	-8.8	-32.2	-73.6	-106.7	-170.7
49	-46.5	-84.2	-110.0	-128.1	-133.0
50	17.2	12.4	7.4	-4.6	-47.9
51	74.3	40.4	-9.0	25.5	-14.7
52	32.1	40.0	-99.3	-162.4	-283.7

Table B1-2: Strain Data, Normal Cycle 2

Strain Gauge	2 MPa (UP)	4 MPa (UP)	6 MPa (UP)	8MPa (UP)	10 MPa (Peak)
54	-24.7	-47.3	-54.0	-30.3	7.9
55	18.7	7.5	-77.4	-163.9	-244.0
56	5.7	-16.0	-60.2	-78.2	-126.5
57	14.2	21.6	28.2	33.7	36.0
58	-18.7	-23.5	-45.4	-30.7	-44.6
59	18.5	5.5	-49.7	-38.7	-36.0
60	-7.3	-9.3	-21.7	-30.7	-34.9
61	-7.0	-23.8	-46.4	-50.4	-53.0
62	15.7	27.6	41.6	70.1	93.3
63	-44.5	-69.3	-125.5	-137.5	-138.2
64	36.6	56.6	55.8	80.9	82.9
65	38.1	60.8	12.5	62.2	88.2
66	7.8	20.8	23.1	45.2	71.7
67	15.6	34.0	10.6	22.9	75.5
68	23.4	22.7	7.7	50.0	138.1
69	3.6	7.2	9.3	15.9	32.9
70	-12.0	-18.3	-39.2	-56.1	-71.2
71	5.8	0.7	-15.7	-41.1	-81.7
72	-46.4	-89.6	-124.4	-160.9	-179.1
73	-17.3	-23.9	-64.0	-71.8	-104.4
74	-17.4	-52.9	-100.5	-144.8	-182.0
75	8.3	3.7	2.9	4.5	8.6
76	3.4	3.2	95.7	-48.9	-173.4
77	154.6	232.0	261.8	145.8	30.0
78	20.0	39.1	104.4	57.2	-52.7
79	-0.9	-13.6	-27.5	-42.3	-53.4
80	-0.2	7.3	3.3	2.1	-11.9
81	-58.8	-90.5	-104.4	-120.1	-128.5
82	-7.0	-33.8	-55.5	-66.9	-51.6
83	6.8	16.5	10.9	15.8	12.4
84	26.0	8.9	-32.1	-23.4	16.9
85	-1.8	-1.0	-4.0	3.8	16.1
86	-61.2	-111.6	-158.8	-202.8	-257.2
87	0.5	24.3	7.0	29.5	32.7
88	-47.4	-54.0	-81.2	-79.7	-77.0
89	5.6	21.3	21.5	38.3	53.1
90	-11.7	-20.1	-33.8	-43.1	-38.5
91	28.9	52.3	68.4	86.8	132.9
92	8.1	18.7	18.4	29.0	35.5

Table B1-2: Strain D

Strain Gauge	8 MPa (DN)	6 MPa (DN)	4 MPa (DN)	2 MPa (DN)	0 MPa (DN)
2	81.2	68.5	55.3	37.1	14.7
3	-69.0	-28.3	15.8	69.6	159.7
4	118.6	115.8	116.0	109.9	130.3
8	31.1	25.1	20.2	14.4	23.1
9	-223.7	-183.5	-138.0	-84.6	32.6
16	-214.5	-171.4	-123.3	-66.3	46.9
17	44.7	38.2	54.3	58.4	61.2
18	-68.7	-56.8	-44.5	-26.1	61.1
19	-143.3	-117.9	-87.8	-48.8	35.9
21	0.0	0.0	0.0	0.0	0.0
22	103.7	106.5	110.0	111.5	129.4
23	-57.9	-40.8	-19.3	-0.5	25.4
24	-116.7	-74.8	-32.1	11.5	35.7
25	108.0	92.8	82.8	71.5	51.9
26	-84.1	-55.9	-25.3	16.1	94.6
27	61.1	56.3	53.3	51.9	70.8
28	413.2	385.4	338.4	307.6	388.2
30	186.6	191.7	213.3	238.5	329.8
31	289.2	354.5	402.6	434.0	555.4
32	69.5	66.7	60.9	54.1	70.1
33	179.2	171.2	162.3	157.4	159.9
34	59.9	60.6	58.8	55.2	75.4
35	66.1	77.2	87.1	98.6	146.2
36	274.7	278.8	276.6	267.3	239.3
37	145.3	150.1	152.6	155.2	151.2
38	-71.9	-47.9	-33.2	10.1	-0.1
39	-22.9	-18.6	-18.7	0.8	-18.8
40	-16.5	-3.9	-0.2	24.9	-2.5
42	-165.8	-134.8	-103.8	-59.0	12.0
43	85.9	102.2	124.2	163.4	218.4
44	32.1	25.2	19.1	12.2	-3.3
45	-140.9	-112.3	-98.4	-22.3	-24.5
46	-14.4	7.8	26.0	50.8	16.8
47	-50.8	-33.5	-17.7	-5.9	-27.4
48	-138.5	-119.3	-97.7	-77.2	-89.9
49	-115.0	-91.9	-65.2	-31.2	11.6
50	-30.4	-15.5	-4.5	6.2	3.9
51	-43.7	-20.0	-5.2	24.8	43.7
52	-208.1	-108.8	-50.3	-7.8	6.5

Table B1-2: Strain Da

Strain Gauge	8 MPa (DN)	6 MPa (DN)	4 MPa (DN)	2 MPa (DN)	0 MPa (DN)
54	56.1	97.7	128.2	159.0	195.1
55	-167.9	-61.4	12.4	75.6	121.8
56	-120.6	-98.2	-70.1	-35.1	-29.5
57	30.2	28.9	30.0	31.9	24.6
58	-51.3	-42.8	-25.1	5.0	17.5
59	-35.3	-10.2	15.1	59.5	60.6
60	-25.1	-11.9	-2.0	6.5	21.7
61	-42.9	-29.5	-11.4	6.9	14.2
62	77.6	66.7	62.0	61.3	51.7
63	-161.6	-124.5	-73.1	-13.6	27.3
64	58.4	54.7	59.2	62.0	34.5
65	27.8	26.5	70.9	108.4	25.6
66	58.0	50.4	49.7	47.6	45.7
67	49.4	59.2	81.6	90.8	99.6
68	119.8	113.6	130.6	147.6	145.4
69	16.4	8.0	7.5	7.1	4.0
70	-44.9	-22.7	-5.2	7.4	28.0
71	-40.1	-5.5	18.0	36.2	25.1
72	-145.1	-106.3	-64.3	-21.1	10.4
73	-105.7	-84.3	-51.1	-12.6	31.9
74	-137.8	-84.4	-29.8	17.8	32.3
75	6.0	8.2	15.2	21.7	19.6
76	49.2	281.0	340.4	359.1	358.0
77	120.0	221.6	278.2	288.0	177.8
78	45.1	81.9	54.5	40.0	19.3
79	-35.0	-14.8	-0.2	15.8	30.0
80	-14.9	-8.9	-8.4	-3.2	11.6
81	-115.3	-99.4	-78.9	-45.1	18.2
82	-32.0	-1.5	23.8	59.2	59.1
83	2.1	1.3	2.4	6.4	15.6
84	2.1	29.8	92.2	139.2	114.7
85	-0.8	10.5	17.8	32.1	42.0
86	-216.0	-165.3	-120.6	-68.1	-4.5
87	0.3	11.0	4.4	21.4	7.0
88	-108.7	-93.7	-93.5	-54.7	-71.2
89	32.5	30.6	21.0	22.7	21.3
90	-39.7	-32.7	-28.1	-12.9	-3.5
91	120.8	95.9	86.8	94.9	9.1
92	16.2	20.4	17.8	28.2	25.8

Table B1-3: Strain Data, Normal Cycle 3

Strain Gauge	2 MPa (UP)	4 MPa (UP)	6 MPa (UP)	8MPa (UP)	10 MPa (Peak)
2	48.0	70.0	100.2	115.6	129.0
3	-713.4	-921.1	-1347.2	-1466.1	-1788.0
4	17.5	24.1	42.0	49.0	62.5
8	25.7	36.0	52.5	59.4	55.7
9	-61.0	-118.8	-158.6	-199.6	-245.5
16	67.8	87.1	139.5	143.6	161.9
17	44.3	38.9	48.1	49.7	49.0
18	-32.8	-45.0	-38.6	-45.8	-54.1
19	-37.1	-73.5	-97.4	-124.6	-162.8
21	5.6	19.1	38.4	48.7	44.6
22	-3.5	-25.6	-37.8	-54.9	-69.6
23	-16.3	-59.0	-90.3	-132.3	-181.9
24	47.2	62.0	82.0	93.1	102.1
25	-60.7	-120.4	-160.9	-200.8	-243.4
26	-19.2	-59.5	-71.3	-89.9	-97.2
27	13.2	16.6	32.2	36.5	37.5
28	-27.5	-59.2	-16.0	26.7	62.9
30	-116.4	-99.1	-82.5	-75.0	-57.3
31	-30.5	-73.2	-63.4	-91.5	-107.4
32	21.1	30.1	50.6	57.0	63.5
33	40.0	43.7	69.3	85.3	96.8
34	26.5	33.5	52.3	57.8	61.6
35	7.9	-3.3	6.2	-0.7	-5.9
36	63.0	81.4	127.6	144.5	172.2
37	-2.4	-7.1	-16.9	-23.5	-43.0
38	-16.3	-29.8	-58.6	-72.1	-98.9
39	-20.5	-24.3	-34.6	-40.2	-57.7
40	-13.4	-19.6	-43.3	-47.1	-61.6
42	-71.5	-114.4	-146.8	-179.7	-220.0
43	-51.0	-95.9	-128.1	-146.6	-153.8
44	21.2	36.4	28.2	27.3	21.8
45	-68.1	-80.7	-122.3	-133.1	-151.4
46	8.0	-5.1	-40.5	-63.2	-100.3
47	18.4	15.0	43.6	20.2	-15.9
48	11.1	-8.6	-0.1	-31.2	-47.3
49	-34.8	-70.1	-103.5	-120.3	-135.2
50	13.7	7.6	12.1	-6.3	-31.6
51	36.4	21.9	19.8	37.1	54.7
52	34.6	12.2	-102.1	-201.4	-306.7

Table B1-3: Strain Data, Normal Cycle 3

Strain Gauge	2 MPa (UP)	4 MPa (UP)	6 MPa (UP)	8MPa (UP)	10 MPa (Peak)
54	-11.9	-33.1	-37.4	-56.7	-22.2
55	-7.8	-36.2	-131.8	-236.3	-350.4
56	-0.2	-17.2	-44.6	-72.7	-114.5
57	22.7	31.6	35.0	32.8	30.4
58	-10.4	-19.8	-33.3	-37.9	-50.3
59	4.7	-12.3	-55.5	-71.3	-38.5
60	-5.4	-6.8	-14.1	-27.2	3.8
61	-11.9	-24.3	-34.1	-53.7	-33.3
62	23.3	35.7	53.7	67.1	99.5
63	-37.2	-63.5	-138.8	-169.2	-207.8
64	27.7	44.0	51.1	56.8	63.0
65	66.3	97.6	66.6	72.0	98.2
66	17.7	29.6	34.5	44.2	72.2
67	77.8	90.0	52.5	50.1	98.5
68	28.4	29.8	34.6	59.6	101.2
69	1.0	6.5	18.7	28.2	45.7
70	-6.6	-15.3	-28.1	-50.1	-76.9
71	7.5	3.7	-0.7	-33.4	-70.3
72	-38.9	-82.5	-120.0	-155.8	-179.5
73	1.0	-19.2	-56.4	-83.9	-111.7
74	-11.2	-47.5	-84.1	-136.5	-176.9
75	14.5	8.5	6.2	6.3	0.3
76	82.0	129.4	106.5	-124.9	-315.1
77	342.6	370.3	247.1	105.8	-14.6
78	71.5	103.3	120.1	50.6	-49.9
79	1.9	-10.0	-21.8	-36.9	-54.2
80	1.0	5.8	8.9	7.0	-4.8
81	-47.1	-78.4	-92.5	-103.9	-115.3
82	-2.0	-27.2	-39.2	-60.1	-63.5
83	-0.5	5.0	9.4	11.2	14.9
84	27.5	23.8	-41.0	-19.7	4.6
85	5.3	4.2	10.4	11.5	18.7
86	-64.9	-113.2	-153.1	-199.7	-252.3
87	1.7	13.9	24.1	27.6	20.4
88	37.9	49.5	16.8	26.3	21.2
89	15.8	27.6	40.6	52.5	58.4
90	19.2	18.4	7.8	13.4	16.8
91	62.0	89.7	21.5	62.1	76.9
92	8.9	13.9	27.0	33.4	39.5

Table B1-3: Strain Da

Strain Gauge	8 MPa (DN)	6 MPa (DN)	4 MPa (DN)	2 MPa (DN)	0 MPa (DN)
2	123.1	111.1	97.3	82.3	57.7
3	-1636.6	-1687.4	-1526.7	-1371.1	-147.8
4	63.4	72.8	71.8	71.0	91.4
8	54.2	52.3	48.4	44.5	57.7
9	-206.5	-161.7	-114.9	-59.3	54.1
16	178.4	215.8	226.6	230.3	234.3
17	55.1	67.8	78.6	84.8	86.9
18	-41.8	-24.4	-13.3	3.2	72.3
19	-135.9	-103.5	-71.3	-30.7	64.3
21	52.2	58.8	62.6	67.3	90.0
22	-51.1	-28.7	-6.4	15.1	41.7
23	-134.4	-82.8	-35.2	9.5	43.4
24	93.8	89.1	80.5	69.0	54.0
25	-202.9	-155.7	-106.8	-51.6	60.4
26	-67.9	-27.5	6.1	43.9	142.0
27	35.4	35.1	32.9	32.2	52.3
28	39.7	5.3	10.0	27.6	125.8
30	-47.8	-44.5	-29.5	42.3	176.0
31	-74.2	-42.9	-8.9	35.2	113.7
32	60.9	65.4	61.0	58.3	75.4
33	93.1	93.5	96.7	100.4	112.0
34	61.6	65.1	62.7	61.5	82.4
35	3.7	19.0	34.8	56.1	112.6
36	173.2	179.2	182.2	178.5	161.8
37	-35.9	-50.0	-49.4	-45.4	-42.5
38	-78.6	-54.4	-29.9	-13.0	-5.9
39	-49.3	-53.0	-45.5	-35.0	-40.0
40	-53.8	-47.7	-40.9	-37.0	-61.1
42	-187.6	-162.4	-126.9	-79.6	4.2
43	-128.4	-103.7	-68.5	-25.4	39.7
44	16.1	4.8	-1.4	-9.7	-25.4
45	-136.8	-117.1	-96.8	-66.9	-60.6
46	-72.7	-49.8	-25.9	-10.2	-42.1
47	15.5	9.6	42.8	67.8	60.2
48	0.1	40.9	75.9	97.9	118.1
49	-108.7	-86.8	-59.5	-32.3	19.3
50	-6.6	8.4	24.1	31.9	40.3
51	111.1	87.5	90.0	73.0	96.0
52	-180.4	-59.4	31.2	55.4	105.2

Table B1-3: Strain Da

Strain Gauge	8 MPa (DN)	6 MPa (DN)	4 MPa (DN)	2 MPa (DN)	0 MPa (DN)
54	44.8	87.6	122.1	144.1	183.1
55	-226.4	-122.5	-37.7	-12.8	54.6
56	-76.9	-55.9	-22.4	-6.6	34.8
57	40.3	39.7	42.5	35.2	36.4
58	-14.5	-24.4	-0.7	3.5	34.9
59	24.8	28.6	68.7	59.6	71.2
60	36.3	53.8	71.6	73.1	90.0
61	9.6	20.5	42.8	44.4	59.8
62	110.4	99.5	101.8	90.2	93.6
63	-135.1	-111.2	-62.4	-44.9	19.4
64	80.0	63.0	66.1	49.2	42.2
65	171.4	154.9	185.9	133.2	130.3
66	78.5	67.0	64.0	51.0	57.2
67	145.5	130.1	145.6	126.0	140.5
68	166.7	167.1	176.1	148.0	160.2
69	39.4	27.4	22.0	18.0	22.9
70	-38.8	-13.6	2.8	9.6	35.6
71	-12.6	12.0	34.3	42.3	36.3
72	-136.3	-99.1	-55.8	-20.5	15.4
73	-72.4	-69.2	-37.8	-22.8	8.5
74	-115.3	-58.6	-5.6	34.7	55.8
75	7.6	6.6	12.9	15.7	18.9
76	-118.5	167.0	317.6	334.3	284.7
77	46.6	132.6	195.0	203.3	75.2
78	41.1	131.4	122.8	98.0	74.4
79	-30.6	-12.5	1.4	14.2	23.6
80	4.9	6.5	5.9	5.7	21.8
81	-100.1	-86.2	-66.4	-34.4	33.1
82	-9.7	23.8	53.6	78.9	87.1
83	23.7	18.5	17.0	10.2	25.3
84	29.0	64.1	116.6	128.6	96.2
85	29.6	31.4	40.4	44.3	63.8
86	-200.3	-153.6	-105.6	-57.0	19.5
87	37.6	22.8	14.1	5.4	3.8
88	81.0	64.4	44.6	25.0	28.7
89	60.0	48.8	38.5	30.5	34.1
90	42.1	43.7	36.4	47.6	56.9
91	110.9	85.8	39.7	3.3	-130.4
92	43.3	34.4	31.7	30.6	34.7

Table B1-4	Note: All Strains at 2 MPa Normal Stress except last (Unloade		
Shear 1	at 0 MPa Normal Stress		
Strain Gauge	Shear Stress = 0 MPa (UP)	0.25 MPa (UP)	0.50 MPa (UP)
2	54.5	53.0	66.6
3	0.0	0.0	0.0
4	30.2	35.9	41.0
8	5.6	14.7	11.9
9	-75.3	-75.4	-72.5
16	29.8	41.2	51.8
17	22.0	31.3	33.6
18	-51.2	-52.1	-46.7
19	-63.6	-64.9	-70.7
21	-21.5	-21.4	-18.2
22	-24.8	-25.9	-28.2
23	-38.5	-43.9	-35.5
24	22.5	25.1	26.1
25	-83.0	-80.8	-77.9
26	-43.7	-38.3	-34.6
27	-7.7	-8.9	-3.9
28	-3.1	-8.4	-2.0
30	35.8	46.1	70.2
31	-41.4	-56.0	-22.4
32	-10.4	-15.9	-12.4
33	7.4	5.7	10.1
34	10.4	10.3	19.4
35	-19.4	-12.9	6.5
36	23.6	25.6	36.4
37	-72.2	-79.7	-82.0
38	-64.6	-36.5	-50.3
39	-56.8	-47.7	-56.5
40	-63.6	-24.6	-57.0
42	-111.3	-97.9	-97.7
43	-78.2	-65.0	-68.5
44	-48.6	-49.8	-50.1
45	-109.5	-61.9	-92.8
46	-46.5	-37.4	-49.1
47	-5.1	-3.6	6.3
48	6.5	3.9	6.6
49	-52.4	-50.9	-50.6
50	-7.3	-8.1	-9.1
51	4.3	43.7	41.6
52	-6.1	10.9	7.1

Table B1-4	Note: All Strains at 2 MPa Normal Stress except last (Unloade
Shear 1	at 0 MPa Normal Stress

Strain Gauge	Shear Stress = 0 MPa (UP)	0.25 MPa (UP)	0.50 MPa (UP)
54	-37.6	-36.3	-35.8
55	-45.5	-39.2	-43.1
56	-18.5	-13.5	-21.7
57	-1.0	3.8	2.5
58	-36.0	-5.9	-6.9
59	-22.8	-1.8	0.1
60	-23.2	-21.2	-20.0
61	-29.0	-18.1	-22.4
62	-1.5	9.5	5.6
63	-79.5	-42.6	-55.9
64	9.1	28.4	19.0
65	-7.2	59.0	41.0
66	-5.2	3.3	0.7
67	-12.1	45.9	12.3
68	-8.7	29.4	14.4
69	-18.8	-11.8	-17.8
70	-27.8	-24.5	-27.5
71	-23.6	-15.0	-20.5
72	-67.5	-55.9	-61.0
73	-36.0	-11.7	-26.5
74	-30.2	-21.5	-21.3
75	-9.5	-4.0	-10.2
76	40.2	45.1	48.7
77	239.3	241.5	243.6
78	36.1	34.7	33.7
79	-14.0	-6.0	-0.7
80	-20.2	-16.5	-22.0
81	-64.8	-70.7	-78.2
82	-29.6	-14.1	-25.0
83	-12.9	-6.4	-13.9
84	-8.6	31.3	14.6
85	-29.2	-11.3	-22.4
86	-82.9	-76.3	-79.4
87	-16.4	10.6	-8.5
88	-68.2	60.4	-3.4
89	-9.4	5.9	-1.8
90	6.4	48.5	23.5
91	-4.2	35.4	23.0
92	-15.0	-2.0	-9.8

Table B1-4	Note: All Strainsd) which is		
Shear 1	at 0 MPa I		
Strain Gauge	Shear Stress = 1.0 MPa (UP)	1.25 MPa (Peak)	1.0 MPa (DN)
2	79.2	103.9	112.5
3	0.0	0.0	0.0
4	47.0	57.6	63.3
8	18.3	23.3	22.9
9	-69.1	-65.7	-62.2
16	46.0	103.1	86.2
17	-9.5	50.2	-13.1
18	-34.6	-33.5	-29.0
19	-69.0	-82.6	-69.3
21	0.0	-10.2	0.0
22	-32.5	-33.6	-25.9
23	-33.9	-32.2	-27.0
24	27.9	29.6	28.1
25	-77.4	-71.0	-72.9
26	-31.2	-21.2	-17.7
27	-1.9	8.5	13.4
28	-1.3	5.4	12.6
30	93.5	136.5	153.9
31	133.1	212.2	228.0
32	-7.5	-6.9	1.0
33	20.2	24.4	40.1
34	38.9	62.1	77.4
35	30.3	63.2	68.6
36	50.3	65.2	67.1
37	-90.1	-97.9	-90.2
38	-51.4	-55.2	-53.9
39	-53.7	-55.9	-54.6
40	-64.9	-74.4	-69.0
42	-74.7	-68.2	-70.8
43	-45.7	-25.4	-24.6
44	-58.3	-72.4	-68.3
45	-88.0	-90.0	-95.5
46	-50.7	-61.5	-58.7
47	36.7	57.0	58.5
48	9.9	18.8	28.7
49	-48.7	-45.3	-40.3
50	-8.6	-8.7	-2.8
51	58.8	31.3	70.7
52	1.4	-21.8	-4.0

Table B1-4	Note: All Strainsd) which is		
Shear 1	at 0 MPa I		
Strain Gauge	Shear Stress = 1.0 MPa (UP)	1.25 MPa (Peak)	1.0 MPa (DN)
54	-38.9	-40.8	-33.4
55	-54.5	-65.8	-53.5
56	-32.6	-41.4	-27.8
57	-0.3	-2.8	3.3
58	2.2	6.6	14.6
59	-11.0	-21.4	-7.1
60	-18.4	-17.4	-13.7
61	-16.3	-13.0	-9.3
62	5.6	4.0	10.7
63	-63.5	-65.3	-58.9
64	18.7	14.5	27.5
65	36.8	18.0	33.3
66	-0.2	-0.6	4.8
67	-5.2	-22.6	1.8
68	9.0	-2.1	8.3
69	-18.0	-20.3	-13.8
70	-30.5	-32.2	-27.0
71	-19.1	-21.1	-16.2
72	-64.4	-71.0	-65.7
73	-27.9	-35.4	-25.4
74	-18.0	-21.1	-18.3
75	-13.6	-16.7	-9.2
76	57.6	60.1	61.7
77	256.1	258.7	265.5
78	36.2	37.0	42.9
79	7.7	7.3	5.4
80	-25.6	-30.4	-25.2
81	-91.0	-94.8	-85.5
82	-27.2	-34.2	-28.7
83	-17.2	-20.0	-13.8
84	-6.5	-27.0	-26.2
85	-27.4	-31.8	-23.9
86	-81.6	-85.6	-82.9
87	-13.9	-18.7	-12.5
88	-47.5	-65.1	-72.0
89	-6.1	-7.5	-3.4
90	-5.9	-15.7	-16.7
91	-35.8	-67.7	-68.8
92	-13.7	-13.7	-11.9

Table B1-4	Note: All Strains				
Shear 1	at 0 MPa I				
Strain Gauge	Shear Stress =	0.5 MPa (DN)	0.25 MPa (DN)	0.0 MPa (DN)	Unloaded
2		111.6	117.1	120.8	108.5
3		0.0	0.0	0.0	0.0
4		59.5	72.9	74.6	81.3
8		18.7	17.8	16.6	24.8
9		-65.2	-63.4	-64.6	26.4
16		109.3	108.7	127.7	113.4
17		32.5	27.6	33.6	-29.0
18		-32.8	-32.5	-33.4	22.5
19		-62.4	-57.5	-46.9	25.1
21		-10.3	-8.8	-9.8	0.0
22		-21.7	-18.9	-13.7	11.0
23		-27.5	-26.0	-25.1	11.9
24		36.6	37.2	36.9	26.9
25		-63.2	-61.9	-59.2	54.0
26		-16.9	-16.9	-12.7	56.1
27		15.9	17.5	21.9	33.7
28		19.5	23.5	30.6	51.8
30		142.6	143.3	154.2	232.9
31		218.2	222.2	201.1	308.6
32		7.0	9.8	15.0	30.7
33		50.6	55.9	71.6	101.4
34		83.2	87.0	97.9	124.1
35		60.2	58.1	61.2	123.2
36		57.4	55.8	52.1	59.1
37		-88.8	-90.9	-100.6	-75.3
38		-47.7	-62.4	-64.9	-32.2
39		-50.1	-58.4	-63.1	-62.3
40		-49.6	-65.0	-40.8	-88.4
42		-80.1	-90.1	-101.6	-29.4
43		-39.8	-51.3	-74.1	-0.2
44		-67.0	-68.4	-67.5	-74.8
45		-85.2	-108.7	-89.9	104.2
46		-52.9	-58.0	-50.6	-57.9
47		39.5	31.5	-3.4	21.0
48		30.7	29.2	20.8	50.6
49		-40.1	-39.0	-33.0	-3.8
50		-3.4	-4.0	-9.3	6.1
51		26.1	26.1	24.1	18.9
52		-27.8	-26.0	-28.3	-21.5

Table B1-4	Note: All Strains				
Shear 1	at 0 MPa I				
Strain Gauge	Shear Stress =	0.5 MPa (DN)	0.25 MPa (DN)	0.0 MPa (DN)	Unloaded
54		-34.6	-30.2	-31.8	9.5
55		-55.9	-50.6	-42.2	-7.3
56		-23.6	-22.4	-23.5	7.6
57		2.1	2.7	1.8	2.5
58		-12.5	-18.0	-37.5	2.4
59		-20.9	-15.9	-9.4	-0.4
60		-16.4	-16.5	-15.6	-3.0
61		-16.4	-15.8	-16.0	-0.9
62		4.8	4.9	2.1	8.9
63		-67.4	-62.3	-15.4	-22.0
64		20.2	18.9	15.0	8.6
65		-3.4	-2.9	14.0	-9.6
66		1.8	3.0	4.2	3.9
67		-14.2	-4.2	16.1	-2.3
68		-8.1	5.9	17.1	-9.0
69		-17.2	-18.3	-20.4	-15.0
70		-25.7	-26.8	-25.2	-1.8
71		-18.6	-20.3	-20.7	-6.6
72		-68.3	-67.7	-59.4	-10.2
73		-34.2	-34.1	-31.5	-19.0
74		-25.7	-29.0	-36.2	4.4
75		-3.4	-5.5	-1.0	0.2
76		57.9	54.6	49.9	34.3
77		269.6	268.5	261.7	90.8
78		45.6	46.2	42.4	15.9
79		-2.4	-7.9	-11.9	3.6
80		-21.3	-24.0	-19.4	-10.3
81		-69.4	-64.8	-54.3	0.9
82		-25.9	-33.1	-27.8	0.0
83		-11.5	-12.6	-10.5	-4.2
84		-28.6	-32.5	13.8	-56.0
85		-17.5	-25.8	-12.8	-13.6
86		-82.2	-86.1	-84.6	-2.6
87		-4.2	-13.7	8.1	-18.7
88		-57.9	-87.0	52.6	121.1
89		0.9	-4.1	9.9	-6.7
90		1.2	-1.0	57.3	8.2
91		-59.5	-57.7	27.2	132.0
92		-7.8	-11.7	0.5	-9.7

Table B1-5	Note: All Strains at 5 MPa Normal Stress except last (Unloaded) which is
Shear 2	at 0 MPa Normal Stress

Strain Gauge	Shear Stress = 0 MPa (UP)	0.5 MPa (UP)	1.0 MPa (UP)	2.0 MPa (UP)
2	248.7	268.6	266.7	281.2
3	0.0	0.0	0.0	0.0
4	333.0	352.9	356.0	382.1
8	11.6	22.2	22.7	30.1
9	-165.9	-157.3	-158.1	-148.1
16	-115.0	-108.1	-111.4	-110.3
17	33.0	54.2	60.8	72.7
18	-33.6	-26.5	-25.4	-11.0
19	-120.1	-123.4	-136.3	-154.5
21	0.0	0.0	0.0	0.0
22	-15.0	-7.9	-6.9	6.5
23	-61.7	-60.9	-66.2	-66.8
24	-108.3	-102.4	-106.8	-101.9
25	59.7	64.9	61.6	64.0
26	-27.1	-12.0	-10.8	-3.2
27	55.4	64.8	63.2	66.3
28	2408.1	2439.7	2436.4	2439.2
30	488.5	556.7	570.5	622.2
31	17.1	31.8	35.2	44.7
32	39.1	47.4	43.5	46.7
33	35.1	48.7	40.6	34.1
34	65.2	72.4	71.3	72.7
35	29.8	63.1	77.7	111.8
36	55.3	75.0	81.3	105.9
37	-68.4	-73.4	-81.0	-95.7
38	-86.4	-78.0	-87.1	-99.8
39	-122.6	-118.0	-126.3	-123.1
40	-108.4	-103.4	-120.8	-143.1
42	-49.4	-51.2	-53.3	-56.2
43	-186.5	-170.9	-163.9	-143.3
44	-228.5	-215.8	-208.0	-191.5
45	-91.7	-92.1	-101.2	-110.2
46	-188.1	-168.0	-175.2	-175.6
47	20.9	24.3	31.5	113.9
48	-13.4	-19.9	-29.7	-40.9
49	-106.2	-103.5	-105.3	-92.2
50	-12.3	-15.9	-25.9	-38.4
51	1.1	15.3	-22.9	15.7
52	-101.7	-105.5	-135.8	-156.3

Table B1-5	Note: All Strains at 5 MPa Normal Stress except last (Unloaded) which is			
Shear 2	at 0 MPa Normal Stress			
Strain Gauge	Shear Stress = 0 MPa (UP)	0.5 MPa (UP)	1.0 MPa (UP)	2.0 MPa (UP)
54	-62.5	-52.6	-62.2	-56.4
55	-114.7	-130.7	-165.0	-196.0
56	-27.5	-32.9	-51.1	-52.3
57	7.2	8.1	0.3	-1.6
58	-46.2	-25.9	-23.1	35.3
59	-51.0	-45.5	-61.5	-37.4
60	-29.2	-27.3	-31.8	-28.8
61	-34.9	-33.5	-43.4	-37.3
62	5.2	9.5	3.9	16.6
63	-111.6	-96.8	-108.9	-55.4
64	34.3	37.5	25.9	47.2
65	16.3	38.3	29.4	112.4
66	4.8	7.4	2.4	15.1
67	-31.5	-29.5	-47.8	15.3
68	7.1	18.1	8.7	51.1
69	-7.9	-5.8	-8.6	2.0
70	-50.7	-49.2	-52.5	-53.2
71	-28.4	-23.0	-24.6	-17.4
72	-128.3	-124.6	-126.2	-126.9
73	-69.6	-62.2	-60.1	-37.0
74	-82.1	-71.6	-64.9	-47.6
75	-34.7	-36.1	-40.5	-44.5
76	56.9	79.3	98.9	158.3
77	204.9	230.5	255.3	340.4
78	74.8	68.3	61.0	64.5
79	-39.7	-25.2	-14.4	3.8
80	-17.0	-16.5	-19.2	-26.3
81	-104.9	-115.8	-130.0	-152.3
82	-86.3	-74.3	-70.3	-59.3
83	-4.5	-3.6	-6.3	-4.1
84	-38.1	2.0	17.1	66.2
85	-25.2	-17.2	-17.7	-14.1
86	-152.4	-147.1	-146.9	-140.7
87	-26.9	-16.9	-18.1	-16.0
88	-83.2	-3.2	27.4	119.1
89	7.8	15.4	16.4	20.1
90	-8.5	17.6	18.8	33.9
91	-71.7	-36.8	-8.6	17.9
92	-7.7	-1.8	-0.2	3.5

Table B1-5 **Shear 2** Strain Gauge	Note: All Strain at 0 MPa Shear Stress =	2.5 MPa (Peak)	1.5 MPa (DN)	0.5 MPa (DN)
2		398.0	409.3	413.5
3		0.0	0.0	0.0
4		498.5	507.5	512.8
8		37.1	28.6	21.7
9		-139.3	-142.7	-147.5
16		-60.0	-54.3	-52.7
17		88.0	81.7	67.8
18		6.3	1.0	-5.1
19		-162.9	-139.9	-119.1
21		0.0	0.0	0.0
22		33.0	28.7	22.7
23		-67.4	-58.1	-50.4
24		-87.0	-88.7	-90.1
25		78.2	80.2	81.3
26		46.2	48.1	46.3
27		104.0	109.3	113.0
28		2556.4	2568.8	2581.2
30		772.6	771.0	764.2
31		531.8	549.0	565.1
32		100.0	112.5	122.9
33		123.6	148.8	168.6
34		126.3	134.0	140.0
35		209.1	196.2	181.9
36		154.8	143.1	127.8
37		-124.7	-122.0	-117.5
38		-123.2	-118.3	-116.2
39		-148.2	-149.4	-156.3
40		-188.3	-170.4	-157.1
42		-65.0	-65.0	-66.3
43		-134.0	-152.2	-172.4
44		-212.8	-224.8	-243.3
45		-131.2	-127.6	-124.2
46		-237.5	-246.7	-259.2
47		191.8	177.2	160.5
48		-41.7	-31.4	-21.8
49		-90.7	-83.6	-85.5
50		-47.2	-38.8	-30.5
51		-4.9	3.7	2.8
52		-200.8	-174.9	-158.0

Table B1-5 **Shear 2** Strain Gauge	Note: All Strain at 0 MPa Shear Stress =	2.5 MPa (Peak)	1.5 MPa (DN)	0.5 MPa (DN)
54		-29.0	-13.6	-3.9
55		-243.2	-205.1	-172.4
56		-67.7	-44.5	-26.1
57		-13.5	-8.5	-5.2
58		31.7	7.8	-15.3
59		-59.1	-51.1	-50.5
60		-17.6	-11.5	-7.7
61		-48.3	-40.9	-35.4
62		14.3	13.7	15.1
63		-91.2	-84.8	-87.5
64		35.2	37.3	39.3
65		77.2	58.2	34.8
66		14.1	17.4	19.6
67		-53.8	-35.4	-20.7
68		24.5	25.8	20.6
69		-5.5	-6.5	-8.4
70		-59.6	-58.9	-60.1
71		-18.3	-22.0	-27.8
72		-129.3	-139.3	-147.2
73		-54.3	-58.6	-67.3
74		-46.2	-64.0	-79.8
75		-60.3	-58.5	-57.0
76		196.1	175.4	146.7
77		385.1	365.6	330.4
78		71.3	76.6	81.4
79		7.9	-12.9	-31.9
80		-39.7	-37.0	-33.3
81		-160.5	-136.5	-113.0
82		-75.0	-82.8	-90.7
83		-16.7	-12.6	-10.0
84		-13.4	-25.6	-45.9
85		-31.1	-29.2	-27.7
86		-145.6	-151.1	-155.6
87		-49.7	-43.9	-41.5
88		-69.0	-83.3	-112.2
89		5.2	6.4	6.7
90		-40.7	-21.7	-13.5
91		-165.2	-171.6	-207.2
92		-7.7	-6.6	-7.4

Table B1-5	Note: All Strain	
Shear 2	at 0 MPa	
Strain Gauge	Shear Stress = 0.0 MPa (DN)	Unloaded
2	458.4	427.3
3	0.0	0.0
4	568.5	578.6
8	17.9	26.1
9	-130.3	22.3
16	-2.3	167.0
17	68.8	27.8
18	4.0	47.0
19	-91.7	16.7
21	0.0	0.0
22	34.2	60.7
23	-33.1	0.5
24	-55.2	36.5
25	87.7	52.4
26	86.7	194.5
27	145.8	151.8
28	2645.4	2664.0
30	837.3	891.2
31	755.2	865.6
32	155.8	156.0
33	226.1	254.9
34	180.5	184.4
35	217.2	294.0
36	148.5	172.2
37	-127.7	-119.6
38	-103.6	-11.6
39	-154.8	-141.8
40	-147.8	-130.8
42	-62.8	-62.0
43	-173.6	-54.3
44	-256.4	-110.9
45	-133.6	-153.1
46	-251.5	-177.4
47	129.2	73.2
48	-20.9	18.3
49	-87.9	-23.3
50	-15.6	11.1
51	38.4	19.1
52	-118.5	-41.6

Table B1-5	Note: All Strain	
Shear 2	at 0 MPa	
Strain Gauge	Shear Stress = 0.0 MPa (DN)	Unloaded
54	9.2	76.5
55	-116.6	-26.2
56	-5.1	44.4
57	10.5	3.2
58	-16.2	10.4
59	-20.3	0.1
60	-4.3	17.3
61	-23.3	1.7
62	19.4	19.4
63	-65.8	9.7
64	56.4	25.7
65	49.7	1.9
66	30.0	14.9
67	30.9	-16.6
68	39.7	14.5
69	-2.2	-10.0
70	-53.9	-17.0
71	-14.9	10.1
72	-144.9	-29.8
73	-65.7	10.2
74	-83.7	15.5
75	-40.1	-22.1
76	99.8	91.8
77	270.0	111.8
78	85.2	10.2
79	-39.2	-5.3
80	-23.4	-13.7
81	-88.4	-4.0
82	-83.7	-5.1
83	-0.9	-3.1
84	-23.5	-43.8
85	-16.7	-10.2
86	-149.1	-9.4
87	-28.6	-45.8
88	-86.3	-93.3
89	16.3	-4.5
90	21.6	29.5
91	-156.1	-231.6
92	1.5	-3.9

Table B1-6	Note: All Strains at 10 MPa Normal Stress except last (Unlo
Shear 3a	is at 0 MPa Normal Stress

Strain Gauge	Shear Stress = 0 MPa (UP)	1.0 MPa (UP)	3.0 MPa (UP)
2	209.6	229.6	239.7
3	0.0	0.0	0.0
4	112.0	129.1	134.4
8	18.7	28.6	39.2
9	-278.2	-273.4	-259.0
16	44.3	42.5	61.9
17	36.6	18.9	27.1
18	-45.9	-39.3	-50.6
19	-64.3	-64.3	-80.9
21	0.0	0.0	0.0
22	-27.4	-21.9	-27.8
23	-33.8	-31.7	-43.9
24	-48.8	-45.2	-67.0
25	16.1	17.8	26.4
26	-144.1	-139.2	-115.7
27	21.5	23.6	19.6
28	79.2	87.0	77.5
30	88.0	107.1	144.4
31	23.3	39.1	19.2
32	27.2	24.4	14.6
33	44.9	33.1	-0.3
34	102.7	108.4	112.2
35	-50.3	-22.9	26.1
36	132.7	154.0	218.9
37	-84.4	-89.5	-112.6
38	-182.0	-200.9	-199.7
39	-96.9	-106.3	-77.4
40	-71.6	-99.2	-108.5
42	-249.2	-231.2	-171.8
43	-202.6	-186.4	-92.9
44	-20.1	-28.4	-29.7
45	-172.5	-192.2	-138.5
46	-116.0	-122.5	-121.8
47	-43.0	-43.8	-33.1
48	-84.2	-95.9	-82.2
49	-124.3	-120.9	-78.0
50	-80.1	-91.7	51.9
51	24.9	-4.0	-13.1
52	-408.8	-460.5	-555.6

Table B1-6	Note: All Strains at 10 MPa Normal Stress except last (Unlo
Shear 3a	is at 0 MPa Normal Stress

Strain Gauge	Shear Stress = 0 MPa (UP)	1.0 MPa (UP)	3.0 MPa (UP)
54	-71.5	-83.3	-29.2
55	-330.8	-398.4	-490.1
56	-101.4	-126.4	-144.8
57	-5.7	-23.0	-130.9
58	-42.9	-32.4	71.4
59	-27.8	-45.8	-5.3
60	18.9	-1.1	-113.9
61	-95.3	-121.8	-93.5
62	66.3	59.4	67.4
63	-204.4	-206.0	-89.3
64	68.1	59.6	93.8
65	86.2	88.8	311.1
66	68.5	59.6	62.6
67	42.7	9.6	136.2
68	63.3	61.4	145.3
69	22.9	26.0	59.6
70	-79.1	-71.4	-53.7
71	-116.0	-104.2	-78.2
72	-191.7	-186.3	-168.4
73	-197.8	-197.5	-151.7
74	-219.1	-200.3	-148.8
75	-23.1	-31.5	-51.7
76	-442.2	-368.6	-234.2
77	-223.7	-186.1	-118.5
78	13.0	33.0	38.8
79	-66.0	-37.0	13.2
80	-23.8	-25.1	-29.3
81	-136.9	-163.1	-211.8
82	-116.5	-110.3	-72.5
83	31.6	30.0	39.5
84	-70.0	-43.2	119.7
85	11.5	9.7	31.2
86	-264.6	-259.6	-242.9
87	-7.6	-11.2	3.9
88	-74.5	-54.0	173.5
89	26.6	27.3	49.5
90	-7.9	-18.7	31.6
91	102.3	129.7	294.9
92	9.8	9.0	20.8

Table B1-6 **Shear 3a** Strain Gauge	Note: All Strainsaded) which is at 0 MP Shear Stress =	5.0 MPa (UP)	6.0 MPa (UP)	7.0 MPa (UP)
2		273.9	296.7	305.7
3		0.0	0.0	0.0
4		157.5	167.7	171.4
8		41.8	27.2	-4.1
9		-248.9	-245.4	-243.0
16		96.7	111.7	119.3
17		44.6	59.4	56.3
18		-37.9	7.1	4.3
19		-79.5	6.7	6.0
21		0.0	0.0	0.0
22		-19.9	3.2	3.8
23		-36.1	-8.8	-10.4
24		-56.3	-1.7	-1.1
25		23.1	-0.5	-1.4
26		-72.4	-44.9	-4.7
27		11.0	4.3	-8.2
28		77.5	173.7	261.6
30		182.2	196.5	195.3
31		23.0	55.3	48.9
32		24.3	41.9	50.2
33		-11.6	2.1	15.8
34		132.7	154.6	156.4
35		109.7	173.0	244.5
36		385.8	453.6	491.1
37		-122.6	-128.9	-132.7
38		-247.4	-281.8	-277.3
39		-49.0	-34.5	-14.9
40		-138.8	-163.2	-164.5
42		-85.6	-40.8	21.0
43		38.3	93.7	170.2
44		-16.4	-20.5	-29.6
45		-134.2	-161.5	-112.0
46		-141.0	-159.6	-175.0
47		299.8	674.1	0.0
48		8.4	191.7	385.5
49		-86.9	-86.2	-22.4
50		318.5	456.4	542.9
51		-97.1	-120.1	-56.9
52		-669.2	-675.0	-657.5

Table B1-6 **Shear 3a** Strain Gauge	Note: All Strainsaded) which is at 0 MP Shear Stress =	5.0 MPa (UP)	6.0 MPa (UP)	7.0 MPa (UP)
54		108.9	186.1	200.2
55		-590.4	-641.5	-647.0
56		-179.3	-103.2	-64.9
57		194.8	287.4	313.5
58		79.5	153.2	231.7
59		-9.5	14.9	18.8
60		-169.4	-127.7	-113.9
61		-182.9	-210.8	-219.6
62		51.8	40.7	54.0
63		-185.3	-147.2	-146.0
64		110.9	195.3	237.8
65		191.8	214.3	289.5
66		59.2	58.5	75.3
67		91.6	109.5	156.6
68		95.4	104.4	149.0
69		94.7	133.8	156.4
70		-41.6	0.2	18.4
71		-88.1	-85.8	-117.9
72		-170.3	-115.5	77.1
73		-157.9	-114.6	-72.0
74		-103.7	-48.4	74.9
75		-102.4	-109.0	14.2
76		-56.0	35.1	320.6
77		-43.7	-83.1	-175.9
78		6.2	-134.7	-267.5
79		56.5	89.3	125.6
80		-64.3	-86.3	-123.3
81		-248.9	-236.2	-220.9
82		-48.9	-8.8	70.0
83		31.0	39.0	48.1
84		143.3	200.7	253.6
85		23.9	17.9	45.7
86		-225.5	-183.5	-114.3
87		-46.6	-35.4	-29.1
88		128.2	82.0	220.7
89		45.9	37.8	41.4
90		-61.6	-119.8	-86.5
91		288.7	256.3	357.1
92		13.5	6.8	21.6

Table B1-6 **Shear 3a** Strain Gauge	Note: All Strains is at 0 MP Shear Stress =	7.58 MPa (PEAK)	Unloaded
2		326.4	271.2
3		0.0	0.0
4		175.9	192.6
8		-36.7	42.8
9		-243.7	31.0
16		119.7	121.6
17		48.0	46.7
18		8.0	10.0
19		3.6	3.9
21		0.0	0.0
22		6.0	6.3
23		-9.1	-9.2
24		0.0	0.6
25		3.6	3.4
26		12.8	58.0
27		-22.1	27.9
28		450.3	567.0
30		168.5	126.7
31		-20.2	152.2
32		43.7	36.7
33		23.7	70.7
34		138.2	129.8
35		281.3	153.8
36		487.2	345.0
37		-132.4	-60.6
38		-293.9	-79.2
39		-9.7	-45.6
40		-158.7	-26.3
42		85.9	-15.6
43		264.5	295.8
44		-88.1	-115.7
45		-123.0	-92.1
46		-189.7	-43.7
47		0.0	0.0
48		544.1	806.5
49		37.7	-24.2
50		632.4	690.6
51		-3.2	241.4
52		-524.3	620.6

Table B1-6 **Shear 3a** Strain Gauge	Note: All Strains is at 0 MP; Shear Stress =	7.58 MPa (PEAK)	Unloaded
54		209.0	301.5
55		-308.1	0.0
56		-42.9	159.8
57		326.8	401.9
58		261.3	109.4
59		17.6	47.5
60		-112.8	356.5
61		-247.7	-43.1
62		48.1	389.7
63		-236.2	48.3
64		241.0	241.3
65		268.5	133.8
66		50.8	244.9
67		98.1	178.7
68		113.4	282.2
69		162.1	154.4
70		27.8	50.2
71		-97.0	146.6
72		84.5	163.6
73		-41.7	135.8
74		65.0	96.9
75		143.8	83.0
76		324.5	179.8
77		-282.2	-308.3
78		-322.4	-221.0
79		213.9	112.0
80		-101.2	68.0
81		-17.2	119.3
82		33.8	143.4
83		52.2	81.6
84		135.8	247.9
85		54.5	95.9
86		-42.8	13.2
87		-72.0	68.1
88		119.0	84.7
89		12.2	57.0
90		-162.7	-17.8
91		218.4	79.1
92		15.1	23.1

Table B1-7 **Shear 3b** Strain Gauge	Note: All Strains at 10 MPa Normal Stress except last (Unloa at 0 MPa Normal Stress Shear Stress = 0 MPa (UP)	1.0 MPa (UP)	3.0 MPa (UP)
2	82.5	86.6	86.0
3	0.0	0.0	0.0
4	12.9	16.1	20.2
8	-6.7	1.8	18.8
9	-304.3	-302.8	-296.3
16	-295.9	-293.4	-296.8
17	-46.5	-34.2	-9.4
18	-58.9	-55.0	-34.3
19	-237.7	-263.2	-312.7
21	0.0	0.0	0.0
22	-44.6	-34.6	-17.3
23	-11.0	-17.6	-14.9
24	-473.6	-477.0	-487.6
25	55.3	55.9	53.3
26	-167.7	-162.7	-145.1
27	-9.6	-8.3	-14.7
28	-41.7	-53.0	-73.6
30	44.9	62.1	86.5
31	-298.5	-294.4	-285.7
32	19.1	16.1	3.2
33	-7.8	-20.6	-45.3
34	23.1	27.0	23.2
35	-139.1	-112.1	-59.4
36	-48.4	-28.6	21.4
37	-76.4	-81.8	-95.7
38	-193.3	-212.0	-241.3
39	-28.2	-36.0	-21.8
40	-49.9	-84.7	-120.1
42	0.0	0.0	0.0
43	-228.2	-212.0	-153.6
44	0.0	0.0	0.0
45	8.9	5.9	3.5
46	-64.4	-88.8	-78.3
47	0.0	0.0	0.0
48	0.0	0.0	0.0
49	-203.5	-238.1	-222.3
50	0.0	0.0	0.0
51	-213.4	-286.3	-299.6
52	-620.9	-652.4	-806.1

Table B1-7	Note: All Strains at 10 MPa Normal Stress except last (Unloa		
Shear 3b	at 0 MPa Normal Stress		
Strain Gauge	Shear Stress = 0 MPa (UP)	1.0 MPa (UP)	3.0 MPa (UP)
54	-34.0	-54.4	-66.9
55	-1741.7	-2455.7	0.0
56	-182.6	-211.2	-201.2
57	-21.1	-29.2	-1.8
58	-101.1	-105.9	-17.0
59	-42.2	-68.6	-39.9
60	-225.9	-265.7	-355.3
61	52.6	-11.6	-47.1
62	-143.0	-176.7	-251.8
63	-216.3	-263.0	-296.7
64	-17.7	-45.4	-30.6
65	-54.9	-117.4	-96.9
66	0.0	0.0	0.0
67	-53.4	-122.4	-129.4
68	-104.0	-121.3	-147.1
69	53.6	47.8	63.0
70	-112.6	-102.3	-73.7
71	76.6	86.0	92.2
72	-145.0	-130.5	-104.2
73	-206.4	-206.7	-174.5
74	-77.6	-59.9	-14.7
75	-59.2	-69.1	-81.7
76	-371.4	-322.5	-228.9
77	188.8	208.5	277.0
78	63.8	73.3	37.6
79	-59.0	-38.3	-6.5
80	-8.5	-10.5	-16.5
81	-101.3	-126.9	-192.2
82	-78.5	-72.8	-45.9
83	-6.9	-9.7	-7.7
84	167.9	171.3	238.5
85	0.3	-8.4	-5.3
86	-285.0	-282.7	-254.9
87	0.0	0.0	0.0
88	-39.1	-58.6	-55.8
89	27.2	18.5	19.7
90	-108.8	-161.5	-238.0
91	293.9	286.0	283.0
92	-3.0	-8.4	-9.1

Table B1-7	Note: All Strains ıded) which is at 0.0 MPa Normal			
Shear 3b	at 0 MPa N			
Strain Gauge	Shear Stress =	5.0 MPa (UP)	6.0 MPa (UP)	7.0 MPa (UP)
2		90.9	96.5	93.8
3		0.0	0.0	0.0
4		18.2	9.0	0.2
8		10.8	-6.1	-39.8
9		-298.5	-298.7	-293.9
16		-281.9	-256.6	-215.4
17		27.1	54.0	91.8
18		-10.8	-9.5	-0.5
19		-376.5	-428.4	-496.8
21		0.0	0.0	0.0
22		12.2	19.3	27.3
23		-21.4	-47.8	-61.2
24		-358.4	-288.3	-220.0
25		47.6	38.5	30.3
26		-114.8	-93.3	-66.2
27		-26.2	-33.2	-47.3
28		-86.3	-82.6	-82.6
30		107.9	115.4	116.5
31		-278.1	-254.6	-244.1
32		1.5	7.2	9.2
33		-55.3	-51.4	-38.4
34		22.8	27.0	21.4
35		18.3	74.6	142.8
36		97.9	129.2	166.2
37		-115.8	-124.4	-130.2
38		-270.7	-286.8	-288.1
39		-0.8	3.7	12.1
40		-154.4	-177.1	-185.3
42		0.0	0.0	0.0
43		-74.4	-23.8	63.6
44		0.0	0.0	0.0
45		2.2	2.3	-17.1
46		-62.3	-65.8	-49.4
47		0.0	0.0	0.0
48		0.0	0.0	0.0
49		-163.3	-139.9	-110.1
50		0.0	0.0	0.0
51		-362.3	-354.4	-288.3
52		-802.1	-817.4	-731.7

Table B1-7 **Shear 3b** Strain Gauge	Note: All Strains ıded) which is at 0.0 MPa Normal at 0 MPa N Shear Stress =	5.0 MPa (UP)	6.0 MPa (UP)	7.0 MPa (UP)
54		-63.0	-75.7	-81.2
55		0.0	0.0	0.0
56		-198.1	-207.8	-221.7
57		21.8	19.3	7.6
58		38.2	58.3	81.5
59		-51.9	-60.8	-77.3
60		-354.5	-371.1	-376.9
61		-107.6	-157.2	-203.5
62		-325.7	-349.1	-354.1
63		-313.7	-335.4	-386.5
64		18.6	26.5	30.3
65		-107.7	-90.6	-57.1
66		0.0	0.0	0.0
67		-158.5	-168.1	-165.7
68		-192.9	-214.5	-172.0
69		76.2	78.0	81.8
70		-19.1	3.8	23.7
71		70.8	6.5	10.2
72		17.1	49.1	28.6
73		-115.1	-111.6	-72.8
74		64.6	67.9	29.6
75		-85.0	-31.4	8.4
76		-163.7	-86.9	-10.3
77		101.0	98.9	133.2
78		-312.7	-285.5	-203.3
79		43.9	66.7	73.8
80		-43.7	-71.8	-80.8
81		-220.9	-228.2	-76.4
82		2.3	10.1	27.5
83		-3.6	-4.0	9.6
84		427.1	396.7	339.1
85		2.9	-5.3	6.3
86		-208.3	-199.3	-182.4
87		0.0	0.0	0.0
88		29.6	14.5	64.9
89		22.6	3.8	-13.8
90		-240.6	-280.6	-256.2
91		332.8	294.6	266.7
92		-8.2	-11.5	-6.5

Table B1-7 **Shear 3b** Strain Gauge	Note: All Strains at 0 MPa N Shear Stress =	8.0 MPa (UP)	9.0 MPa (UP)	9.46 MPa (PEAK)
2		100.5	97.3	93.5
3		0.0	0.0	0.0
4		-8.6	-17.4	-18.9
8		-95.6	-120.7	-135.5
9		-332.2	-411.6	-480.3
16		-169.6	-144.8	-159.6
17		154.2	64.9	76.4
18		188.4	139.3	129.9
19		-667.6	-768.8	-848.5
21		0.0	0.0	0.0
22		36.0	6.3	-6.7
23		-45.4	-47.7	-66.8
24		-114.4	-171.3	-181.2
25		24.0	8.0	3.3
26		-43.1	0.9	50.7
27		-75.7	-86.2	-93.2
28		-70.3	-54.4	-21.2
30		127.6	103.4	89.0
31		-326.5	-317.2	-319.3
32		14.7	21.2	24.9
33		29.9	120.8	147.4
34		14.5	-8.8	-30.4
35		228.2	317.4	357.6
36		240.6	340.7	458.5
37		-143.3	-147.1	-150.9
38		-281.8	-247.6	-211.1
39		27.7	45.2	48.7
40		-138.2	-0.1	105.6
42		0.0	0.0	0.0
43		220.2	537.8	665.8
44		0.0	0.0	0.0
45		-61.7	-84.5	-86.0
46		-54.5	-42.3	-41.5
47		0.0	0.0	0.0
48		0.0	0.0	0.0
49		-123.2	-25.3	72.6
50		0.0	0.0	0.0
51		-253.8	-263.8	-236.0
52		-620.9	-368.4	-269.6

Table B1-7	Note: All Strains			
Shear 3b	at 0 MPa N			
Strain Gauge	Shear Stress =	8.0 MPa (UP)	9.0 MPa (UP)	9.46 MPa (PEAK)
54		-108.9	-76.4	-50.0
55		0.0	0.0	0.0
56		-231.7	-254.4	-280.1
57		0.4	6.3	1.6
58		74.0	70.8	95.3
59		-162.2	-183.2	-184.9
60		-318.0	-143.9	-157.7
61		-215.7	-344.7	-412.0
62		-362.1	-516.7	-581.4
63		-591.0	-695.0	-745.6
64		65.4	116.1	111.7
65		-51.6	-19.1	-37.5
66		0.0	0.0	0.0
67		-264.5	-373.2	-407.1
68		-21.5	315.9	335.7
69		77.7	44.4	148.0
70		42.4	48.8	54.0
71		53.2	122.5	184.3
72		-36.4	-91.8	-6.0
73		-68.6	-78.3	-98.3
74		-30.4	-47.9	89.9
75		61.0	90.7	59.4
76		-104.3	-205.8	-5.0
77		192.8	179.7	-267.8
78		131.1	321.6	-234.2
79		-222.3	-42.8	91.2
80		89.6	139.5	174.2
81		268.8	259.3	60.6
82		24.8	20.9	147.8
83		42.9	31.5	44.1
84		-128.9	-333.0	690.6
85		36.5	40.0	29.3
86		-207.4	-184.8	108.2
87		0.0	0.0	0.0
88		252.2	277.0	657.4
89		-71.1	-131.6	1051.4
90		-183.2	-241.5	-271.1
91		178.7	161.2	1571.3
92		-10.2	-24.3	-26.4

Table B1-7 **Shear 3b** Strain Gauge	Note: All Strains at 0 MPa N Shear Stress =	7.0 MPa (DN)	6.25 MPa (DN)
2		104.8	121.8
3		0.0	0.0
4		-8.5	5.0
8		-140.6	-144.1
9		-429.6	-409.4
16		-134.4	-117.1
17		60.7	118.0
18		127.2	104.8
19		-724.4	-682.3
21		0.0	0.0
22		-0.3	2.1
23		-21.9	-4.3
24		-224.1	-297.2
25		6.8	10.3
26		58.1	78.1
27		-84.4	-57.3
28		17.7	94.3
30		87.3	183.5
31		-322.5	-233.1
32		39.8	83.4
33		214.4	330.0
34		-32.3	38.8
35		244.1	322.5
36		437.3	517.4
37		-111.5	-77.0
38		-164.0	-150.4
39		39.4	38.7
40		150.9	170.5
42		0.0	0.0
43		528.9	507.0
44		0.0	0.0
45		-57.0	-32.5
46		-59.7	-145.3
47		0.0	0.0
48		0.0	0.0
49		123.0	159.5
50		0.0	0.0
51		-188.8	-129.7
52		-229.0	-191.1

Table B1-7	Note: All Strains	
Shear 3b	at 0 MPa N	
Strain Gauge	Shear Stress = 7.0 MPa (DN)	6.25 MPa (DN)
54	27.5	74.0
55	0.0	0.0
56	-167.1	-149.8
57	70.5	121.9
58	52.7	14.7
59	-178.9	-151.9
60	-100.1	-36.3
61	-377.6	-365.4
62	-470.4	-420.9
63	-591.8	-567.1
64	169.6	173.4
65	47.7	8.4
66	0.0	0.0
67	-242.7	-82.3
68	371.6	366.5
69	218.7	234.6
70	32.6	24.1
71	129.6	120.0
72	72.1	91.4
73	-118.4	-121.9
74	184.0	182.1
75	64.3	57.0
76	-89.8	-165.2
77	128.3	229.7
78	-312.2	-59.4
79	41.9	56.6
80	174.9	179.3
81	163.4	160.0
82	146.7	142.9
83	34.0	9.9
84	1094.5	962.1
85	5.4	21.0
86	72.6	24.6
87	0.0	0.0
88	-167.6	-193.8
89	933.7	882.9
90	-109.2	-123.7
91	1642.9	1880.3
92	13.6	5.5

Appendix B2: Tabulated Flow Data for Lengthwise Flow Configurations.

Tables B2-1 through B2-7 provide the flow data recovered during the testing of LSR-2.

Table B2-8 lists the loading steps, and the flow tests performed.

Flow rates are ml/second, and heads are metres. Refer to Figure 2-4 for the placement of the ports and model dimensions.

Table B2-1 Flow Data, Normal Cycle 1

N_LOAD (MPa)	Q (ml/sec.)	Port 13 PTRANS.2 (metres)	Port16 PTRANS.3 (metres)	Port7 PTRANS.4 (metres)	Port 4 PTRANS.5 (metres)	Port 6 PTRANS.6 (metres)	Port 2 PTRANS.7 (metres)	Port 1 PTRANS.8 (metres)
0.1	0.667	1.642	1.350	1.838	1.981	1.448	1.360	0.756
0.2	0.684	1.673	1.200	1.862	1.959	1.348	1.227	0.711
0.5	0.711	1.645	1.295	1.887	2.002	1.382	1.251	0.658
1	0.754	1.690	1.361	1.949	2.039	1.413	1.432	0.650
2	0.771	1.527	1.398	1.794	2.040	1.375	1.549	0.594
4	0.727	1.626	1.464	1.931	2.140	1.390	1.732	0.690
6	0.722	1.661	1.489	1.990	2.162	1.425	1.695	0.673
8	0.758	1.563	1.674	1.905	2.029	1.550	1.603	0.711
10	0.721	1.554	1.699	1.897	1.976	1.608	1.595	0.776
10	0.766	1.554	1.713	1.900	1.978	1.645	1.597	0.800
8	0.725	1.550	1.708	1.877	1.941	1.577	1.594	0.787
6	0.724	1.554	1.718	1.890	1.955	1.625	1.594	0.830
4	0.763	1.565	1.829	1.861	1.900	1.644	1.596	1.002
2	0.791	1.563	1.789	1.832	1.869	1.667	1.593	1.007
1	0.762	1.557	1.744	1.843	1.858	1.664	1.591	1.024
1	0.747	1.546	1.823	1.797	1.880	1.635	1.591	1.115
0.5	0.765	1.543	1.838	1.797	1.881	1.618	1.588	1.126
0.2	0.778	1.544	1.838	1.794	1.850	1.553	1.588	1.158
0.2	0.000	1.465	1.339	1.546	1.649	1.320	1.543	1.052

N_LOAD (MPa)	Q (ml/sec.)	Port 15 PTRANS.2 (metres)	Port 12 PTRANS.4 (metres)	Port 8 PTRANS.5 (metres)	Port 17 PTRANS.6 (metres)	Port 10 PTRANS.7 (metres)	Port 11 PTRANS.8 (metres)
0.1	0.667	1.664	1.692	2.152	1.509	1.735	0.805
0.2	0.684	1.648	1.693	2.140	1.557	1.745	0.777
0.5	0.711	1.689	1.709	2.207	1.635	1.788	0.817
1	0.754	1.677	1.700	2.194	1.629	1.764	0.757
2	0.771	1.418	1.575	2.030	1.919	1.634	0.880
4	0.727	1.606	1.684	2.144	2.045	1.765	1.019
6	0.722	1.608	1.677	2.136	2.031	1.771	1.015
8	0.758	1.582	1.581	2.075	1.977	1.689	1.093
10	0.721	0.966	1.371	1.746	1.467	1.275	0.325
10	0.766	1.316	1.575	2.012	1.894	1.673	0.958
8	0.725	1.370	1.584	1.981	1.879	1.664	0.945
6	0.724	1.488	1.570	1.990	1.868	1.665	0.939
4	0.763	1.566	1.575	1.971	1.813	1.681	1.334
2	0.791	1.548	1.573	1.929	1.797	1.657	1.298
1	0.762	1.547	1.580	1.923	1.770	1.645	1.272
1	0.747	1.561	1.591	1.891	1.773	1.646	1.250
0.5	0.765	1.552	1.574	1.879	1.778	1.639	1.235
0.2	0.778	1.550	1.586	1.846	1.769	1.637	1.240
0.2	0.000	1.464	1.539	1.648	1.595	1.540	1.107

Table B2-2 Flow Data, Normal Cycle 2

N_LOAD (MPa)	Q (ml/sec.)	Port 13 PTRANS.2 (metres)	Port16 PTRANS.3 (metres)	Port7 PTRANS.4 (metres)	Port 4 PTRANS.5 (metres)	Port 6 PTRANS.6 (metres)	Port 2 PTRANS.7 (metres)	Port 1 PTRANS.8 (metres)
0.2	1.277	1.760	2.157	2.254	1.977	2.018	1.768	1.416
0.2	1.330	1.710	2.087	2.175	1.936	1.942	1.714	1.374
0.5	1.265	1.705	2.008	1.895	1.754	2.016	1.742	1.387
0.5	1.290	1.729	2.103	2.162	1.976	1.926	1.748	1.446
1	1.343	1.729	2.128	2.183	2.007	1.949	1.755	1.462
1	1.318	1.603	2.004	2.141	2.187	2.031	1.668	1.466
1	1.186	1.587	1.988	2.055	2.130	1.931	1.647	1.436
2	1.206	1.603	1.995	2.080	2.153	1.953	1.650	1.438
2	1.322	1.623	4.634	2.117	2.181	1.992	1.662	1.450
4	1.198	1.599	1.980	2.079	2.159	1.925	1.653	1.410
4	1.318	1.624	2.025	2.111	2.185	1.956	1.660	1.422
6	1.190	1.610	1.971	2.088	2.146	1.959	1.648	1.371
6	1.398	1.636	2.057	2.189	2.185	2.050	1.671	1.386
6	1.360	1.623	2.047	2.150	2.158	2.025	1.663	1.383
6	1.404	1.631	2.047	2.155	2.158	2.025	1.666	1.376
6	1.376	1.630	2.032	2.123	2.137	2.016	1.672	1.350
6	1.400	1.624	2.033	2.114	2.116	2.010	1.668	1.335
6	1.386	1.615	2.028	2.104	2.100	2.001	1.664	1.320
6	1.379	1.628	2.038	2.114	2.101	2.009	1.670	1.320
6	1.363	1.608	2.004	2.088	2.070	1.984	1.668	1.294
6	0.740	1.525	1.868	1.849	1.874	1.777	1.617	1.143
6	0.743	1.521	1.873	1.863	1.879	1.830	1.618	1.134
6	0.750	1.531	1.879	1.853	1.880	1.835	1.617	1.140
6	0.727	1.524	1.873	1.861	1.878	1.818	1.617	1.142
8	0.740	1.532	1.870	1.844	1.881	1.799	1.618	1.143
8	0.730	1.531	1.880	1.860	1.880	1.797	1.618	1.133
8	0.740	1.533	1.890	1.848	1.887	1.805	1.619	1.142
8	0.711	1.520	1.874	1.847	1.870	1.784	1.615	1.112
8	0.748	1.535	1.890	1.865	1.884	1.791	1.618	1.138
8	0.745	1.537	1.880	1.868	1.883	1.790	1.618	1.141
10	0.730	1.539	1.890	1.880	1.893	1.815	1.621	1.161
10	0.734	1.539	1.875	1.879	1.887	1.802	1.621	1.160
10	0.764	1.537	1.880	1.880	1.893	1.801	1.621	1.161
10	0.740	1.540	1.870	1.890	1.895	1.808	1.621	1.169
10	0.782	1.554	1.897	1.950	1.950	1.891	1.627	1.220
10	0.767	1.548	1.917	1.960	1.931	1.886	1.614	1.211
8	0.734	1.902	2.182	1.981	2.184	2.058	2.017	1.547
8	0.748	1.557	1.898	1.902	1.914	1.856	1.621	1.229
6	0.748	1.555	1.874	1.881	1.911	1.847	1.621	1.240
6	0.732	1.559	1.868	1.883	1.905	1.856	1.621	1.246
6	0.732	1.549	1.898	1.503	1.605	1.573	1.621	0.930
6	0.781	1.561	1.864	1.883	1.995	1.939	1.621	1.292
6	0.739	1.557	1.869	1.878	2.001	1.929	1.621	1.289
6	0.750	1.561	1.870	1.885	2.001	1.941	1.624	1.289
4	0.748	1.565	1.875	1.870	1.977	1.901	1.621	1.283
4	0.732	1.555	1.865	1.863	1.965	1.913	1.621	1.284
4	0.743	1.555	1.865	1.863	1.960	1.898	1.621	1.290
4	0.731	1.564	1.880	1.872	1.956	1.905	1.621	1.292
2	0.763	1.558	1.866	1.866	1.934	1.890	1.621	1.305
2	0.773	1.564	1.881	1.865	1.932	1.896	1.621	1.314

1	0.749	1.558	1.866	1.837	1.900	1.852	1.618	1.294
1	0.758	1.559	1.861	1.835	1.893	1.847	1.615	1.296
1	0.732	1.549	1.860	1.833	1.961	1.843	1.618	1.306
1	0.732	1.556	1.871	1.829	1.946	1.822	1.615	1.314
0.5	0.732	1.544	1.856	1.819	1.925	1.817	1.615	1.321
0.2	0.739	1.552	1.851	1.796	1.894	1.795	1.612	1.320
0.2	0.000	1.479	1.725	1.581	1.718	1.607	1.570	1.211

Table B2-2 Flow Data, Normal Cycle 2 (Continued)

N_LOAD (MPa)	Q (ml/sec.)	Port 15 PTRANS.2 (metres)	Port 12 PTRANS.4 (metres)	Port 8 PTRANS.5 (metres)	Port 17 PTRANS.6 (metres)	Port 10 PTRANS.7 (metres)	Port 11 PTRANS.8 (metres)
0.2	1.277	1.701	1.657	2.262	2.040	1.805	1.521
0.2	1.330	1.729	1.632	2.243	2.040	1.829	1.539
0.5	1.265	1.759	1.731	2.264	2.062	1.858	1.561
0.5	1.290	1.759	1.725	2.250	2.068	1.848	1.558
1	1.343	1.781	1.737	2.275	2.092	1.880	1.583
1	1.318	1.626	1.637	2.181	1.999	1.768	1.458
1	1.186	1.593	1.624	2.131	1.968	1.742	1.420
2	1.206	1.614	1.625	2.141	1.964	1.757	1.420
2	1.322	1.623	1.619	2.150	2.002	1.781	1.427
4	1.198	1.608	1.639	2.129	1.968	1.775	1.388
4	1.318	1.620	1.627	2.159	1.980	1.782	1.400
6	1.190	1.627	1.620	2.170	1.988	1.787	1.405
6	1.398	1.601	1.622	2.119	1.971	1.764	1.362
6	1.360	1.664	1.645	2.159	2.035	1.802	1.356
6	1.404	1.654	1.640	2.136	2.005	1.788	1.356
6	1.376	1.654	1.642	2.137	1.998	1.791	1.351
6	1.400	1.655	1.640	2.124	1.978	1.791	1.341
6	1.386	1.649	1.636	2.103	1.970	1.786	1.329
6	1.379	1.644	1.643	2.095	1.958	1.786	1.318
6	1.363	1.648	1.647	2.091	1.966	1.792	1.320
6	0.740	1.628	1.628	2.069	1.936	1.781	1.295
6	0.743	1.528	1.612	1.875	1.759	1.672	1.146
6	0.750	1.529	1.610	1.873	1.766	1.669	1.147
6	0.727	1.522	1.609	1.872	1.769	1.669	1.141
8	0.740	1.535	1.613	1.880	1.786	1.682	1.150
8	0.730	1.533	1.623	1.873	1.776	1.676	1.150
8	0.740	1.536	1.607	1.882	1.777	1.680	1.149
8	0.711	1.521	1.612	1.860	1.764	1.673	1.123
8	0.748	1.533	1.618	1.876	1.763	1.679	1.140
8	0.745	1.539	1.614	1.868	1.724	1.606	1.037
10	0.730	1.550	1.604	1.891	1.774	1.688	1.164
10	0.734	1.546	1.608	1.881	1.764	1.688	1.164
10	0.764	1.520	1.607	1.878	1.761	1.681	1.161
10	0.740	1.550	1.612	1.886	1.766	1.688	1.179
10	0.782	1.574	1.617	1.928	1.803	1.697	1.222
10	0.767	1.559	1.615	1.905	1.794	1.688	1.212
8	0.734	1.576	1.614	1.900	1.759	1.688	1.235
8	0.748	1.574	1.611	1.897	1.775	1.688	1.232
6	0.748	1.567	1.602	1.893	1.768	1.689	1.240
6	0.732	1.571	1.611	1.893	1.778	1.688	1.246
6	0.732	1.563	1.229	1.598	1.501	1.688	0.937
6	0.781	1.593	1.609	1.988	1.865	1.691	1.297

6	0.739	1.590	1.609	1.996	1.863	1.691	1.289
6	0.750	1.593	1.604	1.987	1.857	1.694	1.291
4	0.748	1.593	1.600	1.968	1.836	1.688	1.285
4	0.732	1.582	1.602	1.959	1.840	1.685	1.288
4	0.743	1.578	1.601	1.956	1.830	1.688	1.295
4	0.731	1.578	1.598	1.936	1.825	1.682	1.289
2	0.763	1.580	1.607	1.926	1.820	1.685	1.310
2	0.773	1.586	1.606	1.924	1.830	1.685	1.314
1	0.749	1.573	1.607	1.897	1.792	1.673	1.298
1	0.758	1.572	1.610	1.890	1.783	1.673	1.301
1	0.732	1.560	1.619	1.960	1.785	1.670	1.312
1	0.732	1.561	1.611	1.947	1.777	1.667	1.319
0.5	0.732	1.544	1.618	1.926	1.761	1.664	1.324
0.2	0.739	1.552	1.606	1.897	1.743	1.655	1.321
0.2	0.000	1.470	1.579	1.725	1.597	1.573	1.213

Table B2-3 Flow Data, Normal Cycle 3

N_LOAD (MPa)	Q (ml/sec.)	Port 13 PTRANS.2 (metres)	Port16 PTRANS.3 (metres)	Port7 PTRANS.4 (metres)	Port 4 PTRANS.5 (metres)	Port 6 PTRANS.6 (metres)	Port 2 PTRANS.7 (metres)	Port 1 PTRANS.8 (metres)
0.2	0.749	1.578	1.862	1.773	2.038	1.856	1.616	1.589
0.2	0.799	1.590	1.867	1.795	2.048	1.846	1.619	1.592
0.2	0.796	1.588	1.867	1.774	2.047	1.840	1.619	1.594
0.2	0.749	1.578	1.857	1.754	2.028	1.817	1.616	1.582
0.2	0.780	1.584	1.873	1.789	2.025	1.821	1.619	1.597
0.2	0.749	1.570	1.857	1.766	2.007	1.814	1.616	1.586
0.2	0.749	1.570	1.838	1.770	2.009	1.809	1.616	1.586
0.5	0.778	1.587	1.858	1.790	2.034	1.836	1.622	1.602
0.5	0.755	1.581	1.853	1.782	2.021	1.824	1.618	1.596
0.5	0.748	1.580	1.853	1.778	2.020	1.822	1.616	1.599
0.5	0.780	1.571	1.857	1.790	2.033	1.837	1.618	1.606
0.5	0.766	1.585	1.853	1.789	2.034	1.837	1.619	1.606
1	0.797	1.591	1.868	1.817	2.061	1.858	1.622	1.622
1	0.798	1.581	1.882	1.815	2.060	1.856	1.622	1.622
1	0.747	1.582	1.873	1.795	2.058	1.839	1.618	1.612
1	0.746	1.587	1.863	1.802	2.047	1.842	1.618	1.614
1	0.741	1.573	1.840	1.787	2.101	1.872	1.618	1.606
1	0.748	1.573	1.866	1.778	2.104	1.858	1.614	1.597
2	0.748	1.586	1.878	1.805	2.093	1.865	1.617	1.612
2	0.749	1.587	1.872	1.806	2.089	1.861	1.617	1.612
2	0.743	1.747	2.173	2.344	2.452	2.369	1.758	1.927
2	0.795	1.611	2.039	2.261	2.368	2.309	1.773	1.964
2	0.747	1.744	2.154	2.266	2.381	2.282	1.748	1.883
2	0.815	1.606	1.906	1.915	2.043	1.916	1.628	1.654
2	0.794	1.603	1.906	1.899	2.029	1.905	1.626	1.659
2	0.740	1.592	1.876	1.863	1.998	1.866	1.622	1.636
2	0.741	1.597	1.866	1.850	2.000	1.866	1.621	1.630
2	0.785	1.599	1.876	1.869	2.005	1.872	1.628	1.647
4	0.791	1.605	1.911	1.882	2.006	1.884	1.627	1.641
4	0.799	1.600	1.901	1.871	2.000	1.882	1.627	1.642
4	0.740	1.593	1.891	1.854	1.980	1.859	1.624	1.627
4	0.740	1.598	1.896	1.849	1.977	1.861	1.624	1.625
4	0.782	1.593	1.911	1.880	1.992	1.873	1.630	1.634
4	0.787	1.602	1.917	1.875	1.997	1.876	1.627	1.625
6	0.791	1.594	1.911	1.890	2.001	1.883	1.631	1.630
6	0.799	1.593	1.926	1.885	2.000	1.887	1.630	1.624
6	0.744	1.593	1.902	1.855	1.982	1.856	1.625	1.618
6	0.747	1.597	1.892	1.852	1.976	1.865	1.624	1.614
6	0.796	1.604	1.917	1.875	1.998	1.882	1.626	1.622
6	0.796	1.592	1.901	1.886	1.996	1.881	1.626	1.620
6	0.730	1.745	2.172	2.298	2.269	2.329	1.754	1.859
6	0.730	1.731	2.141	2.227	2.187	2.214	1.699	1.792
6	0.777	1.724	2.141	2.191	2.217	2.214	1.733	1.811
6	0.730	1.709	2.072	2.090	2.158	2.107	1.723	1.743
6	0.729	1.711	2.072	2.080	2.154	2.102	1.715	1.731

6	0.780	1.707	2.066	2.099	2.171	2.124	1.724	1.755
6	0.732	1.707	2.087	2.071	2.159	2.106	1.721	1.731
6	0.714	1.697	2.076	2.057	2.160	2.084	1.721	1.720
8	0.716	1.697	2.062	2.058	2.156	2.090	1.721	1.709
8	0.777	1.731	2.087	2.106	2.191	2.131	1.739	1.740
8	0.783	1.700	2.057	2.076	2.166	2.091	1.724	1.738
10	0.730	1.533	1.903	1.894	1.988	1.965	1.571	1.538
10	0.786	1.618	2.002	2.030	2.115	2.019	1.635	1.624
10	0.731	1.542	1.922	1.952	2.062	1.964	1.630	1.579
10	0.732	1.546	1.918	1.953	2.068	1.975	1.630	1.574
10	0.731	1.532	1.901	1.948	2.079	1.963	1.630	1.564
10	0.783	1.541	1.947	1.971	2.100	2.001	1.633	1.579
10	0.790	1.632	1.922	1.980	2.285	2.106	1.657	1.554
10	0.792	1.638	1.928	1.930	2.278	2.102	1.657	1.543
10	0.729	1.623	1.898	1.863	2.253	2.061	1.651	1.501
8	0.805	1.630	1.909	1.843	2.253	2.085	1.655	1.504
8	0.796	1.593	1.869	1.897	2.188	2.040	1.630	1.441
8	0.807	1.606	1.889	1.915	2.179	2.043	1.633	1.440
6	0.729	1.585	1.864	1.891	2.131	1.989	1.627	1.400
6	0.749	1.583	1.873	1.907	2.123	1.985	1.627	1.400
6	0.800	1.602	1.900	1.935	2.130	2.002	1.632	1.411
6	0.740	1.587	1.868	1.948	2.097	1.986	1.627	1.357
6	0.748	1.587	1.882	1.984	2.098	1.995	1.633	1.367
4	0.745	1.589	1.868	1.960	2.060	1.968	1.633	1.348
4	0.757	1.587	1.868	1.952	2.046	1.956	1.630	1.334
2	0.739	1.580	0.746	1.934	2.000	1.927	1.630	1.312
2	0.745	1.570	1.853	1.937	2.000	1.912	1.630	1.303
1	0.748	1.572	1.855	1.921	1.971	1.894	1.624	1.274
1	0.733	1.558	1.839	1.927	1.962	1.888	1.624	1.269
1	0.746	1.553	1.825	1.923	1.981	1.912	1.618	1.237
0.5	0.790	1.557	1.836	1.932	1.970	1.908	1.621	1.234
0.5	0.790	1.559	1.836	1.925	1.967	1.910	1.621	1.233
0.2	0.733	1.545	1.806	1.877	1.933	1.864	1.615	1.209
0.2	0.000	1.470	1.676	1.635	1.750	1.641	1.569	1.082

N_LOAD (MPa)	Q (ml/sec.)	Port 15 PTRANS.2 (metres)	Port 12 PTRANS.4 (metres)	Port 8 PTRANS.5 (metres)	Port 17 PTRANS.6 (metres)	Port 10 PTRANS.7 (metres)	Port 11 PTRANS.8 (metres)
0.2	0.749	1.585	1.581	2.055	1.780	1.665	1.593
0.2	0.799	1.597	1.589	2.057	1.779	1.668	1.601
0.2	0.796	1.595	1.597	2.050	1.783	1.668	1.602
0.2	0.749	1.587	1.596	2.036	1.766	1.658	1.592
0.2	0.780	1.592	1.599	2.035	1.771	1.664	1.603
0.2	0.749	1.578	1.602	2.023	1.763	1.658	1.593
0.2	0.749	1.576	1.599	2.028	1.764	1.655	1.591
0.5	0.778	1.595	1.589	2.054	1.780	1.668	1.610
0.5	0.755	1.592	1.594	2.034	1.773	1.661	1.602
0.5	0.748	1.590	1.577	1.934	1.649	1.661	1.605
0.5	0.780	1.582	1.592	2.051	1.783	1.667	1.613
0.5	0.766	1.594	1.596	2.054	1.781	1.667	1.612

1	0.797	1.606	1.597	2.080	1.794	1.677	1.623
1	0.798	1.596	1.599	2.078	1.797	1.676	1.630
1	0.747	1.596	1.594	2.073	1.779	1.667	1.617
1	0.746	1.599	1.592	2.064	1.783	1.667	1.617
1	0.741	1.587	1.580	2.135	1.806	1.663	1.605
1	0.748	1.585	1.578	2.139	1.804	1.663	1.598
2	0.748	1.590	1.580	2.126	1.796	1.672	1.612
2	0.749	1.590	1.573	2.125	1.791	1.672	1.613
2	0.743	1.814	1.712	2.513	2.188	1.919	1.926
2	0.795	1.830	1.711	2.527	2.210	1.925	1.958
2	0.747	1.781	1.701	2.412	2.119	1.876	1.896
2	0.815	1.603	1.589	2.043	1.815	1.698	1.633
2	0.794	1.602	1.594	2.071	1.811	1.696	1.637
2	0.740	1.592	1.587	2.035	1.783	1.686	1.624
2	0.741	1.594	1.597	2.014	1.780	1.685	1.619
2	0.785	1.599	1.592	2.035	1.791	1.695	1.636
4	0.791	1.609	1.602	2.034	1.809	1.697	1.636
4	0.799	1.604	1.595	2.037	1.799	1.700	1.636
4	0.740	1.604	1.590	2.011	1.784	1.691	1.626
4	0.740	1.606	1.592	2.006	1.782	1.688	1.623
4	0.782	1.604	1.604	2.025	1.793	1.700	1.628
4	0.787	1.607	1.597	2.037	1.796	1.700	1.622
6	0.791	1.610	1.601	2.034	1.807	1.704	1.632
6	0.799	1.606	1.597	2.033	1.806	1.703	1.623
6	0.744	1.606	1.594	2.014	1.789	1.695	1.614
6	0.747	1.609	1.590	2.008	1.789	1.694	1.614
6	0.796	1.620	1.595	2.036	1.803	1.706	1.626
6	0.796	1.607	1.595	2.029	1.801	1.702	1.618
6	0.730	1.816	1.705	2.257	2.183	1.919	1.856
6	0.730	1.789	1.690	2.207	2.126	1.870	1.810
6	0.777	1.787	1.701	2.187	2.082	1.870	1.797
6	0.730	1.753	1.695	2.120	2.025	1.836	1.760
6	0.729	1.748	1.687	2.126	2.009	1.833	1.747
6	0.780	1.751	1.688	2.161	2.027	1.843	1.760
6	0.732	1.729	1.688	2.150	2.006	1.834	1.743
6	0.714	1.718	1.689	2.159	1.994	1.828	1.732
8	0.716	1.730	1.697	2.162	2.000	1.831	1.728
8	0.777	1.781	1.720	2.201	2.034	1.864	1.775
8	0.783	1.741	1.710	2.185	2.018	1.849	1.757
10	0.730	1.638	1.600	2.093	1.893	1.745	1.631
10	0.786	1.677	1.615	2.164	1.954	1.782	1.675
10	0.731	1.634	1.592	1.990	1.878	1.730	1.596
10	0.732	1.643	1.594	1.995	1.897	1.730	1.593
10	0.731	1.634	1.589	1.996	1.887	1.727	1.579
10	0.783	1.656	1.592	2.024	1.915	1.743	1.600
10	0.790	1.662	1.581	2.216	2.015	1.761	1.565
10	0.792	1.661	1.561	2.210	2.004	1.755	1.551
10	0.729	1.645	1.516	2.182	1.979	1.740	1.503
8	0.805	1.654	1.480	2.189	1.998	1.746	1.503
8	0.796	1.627	1.565	2.136	1.964	1.727	1.447
8	0.807	1.630	1.565	2.157	1.958	1.724	1.439
6	0.729	1.606	1.576	2.110	1.912	1.712	1.389
6	0.749	1.608	1.581	2.103	1.906	1.709	1.403
6	0.800	1.619	1.596	2.112	1.914	1.724	1.409

6	0.740	1.619	1.639	2.119	1.911	1.715	1.363
6	0.748	1.620	1.651	2.118	1.911	1.718	1.370
4	0.745	1.607	1.661	2.075	1.888	1.712	1.346
4	0.757	1.604	1.652	2.060	1.877	1.712	1.338
2	0.739	1.599	1.645	2.020	1.854	1.703	1.313
2	0.745	1.582	1.635	2.012	1.844	1.703	1.306
1	0.748	1.579	1.666	1.991	1.828	1.691	1.274
1	0.733	1.569	1.662	1.982	1.821	1.691	1.267
1	0.746	1.571	1.666	2.007	1.843	1.685	1.237
0.5	0.790	1.571	1.675	1.998	1.840	1.688	1.234
0.5	0.790	1.571	1.665	2.000	1.838	1.685	1.229
0.2	0.733	1.546	1.667	1.955	1.807	1.667	1.206
0.2	0.000	1.468	1.637	1.761	1.643	1.569	1.079

Table B2-4 Flow Data, Shear Cycle 1

N_LOAD (MPa)	S_LOAD (MPa)	Q (ml/sec.)	Port 13 PTRANS.2 (metres)	Port16 PTRANS.3 (metres)	Port7 PTRANS.4 (metres)	Port 4 PTRANS.5 (metres)	Port 6 PTRANS.6 (metres)	Port 2 PTRANS.7 (metres)	Port 1 PTRANS.8 (metres)
0.2	0.0	0.714	1.694	1.753	2.084	2.006	2.188	1.723	1.898
0.2	0.0	0.731	1.679	1.909	2.015	1.997	2.120	1.714	1.886
0.2	0.0	0.732	1.673	1.879	1.982	1.985	2.089	1.714	1.888
0.2	0.0	0.731	1.660	1.873	1.962	1.971	2.070	1.714	1.865
0.2	0.0	0.731	1.673	1.890	1.956	1.979	2.062	1.721	1.868
0.2	0.0	0.715	1.666	1.885	1.939	1.969	2.043	1.713	1.859
0.2	0.0	0.742	1.653	1.859	1.933	1.965	2.030	1.710	1.850
0.2	0.0	0.714	1.649	1.865	1.916	1.955	2.012	1.703	1.841
0.5	0.0	0.731	1.645	1.856	1.923	1.969	2.016	1.693	1.836
0.5	0.0	0.731	1.647	1.851	1.925	1.962	2.011	1.696	1.831
0.5	0.0	0.728	1.628	1.840	1.899	1.962	2.004	1.689	1.827
0.5	0.0	0.731	1.634	1.826	1.905	1.970	1.991	1.689	1.818
1.0	0.0	0.732	1.639	1.827	1.938	1.970	2.005	1.685	1.826
1.0	0.0	0.732	1.627	1.836	1.921	1.965	1.992	1.676	1.807
1.0	0.0	0.725	1.625	1.836	1.919	1.976	1.988	1.673	1.805
1.0	0.0	0.729	1.629	1.847	1.919	1.988	1.997	1.682	1.812
2.0	0.0	0.716	1.630	1.854	1.936	1.994	2.003	1.683	1.819
2.0	0.0	0.725	1.635	1.837	1.929	2.003	2.001	1.681	1.820
2.0	0.0	0.726	1.638	1.838	1.947	2.021	2.011	1.685	1.822
2.0	0.0	0.729	1.639	1.862	1.940	2.024	2.006	1.676	1.823
2.0	0.0	0.720	1.636	1.853	1.939	2.010	2.013	1.676	1.828
2.0	0.0	0.713	1.596	1.828	1.930	2.183	1.994	1.624	1.839
2.0	0.0	0.722	1.581	1.812	1.919	2.169	1.984	1.623	1.835
2.0	0.0	0.725	1.576	1.818	1.903	2.170	1.975	1.618	1.833
2.0	0.0	0.774	1.589	1.808	1.911	2.164	1.967	1.617	1.825
2.0	0.3	0.716	1.590	1.809	1.882	2.159	1.963	1.629	1.826
2.0	0.3	0.729	1.589	1.789	1.898	2.165	1.955	1.624	1.827
2.0	0.3	0.730	1.582	1.793	1.891	2.168	1.957	1.624	1.813
2.0	0.5	0.730	1.585	1.789	1.869	2.148	1.949	1.623	1.811
2.0	0.5	0.730	1.580	1.800	1.873	2.140	1.940	1.623	1.808
2.0	0.5	0.729	1.572	1.780	1.866	2.127	1.929	1.623	1.805
2.0	0.8	0.728	1.581	1.780	1.866	2.127	1.931	1.617	1.810
2.0	0.8	0.723	1.576	1.780	1.866	2.127	1.932	1.614	1.812
2.0	0.8	0.732	1.578	1.795	1.860	2.130	1.932	1.616	1.815
2.0	1.0	0.731	1.584	1.780	1.865	2.127	1.937	1.616	1.818
2.0	1.0	0.730	1.582	1.780	1.861	2.135	1.931	1.619	1.824
2.0	1.0	0.712	1.583	1.775	1.867	2.129	1.934	1.616	1.816
2.0	1.0	0.732	1.579	1.775	1.870	2.133	1.932	1.616	1.827
2.0	1.3	0.727	1.586	1.750	1.866	2.140	1.930	1.616	1.827
2.0	1.3	0.732	1.578	1.744	1.867	2.136	1.937	1.617	1.830
2.0	1.3	0.732	1.596	1.780	1.850	2.187	1.951	1.614	1.849
2.0	1.3	0.729	1.593	1.779	1.845	2.176	1.947	1.609	1.851
2.0	1.0	0.728	1.576	1.774	1.864	2.172	1.944	1.612	1.846
2.0	1.0	0.731	1.583	1.780	1.871	2.169	1.946	1.609	1.856
2.0	1.0	0.723	1.585	1.795	1.854	2.150	1.935	1.614	1.859
2.0	0.5	0.732	1.582	1.765	1.869	2.152	1.934	1.610	1.865
2.0	0.5	0.746	1.590	1.770	1.869	2.159	1.934	1.616	1.863
2.0	0.0	0.731	1.586	1.770	1.861	2.164	1.934	1.609	1.876
1.0	0.0	0.735	1.582	1.748	1.851	2.169	1.933	1.612	1.946
0.5	0.0	0.723	1.578	1.729	1.824	2.161	1.917	1.608	1.938

Table B2-4 Flow Data, Shear Cycle 1 (Continued)

N_LOAD (MPa)	S_LOAD (MPa)	Q (ml/sec.)	Port 15 PTRANS.2 (metres)	Port 12 PTRANS.4 (metres)	Port 8 PTRANS.5 (metres)	Port 17 PTRANS.6 (metres)	Port 10 PTRANS.7 (metres)	Port 11 PTRANS.8 (metres)
0.2	0.0	0.714	1.741	1.690	2.421	2.087	1.821	1.924
0.2	0.0	0.731	1.714	1.685	2.354	2.040	1.796	1.900
0.2	0.0	0.732	1.703	1.682	2.335	2.022	1.790	1.895
0.2	0.0	0.731	1.685	1.688	2.305	2.001	1.781	1.880
0.2	0.0	0.731	1.703	1.690	2.307	2.001	1.794	1.892
0.2	0.0	0.715	1.690	1.682	2.291	1.984	1.780	1.874
0.2	0.0	0.742	1.669	1.688	2.271	1.969	1.771	1.861
0.2	0.0	0.714	1.666	1.677	2.248	1.952	1.758	1.851
0.5	0.0	0.731	1.665	1.663	2.258	1.952	1.760	1.846
0.5	0.0	0.731	1.659	1.665	2.242	1.944	1.757	1.832
0.5	0.0	0.728	1.646	1.652	2.240	1.936	1.753	1.837
0.5	0.0	0.731	1.647	1.654	2.232	1.926	1.747	1.827
1.0	0.0	0.732	1.660	1.663	2.233	1.933	1.749	1.833
1.0	0.0	0.732	1.650	1.652	2.221	1.924	1.743	1.812
1.0	0.0	0.725	1.647	1.654	2.223	1.920	1.743	1.815
1.0	0.0	0.729	1.651	1.653	2.229	1.924	1.746	1.816
2.0	0.0	0.716	1.658	1.654	2.236	1.932	1.756	1.827
2.0	0.0	0.725	1.660	1.657	2.236	1.928	1.754	1.832
2.0	0.0	0.726	1.666	1.658	2.243	1.936	1.759	1.838
2.0	0.0	0.729	1.665	1.654	2.245	1.934	1.761	1.837
2.0	0.0	0.720	1.664	1.655	2.241	1.936	1.761	1.831
2.0	0.0	0.713	1.623	1.598	2.205	1.918	1.715	1.847
2.0	0.0	0.722	1.608	1.593	2.195	1.910	1.708	1.843
2.0	0.0	0.725	1.602	1.594	2.195	1.901	1.703	1.840
2.0	0.0	0.774	1.613	1.591	2.183	1.897	1.703	1.834
2.0	0.3	0.716	1.615	1.599	2.179	1.891	1.705	1.836
2.0	0.3	0.729	1.614	1.607	2.186	1.887	1.703	1.834
2.0	0.3	0.730	1.604	1.602	2.182	1.894	1.703	1.825
2.0	0.5	0.730	1.608	1.593	2.170	1.873	1.696	1.822
2.0	0.5	0.730	1.603	1.603	2.163	1.871	1.696	1.815
2.0	0.5	0.729	1.599	1.589	2.152	1.863	1.690	1.812
2.0	0.8	0.728	1.608	1.593	2.153	1.867	1.693	1.822
2.0	0.8	0.723	1.603	1.590	2.143	1.856	1.688	1.815
2.0	0.8	0.732	1.602	1.593	2.146	1.862	1.690	1.815
2.0	1.0	0.731	1.606	1.590	2.153	1.862	1.689	1.830
2.0	1.0	0.730	1.599	1.593	2.145	1.851	1.686	1.825
2.0	1.0	0.712	1.602	1.597	2.148	1.858	1.689	1.827
2.0	1.0	0.732	1.605	1.594	2.156	1.864	1.690	1.833
2.0	1.3	0.727	1.606	1.596	2.148	1.857	1.689	1.832
2.0	1.3	0.732	1.598	1.602	2.142	1.856	1.690	1.836
2.0	1.3	0.732	1.608	1.590	2.203	1.877	1.681	1.852
2.0	1.3	0.729	1.604	1.590	2.194	1.874	1.679	1.859
2.0	1.0	0.728	1.598	1.590	2.191	1.868	1.679	1.863
2.0	1.0	0.731	1.601	1.591	2.194	1.869	1.679	1.859
2.0	1.0	0.723	1.606	1.593	2.176	1.865	1.684	1.870
2.0	0.5	0.732	1.598	1.600	2.176	1.861	1.680	1.875
2.0	0.5	0.746	1.605	1.596	2.175	1.858	1.680	1.876
2.0	0.0	0.731	1.609	1.592	2.185	1.860	1.679	1.884
1.0	0.0	0.735	1.607	1.592	2.190	1.857	1.679	1.948
0.5	0.0	0.723	1.592	1.583	2.183	1.849	1.669	1.946

Table B2-5 Flow Data, Shear Cycle 2

N_LOAD (MPa)	S_LOAD (MPa)	Q (ml/sec.)	Port 13 PTRANS.2 (metres)	Port16 PTRANS.3 (metres)	Port7 PTRANS.4 (metres)	Port 4 PTRANS.5 (metres)	Port 6 PTRANS.6 (metres)	Port 2 PTRANS.7 (metres)	Port 1 PTRANS.8 (metres)
0.2	0	0.731	1.690	1.871	1.940	2.362	2.043	1.697	2.003
0.2	0	0.724	1.714	1.875	1.947	2.388	2.052	1.708	2.016
0.2	0	0.733	1.701	1.880	1.946	2.388	2.061	1.704	2.017
0.2	0	0.740	1.693	1.886	1.948	2.388	2.058	1.698	2.013
0.2	0	0.747	1.696	1.887	1.945	2.380	2.047	1.698	2.006
0.2	0	0.728	1.699	1.872	1.934	2.379	2.039	1.698	1.987
0.5	0	0.749	1.697	1.872	1.951	2.378	2.046	1.689	1.977
0.5	0	0.733	1.674	1.851	1.929	2.354	2.032	1.680	1.968
0.5	0	0.749	1.668	1.837	1.935	2.352	2.023	1.677	1.952
0.5	0	0.719	1.665	1.838	1.909	2.333	2.004	1.652	1.921
0.5	0	0.731	1.661	1.832	1.905	2.331	1.998	1.720	1.901
0.5	0	0.755	1.651	1.840	1.910	2.333	1.999	1.667	1.897
0.5	0	0.747	1.658	1.839	1.897	2.327	1.993	1.661	1.880
0.5	0	0.738	1.652	1.828	1.887	2.315	1.984	1.658	1.871
0.5	0	0.736	1.644	1.829	1.881	2.313	1.980	1.649	1.855
0.5	0	0.731	1.645	1.829	1.881	2.307	1.972	1.649	1.839
1	0	0.743	1.623	1.823	1.907	2.318	1.993	1.643	1.800
1	0	0.732	1.627	1.829	1.931	2.319	1.990	1.640	1.792
1	0	0.732	1.623	1.819	1.885	2.299	1.972	1.637	1.772
1	0	0.733	1.626	1.819	1.877	2.297	1.968	1.632	1.763
1	0	0.734	1.621	1.820	1.886	2.294	1.967	1.634	1.748
1	0	0.732	1.606	1.813	1.888	2.294	1.968	1.631	1.731
1	0	0.731	1.603	1.813	1.879	2.286	1.966	1.631	1.722
1	0	0.731	1.615	1.809	1.877	2.284	1.959	1.631	1.712
2	0	0.725	1.606	1.810	1.906	2.281	1.974	1.627	1.632
2	0	0.747	1.602	1.810	1.903	2.270	1.972	1.626	1.618
2	0	0.733	1.591	1.804	1.899	2.272	1.972	1.624	1.612
2	0	0.718	1.677	1.993	2.136	2.481	2.239	1.689	1.682
2	0	0.742	1.685	2.013	2.134	2.488	2.232	1.715	1.702
2	0	0.715	1.699	2.009	2.118	2.487	2.206	1.716	1.675
2	0	0.712	1.700	2.009	2.110	2.478	2.196	1.719	1.659
2	0	0.712	1.740	2.034	2.137	2.476	2.198	1.753	1.685
2	0	0.713	1.697	2.000	2.099	2.464	2.179	1.732	1.662
2	0	0.721	1.718	1.994	2.095	2.463	2.165	1.736	1.648
2	0	0.722	1.680	1.963	2.076	2.459	2.156	1.725	1.642
5	0	0.730	1.630	1.903	2.053	2.392	2.105	1.675	1.586
5	0	0.714	1.686	1.980	2.103	2.437	2.155	1.722	1.634
5	0	0.730	1.694	1.974	2.093	2.431	2.153	1.727	1.626
5	0	0.723	1.683	1.968	2.088	2.412	2.143	1.719	1.627
5	0	0.724	1.383	1.858	1.986	2.325	2.044	1.616	1.556
5	0	0.730	1.403	1.863	1.999	2.346	2.065	1.619	1.579
5	0	0.731	1.402	1.858	1.975	2.352	2.066	1.619	1.582
5	0	0.716	1.499	1.799	1.990	2.137	2.026	1.620	1.805
5	0	0.732	1.520	1.813	2.012	2.138	2.035	1.628	1.828
5	0	0.739	1.514	1.810	1.999	2.121	2.027	1.618	1.826
5	0	0.725	1.664	1.871	2.151	2.154	2.159	1.643	1.931
5	0	0.730	1.667	1.881	2.135	2.143	2.146	1.642	1.930
5	0	0.727	1.664	1.861	2.114	2.135	2.133	1.641	1.919
5	0	0.715	1.669	1.871	2.088	2.121	2.112	1.641	1.909
5	0	0.730	1.669	1.866	2.095	2.116	2.115	1.659	1.918

5	0	0.741	1.677	1.875	2.085	2.115	2.117	1.668	1.924
5	0	0.725	1.673	1.865	2.089	2.100	2.108	1.664	1.908
5	0	0.729	1.686	1.861	2.092	2.095	2.105	1.663	1.914
5	0	0.730	1.676	1.875	2.098	2.100	2.112	1.672	1.918
5	0	0.733	1.711	1.892	2.116	2.114	2.119	1.688	1.953
5	0	0.747	1.709	1.895	2.120	2.118	2.133	1.696	1.938
5	0	0.736	1.712	1.897	2.115	2.113	2.129	1.689	1.929
5	0	0.731	1.712	1.892	2.105	2.101	2.118	1.684	1.926
5	0.5	0.731	1.710	1.903	2.120	2.107	2.125	1.687	1.930
5	0.5	0.735	1.714	1.903	2.138	2.113	2.130	1.700	1.941
5	0.5	0.731	1.716	1.902	2.115	2.112	2.127	1.703	1.942
5	0.5	0.735	1.702	1.896	2.120	2.102	2.124	1.702	1.944
5	0.5	0.734	1.701	1.903	2.115	2.098	2.122	1.703	1.943
5	0.5	0.734	1.714	1.893	2.220	2.101	2.118	1.700	1.939
5	0.5	0.730	1.711	1.897	2.110	2.101	2.127	1.711	1.931
5	0.5	0.732	1.723	1.918	2.112	2.097	2.126	1.713	1.953
5	1	0.716	1.703	1.901	2.109	2.085	2.114	1.708	1.946
5	1	0.723	1.720	1.897	2.111	2.083	2.114	1.707	1.944
5	1	0.714	1.714	1.902	2.107	2.084	2.110	1.707	1.950
5	1.5	0.713	1.697	1.872	2.113	2.063	2.105	1.703	1.946
5	1.5	0.716	1.701	1.898	2.105	2.060	2.102	1.698	1.946
5	1.5	0.713	1.706	1.893	2.103	2.058	2.098	1.693	1.943
5	2	0.723	1.708	1.898	2.145	2.065	2.115	1.699	1.957
5	2	0.714	1.700	1.889	2.122	2.058	2.107	1.694	1.953
5	2	0.713	1.692	1.892	2.116	2.048	2.103	1.695	1.956
5	2	0.727	1.699	1.909	2.131	2.053	2.102	1.694	1.953
5	2.5	0.715	1.688	1.899	2.154	2.024	2.112	1.670	1.962
5	2.5	0.714	1.677	1.882	2.155	2.014	2.105	1.669	1.957
5	2.5	0.731	1.690	1.894	2.170	2.023	2.114	1.679	1.970
5	2.5	0.716	1.641	1.850	2.102	1.962	2.062	1.621	1.921
5	2.5	0.731	1.641	1.840	2.106	1.963	2.053	1.620	1.922
5	2.5	0.715	1.630	1.833	2.102	1.960	2.058	1.621	1.931
5	1.5	0.715	1.640	1.839	2.099	1.950	2.054	1.621	1.924
5	1.5	0.723	1.647	1.849	2.112	1.953	2.062	1.620	1.926
5	1.5	0.722	1.639	1.838	2.101	1.951	2.051	1.619	1.914
5	0	0.715	1.637	1.839	2.119	1.955	2.057	1.619	1.929
5	0	0.722	1.645	1.839	2.101	1.947	2.056	1.619	1.927
5	0	0.733	1.642	1.848	2.109	1.950	2.060	1.619	1.931
5	0	0.714	1.664	1.868	2.143	2.021	2.128	1.623	1.950
5	0	0.714	1.649	1.855	2.138	2.010	2.115	1.619	1.945
2.5	0	0.714	1.682	1.872	2.138	2.027	2.126	1.644	1.957
0.2	0	0.713	1.675	1.826	2.008	1.964	2.034	1.649	1.922

N_LOAD (MPa)	S_LOAD (MPa)	Q (ml/sec.)	Port 15 PTRANS.2 (metres)	Port 12 PTRANS.4 (metres)	Port 8 PTRANS.5 (metres)	Port 17 PTRANS.6 (metres)	Port 10 PTRANS.7 (metres)	Port 11 PTRANS.8 (metres)
0.2	0	0.731	1.730	1.698	2.428	1.977	1.758	2.011
0.2	0	0.724	1.742	1.695	2.435	1.982	1.763	2.016
0.2	0	0.733	1.721	1.689	2.437	1.984	1.762	2.014
0.2	0	0.740	1.725	1.681	2.426	1.981	1.756	2.008
0.2	0	0.747	1.729	1.679	2.415	1.970	1.750	1.997
0.2	0	0.728	1.724	1.674	2.402	1.965	1.750	1.993
0.5	0	0.749	1.720	1.669	2.416	1.964	1.750	1.981
0.5	0	0.733	1.696	1.671	2.397	1.949	1.740	1.977

0.5	0	0.749	1.691	1.663	2.385	1.941	1.735	1.961
0.5	0	0.719	1.686	1.656	2.364	1.930	1.725	1.931
0.5	0	0.731	1.687	1.659	2.364	1.924	1.729	1.915
0.5	0	0.755	1.671	1.649	2.358	1.923	1.724	1.906
0.5	0	0.747	1.676	1.647	2.351	1.914	1.722	1.887
0.5	0	0.738	1.667	1.638	2.346	1.907	1.716	1.878
0.5	0	0.736	1.663	1.637	2.342	1.905	1.713	1.861
0.5	0	0.731	1.658	1.633	2.334	1.900	1.707	1.838
1	0	0.743	1.645	1.628	2.335	1.899	1.707	1.802
1	0	0.732	1.649	1.631	2.337	1.898	1.704	1.794
1	0	0.732	1.643	1.629	2.330	1.891	1.701	1.781
1	0	0.733	1.645	1.618	2.329	1.888	1.696	1.766
1	0	0.734	1.643	1.620	2.325	1.887	1.698	1.752
1	0	0.732	1.630	1.622	2.322	1.889	1.698	1.741
1	0	0.731	1.626	1.619	2.317	1.881	1.695	1.730
1	0	0.731	1.634	1.618	2.315	1.880	1.695	1.716
2	0	0.725	1.630	1.613	2.312	1.887	1.697	1.640
2	0	0.747	1.628	1.625	2.307	1.883	1.696	1.629
2	0	0.733	1.616	1.614	2.311	1.884	1.694	1.620
2	0	0.718	1.753	1.672	2.253	2.138	1.844	1.710
2	0	0.742	1.740	1.693	2.243	2.126	1.840	1.686
2	0	0.715	1.763	1.692	2.214	2.107	1.835	1.673
2	0	0.712	1.755	1.698	2.227	2.104	1.838	1.666
2	0	0.712	1.770	1.729	2.241	2.117	1.863	1.683
2	0	0.713	1.750	1.710	2.210	2.095	1.845	1.663
2	0	0.721	1.760	1.731	2.198	2.084	1.843	1.658
2	0	0.722	1.705	1.706	2.181	2.064	1.826	1.652
5	0	0.730	1.669	1.658	2.189	2.011	1.788	1.596
5	0	0.714	1.711	1.708	2.234	2.057	1.832	1.638
5	0	0.730	1.711	1.703	2.231	2.051	1.834	1.630
5	0	0.723	1.706	1.699	2.221	2.044	1.828	1.629
5	0	0.724	1.613	1.612	2.142	1.945	1.723	1.585
5	0	0.730	1.598	1.597	2.165	1.958	1.722	1.591
5	0	0.731	1.599	1.588	2.170	1.963	1.719	1.604
5	0	0.716	1.648	1.621	1.992	1.923	1.718	1.847
5	0	0.732	1.642	1.630	1.991	1.925	1.722	1.859
5	0	0.739	1.651	1.614	1.988	1.922	1.713	1.853
5	0	0.725	1.729	1.628	1.701	2.025	1.762	1.996
5	0	0.730	1.726	1.629	1.686	2.015	1.764	1.976
5	0	0.727	1.709	1.628	1.679	1.993	1.754	1.959
5	0	0.715	1.734	1.628	1.683	1.986	1.754	1.958
5	0	0.730	1.690	1.644	1.703	1.989	1.769	1.954
5	0	0.741	1.733	1.661	1.694	1.994	1.775	1.955
5	0	0.725	1.713	1.651	1.707	1.992	1.770	1.942
5	0	0.729	1.724	1.655	1.702	1.990	1.773	1.953
5	0	0.730	1.671	1.670	1.707	1.988	1.779	1.952
5	0	0.733	1.718	1.678	1.735	2.011	1.797	1.968
5	0	0.747	1.709	1.687	1.739	2.013	1.802	1.969
5	0	0.736	1.712	1.688	1.746	2.011	1.799	1.969
5	0	0.731	1.740	1.672	1.743	2.004	1.794	1.961
5	0.5	0.731	1.702	1.684	1.754	2.000	1.800	1.962
5	0.5	0.735	1.746	1.692	1.769	2.011	1.807	1.969
5	0.5	0.731	1.750	1.694	1.782	2.012	1.809	1.974
5	0.5	0.735	1.709	1.698	1.772	2.007	1.808	1.976
5	0.5	0.734	1.703	1.699	1.778	2.006	1.807	1.977
5	0.5	0.734	1.710	1.700	1.795	1.999	1.804	1.965

5	0.5	0.730	1.707	1.698	1.802	2.006	1.811	1.957
5	0.5	0.732	1.741	1.701	1.807	2.006	1.814	1.978
5	1	0.716	1.700	1.693	1.812	2.000	1.808	1.976
5	1	0.723	1.711	1.690	1.818	1.999	1.808	1.980
5	1	0.714	1.731	1.691	1.814	1.992	1.808	1.979
5	1.5	0.713	1.714	1.687	1.807	1.986	1.801	1.972
5	1.5	0.716	1.727	1.686	1.822	1.982	1.799	1.979
5	1.5	0.713	1.706	1.686	1.813	1.979	1.794	1.972
5	2	0.723	1.731	1.705	1.844	1.992	1.806	1.985
5	2	0.714	1.705	1.689	1.831	1.982	1.797	1.978
5	2	0.713	1.685	1.684	1.845	1.980	1.796	1.982
5	2	0.727	1.749	1.692	1.855	1.980	1.800	1.985
5	2.5	0.715	1.728	1.655	1.882	1.971	1.786	1.983
5	2.5	0.714	1.727	1.672	1.875	1.972	1.788	1.990
5	2.5	0.731	1.733	1.681	1.894	1.980	1.798	2.000
5	2.5	0.716	1.686	1.598	2.007	1.916	1.734	1.943
5	2.5	0.731	1.682	1.598	2.007	1.916	1.733	1.940
5	2.5	0.715	1.671	1.596	2.005	1.918	1.737	1.949
5	1.5	0.715	1.675	1.598	1.995	1.919	1.737	1.943
5	1.5	0.723	1.675	1.601	2.001	1.922	1.735	1.943
5	1.5	0.722	1.672	1.587	1.997	1.913	1.732	1.929
5	0	0.715	1.669	1.599	1.996	1.915	1.735	1.943
5	0	0.722	1.690	1.594	2.005	1.920	1.735	1.945
5	0	0.733	1.684	1.603	2.003	1.918	1.738	1.948
5	0	0.714	1.582	1.596	2.075	1.977	1.748	1.972
5	0	0.714	1.583	1.590	2.061	1.968	1.747	1.979
2.5	0	0.714	1.729	1.629	2.082	2.001	1.781	2.016
0.2	0	0.713	1.670	1.631	1.982	1.932	1.732	1.953

Table B2-6 Flow Data, Shear Cycle 3a

N_LOAD (MPa)	S_LOAD (MPa)	Q (ml/sec.)	Port 13 PTRANS.2 (metres)	Port16 PTRANS.3 (metres)	Port7 PTRANS.4 (metres)	Port 4 PTRANS.5 (metres)	Port 6 PTRANS.6 (metres)	Port 2 PTRANS.7 (metres)	Port 1 PTRANS.8 (metres)
0.2	0	0.731	1.623	1.768	1.924	1.859	1.975	1.620	1.638
0.2	0	0.736	1.600	1.742	1.907	1.839	1.960	1.606	1.628
0.2	0	0.723	1.609	1.739	1.902	1.839	1.960	1.605	1.627
0.2	0	0.713	1.610	1.739	1.900	1.837	1.954	1.605	1.625
0.2	0	0.728	1.598	1.742	1.900	1.835	1.953	1.604	1.621
0.5	0	0.725	1.611	1.760	1.981	1.858	2.005	1.608	1.644
0.5	0	0.732	1.609	1.760	1.982	1.857	2.005	1.610	1.638
0.5	0	0.728	1.619	1.760	1.981	1.856	2.005	1.607	1.637
0.5	0	0.733	1.604	1.753	1.991	1.863	2.004	1.616	1.659
1	0	0.718	1.628	1.791	2.062	1.896	2.048	1.613	1.668
1	0	0.731	1.621	1.786	2.037	1.880	2.036	1.615	1.671
1	0	0.732	1.619	1.784	2.051	1.885	2.050	1.613	1.690
1	0	0.738	1.623	1.791	2.048	1.882	2.045	1.613	1.677
2.5	0	0.731	1.646	1.812	2.136	1.924	2.087	1.618	1.730
2.5	0	0.731	1.628	1.804	2.129	1.915	2.085	1.615	1.710
2.5	0	0.714	1.639	1.802	2.118	1.913	2.090	1.616	1.715
2.5	0	0.731	1.630	1.816	2.135	1.915	2.090	1.620	1.715
5	0	0.737	1.653	1.843	2.249	1.952	2.132	1.620	1.738
5	0	0.729	1.650	1.858	2.255	1.963	2.149	1.619	1.745
5	0	0.722	1.647	1.828	2.254	1.952	2.144	1.619	1.744
5	0	0.724	1.652	1.843	2.258	1.953	2.150	1.619	1.748
7.5	0	0.746	1.669	1.874	2.414	1.995	2.251	1.629	1.784
7.5	0	0.717	1.657	1.878	2.416	1.995	2.221	1.625	1.774
7.5	0	0.716	1.662	1.873	2.419	1.998	2.225	1.625	1.770
7.5	0	0.724	1.652	1.882	2.436	2.004	2.236	1.625	1.777
7.5	0	0.734	1.670	1.883	2.434	2.009	2.247	1.625	1.785
10	0	0.714	1.666	1.913	2.576	2.041	2.298	1.629	1.806
10	0	0.726	1.681	1.908	2.611	2.053	2.308	1.628	1.835
10	0	0.735	1.677	1.922	2.661	2.067	2.332	1.633	1.831
10	0	0.726	1.687	1.929	2.684	2.066	2.327	1.632	1.830
10	0	0.717	1.692	1.929	2.647	2.069	2.330	1.630	1.832
10	0	0.733	1.693	1.919	2.743	2.104	2.369	1.635	1.849
10	0	0.744	1.688	1.933	2.693	2.081	2.342	1.635	1.849
10	0	0.712	1.678	1.922	2.688	2.079	2.339	1.631	1.846
10	0	0.715	1.691	1.939	2.687	2.082	2.337	1.631	1.842
10	0	0.716	1.687	1.928	2.692	2.080	2.341	1.630	1.848
10	0	0.738	1.856	2.180	2.842	2.353	2.597	1.747	2.167
10	0	0.719	1.863	2.165	2.849	2.341	2.586	1.751	2.155
10	0	0.710	1.814	2.150	2.821	2.333	2.564	1.726	2.135
10	0	0.732	1.811	2.138	2.803	2.311	2.552	1.729	2.121
10	1	0.717	1.819	2.100	2.774	2.276	2.511	1.720	2.083
10	1	0.716	1.812	2.109	2.794	2.287	2.521	1.716	2.100
10	1	0.724	1.819	2.084	2.769	2.261	2.494	1.706	2.075
10	3	0.717	1.808	2.102	2.870	2.304	2.549	1.702	2.112
10	3	0.712	1.791	2.101	2.842	2.291	2.534	1.691	2.092
10	3	0.715	1.808	2.100	2.868	2.297	2.545	1.696	2.089
10	3	0.708	1.841	2.316	3.408	2.553	2.890	1.680	2.282
10	3	0.714	1.866	2.336	3.440	2.558	2.915	1.688	2.301
10	3	0.715	1.841	2.343	3.458	2.574	2.937	1.694	2.319
10	5	0.690	1.883	2.372	3.432	2.639	3.022	1.694	2.373
10	5	0.698	1.870	2.394	3.471	2.662	3.052	1.701	2.398

10	6	0.664	2.021	2.847	4.297	3.181	3.783	1.652	2.862
10	6	0.681	2.101	2.979	4.538	3.341	3.980	1.648	2.997
10	6	0.681	2.164	3.109	4.673	3.464	4.114	1.664	3.113
10	6	0.674	2.270	3.233	4.907	3.610	4.303	1.673	3.231
10	6	0.683	2.294	3.284	4.981	3.674	4.376	1.665	3.279
10	6.4	0.632	2.325	3.792	5.731	4.239	5.046	1.635	3.782
10	6.8	0.615	2.444	4.557	6.737	5.063	5.970	1.635	4.556
10	7	0.565	3.100	5.007	7.295	5.532	6.435	1.654	5.039
10	7.2	0.500	3.429	2.348	8.006	6.182	7.064	1.654	5.761
10	7.2	0.500	3.417	2.338	8.025	6.256	7.247	1.654	5.545
10	7.4	0.500	3.625	6.018	8.351	6.569	7.474	1.654	6.120

N_LOAD (MPa)	S_LOAD (MPa)	Q (ml/sec.)	Port 15 PTRANS.2 (metres)	Port 12 PTRANS.4 (metres)	Port 8 PTRANS.5 (metres)	Port 17 PTRANS.6 (metres)	Port 10 PTRANS.7 (metres)	Port 11 PTRANS.8 (metres)
0.2	0	0.731	1.647	1.608	1.909	1.897	1.702	1.668
0.2	0	0.736	1.617	1.592	1.889	1.878	1.685	1.655
0.2	0	0.723	1.623	1.593	1.890	1.877	1.685	1.659
0.2	0	0.713	1.629	1.593	1.886	1.874	1.681	1.653
0.2	0	0.728	1.615	1.592	1.882	1.870	1.680	1.649
0.5	0	0.725	1.633	1.591	1.920	1.902	1.699	1.671
0.5	0	0.732	1.630	1.585	1.918	1.896	1.698	1.666
0.5	0	0.728	1.632	1.594	1.913	1.892	1.698	1.665
0.5	0	0.733	1.621	1.588	1.928	1.897	1.698	1.670
1	0	0.718	1.652	1.586	1.944	1.911	1.714	1.691
1	0	0.731	1.647	1.587	1.945	1.914	1.715	1.697
1	0	0.732	1.642	1.588	1.949	1.913	1.717	1.705
1	0	0.738	1.649	1.594	1.948	1.915	1.717	1.704
2.5	0	0.731	1.680	1.593	2.002	1.941	1.740	1.744
2.5	0	0.731	1.675	1.590	2.006	1.947	1.743	1.747
2.5	0	0.714	1.676	1.588	1.996	1.943	1.738	1.744
2.5	0	0.731	1.666	1.591	1.994	1.941	1.742	1.752
5	0	0.737	1.701	1.590	2.061	1.972	1.766	1.780
5	0	0.729	1.697	1.592	2.061	1.975	1.766	1.784
5	0	0.722	1.697	1.593	2.058	1.969	1.762	1.779
5	0	0.724	1.694	1.597	2.058	1.970	1.763	1.789
7.5	0	0.746	1.725	1.595	2.131	2.014	1.793	1.822
7.5	0	0.717	1.720	1.590	2.133	2.003	1.790	1.817
7.5	0	0.716	1.720	1.595	2.135	2.000	1.793	1.812
7.5	0	0.724	1.714	1.597	2.144	2.010	1.796	1.823
7.5	0	0.734	1.727	1.589	2.149	2.010	1.796	1.828
10	0	0.714	1.748	1.583	2.217	2.043	1.824	1.857
10	0	0.726	1.764	1.591	2.242	2.050	1.832	1.879
10	0	0.735	1.756	1.598	2.251	2.059	1.837	1.886
10	0	0.726	1.769	1.592	2.258	2.057	1.833	1.885
10	0	0.717	1.774	1.588	2.258	2.058	1.837	1.887
10	0	0.733	1.775	1.591	2.278	2.068	1.842	1.906
10	0	0.744	1.767	1.598	2.281	2.068	1.845	1.912
10	0	0.712	1.770	1.590	2.281	2.056	1.839	1.910
10	0	0.715	1.772	1.595	2.282	2.056	1.838	1.901
10	0	0.716	1.774	1.592	2.288	2.068	1.844	1.915
10	0	0.738	1.999	1.715	2.539	2.317	2.079	2.215
10	0	0.719	1.990	1.713	2.531	2.307	2.071	2.203
10	0	0.710	1.977	1.683	2.510	2.292	2.049	2.183
10	0	0.732	1.952	1.687	2.483	2.272	2.037	2.162
10	1	0.717	1.940	1.668	2.461	2.238	2.007	2.130

10	1	0.716	1.936	1.667	2.467	2.240	2.012	2.134
10	1	0.724	1.936	1.664	2.450	2.220	1.995	2.117
10	3	0.717	1.946	1.652	2.497	2.237	2.006	2.119
10	3	0.712	1.951	1.648	2.514	2.247	2.008	2.123
10	3	0.715	1.961	1.655	2.520	2.248	2.013	2.128
10	3	0.708	2.145	1.658	2.878	2.496	2.213	2.334
10	3	0.714	2.146	1.651	2.877	2.483	2.213	2.336
10	3	0.715	2.149	1.656	2.913	2.520	2.246	2.361
10	5	0.690	2.227	1.661	2.943	2.580	2.282	2.443
10	5	0.698	2.248	1.662	2.954	2.597	2.286	2.451
10	6	0.664	2.834	1.633	3.692	3.246	2.822	3.028
10	6	0.681	2.847	1.635	3.743	3.278	2.855	3.047
10	6	0.681	2.989	1.628	3.882	3.413	2.984	3.176
10	6	0.674	3.170	1.623	4.061	3.561	3.106	3.315
10	6	0.683	3.168	1.616	4.080	3.577	3.116	3.320
10	6.4	0.632	3.780	1.598	4.827	4.261	3.675	3.946
10	6.8	0.615	4.517	1.605	5.704	5.132	4.378	4.755
10	7	0.565	4.925	1.596	6.167	5.592	4.699	5.217
10	7.2	0.500	5.671	1.596	6.856	6.285	5.212	5.897
10	7.2	0.500	5.668	1.591	6.876	6.279	5.201	5.889
10	7.4	0.500	5.968	1.589	7.117	6.602	5.430	6.245

Table B2-7 Flow Data, Shear Cycle 3b

Due to fracturing of the model, no useful flow data were recovered.

Appendix B2 Summary of Flow Tests run on LSR-2
Table B2-8

Test	Normal Stress (MPa)	Shear Stress (MPa)	Flow Test *	Test	Normal Stress (MPa)	Shear Stress (MPa)	Flow Test *
N-1	0.1	0.0	L	N-3 cont.	6.0	0.0	L, C
	0.2	0.0	L		8.0	0.0	L
	0.5	0.0	L		10.0	0.0	L, C
	1.0	0.0	L, C		8.0	0.0	L
	2.0	0.0	L		6.0	0.0	L, C
	4.0	0.0	L		4.0	0.0	L
	6.0	0.0	L, C		2.0	0.0	L
	8.0	0.0	L		1.0	0.0	L, C
	10.0	0.0	L, C		0.5	0.0	L
	8.0	0.0	L				
	6.0	0.0	L, C	S-1	0.2	0.0	L
	4.0	0.0	L		0.5	0.0	L
	2.0	0.0	L		1.0	0.0	L
	1.0	0.0	L,C		2.0	0.0	L, C
	0.5	0.0	L		2.0	0.3	L
	0.2	0.0	L		2.0	0.5	L
					2.0	0.8	L
N-2	0.2	0.0	L		2.0	1.0	L
	0.5	0.0	L		2.0	1.1	L
	1.0	0.0	L, C		2.0	1.2	L
	2.0	0.0	L		2.0	1.3	L, C
	4.0	0.0	L		2.0	1.0	L
	6.0	0.0	L, C		2.0	0.5	L
	8.0	0.0	L		2.0	0.0	L
	10.0	0.0	L, C		1.0	0.0	L
	8.0	0.0	L		0.5	0.0	L
	6.0	0.0	L, C				
	4.0	0.0	L	S-2	0.2	0.0	L
	2.0	0.0	L		0.5	0.0	L
	1.0	0.0	L, C		1.0	0.0	L
	0.5	0.0	L		2.0	0.0	L, C
	0.2	0.0	L		5.0	0.0	L, C
					5.0	0.5	L
N-3	0.2	0.0	L		5.0	1.0	L
	0.5	0.0	L		5.0	1.5	L
	1.0	0.0	L, C		5.0	2.0	L
	2.0	0.0	L		5.0	2.5	L, C
	4.0	0.0	L		5.0	1.5	L, C

Appendix B2 Summary of Flow Tests run on LSR-2
Table B2-8

Test	Normal Stress (MPa)	Shear Stress (MPa)	Flow Test *	Test	Normal Stress (MPa)	Shear Stress (MPa)	Flow Test *
S-3a	2.5	0.0	L	S-3b	0.2	0.0	L
	0.2	0.0	L		5.0	0.0	L
	0.5	0.0	L		10.0	0.0	L, C
	1.0	0.0	L		10.0	1.0	L
	2.5	0.0	L		10.0	3.0	L
	5.0	0.0	L		10.0	5.0	L
	7.5	0.0	L, C		10.0	7.4	L
	10.0	1.0	L				
	10.0	3.0	L				
	10.0	5.0	L, C				
	10.0	6.4	L				
	10.0	6.8	L				
	10.0	7.0	L				
	10.0	7.2	L				
	10.0	7.4	L				

* Flow Test: L = Lengthways, C = Crossways

Appendix C- Strain Gauge Completion Bridges

The standard method for measuring strains is by the use of electrical resistance strain gauges. These are read by a precision voltmeter measuring the output of a balanced Wheatstone Bridge composed of three precision resistors (120 ohms, 0.1 percent tolerance) and a strain gauge, whose resistance varies with the amount of strain applied to the gauge. Figure C-1 illustrates a typical Wheatstone bridge circuit connected to a voltmeter, such as a HP3455A, which was used in the testing of LSR-2.

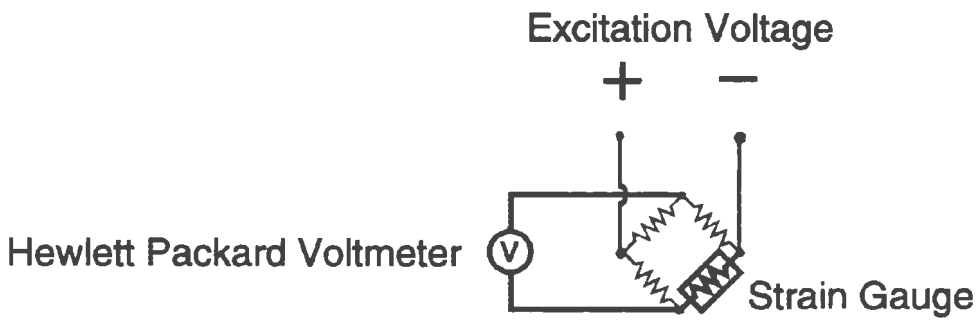

Figure C-1. Typical Wheatstone Bridge Circuit

Suitable equipment for the measurement of strain was in short supply during the testing of LSR-2. Completion equipment to monitor 40 strain gauges

was built in house at Memorial University as an economic alternative to buying or renting commercial equipment. These completion bridges were connected to a Hewlett Packard HP 3455A precision (6 1/2 digit) voltmeter, through a HP3495A forty channel switch. The data was recorded by a scanning program written in the Viewdac programming language, run on the PC that controlled the loading of LSR-2 .

The completion bridges were built on glass-epoxy etched circuit boards, with 10 channels per board. Figure C-2 is the circuit board pattern. Note that the board is set up for 2 or 3 wire strain gauge configuration. Details on 3 wire configuration can be obtained from any standard text on strain gauges, or manufacturers notes. For the testing of LSR-2 , two wire configuration was used.

The system was tested for accuracy with a cantilever beam arrangement, with a single strain gauge on the top of the beam. The beam was securely mounted, and four equal weights were added to a hook attached to the other end of the beam. The resultant strains were monitored with a HP3497A strain gauge set-up, and with the "Home Built" bridges. Output from the test

is presented as Figure C-3, Microstrains versus Time, for each apparatus. Note that the output is in positive microstrains for tensile strain.

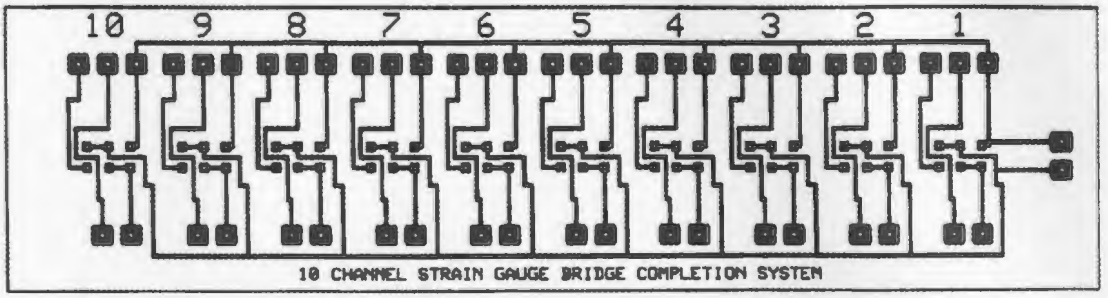

Figure C-2 Circuit Board Pattern for Strain Gauge completion bridges. The Voltmeter terminals are along the bottom of the diagram, power supply excitation is on the left end, and the strain gauges are connected along the top. For two wire configuration, the middle and right terminal of each group of three were joined. The full size dimensions of the board are 190 mm by 50 mm.

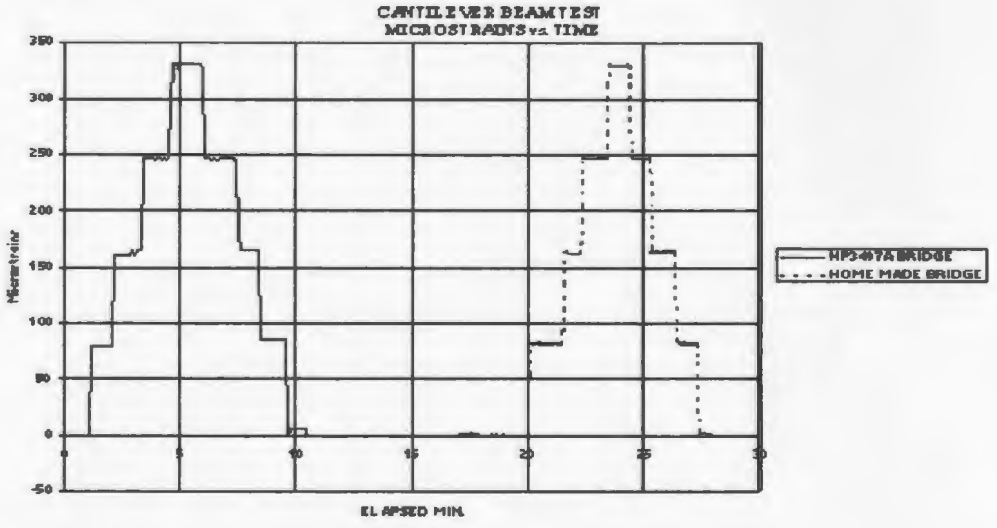

Figure C-3 Results of the Cantilever Beam test on the strain gauge bridges.

Appendix D - Determination of Thermal Characteristics of LSR-2 and Strain Drift Correction Procedures

D-1 Determination of Thermal Characteristics of LSR-2

Prior to the construction of the model for this series of experiments, a test block was constructed to investigate the effects of the heat sinks and cooling loops on the thermally induced strain gauge drift. This block contained 9 strain gauges, brass heat sinks, and a cooling loop of similar configuration to that incorporated in LSR-2. As well, several temperature monitoring ports were incorporated into the block, to measure the internal temperature variations due to the strain gauges and the application of cooling water to the cooling loop. Initial results were encouraging for a direct temperature - drift relationship. However, when similar procedures were applied to LSR-2, it was found that with 78 active gauges in a block of similar size, a relationship couldn't be determined due to the overlapping effects of the many gauges in close proximity to each other, unless the temperature could be monitored at each individual strain gauge. It was noted that the application of cooling did help reduce (but not eliminate) the drift in the strain readings. Further experimentation with the test block, and LSR-2 prior to the testing, showed that the drift could be reduced even further by turning on the

strain gauge excitation voltage immediately prior to the strain reading, and shutting it off after, to allow the heat to dissipate from the gauge. The duty cycle eventually selected was to turn on the power to all gauges for 20 seconds to allow the power supply to stabilise, scan all gauges (2 minutes) and then shut off the power for 7 minutes 40 seconds. Throughout all these tests, the power supply was run at 3.4 volts output, which was the minimum voltage the supply could be set at.

Butt (1994) noted that the self heating curves for the strain gauges used in his experiment had self heating curves of the form $f(t) = At^b$. To verify this, four 5 day data collection background surveys were run prior to testing. It was noted that after the first 24 to 36 hours of strain gauge monitoring, the drift was essentially linear for most gauges. However, from test to test, the slope of the drift curves for each gauge were never the same. Therefore, to aid in the removal of a linear drift from the gauges, the strain gauge record was started approximately 2 days prior to the test.

D-2 Strain Drift Correction Procedures

The strain gauge data were measured by two Hewlett Packard datalogger configurations. The first configuration was an HP-3497A with five 10

channel strain gauge cards, for a total of 50 channels. The second configuration was an HP-3455A Voltmeter in combination with its HP-3495A scanner unit, with four 10 channel in house built strain gauge cards. This latter 40 channel configuration, combined with the first configuration, gave a total of 90 strain gauge channels read. The data were recorded on a PC running Keithley/Viewdac software in 9 groups of 10 channels, plus a tenth group recording the loads and internal model temperatures.

Data collection were run continuously throughout the duration of the testing schedule to record background data. This was essential for the removal of the self heating drift of the strain gauges.

The raw data were imported into Microsoft Excel 5.0, where they were converted to microstrains, and plotted against time, for each group of 10 strain gauges (Figure D-1).

From this point, the raw microstrains were corrected by subtracting out the drift data obtained from the dummy gauges imbedded in the Thermal 1 test block. This drift was seen to be generally small with respect to the overall thermal drift in LSR-2, and is attributed to the effects of room temperature on

the strain gauge wiring. These effects were most noticeable during the days of severe weather conditions during the testing process. The slope of each data curve was determined over a 20 hour period prior to the test. This slope was subtracted from the data in the form: corrected data = raw data - (slope of background * elapsed time since data record began), which flattened out the data records. All strain gauge data were then zeroed at the beginning of the test by subtracting that value from all of the values in the data file (Figure D-2).

Once the thermal drift has been removed, the strain gauge data were then tabulated and plotted against stress (Figure D-3).

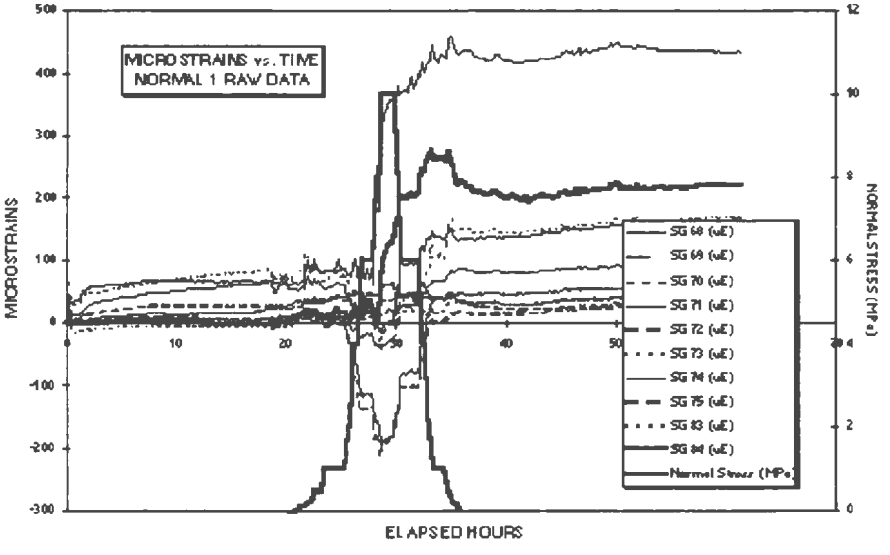

Figure D-1. Typical plot of uncorrected microstrains versus time. Note the plot of Normal Stress versus time superimposed over the data. The strain gauge data on either side of the loading data curve are background data essential to the removal of the strain gauge drift.

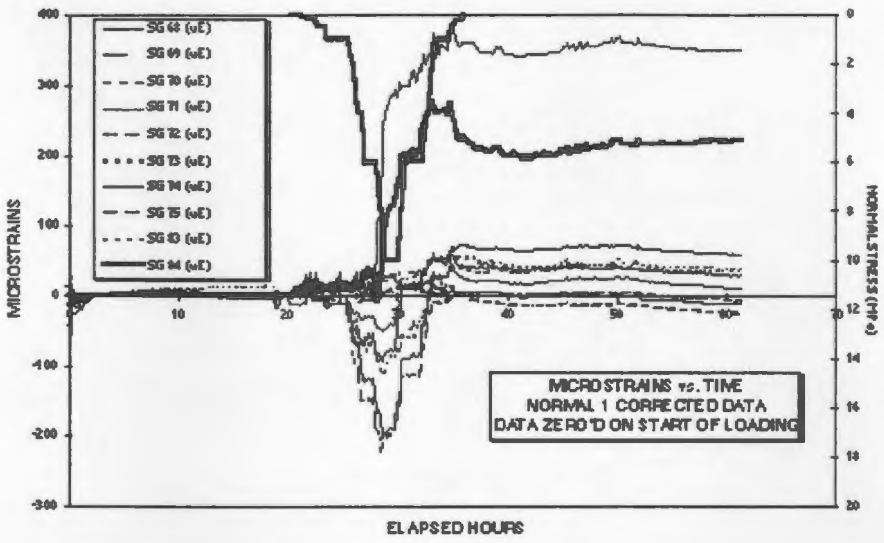

Figure D-2 Data are flattened on the pre-test background, then zeroed at the start of loading.

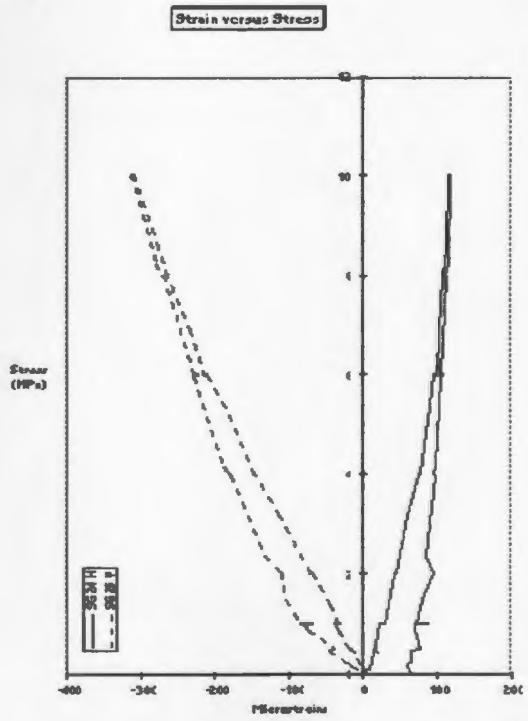

Figure D-3 Typical plot of stress versus corrected strains.